

INNOVATIVE HEAT EXCHANGERS FOR SOLAR WATER HEATERS

by

Yen Chean Soo Too

BE (Hons)

A thesis submitted in partial fulfilment
of the requirements for the degree of
Doctor of Philosophy

School of Mechanical and Manufacturing Engineering
University of New South Wales

December 2007

PLEASE TYPE**THE UNIVERSITY OF NEW SOUTH WALES
Thesis/Dissertation Sheet**

Surname or Family name: SOO TOO

First name: Yen Chean

Other name/s:

Abbreviation for degree as given in the University calendar:

PhD

School: Mechanical and Manufacturing Engineering

Faculty: Engineering

Title: Innovative Heat Exchangers for Solar Water Heaters

Abstract 350 words maximum: (PLEASE TYPE)

The performance of two innovative collector-loop heat exchangers used in pumped-circulation solar water heaters was investigated experimentally and numerically, and TRNSYS simulation models were developed for evaluating long-term performance. The heat exchangers evaluated are a narrow gap mantle on a vertical tank and a falling film system in a standard gas hot water tank. The falling film system is based on minor changes to a mass produced tank and does not require the addition of a special purpose heat exchanger.

The heat exchangers were assessed for a range of operating conditions to quantify the overall heat exchanger UA_{nx} value and the effect of thermal stratification in the tank. Flow visualisation experiments and CFD modelling were also performed to provide detailed understanding of the operation characteristics of the heat exchangers.

For each heat exchanger, the measured and computed collector loop side heat transfer coefficients were correlated by developing new Nusselt number versus Reynolds and Prandtl number functions. New heat transfer correlations were developed for both types of heat exchanger and have been implemented into full solar water heater simulation models in TRNSYS. Predictions of tank stratification conditions in each heat exchanger were in good agreement with experimental data.

Compared to a standard direct-circulation system, the annual performance of the mantle system and falling film system are 8% and 18% less respectively. The decrease in system performance is due to the heat exchanger penalty and reduced thermal stratification in the storage tank, however they have the added features of freeze protection and suitability for hard water areas. They are also cheaper to manufacture than convectional heat exchange systems. The annual performance of a falling film solar water heater was shown to be affected by de-stratification if an in-tank electric booster was used. However, improved performance can be achieved if an advanced switching controller is used to modulate the flow rate such that the collector return temperature is always higher than the temperature in the top of the tank.

Declaration relating to disposition of project thesis/dissertation

I hereby grant to the University of New South Wales or its agents the right to archive and to make available my thesis or dissertation in whole or in part in the University libraries in all forms of media, now or here after known, subject to the provisions of the Copyright Act 1968. I retain all property rights, such as patent rights. I also retain the right to use in future works (such as articles or books) all or part of this thesis or dissertation.

I also authorise University Microfilms to use the 350 word abstract of my thesis in Dissertation Abstracts International (this is applicable to doctoral theses only).

.....
Signature.....
Witness.....
Date

The University recognises that there may be exceptional circumstances requiring restrictions on copying or conditions on use. Requests for restriction for a period of up to 2 years must be made in writing. Requests for a longer period of restriction may be considered in exceptional circumstances and require the approval of the Dean of Graduate Research.

FOR OFFICE USE ONLY

Date of completion of requirements for Award:

THIS SHEET IS TO BE GLUED TO THE INSIDE FRONT COVER OF THE THESIS

ORIGINALITY STATEMENT

'I hereby declare that this submission is my own work and to the best of my knowledge it contains no materials previously published or written by another person, or substantial proportions of material which have been accepted for the award of any other degree or diploma at UNSW or any other educational institution, except where due acknowledgement is made in the thesis. Any contribution made to the research by others, with whom I have worked at UNSW or elsewhere, is explicitly acknowledged in the thesis. I also declare that the intellectual content of this thesis is the product of my own work, except to the extent that assistance from others in the project's design and conception or in style, presentation and linguistic expression is acknowledged.'

Signed

Date

COPYRIGHT STATEMENT

'I hereby grant the University of New South Wales or its agents the right to archive and to make available my thesis or dissertation in whole or part in the University libraries in all forms of media, now or here after known, subject to the provisions of the Copyright Act 1968. I retain all proprietary rights, such as patent rights. I also retain the right to use in future works (such as articles or books) all or part of this thesis or dissertation.

I also authorise University Microfilms to use the 350 word abstract of my thesis in Dissertation Abstract International (this is applicable to doctoral theses only).

I have either used no substantial portions of copyright material in my thesis or I have obtained permission to use copyright material; where permission has not been granted I have applied/will apply for a partial restriction of the digital copy of my thesis or dissertation.'

Signed

Date

AUTHENTICITY STATEMENT

'I certify that the Library deposit digital copy is a direct equivalent of the final officially approved version of my thesis. No emendation of content has occurred and if there are any minor variations in formatting, they are the result of the conversion to digital format.'

Signed

Date

Acknowledgement

I would like to express my sincere gratitude and appreciation to my thesis supervisors, Em Prof Graham L. Morrison, Prof Masud Behnia (Dean of Graduate Studies, University of Sydney) and Dr Tracie Barber for their excellent supervision, suggestions and patience throughout my PhD.

I would also like to thank Rheem Australia Pty. Ltd, in particular Senior Product Development Engineer, Mr Brendon Brouke, for providing the prototype test units.

Further acknowledgement must be given to Mr Enoch Grace for his technical support and help throughout my project.

In addition, I would like to thank all my colleagues during this project, especially Indra Budihardjo for his assistance and advice on PIV and FLUENT.

Finally, I would like to thank my family for their encouragement and support.

Abstract

The performance of two innovative collector-loop heat exchangers used in pumped-circulation solar water heaters was investigated experimentally and numerically, and TRNSYS simulation models were developed for evaluating long-term performance. The heat exchangers evaluated are a narrow gap mantle on a vertical tank and a falling film system in a standard gas hot water tank. The falling film system is based on minor changes to a mass produced tank and does not require the addition of a special purpose heat exchanger.

The heat exchangers were assessed for a range of operating conditions to quantify the overall heat exchanger UA_{hx} value and the effect of thermal stratification in the tank. Flow visualisation experiments and CFD modelling were also performed to provide detailed understanding of the operation characteristics of the heat exchangers.

For each heat exchanger, the measured and computed collector loop side heat transfer coefficients were correlated by developing new Nusselt number versus Reynolds and Prandtl number functions. New heat transfer correlations were developed for both types of heat exchanger and have been implemented into full solar water heater simulation models in TRNSYS. Predictions of tank stratification conditions in each heat exchanger were in good agreement with experimental data.

Compared to a standard direct-circulation system, the annual performance of the mantle system and falling film system are 8% and 18% less respectively. The decrease in system performance is due to the heat exchanger penalty and reduced thermal stratification in the storage tank, however they have the added features of freeze protection and suitability for hard water areas. They are also cheaper to manufacture than convectional heat exchange systems. The annual performance of a falling film solar water heater was shown to be affected by de-stratification if an in-tank electric booster was used. However, improved performance can be achieved if an advanced switching controller is used to modulate the flow rate such that the collector return temperature is always higher than the temperature in the top of the tank.

Table of Contents

Abstract	II
Acknowledgement	III
Table of Contents	IV
Nomenclature	IX
List of Publications	XII
CHAPTER 1: AN OVERVIEW	1
1.1 INTRODUCTION	1
1.2 CLASSIFICATION OF SOLAR WATER HEATERS	2
1.3 TYPES OF COLLECTOR-LOOP HEAT EXCHANGERS	3
1.4 PROPOSED COLLECTOR-LOOP HEAT EXCHANGERS	7
1.4.1 Mantle heat exchangers with two-pass flow arrangement	7
1.4.2 Falling film heat exchangers	8
1.5 THESIS SCOPE	9
CHAPTER 2: LITERATURE REVIEW	12
2.1 INTRODUCTION	12
2.2 PERFORMANCE OF COLLECTOR-LOOP HEAT EXCHANGERS	13
2.2.1 Review of internal and external heat exchangers	13
2.2.2 Previous studies of mantle heat exchangers	16
2.3 FUNDAMENTAL STUDIES: FORCED CONVECTION	21
2.4 FALLING FILM FLOWS	24
2.4.1 Film flow regimes: theoretical studies	25
2.4.2 Mean film thicknesses: experimental studies	28
2.4.3 Heat transfer through falling films	32
2.5 SUMMARY	33

CHAPTER 3: EXPERIMENTAL APPARATUS AND TECHNIQUES	35
3.1 INTRODUCTION	35
3.2 MANTLE HEAT EXCHANGER PERFORMANCE MEASUREMENTS	36
3.3 FLOW VISUALISATION IN RECTANGULAR MANTLES	39
3.3.1 Experimental Setup	40
3.3.2 Dye Tracing	42
3.3.3 Particle image velocimetry (PIV) measurements	42
3.3.3.1 PIV technique	43
3.3.3.2 PIV measurement setup	43
3.3.3.3 Cross-correlation techniques	46
3.4 FALLING FILM SYSTEM MEASUREMENTS	47
3.4.1 Construction of falling film heat exchanger	47
3.4.2 Steady flow test rig for falling film	49
3.4.3 Collector flow rate controller	51
3.5 SUMMARY	53
CHAPTER 4: NUMERICAL SIMULATION TECHNIQUES	54
4.1 INTRODUCTION	54
4.2 FUNDAMENTALS OF CFD	55
4.3 TURBULENCE MODELLING	56
4.4 FLUID PROPERTIES	57
4.5 DISCRETISATION AND SOLUTION PROCEDURES	58
4.5.1 Discretisation of equations	58
4.5.2 Pressure-velocity coupling	58
4.6 GRID DEPENDENCE	59
4.7 SUMMARY	59
CHAPTER 5: FLOW IN RECTANGULAR MANTLES	60
5.1 INTRODUCTION	60
5.2 FLOW VISUALISATION	60
5.2.1 Narrow gap mantle: Dye tracing	62
5.2.2 Medium and wide gap mantles: Particle Image Velocimetry (PIV)	64
5.3 CFD MODELLING IN RECTANGULAR MANTLES	68
5.3.1 Computational domain	68
5.3.2 Grid dependence of numerical models	69
5.4 VALIDATION OF NUMERICAL MODEL	70
5.4.1 Flow in narrow gap mantles: CFD vs dye tracing	70

5.4.2	Flow in wide gap mantles: CFD vs PIV	72
5.4.3	Flow in medium gap mantles: CFD vs PIV	75
5.4.3	Heat transfer: CFD vs experiments	78
5.5	SUMMARY	79
CHAPTER 6: HEAT TRANSFER IN NARROW GAP MANTLE HEAT		
EXCHANGERS		
		80
6.1	INTRODUCTION	80
6.2	MEASUREMENTS OF HEAT EXCHANGER CHARACTERISTICS	81
6.2.1	Charging conditions	83
6.2.2	Preheated tank conditions	85
6.3	OVERALL HEAT TRANSFER PERFORMANCE	87
6.3.1	Heat transfer coefficients	87
6.3.2	Overall heat exchanger UA_{hx}	89
6.4	MANTLE HEAT EXCHANGER MODELLING	92
6.4.1	Computational domains	92
6.4.2	Grid refinement	95
6.4.3	Validation of numerical models	96
6.4.4	Flow and heat flux distribution	98
6.5	NON-DIMENSIONAL HEAT TRANSFER ANALYSIS	100
6.5.1	Mantle-side heat transfer correlation	100
6.5.1.1	Effect of flow rate	102
6.5.1.2	Effect of fluid properties	103
6.5.1.3	Effect of buoyancy	104
6.5.1.4	Development of mean Nusselt number correlation	105
6.5.1.5	Local heat transfer in developing flow	107
6.5.2	Tank side heat transfer correlation	108
6.6	EFFECT OF HEAT EXCHANGER SIZE	110
6.7	PREHEATED TANK CONDITIONS	113
6.8	OTHER MANTLE SPACINGS	115
6.9	SUMMARY	117
CHAPTER 7: CHARACTERISTICS OF FALLING FILM HEAT EXCHANGERS		
		119
7.1	INTRODUCTION	119
7.2	THERMAL MEASUREMENTS FOR CONSTANT FLOW RATE	120
7.3	ADVANCED CONTROLLER STRATEGY	125
7.3.1	Charging conditions	126

7.3.2	Preheated conditions	129
7.4	OVERALL HEAT TRANSFER CHARACTERISTICS	132
7.5	FILM FLOW BEHAVIOUR	136
7.6	FILM THICKNESS	140
7.7	HEAT TRANSFER CORRELATIONS	141
7.7.1	Film side convection heat transfer	141
7.7.1.1	Comparison of analytical solution and measurements	142
7.7.1.2	Non-dimensional correlation	144
7.7.1.3	Applicability of steady flow correlation	145
7.7.2	Correlation of tank side natural convection heat transfer	146
7.8	SUMMARY	147
 CHAPTER 8: SYSTEM MODELLING		 149
8.1	INTRODUCTION	149
8.2	MODELLING SOLAR WATER HEATERS	149
8.3	ONE-DIMENSIONAL HEAT EXCHANGER MODEL	151
8.3.1	Standard TYPE 60 model	151
8.3.2	Modifications of TYPE 60 model and verification	152
8.3.1.1	Mantle heat exchanger model	153
8.3.1.2	Falling film heat exchanger model	156
8.4	COMPLETE SOLAR WATER HEATER MODELS	161
8.4.1	Solar water heater with a mantle heat exchanger	161
8.4.2	Falling film system with an advanced controller	162
8.5	LOAD CYCLE SIMULATIONS	166
8.6	LONG-TERM PERFORMANCE OF MANTLE HEAT EXCHANGER SOLAR WATER HEATERS	169
8.6.1	Comparison of different system configurations	169
8.6.2	Effect of auxiliary element position	171
8.6.3	System size	172
8.6.4	Comparison of performance in different climatic conditions	173
8.7	LONG-TERM PERFORMANCE OF FALLING FILM SOLAR WATER HEATERS	174
8.7.1	Single-tank systems with in-tank boosting	174
8.7.2	Solar pre-heater systems	175
8.7.3	Effect of advanced controller strategy	177
8.7.4	Comparison of performance in different climatic conditions	180
8.7.5	Effect of film wettability	181
8.8	SUMMARY	182

CHAPTER 9: CONCLUSIONS AND FUTURE WORK	184
9.1 OVERVIEW	184
9.2 CONCLUDING REMARKS	185
9.2.1 Mantle heat exchangers	185
9.2.2 Falling film heat exchangers	186
9.2.3 Long-term performance	186
9.3 SUGGESTED FUTURE WORK	188
List of References	190
Appendices	198

Nomenclature

A_c	cross sectional area (m ²)
b	circumference of the falling film tube (m)
c_p	specific heat (J/kgK)
d_h	hydraulic diameter (m)
E	specific total enthalpy (J/kg)
F	correction factor for cross-flow heat exchanger
f_R	monthly average solar energy contribution
g	acceleration due to gravity (m/s ²)
Gr_d	Grashof number based on hydraulic diameter
H	tank height (m)
H_m	mantle height (m)
\bar{h}	mean convective heat transfer coefficient (W/m ² K)
h_x	local convective heat transfer coefficient (W/m ² K)
k	thermal conductivity (W/mK)
L	mantle length (m)
\dot{m}	mass flow rate (kg/s)
M	mass (kg)
\bar{Nu}	mean Nusselt number
Nu_x	local Nusselt number based on mantle length position
p	static pressure (kg/ms ²)
Q	volume flow rate (L/s)

\dot{Q}	heat transfer rate (W)
\dot{Q}_{loss}	heat loss (W)
\dot{Q}_{vol}	heat transfer rate to each tank volume (W)
\dot{q}_x	heat flux (W/m ²)
Pr	Prandtl number
r^*	radius ratio
R	thermal resistance (K/W)
Ra_H	Rayleigh number based on heat exchanger height
Ra_y	local Rayleigh number based on mantle vertical position
Re_d	Reynolds number based on hydraulic diameter
Re_δ	film Reynolds number based on film thickness
Re_f	film Reynolds number based on hydraulic diameter
Re_i	inlet Reynolds number
St	stratification correction parameter
T_a	ambient temperature (K)
$T_{col,o}$	collector outlet temperature (K)
$T_{col,i}$	collector inlet temperature (K)
T_i	heat exchanger inlet temperature (K)
T_o	heat exchanger outlet temperature (K)
T_t	tank temperature (K)
$T_{t,top}$	average temperature of the top half of the tank (K)
T_w	wall temperature (K)
ΔT_{lm}	log-mean temperature difference (K)
ΔT_{rise}	temperature rise across the collector (K)
ΔT_{start}	temperature difference between $T_{col,o}$ and $T_{t,top}$ (K)
t	time (s)

t_w	wall thickness (m)
UA_{hx}	overall heat transfer coefficient and area product (W/K)
U_L	tank heat loss coefficient (W/m ² K)
v	velocity (m/s)
V_i	volume of each tank element (m ³)
w	mantle spacing (m)
x^*	dimensionless thermal entrance length
x	coordinate in direction L (m)
y	coordinate in direction H (m)
z	coordinate in direction w (m)

Greek symbols

β	thermal expansion coefficient (1/K)
ε^*	modified heat exchanger effectiveness
δ	film thickness (m)
$\bar{\delta}$	mean film thickness (m)
η_c	collector efficiency
ρ	density (kg/m ³)
μ	dynamic viscosity (Pa s)
ν	kinematic viscosity (m ² /s)

Subscripts

f	falling film side
i	inlet
m	mantle side
o	outlet
t	tank

List of Publications

Journal Article

Soo Too Y.C., Morrison G.L. and Behnia M., 2007, "Performance of solar water heaters with vertical mantle heat exchangers," *Solar Energy*, submitted.

Peer-reviewed Conference Papers

1. Soo Too Y.C., Morrison G.L. and Behnia M., 2004, "Vertical mantle heat exchangers for solar water heaters," In *Proceedings of ANZSES Annual Conference*, December, Perth, Australia.
2. Soo Too, Y.C., Morrison, G.L. and Behnia, M., 2005, "Heat transfer and flow visualisation in vertical mantle heat exchangers for solar water heaters," *6th World Conference on ExHFT*, April, Matshushima, Miyagi, Japan.
3. Soo Too, Y.C., Morrison, G.L. and Behnia, M., 2005, "Experimental and numerical evaluation of solar water heaters with vertical mantle heat exchangers," *ISES Solar World Congress*, August, Orlando, USA.
4. Soo Too Y.C. and Morrison G.L., 2005, "Performance of a solar water heater with a vertical mantle heat exchanger," In *Proceedings of ANZSES Annual Conference*, November, Dunedin, New Zealand.
5. Soo Too Y.C. and Morrison G.L., 2006, "Design of mantle heat exchangers for solar water heaters," *13th International Heat Transfer Conference*, August, Sydney, Australia.
6. Soo Too Y.C., Morrison G.L. and Behnia M., 2006, "Falling film heat exchangers for solar water heaters," In *Proceedings of ANZSES Annual Conference*, September, Canberra, Australia.
7. Soo Too, Y.C., Morrison, G.L. and Behnia, M., 2007, "Performance of falling film heat exchangers for solar water heaters," *ISES Solar World Congress*, September, Beijing, China.

- CHAPTER 1 -

AN OVERVIEW

1.1 INTRODUCTION

Solar hot water systems offer an environmental friendly way to transfer solar radiation directly to thermal energy for heating water. In the last decade, the utilisation of solar energy as a sustainable alternative to fossil fuel for water heating has received favourable attention and as a result, the world market for solar hot water products has increased significantly. Over the year 2003, the reported annual domestic and commercial solar hot water collector installed capacity was approximately 91.6 GW, corresponding to 130.8 million square meters of collector area in operation around the world (IEA SHC, 2005). These products achieved a substantial energy savings, particularly in the domestic sector, and a reduction of 24.1 million tons of CO₂ emissions annually (IEA SHC, 2005). In countries like China, Australia, Greece, Israel and Germany, solar water heater production has become a major industry. This has led to the development of cost-effective systems, including new concepts to reduce manufacturing cost, improve performance and optimise the energy utilisation. An inherent problem with solar water heaters is the need to provide economical and reliable freeze protection for systems installed under climatic conditions with potential to freeze. The most common and effective freeze protection configuration is the use of an anti-freeze solution in a closed-loop collector circuit with a heat exchanger. The work presented in this thesis involves assessment of the heat exchange characteristics and evaluation of the long-term performance of two collector-loop heat exchangers: the mantle heat exchanger and the falling film heat exchanger. In this chapter, an overview of solar water heater classification and existing collector-loop heat exchanger designs is presented.

1.2 CLASSIFICATION OF SOLAR WATER HEATERS

The basic configurations of a solar water heater for water heating ($<70^{\circ}\text{C}$) in residential applications consists of:

- 1) A solar collector that absorbs solar energy and transfers heat to the working fluid. The collectors can be in the form of a flat absorber plate or a tubular absorber envelope with a vacuum tube,
- 2) A means of transferring energy from the collector to the storage tank,
- 3) An auxiliary heat source, such as a separate electric and gas storage water heater or in-tank electric boosting, used when the solar water heater operates under low solar radiation conditions.

Solar water heaters can be classified by the method of energy transfer between the collector working fluid and the potable water in the storage tank. The simplest type of solar water heater, which is referred to as a direct system, consists of a solar collector array linked directly to a storage tank. Water heated in the solar collector is transferred directly to the potable water either via natural convection circulation of potable water between the collector and the storage tank (thermosyphon system), or with the aid of a low-flow circulation pump. Such systems are low in cost and offer a thermodynamically efficient way of heating potable water. However, direct systems installed in cold climates or in locations with low night-sky temperature often experience freezing in the collector riser tubes and as a result, the collector can be damaged due to the expansion of ice in the collector or plumbing. Several techniques have been employed in direct systems to prevent freezing, including the use of water dump valves, drain-back or drain-down concepts, an electric heater in the collector header and tapered collector riser tube design to control ice growth in the collector riser (Xinian *et al.*, 1994). However, these techniques only provide sufficient freeze protection for systems installed in locations with occasional freezing problems. Another problem associated with direct circulation systems is that contaminants in the potable water tend to deposit in the riser tubes and bottom header of the collector, resulting in clogging of the collector fluid passageways.

To overcome such problems, separating the collector fluid from the potable water in the storage tank is the most effective method. This can be achieved by incorporating a heat exchanger between the collector and the storage tank. This configuration is known as an indirect system. In an indirect system an anti-freeze solution (propylene glycol/water mixture) can be used in the closed collector-heat-exchanger loop as the working fluid to transfer heat from the collector to the water in the tank, and provide freeze protection. Although indirect systems provide reliable freeze protection, the inclusion of a collector-loop heat exchanger has limitations, such as thermodynamic penalty, higher capital cost and complex construction. Furthermore, appropriate integration of the heat exchanger with the storage tank is an important consideration so that thermal stratification in the tank can be promoted to achieve optimum system performance. The benefit of a thermally stratified storage tank over fully mixed tank is that the top of the solar preheat section is maintained close to the desired load temperature, therefore reducing the use of auxiliary energy. Additionally, a lower return temperature to collector results in higher collector efficiency.

1.3 TYPES OF COLLECTOR-LOOP HEAT EXCHANGERS

In this section, an overview of collector-loop heat exchanger development for solar water heaters is presented. Previous collector-loop heat exchanger configurations varied from simple immersed bare tubes in the tank to external compact heat exchangers with tubes and fins. The most common types of collector-loop heat exchangers used in closed-loop solar water heaters are shown in Fig. 1.1.

1. AN OVERVIEW

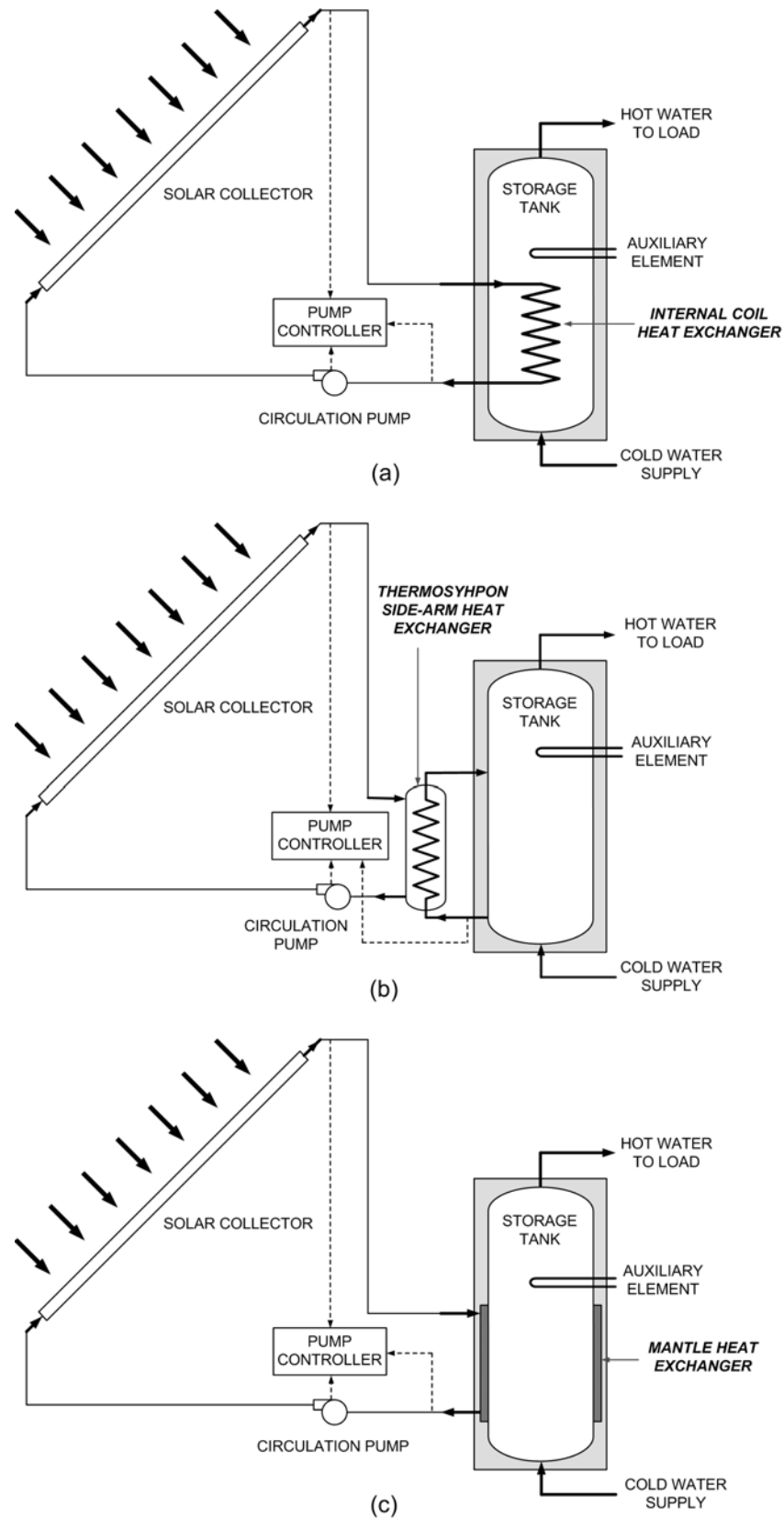


Fig. 1.1 Closed loop pumped-circulation solar water heaters with, (a) internal coil heat exchanger, (b) thermosyphon side-arm heat exchanger, (c) mantle heat exchanger.

In the 1980's, there were a number of investigations of the performance of internal heat exchangers in vertical and horizontal tanks for thermosyphon systems (Mertol *et al.*, 1981; Webster *et al.*, 1987), and vertical-tank pumped-circulation systems (Feiereisen *et al.*, 1982; Farrington and Bingham, 1986). In pumped-circulation systems, the typical heat exchanger design is based on a helical coil tube that is immersed in the bottom half of a vertical-tank (Fig. 1.1a) just below the in-tank auxiliary boosting element. These immersed-coil heat exchangers are low cost and have been widely adopted in single-family solar water heaters in Europe. As the hot water rises in the tank as a plume, it can cause mixing, resulting in a low degree of thermal stratification in the storage tank. In some designs, a diffuser is used above the coil so that water heated by the immersed coil can be distributed near its thermal equilibrium level. Internal heat exchangers used for pumped-circulation solar water heaters can provide adequate heat transfer between the collector loop and the tank, depending on the design, location and orientation of the heat exchanger. However, such arrangements are difficult to incorporate into convention enamelled steel hot water tanks.

For domestic solar water heating in North America and Canada, pumped-circulation systems are commonly based by retrofitting an external heat exchanger to a standard mass-produced hot water tank. Such external heat exchangers (Fig. 1.1b) are based on a shell and tube arrangement in which the collector fluid is pumped through the shell and the tank-water-side thermosyphons through the tubes of the heat exchanger and to the top section of the tank to enhance storage stratification. This type of collector-loop heat exchanger is usually known as a natural convection heat exchanger or a side-arm heat exchanger (Parent *et al.*, 1990; Fraser *et al.*, 1995; Purdy *et al.*, 1998). An inherent problem with this design is that contaminants in the potable water tend to build up in the tube section of the heat exchanger on the tank-water-side of the heat exchanger. To overcome the fouling problem in the heat exchanger, Harrison (2005) has reported a way of using the load flow to back-flush the heat exchanger tube without interrupting the system operation.

Another type of collector-loop heat exchanger used for solar water heating utilises two concentric cylinders to form an annular space jacketed around the core storage tank.

Heat is transferred from the collector fluid to the potable water in the tank through the cylindrical tank wall. This collector-loop heat exchanger is known as a jacket or mantle heat exchanger (Fig. 1.1c). In general, mantle heat exchangers are easy to construct and provide large heat transfer area and improved performance (Furbo, 1993), resulting in extensive use of such systems as an alternative to external and internal collector-loop heat exchangers. Mantle heat exchangers have been widely used for horizontal-tank thermosyphon systems (Morrison *et al.*, 1999) in Australia, Greece and Israel, and recently, they have also being adopted on vertical-tank pumped-circulation systems (Shah, 1999; Knudsen, 2004) based on the low-flow concept. Typical annular spacings used in commercial horizontal tank mantle heat exchangers are in a range of 5 to 10 mm and the annular mantle is normally wrapped around the full circumferential of the tank. For systems designed to be solar pre-heaters, the collector return is commonly located at the top of the mantle in order to achieve optimum thermosyphon circulation in the closed collector loop and to promote thermal stratification in the tank. When an in-tank electric boosting element is used in horizontal mantle tanks, the collector return has to be mounted beneath the electric element or at the bottom of the mantle.

In Europe, mantle heat exchangers are used for vertical-tank pumped circulation systems with a low collector flow rate (approximately 0.2 L/min/m^2 collector). The typical annular spacing varies from 20 to 35 mm. The mantle is commonly wrapped around the bottom half of the storage tank just below the in-tank electric heating element. In some designs, the mantle extends over the full height of the tank in order to obtain the largest possible heat transfer area. However, there is a possibility of de-stratification in the tank when the collector return is cooler than the hot layer at the tank top. For a wider annular mantle wrapped around the bottom half of the tank, the flow in the gap is mainly governed by buoyancy driven circulation and most of the heat transfer occurs in the top 20% of the mantle (Shah, 1999; Knudsen, 2004). As a result, a high degree of thermal stratification is observed inside the storage tank for this design.

1.4 PROPOSED COLLECTOR-LOOP HEAT EXCHANGERS

There have been many types of collector-loop heat exchanger designs proposed for use in solar water heaters based on common plumbing practices and solar market considerations in different countries. However, the primary consideration of manufacturers is to minimise the capital cost while retaining optimum performance. In this thesis, two innovative heat exchanger designs are proposed for use in vertical-tank pumped-circulation solar water heaters. They have the potential to offer a cost-effective way of transferring solar heat from the collector array to the potable water in the storage tank. These collector-loop heat exchangers are referred to as a mantle heat exchanger with a two-pass flow arrangement and a falling film heat exchanger. The main features of these heat exchangers are presented in the following sections.

1.4.1 Mantle heat exchangers with two-pass flow arrangement

The first proposed collector-loop heat exchanger design incorporates a narrow mantle with 3 mm spacing jacketed around the bottom half of the storage tank. They are cheap and easy to manufacture. A horizontal divider is placed halfway down the mantle (Fig. 1.2) to force the collector fluid to flow circumferentially around the tank in two passes. The combined features of the narrow mantle gap and longer flow path means that the contact between the hot collector fluid and the tank wall increases so that the heat transfer area can be effectively utilised, thereby improving the heat exchanger effectiveness.

The mantle heat exchanger design presented in this thesis differs from typical European mantles (Shah and Furbo, 1998; Knudsen, 2004) which have annular spacing approximately 10 times larger and operate with a very low collector flow rate. The flow in a narrower-gap mantle is expected to spread evenly over the mantle heat transfer surface compared to the recirculation flow at the top 20% of a wider gap mantle found by Shah *et al.* (1999).

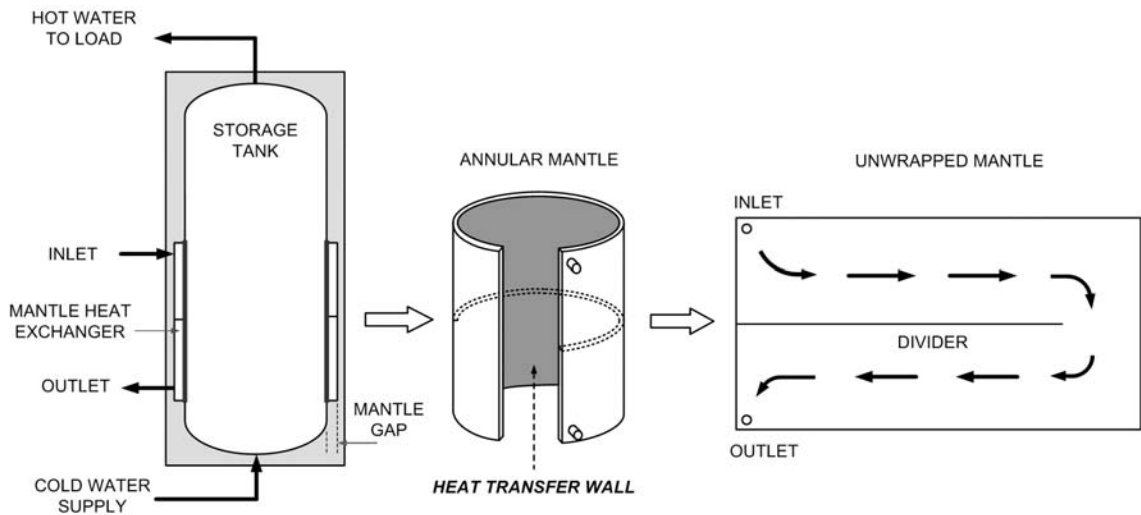


Fig. 1.2 Unwrapping annular mantle heat exchanger with a two-pass arrangement on a vertical tank.

1.4.2 Falling film heat exchangers

The second collector-loop heat exchanger design investigated in this thesis is known as a falling film heat exchanger. The falling film heat exchanger (Fig. 1.3) consists of a core tube down the centre of a water storage tank with the hot collector fluid flowing over the inner surface of the core tube as a thin film. The heat exchanger and tank are based on standard mass-produced gas storage hot water tanks. The heat exchanger tube is the chimney for gas combustion when the tank is used as a standard gas water heater. By adapting such a readily available hot water tank for solar hot water applications, it is possible to construct a system with a collector loop heat exchanger without the need to construct a special purpose heat exchanger. Such systems also offer reliable freeze protection by draining the collector fluid back to the core tube when the circulation pump is turned off. However, as the falling film tube extends from the top to the bottom of the storage tank, there is a possibility of de-stratification in the tank if the collector return temperature is lower than the temperature in the top portion of the tank. To overcome possible de-stratification, a programmed collector flow rate controller is implemented to modulate the flow rate so that a positive heat input to the top portion of the tank is always achieved.

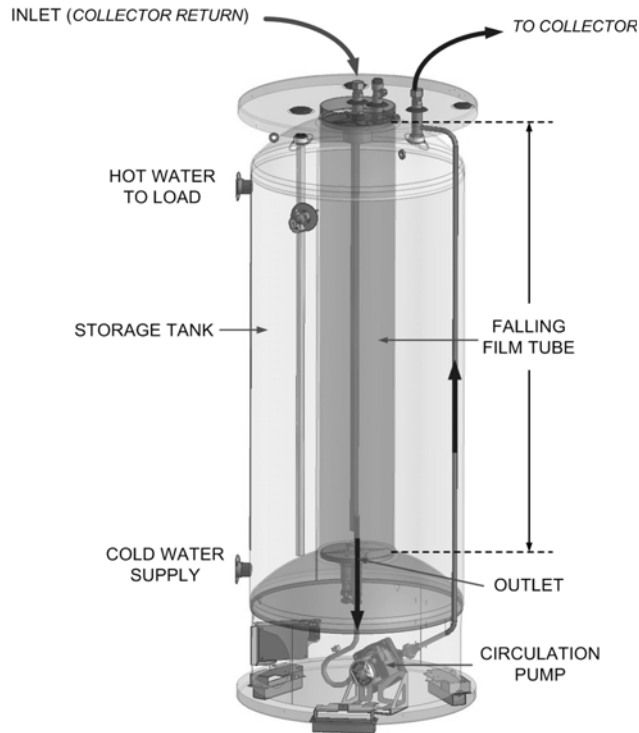


Fig. 1.3 Falling film heat exchanger and storage tank.

1.5 THESIS SCOPE

Although wide gap mantle heat exchangers have been intensively investigated for use in low-flow pumped systems, there has not been an investigation of narrow gap mantles where forced convection is dominant. The falling film heat exchanger is based on minor changes to a mass produced tank and does not require the addition of a special purpose heat exchanger (new concept for solar water applications). The long-term performance of solar water heaters incorporating these heat exchangers has not been evaluated and published in literature.

The work presented in this thesis aims to investigate the heat transfer characteristics of both the mantle heat exchanger with two-pass flow arrangement and the falling film heat exchanger, and evaluate the long-term performance for both systems using the TRNSYS solar simulation program (Klein *et al.*, 2001). Although models of heat exchangers in hot water storage tanks are available in TRNSYS, the standard pipe flow heat exchanger routines are not applicable for characterising the dependency of the

proposed heat exchangers' performance on product design parameters. To extend the TRNSYS program to cover the new heat exchanger designs, new heat transfer correlations for the proposed heat exchangers are required.

In this thesis, the performance of the two new heat exchangers has been evaluated in several stages:

- The heat exchangers are assessed by carrying out heat-up tests for a range of operating conditions. These experiments are aimed to quantify the overall heat exchanger UA_{hx} value and the effect of thermal stratification in the tank.
- Flow visualisation experiments and CFD modelling (FLUENT, 2005) are performed to provide detailed understanding of the operation characteristics of the heat exchangers.
- Measurements of the heat transfer coefficients for the heat exchangers are aimed to characterise the heat transfer rate of the heat exchangers as a function of dependent variables.
- System simulation models in TRNSYS are developed to predict the long-term performance of solar water heaters incorporating these heat exchangers and to provide a design tool for system optimisation.

The outline of the thesis is as follows:

Chapter 2: Previous studies of the characteristics of collector loop heat exchangers. Literature survey of the types of flows and heat transfer processes related to mantle and falling film heat exchangers are reviewed.

Chapter 3: Outline of experimental techniques used to assess the flow behaviour and heat transfer characteristics of both novel types of heat exchangers.

Chapter 4: Fundamentals of Computational Fluid Dynamics (CFD) simulation program, FLUENT.

Chapter 5: The steady-state flow and heat transfer rate in a scaled rectangular mantle as a simplified geometric representation of a cylindrical mantle are investigated. CFD results are compared against the experimental results to evaluate the validity of the numerical model.

Chapter 6: Heat transfer characteristics of a narrow gap mantle on a cylindrical tank are assessed experimentally and numerically. An empirical heat transfer correlation for the narrow gap mantle heat exchanger is developed in terms of Reynolds number and Prandtl number.

Chapter 7: Thermal performance of a falling film heat exchanger is examined. The use of an advanced flow rate controller to minimise de-stratification is investigated. A non-dimensional heat transfer correlation of the falling film side is developed.

Chapter 8: The heat transfer correlations developed for both novel collector-loop heat exchangers are implemented in the widely used solar simulation program TRNSYS to predict annual system performance. Performance of systems are compared to a typical direct circulation system. The influences of system configuration on the long-term performance of both systems are evaluated for a range of climatic conditions.

Chapter 9: Conclusions and recommendations for future works are presented.

- CHAPTER 2 -

LITERATURE REVIEW

2.1 INTRODUCTION

Appropriate integration of a heat exchanger in a solar water heater is essential so that optimum performance can be achieved in areas with low water quality and adverse climatic conditions. Unlike a conventional heat exchanger, the thermal performance of a solar collector-loop heat exchanger can significantly influence the operation of other components of the system.

The first part of this chapter highlights previous studies concerning the characteristics of different collector-loop heat exchanger designs for use in solar water heaters. Particular attention is paid to detailed investigations conducted to evaluate the performance of mantle heat exchangers. As the falling film heat exchanger is a new concept in solar water heating system, there is no available literature on the thermal performance of these systems.

The second part of the chapter presents a literature survey of the types of flows and heat transfer processes that occur in the proposed heat exchangers. Fundamentals of forced convection heat transfer that occurs in narrow-gap mantle heat exchangers are presented. Film thickness relationships and heat transfer solutions for free falling film flows relevant to falling film heat exchangers in this thesis are also reviewed.

2.2 PERFORMANCE OF COLLECTOR-LOOP HEAT EXCHANGERS

To characterise the thermal performance of solar collector-loop heat exchangers, the early investigations were usually based on a combination of mathematical models and short-term experiments.

2.2.1 Review of internal and external heat exchangers

Mertol *et al.* (1981) developed an analytical detailed loop model to predict the performance of thermosyphon systems with a heat exchanger consisting of three straight copper tubes immersed inside a vertical storage tank. In this model, a constant overall heat transfer coefficient of the heat exchanger tubes was assumed to be $170 \text{ W/m}^2\text{K}$ and linear tank temperature stratification was specified to simplify the complicated calculations of the natural convection process on the tank side of the heat exchanger. They found that the predicted daily performance for the system with the heat exchanger tubes was approximately 90% of that for a standard thermosyphon system without a heat exchanger. Based on their simulated results, the effect of tank stratification on the system performance was found to be minimal compared to that for a fully mixed system. However, this simplified model could not be used to predict the long-term performance of a solar water heater and further experimental validation was required.

This preliminary work was then extended by Webster *et al.* (1986) for heat exchanger configurations based on eight copper tubes mounted in parallel in the bottom of a horizontal thermosyphon tank. In their model a heat exchanger penalty factor was used to estimate the degradation in the collector performance caused by the heat exchanger. Their theoretical model was in good agreement with the experiments. The measurements suggested that the reduction of instantaneous performance of the system could be limited to less than 10% if heat exchanger tubes with relatively large heat transfer area were used. However, the effect of tank stratification on system performance was not determined. In these early investigations, only instantaneous performance predictions were reported for comparing systems with and without a heat exchanger. Furthermore, the mathematical models were usually restricted with simplified calculations on the natural convection inside the tank.

Farrigton and Bingham (1986) tested several internal heat exchangers, ranging from a smooth coil to finned spiral heat exchangers for use in solar water heaters. They found that the heat exchanger effectiveness decreased dramatically at low temperature difference between the heat exchanger inlet and the storage tank. They also suggested that the performance of the smooth coil heat exchanger would not be significantly enhanced with the addition of fins on the heat exchanger. In 1995, Newton extended the TRNSYS standard stratified tank model to include the immersed-coil heat exchangers as tested by Farrigton and Bingham (1986). The heat exchanger model is based on simple mathematical correlations to predict the heat transfer rate across the heat exchanger and only requires minimum geometry details of the heat exchanger. The predictions showed reasonable agreement with the experimental data reported by Farrigton and Bingham (1986). Although this model is empirical, it provides flexibility to accommodate other heat exchanger configurations for use in solar water heating application.

Miller and Hittle (1995) characterised the thermal performance of a wrap-around heat exchanger for use in pumped systems based on TRNSYS modelling and controlled-indoor measurements with constant heat input to the heat exchanger. The wrap-around heat exchanger design consists of a copper coil spirally wrapped around the bottom half of the storage tank. These systems are popular in the USA. In Miller's model, the heat transfer coefficients across the heat exchanger were estimated using Gnielinski's correlation for turbulent forced-flow in the heat exchanger tube and standard turbulent free convection correlation on the tank side. The predicted overall heat transfer coefficient-area product for the heat exchanger was approximately doubled the measured values (~173-193 W/K). This was thought to be due to the conduction heat transfer resistances through the double-wall and the bond between the tube and tank wall, which were not accounted for in their model. In order to match the experimental data, a procedure for normalizing their model to the measured data was undertaken by scaling the individual heat transfer coefficients.

For natural convection heat exchangers (NCHEs) that are popular in North America and Canada, Parent *et al.* (1990) developed two theoretical models for designing this type of

heat exchanger loop where the collector fluid is pumped through the shell, and the tank-water-side is thermosyphoning through the tubes of the heat exchanger. Parent used a modified effectiveness as given in Eqn. 2.1 for characterising the NCHEs. Due to the dependency of the natural convection flow rate on the pump driven collector flow rate, the modified effectiveness used the collector side capacitance rate in place of the minimum capacitance rate as found in the conventional expression for effectiveness. Their predicted modified effectiveness for a shell-and-tube type NCHE ranged from 40 to 99% and showed good agreement with the experimental data.

$$\varepsilon^* = \frac{\dot{Q}_{actual}}{\dot{Q}_c} = \frac{(\dot{m}c_p)_s (T_{so} - T_{si})}{(\dot{m}c_p)_c (T_{co} - T_{si})} \quad (2.1)$$

where: \dot{Q}_{actual} and \dot{Q}_c are the actual heat transfer rate and maximum possible heat transfer rate (W),

$(\dot{m}c_p)_s$ and $(\dot{m}c_p)_c$ are the product of the mass flow rate and the specific heat for the thermosyphon side and collector side respectively (W/K),

T_{si}, T_{so}, T_{co} are the thermosyphon side inlet and outlet, and collector outlet temperatures (K).

Fraser *et al.* (1995) extended Parent's models so they were applicable for other natural convection heat exchanger configurations. This model could be implemented in solar simulation program like TRNSYS or WATSUN. The heat exchanger performance was determined based on two empirical relationships: the modified heat exchanger effectiveness (Eqn. 2.1) and the pressure drop as a function of thermosyphon flow rate on the cold side of the heat exchanger. For a coil-in-shell type NCHE, the ε^* was found to vary from 20 to 88% for thermosyphon flow rates of 0.004 to 0.02 kg/s, with a limiting value of 88% for flow rates above 0.02 kg/s.

Purdy *et al.* (1998) included a NCHE unit model into TRNSYS using the approach of Fraser *et al.* (1995). To evaluate the validity of the model, they tested a number of compact counter-flow plate-type heat exchanger used as a NCHE. Based on a clear day and cold start conditions, the simulated ε^* of the heat exchanger was found to be

approximately 45% for a system operating under peak solar radiation with a thermosyphon flow rate of 35 kg/hr. The simulated results also showed that the natural convection flow rate on the tank side and the modified effectiveness of the heat exchanger were reduced when the tank was fully charged in the late afternoon.

2.2.2 Previous studies of mantle heat exchangers

Mantle heat exchangers have been widely used for horizontal-tank thermosyphon systems and they have also been adopted on vertical-tank pumped-circulation systems based on the low-flow concept (Furbo, 1993). For mantle heat exchangers, the performance characteristics could not be defined using the convectational heat exchanger effectiveness or NCHE modified effectiveness methods due to the unknown flow rate on the tank side and the complexity of the flow structure in the mantle spacing. Previous studies of mantle heat exchanger designs are presented in the following section and the heat transfer correlations developed for particular mantle configurations are summarised in Table 2.1.

Vertical mantle heat exchangers

In 1993, Baur *et al.* developed a mathematical model that could be implemented in the TRNSYS package to predict the performance of a vertical mantle heat exchanger. They modelled a 20 mm mantle gap using an empirical heat transfer correlation for laminar forced flow between parallel flat plates (Mercer *et al.*, 1967). On the tank side, the heat transfer coefficient was assumed to be constant to simulate the natural convective heat transfer resistance. To match the simulated and measured results, they found that a correction factor of the order of 1.8 was needed in the standard parallel plate heat transfer coefficient correlation. The reason for the high heat transfer coefficient was thought to be due to the use of pure forced flow correlation for the mixed convection process in the 20 mm wide mantle gap and mixing induced by the higher velocities near the inlet port.

Investigations of vertical mantle heat exchangers with a 33.5 mm mantle gap and top inlet configuration have been carried out by Shah and Furbo (1998) based on typical Danish low-flow (0.4 kg/min) pumped-circulation systems. Their results obtained from

CFD simulations showed that the heat transfer in the mantle was dominated by natural convection and thus the local Nusselt number was correlated in terms of local Rayleigh number. Their CFD simulations also showed that thermal stratification in the tank was not disturbed by a cooler fluid flowing into the mantle. Using PIV techniques and CFD modelling, Shah *et al.* (1999) investigated the detailed flow pattern in the mantle. Good agreement of flow pattern prediction was obtained from the two approaches. For a high inlet temperature into the mantle, they found that the flow was dominated by buoyancy and complex recirculation paths were observed in the top 20% of the mantle. When the inlet temperature was lower than the tank temperature at the top of the mantle, a large re-circulation zone was induced at the top two-thirds of the mantle, resulting in lower heat transfer.

Shah (2000) extended the analysis for a wider range of geometry designs, including mantle gaps of 18, 36 and 54 mm and tank height/diameter ratios of 1.11, 3.75 and 6.9. The smallest mantle gap in Shah's analysis was 18 mm where buoyancy effect is still dominant. A new local Nusselt number correlation as given in Eqn 2.2 was developed for wide gap mantle heat exchangers with a top inlet port.

$$Nu_y = 0.28 \left(\frac{w}{r_i} \right)^{-0.63} \left(Ra_y \frac{y}{H_m} \right)^{0.28} \quad \text{for } Ra_y < 10^{10} \quad (2.2)$$

where r_i is the outer radius of the inner wall of the mantle and H_m is the height of the mantle. Although this correlation was valid for a wider range of mantle heat exchanger designs than that derived by Shah and Furbo (1998), some discrepancies of the heat transfer predictions at the top section of the mantle were found. These inaccuracies reflect the mixed convection possibly occurring near the inlet region, and the inlet Reynolds number might need to be included into the heat transfer correlation as suggested by Knudsen (2004). On the tank side, the local natural convection Nusselt number was correlated as a function of local Rayleigh number.

More recently, Knudsen and Furbo (2004) continued this research by conducting experimental and numerical investigations of the flow pattern and the heat transfer in vertical mantle heat exchangers for low-flow systems with both top and lower mantle inlet positions. When the inlet temperature was lower than the tank temperature at the

mantle level, they found that the lower mantle inlet port design helped to maintain the tank thermal stratification as the scale of the recirculation zone at the top of the mantle decreased compared to the top mantle inlet. This was different from the investigations made by Shah *et al.* (1999) based on an initially mixed tank. Knudsen *et al.* (2004) also investigated the detailed flow pattern in the mantle using PIV techniques and CFD modelling. Similar flow behaviour was found as that reported by Shah *et al.* (1999) in which the buoyancy effect induced a complex recirculation path in the top 20% of the mantle, resulting in most of the heat transfer occurring in the top section of the mantle.

Using the CFD modelling results of vertical mantle heat exchangers with lower inlet port positions, Knudsen (2004) derived a local Nusselt number correlation by dividing the mantle into an upper half (mixed convection) and a lower half (natural convection). In the upper half of the mantle, the Nusselt number was correlated as a function of Rayleigh number and inlet Reynolds number as expressed:

$$\text{Above mantle inlet: } Nu_y = 23.79 \left(\frac{Ra_y}{Re_i^2} \frac{y}{H_1} \right)^{0.22} \quad \text{for } Ra_y / Re_i^2 < 10^4 \quad (2.3)$$

$$\text{Below mantle inlet: } Nu_y = 33.37 \left(\frac{Ra_y}{Re_i^2} \frac{y}{H_2} \right)^{0.25} \quad \text{for } Ra_y / Re_i^2 < 10^4 \quad (2.4)$$

where H_1 and H_2 are the distance from the mantle inlet to the top of the mantle and to the bottom of the mantle respectively. In the lower half of the mantle, Knudsen found that the local Nusselt number was independent of Rayleigh number and could be expressed in terms of mantle geometry as given in Eqn. 2.5. This was due to the small amount of the heat transfer taking place at the bottom half of the mantle. On the tank side, Knudsen (2004) derived localised Nusselt number correlations for two ranges of aspect ratio (height/diameter) for $Ra_y < 10^{11}$.

$$Nu_y = 403.9 \left(\frac{A_{flow}}{A_{heat\ transfer}} \right) + 0.98 \quad \text{for } A_{flow} / A_{heat\ transfer} < 0.08 \quad (2.5)$$

where: A_{flow} is the horizontal flow area of the mantle gap (m^2),

$A_{heat\ transfer}$ is the heat transfer area at the inner mantle wall (m^2).

It was concluded that heat transfer predicted by these correlations showed good agreement with CFD modelling and better predictions were obtained than those reported by Shah (2000). The heat transfer correlations given in Eqns. 2.3 to 2.5 were implemented in a simulation program, MantlSim, to predict the annual performance of low-flow pumped systems incorporating wide gap mantle heat exchangers. The simulation program was originally developed by Berg (1990) and then modified by Shah and Furbo (1996). The simulation results showed that the thermal performance of the typical Danish low-flow system with a wide gap mantle heat exchanger could be improved by up to 26% by simple changes in the design, such as the use of thicker insulation, larger tank height/diameter ratio and the use of stainless steel as the tank wall material.

Horizontal mantle heat exchangers

Apart from the wide gap mantle heat exchangers where buoyancy driven flows are dominant, mantle heat exchangers with gaps of 5-10 mm are also used in horizontal thermosyphon tanks. To investigate the flow patterns and heat transfer in horizontal mantle heat exchangers, Morrison *et al.* (1998) conducted flow visualisation experiments using dye tracing and compared the results with CFD simulations for both mixed and stratified tank conditions. The study was based on a 5 mm width mantle wrapped around a horizontal tank with the inlet and outlet both located at the bottom of the mantle. For mixed tank conditions, the flow stream penetrated to the tank top where heat transfer occurred over the full height of the tank. However, for stratified tank conditions, the heat transfer was confined in the bottom section of the tank just below the thermal equilibrium level, resulting in poor thermal stratification in the tank. The reason for locating the mantle inlet port at the bottom of the tank for thermosyphon systems is to avoid reverse circulation flow extracting the hot tank contents back to the collector-loop at night-time.

Rosengarten *et al.* (2001) extended this work by using a rectangular cavity as a simplified geometric representation of a horizontal MHE. The effect of wall curvature on the flow and heat transfer in the heat exchanger was shown to be negligible. Instead of investigating the full mantle-tank a simplified rectangular mantle was isolated from

the storage tank by adopting different temperature boundary conditions (isothermal and non-isothermal) at the heat transfer wall. Their investigations showed that flow in the mantle was governed by mixed convection, which is the combination of inertia and buoyancy forces. Based on the temperature difference between the inlet and the heat transfer wall, a mean Nusselt number correlation as given in Eqn 2.6 was developed for a range of geometries ($w/L < 0.02$ and $w/H < 0.07$) and boundary conditions ($1 < Re_w < 100$ and $5 < Pr < 14$). Their correlation included a stratification correction parameter (Eqn 2.7) that described the effect of stratification in the storage tank.

$$\overline{Nu}_w = Re_w Pr St \frac{w}{L} \left(1 - \exp\left(\frac{-1}{Re_w Pr} \frac{363L}{k} \right) \right) \quad (2.6)$$

$$St = \frac{\overline{Nu}_w}{\overline{Nu}_{w,i}} = Re_w^{-0.176(\ln \eta)^{0.3}} \left(1 + 2.268(\ln \eta)^{0.56} \right) \quad (2.7)$$

where: St is the stratification correction parameter,

L is the cavity length (m),

$\overline{Nu}_{w,i}$ is the mean Nusselt number based on isothermal boundary condition at the heat transfer wall,

η is the stratification efficiency ratio.

Morrison *et al.* (1999) implemented the mean Nusselt number correlation (Eqn 2.6) in TRNSYS to predict the long-term performance of a thermosyphon system incorporating a horizontal mantle heat exchanger. To evaluate the validity of the model, they performed extended outdoor measurements and found that the predicted monthly energy savings were within two-percentage error points of outdoor measurements.

The majority of the reported mantle side heat transfer correlations were developed for buoyancy driven flows in vertical mantles with annular spacings of 20-35 mm, and mixed convective flows in horizontal mantles with annular spacings of 5-10 mm as summarise in Table 2.1. For the mantle heat exchangers proposed in this thesis, the mantle flows are expected to be dominated by forced convection. A survey of literature relevant to flow and heat transfer studies in narrow gap mantle heat exchangers is presented in the following section.

2. LITERATURE REVIEW

Table 2.1 Summary of heat transfer correlations developed for mantle heat exchangers (MHEs).

GEOMETRY	CONDITIONS	CORRELATION	MODEL	REFERENCE
Vertical MHE with 20 mm spacing	Constant h_{tank}	$\overline{Nu} = 4.86 + \frac{0.606(x^*)^{1.2}}{1 + 0.0909(x^*)^{-0.7} Pr^{0.17}}$	TRNSYS	Baur <i>et al.</i> (1993) <i>Correlation by:</i> Mercer <i>et al.</i> (1967)
Vertical MHE with 33.5 mm spacing and top inlet	$Ra_y < 10^{10}$	$Nu_y = 0.28 \left(\frac{w}{r_i} \right)^{-0.63} \left(Ra_y \frac{y}{H_m} \right)^{0.28}$	MantlSim	Shah (2001)
Vertical MHE with 33.5 mm spacing and lower inlet	Above inlet, $Ra_y/Re_i^2 < 10^4$	$Nu_y = 23.79 \left(\frac{Ra_y}{Re_i^2} \frac{y}{H_1} \right)^{0.22}$	MantlSim	Knudsen (2004)
	Below inlet, $Ra_y/Re_i^2 < 10^4$	$Nu_y = 33.37 \left(\frac{Ra_y}{Re_i^2} \frac{y}{H_2} \right)^{0.25}$		
	Bottom half of the mantle	$Nu_y = 403.9 \left(\frac{A_{flow}}{A_{heat\ transfer}} \right) + 0.98$		
Rectangular cavity (horizontal MHE with bottom inlet and outlet)	$1 < Re_w < 100$ $5 < Pr < 14$ $w/L < 0.02$ $w/H < 0.07$	$\overline{Nu}_w = Re_w Pr St \frac{w}{L} \left(1 - \exp \left(\frac{-363L}{Re_w Pr k} \right) \right)$	TRNSYS	Rosengarten <i>et al.</i> (2001)

2.3 FUNDAMENTAL STUDIES: FORCED CONVECTION

For a narrow gap mantle heat exchanger, the simplest representation of the mantle flow behaviour is laminar fully developed forced convective flow in an annular duct (annulus). The influence of buoyancy forces on the mantle flow in this study is anticipated to be minimal. In general, the thermal boundary conditions of the mantle consist of one wall with temperature coupled to the tank temperature stratification and the other wall of the mantle insulated (adiabatic wall). These boundary conditions can be ideally classified as the fundamental 3rd kind solution for forced-flow between parallel plates (Shah and London, 1978).

It has been shown in the fundamental studies (Shah and London, 1978) that the fluid flow and heat transfer problems for the limiting case of a concentric annulus with the radius ratio (r^*) approaching one can be approximated as that for the parallel plates

geometry. The typical radius ratio for the narrow gap mantle as proposed in this study is 0.985, therefore the narrow-gap mantle in this study can be represented by two parallel plates with boundary conditions of 3rd kind as illustrated in Fig. 2.1.

With the above considerations, the scope of the literature survey for the narrow gap mantle heat exchanger is focused on forced convection heat transfer characteristics in flat ducts (parallel plate channel) with boundary conditions of the 3rd kind. Information is presented for fully developed flow and developing flow.

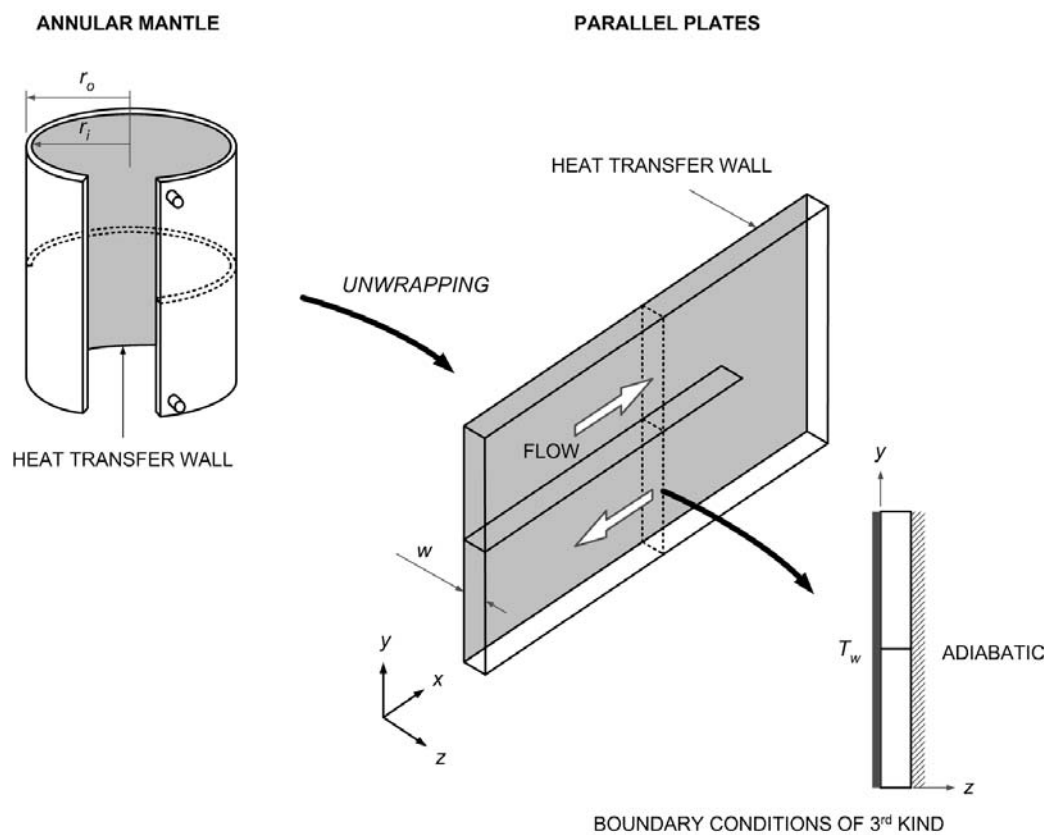


Fig. 2.1 Unwrapping a cylindrical mantle heat exchanger into a rectangular enclosure, showing boundary conditions of third kind.

Fully developed laminar flow

For parallel plates with boundary conditions of the third kind, the laminar fully developed forced flow Nusselt number based on the hydraulic diameter ($d_h = 2w$) was analytically determined to be 4.86 (Shah and London, 1978). The constant Nusselt

number indicates that fully developed heat transfer coefficient is independent of flow rate. This value may be used as a first approximation of the heat transfer coefficient in forced-flow dominated mantle heat exchanger.

Developing laminar flow

In practice, flow in a duct is neither thermally nor hydrodynamically fully developed at the entrance region for intermediate Prandtl number fluid (e.g. water). Higher heat transfer rates would be expected in the developing region of the duct before fully developed heat transfer is reached in a sufficient long duct.

Sparrow (1955) applied the Karman-Pohlhausen method to study simultaneous thermally and hydrodynamically developing flow at the entrance region between parallel plates for both plates with the same uniform temperature, and one plate with a uniform temperature and the other plate insulated. For the case where heat transfer only taking place at one plate, Sparrow's solutions were only restricted to the developing flow region for $0.01 < Pr < 50$.

The well accepted mean Nusselt number correlation for laminar developing forced-flow was developed by Mercer *et al.* (1967) using the finite difference method. They correlated the results as expressed in Eqn. 2.8 which is the same function proposed by Stephan (1959) for parallel ducts with constant temperature walls. The empirical correlation consists of the asymptotic Nusselt number for fully developed flow and the dimensionless thermal entrance length term to account for the effect of developing flow. The mean Nusselt number was based on log-mean temperature difference. Interferometer measurements were undertaken to investigate the thermal entrance region for the case of parallel plates with boundary conditions of the third kind. Good agreement was obtained between the measured data and the values obtained from the analytical correlations. This correlation was used by Baur *et al.* (1993) to model the performance of solar water heaters with a 20 mm gap mantle heat exchanger as mentioned before.

$$\overline{Nu} = 4.86 + \frac{0.606(x^*)^{-1.2}}{1 + 0.0909(x^*)^{-0.7} Pr^{0.17}}, \text{ for } 0.1 \leq Pr \leq 10.0 \quad (2.8)$$

where: $x^* = \frac{x}{d_h Re_d Pr}$ is the dimensionless thermal entrance length. (2.9)

In general, the functional dependence of the laminar forced flow Nusselt number for simultaneously developing flow in ducts is given by Shah and London (1978) as the following,

$$Nu_x = Nu(\text{duct geometry, boundary conditions, } x^*, Pr) \quad (2.10)$$

where the dimensionless thermal entry length (x^*) is of the most important parameter.

Turbulent flow

The critical Reynolds numbers for transition and turbulent flow between parallel plates has not been determined as clearly as for the case of circular duct. Several early attempts have been undertaken and the results showed that the critical Reynolds number ranged between 2200 and 3400 depending on the entrance configuration (summarised in Kakac *et al.*, 1987). Beavers *et al.* (1970) studied experimentally the effect of a variety of entrance configurations and different disturbance sources at the channel entry on the lower limit of the critical Reynolds number. For a smooth rounded entry, the Re_{crit} was found to be 3400 while the lowest Re_{crit} was 2200 for a square entrance with disturbance sources located inside the channel near the inlet entry region. Due to limited information of heat transfer correlations for turbulent flow between parallel plates, solutions for turbulent pipe flows are usually adapted by replacing the tube diameter with the hydraulic diameter.

2.4 FALLING FILM FLOWS

For the falling film heat exchangers used in solar water heating applications as reported in this thesis, the thin liquid film covers the inner surface of the falling film tube where heat being transferred to the tank contents through a cylindrical wall. The falling film velocity is governed by viscosity, gravity and surface tension if the film does not fully wet the tube. In most heating or cooling applications involving falling films, determination of the film thickness is of importance in heat or mass transfer calculation.

Although there are numerous literature reviews involving the detailed study of the heat transfer characteristics in two-phase film flows, the research on the film thickness is usually simplified and performed independently without an adjoining gas stream. An overview of the theoretical and experimental approaches for determining film thickness reported in previous studies is presented. The information is arranged from the classical theories to the experimental studies. A summary of the film thickness correlations for free liquid film flows reported by previous researchers is also presented.

2.4.1 Film flow regimes: theoretical studies

The prediction of the film thickness in film flow down vertical boundaries is complicated by the presence of the free surface which can cause complicated wave phenomena. Early attempts to understand falling films and to predict film thickness were mainly based on an analytical treatment of the problem with reasonable assumptions. Several experimental studies were also undertaken of film thickness characteristics, however they were limited to a certain extent due to the flow complexity and limited accuracy of the instruments in the early years. In this section, the classical solutions of film thickness for three basic flow regimes are reviewed:

- 1) Smooth and laminar film flows,
- 2) Wavy and laminar film flows,
- 3) Turbulent film flows.

As pointed out by Fulford (1964), the transition from laminar to turbulent film flow cannot be identified with distinct critical Reynolds number as in the case of duct flow due to the complexity of the wave phenomena.

Smooth and laminar film flow

The first analytical treatment for the flow of falling films was carried out by Nusselt (1923) for a smooth, laminar and two-dimensional flow on an infinitely wide plate. This classical model assumes that only gravity and viscous forces were present in the film and wave motion was neglected at the free surface. These assumptions significantly simplified the boundary conditions and solutions obtained from the

Navier-Stokes and continuity equations. The analytically determined film thickness (δ) for a smooth, laminar and vertical falling film is expressed in terms of Reynolds number as follows:

$$\delta = \left(\frac{3\mu^2}{4\rho^2 g} \right)^{1/3} Re_f^{1/3} \quad (2.11)$$

where Reynolds number, $Re_f = \frac{4\rho Q}{\mu b}$ (2.12)

The analytical solution for a smooth laminar film flow is limited to Reynolds numbers of the order of $Re_f < 20$ as the free surface of the film starts to become unstable at higher Reynolds number. It is also important to note that the Reynolds number here is based on hydraulic diameter ($d_h = 4\delta$) of an infinitely wide film. Although some of the literature used the fully developed film thickness as the characteristic length, there is no significant advantage of either definition.

Wavy and laminar film flow

Due to the presence of the free surface in vertical falling liquid films, the film is rarely smooth even if the Reynolds number is relatively small. The films may be influenced by gravity or surface tension or mixed gravity-surface tension effects, resulting in complex wavy flows. The earliest evaluation of wavy laminar films thickness was carried out by Kapitsa (1948) for the case of two-dimensional film flows along a vertical plate as expressed in Eqn. 2.13.

$$\bar{\delta} = \left(\frac{2.4\mu^2}{4\rho^2 g} Re_f \right)^{1/3} = 0.94\delta_{smooth} \quad (2.13)$$

Kapitsa's solutions showed that the mean thickness of a wavy film is approximately 6% thinner than that for the smooth film derived by Nusselt (Eqn. 2.11). The reduction in the film thickness as predicted by Kapitsa's theory has been supported by film thickness measurements by Feind (1960). However, this classical solution has proved to fail in predicting the wave characteristics. Hence, a massive amount of detailed studies have been undertaken including a study of the stability of the free wavy surface and the hydrodynamics of wave formation. Due to large amount and complexity of findings,

the results will not be described in further detail here. Selected literature includes the linear stability analysis for small amplitude sinusoidal waves (Krantz and Goren, 1971), long-wave theory for finite amplitude waves (Benney, 1966), finite-amplitude two-dimensional waves (Trifonov and Tselodub, 1991), hydrodynamics of wave formation (Chang, 1994) and large amplitude non-periodic waves (Yu *et al.*, 1995). In general, the efforts on understanding and modelling of falling film involving wave growth lead to the development of complex solutions.

Turbulent film flow

The presence of waves on the free surface of turbulent films made early attempts of solving the problem even more difficult. As a result, the common theoretical treatment of fully turbulent flow problems was to assume smooth free surface film by neglecting the complexity of surface waves formation in the flow. An analytical solution for smooth turbulent falling film was derived as given in Eqn. 2.14 assuming a general power law velocity profile (Brauner, 1987).

$$\delta = 0.135 \left(\frac{\mu^2}{\rho^2 g} \right)^{1/3} Re_f^{7/12} \quad (2.14)$$

However, this theoretical solution may not reflect the real turbulent film flows behaviour due to the influence of waves. Brauner (1987) analytically derived two expressions of mean film thicknesses for laminar (intermediate to high Re) and turbulent flows that accounted for the influence of the formation of large waves (rolling waves) as follows:

$$\bar{\delta} = \left(\frac{3\mu^2}{8\rho^2 g} Re_f \right)^{1/3} = 0.794 \delta_{smooth}, \text{ for laminar wavy flow} \quad (2.15)$$

$$\bar{\delta} = 0.104 \left(\frac{\mu^2}{\rho^2 g} \right)^{1/3} Re_f^{7/12}, \text{ for turbulent wavy flow} \quad (2.16)$$

The mean film thickness predictions for turbulent wavy flows as given in Eqn. 2.16 agreed well with experimental data reported by Webb and Hewitt (1975) and Chu and Dukler (1975) at $10^3 < Re_f < 10^4$. On the other hand, the predicted mean film thicknesses for laminar wavy flows (Eqn. 2.15) at $100 < Re_f < 1000$ were thinner than

that of Nusselt and Kapitza correlations. Further modelling work presented by Brauner (1989) included different mechanisms that control the various wave zones. Due to the complexity of solving the wavy film flows analytically, most of the film thickness correlations for wavy film flows are based on correlation of experimental data.

2.4.2 Mean film thicknesses: experimental studies

In parallel to theoretical analyses, many experimental investigations have been made to provide more reliable statistical film thickness data. A brief literature review concerning the measurement of mean film thickness for free falling film is presented in this section. The early experimental attempts for measuring film thickness in both smooth and wavy flows were based on simple measuring techniques, such as drainage technique and the use of micrometer and pointer. Brauer (1956) measured the film thickness of flows falling over the outer surface of a tube (diameter of 43 mm and 1.3 m long) using needle and micrometer. For $Re_f > 1600$, an empirical correlation of the mean film thickness was developed as given in Eqn. 2.17.

$$\bar{\delta} = 0.302 \left(\frac{3\mu^2}{4\rho^2 g} \right)^{1/3} Re_f^{8/15} \quad (2.17)$$

A sample of the earlier non-dimensional film thickness data against the Reynolds number as summarised and plotted by Fulford (1964) is shown in Fig. 2.2. The Reynolds number (Re_δ) in this graph was based on the film thickness instead of the hydraulic diameter. In this figure, the measured data for low Reynolds number ($Re_\delta < 400$ or $Re_f < 1600$) was found to be in good agreement with the classical Nusselt's theory. At $Re_\delta > 400$ ($Re_f > 1600$), the measured data deviates from Nusselt's correlation.

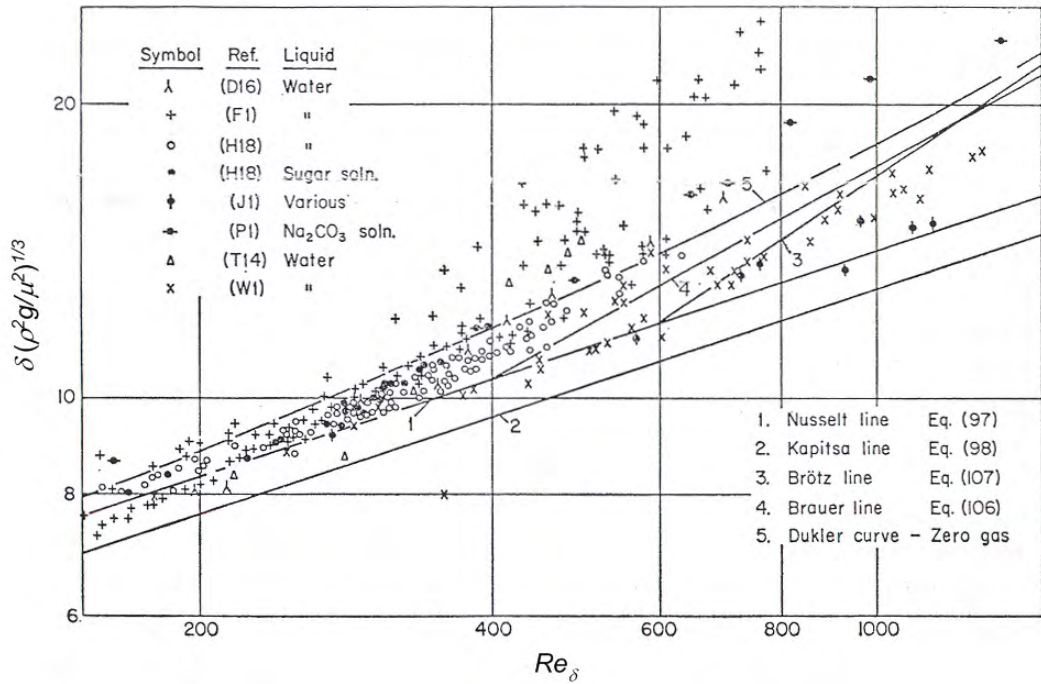


Fig. 2.2 Sample of film thickness data for the case without a concurrent gas stream, plotted in terms of the Nusselt thickness dimensionless number and the Reynolds number based on the film thickness (adapted from Fulford, 1964).

In 1980, Takahama and Kato suggested that the film flow characteristics are dependent on the longitudinal distance (flow direction). They experimentally studied the flow characteristics of a free falling film along the outer surface of a vertical tube (diameter of 45 mm and 2 m long) using both needle contact and electric capacity techniques. At Reynolds number based on hydraulic diameter as low as 800, a reduction of 3% in mean film thickness between the upstream and downstream of the tube was found. As the Reynolds number was increased to 3988, thicker film was found at distance 0.5 m from the entry which then approached a constant value. The results showed that wavy conditions were observed even though there was a smooth film at the entrance region. At flow regime of $Re_f < 1600$, the measured mean film thicknesses agreed with Nusselt's correlation to within 5% whereas at $1600 < Re_f < 8000$, an empirical correlation for the mean film thickness was developed as follows:

$$\bar{\delta} = 0.473 \left(\frac{\mu^2}{4\rho^2 g} \right)^{1/3} Re_f^{0.526} \quad (2.18)$$

Karapantsios and Karabelas (1995) also conducted experiments to measure the instantaneous local film thickness along the outer surface of a vertical tube (diameter of 50 mm and 2.66 m long) at downstream of the tube (section 1.7 - 2.5 m) using parallel-wire electrical conductance technique. The film thickness can be determined by knowing the electrical resistance, which is inverse proportional to the liquid covering the fine wires fitted perpendicular to the flow. Although Karapantsios's measurements obtained at the downstream region where large waves formed ($370 < Re_f < 11020$), the experimental data agreed very well with Takahama's correlation. Uniform mean film thicknesses in the downstream section of the flow was also obtained as reported by Takahama and Kato (1980).

All previous experiments were conducted for liquid film flows at room temperature. Ambrosini *et al.* (2002) experimentally investigated the characteristics of a water film falling down over a flat plate at different temperatures (20-70°C) and inclinations (0 and 45°) using capacitance probes. Compared to previous film thickness measuring techniques, the capacitance probes are non-intrusive instruments in which the disturbance of the film flow by introducing the instrument would not occur. The capacitance probes consist of two parallel conducting plates with one plate fixed in position and the second plate adjusted to the suitable gap for the film thickness. The capacitance of the probes is directly proportional to the dielectric constant of the fluid between the plates. The measured data showed that the film was gradually thinning with increasing temperature, due to a reduction of water viscosity. At flow regime of $Re_f < 1000$, the measured mean film thicknesses agreed reasonably with Nusselt's correlation. On the other hand, the experimental data at $1000 < Re_f < 3000$ also agreed well with the empirical correlation developed by Takahama and Kato (1980) for wavy flow at high Reynolds number.

Drosos *et al.* (2004) conducted visual observations of developing free falling films at intermediate Reynolds number ($Re_f < 400$) over a vertical plate (length of 38 cm) with smooth inlet conditions. The results graphically display the longitudinal flow characteristics as suggested by Takahama and Kato (1980) and Karapantsios and Karabelas (1995). According to wave structures for water at Reynolds numbers of 128

and 282 captured by Drosos (Fig. 2.3), initially smooth film flows for both cases were observed at the entrance region and wave formation became visible at a distance approximately 10 cm from the entry. At Reynolds number of 282, the transition from two-dimensional waves to three-dimensional larger waves was pronounced at the downstream region as shown in Fig. 2.3. These observations suggested that wavy flow occurs in vertical falling film flow even at Reynolds number as low as 128.

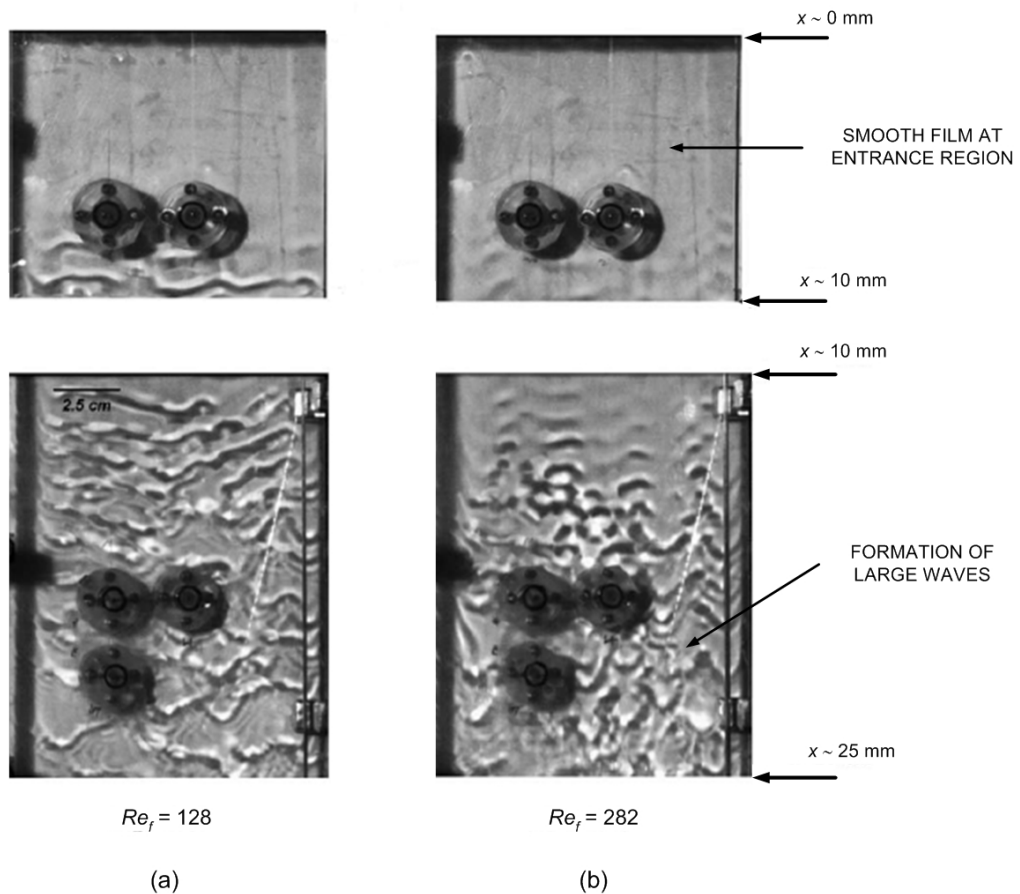


Fig. 2.3 Photographs of water falling film flow on the vertical plate for (embedded probes shown in the background), (a) Re_f of 128, (b) Re_f of 282, (adapted from Drosos *et al.*, 2004).

2. LITERATURE REVIEW

Table 2.2 Summary of film thickness correlations for liquid film flows without interfacial shear.

GEOMETRY	CONDITIONS	METHODS	FILM THICKNESS CORRELATION	REFERENCE
Flat plate	Smooth and laminar $Re_f < 20$	Analytical	$\delta = \left(\frac{3\mu^2}{4\rho^2g} Re_f \right)^{1/3}$	Nusselt (1916)
Flat plate	Wavy and laminar	Analytical	$\bar{\delta} = \left(\frac{2.4\mu^2}{4\rho^2g} Re_f \right)^{1/3}$	Kapitsa (1948)
Pipe outside	$Re_f > 1600$	Needle and micrometer	$\bar{\delta} = 0.302 \left(\frac{3\mu^2}{4\rho^2g} \right)^{1/3} Re_f^{8/15}$	Brauer (1956)
Pipe outside	$400 < Re_f < 2000$	Needle contact and electric capacity techniques	$\bar{\delta} = 0.473 \left(\frac{\mu^2}{4\rho^2g} \right)^{1/3} Re_f^{0.526}$	Takahama and Kato (1980)
Flat plate	$10^2 < Re_f < 10^3$ $10^3 < Re_f < 10^4$	Analytical	$\bar{\delta} = \left(\frac{3\mu^2}{8\rho^2g} Re_f \right)^{1/3}$ $\bar{\delta} = 0.104 \left(\frac{\mu^2}{\rho^2g} \right)^{1/3} Re_f^{7/12}$	Brauner (1987)
Flat plat	$400 < Re_f < 3000$	Capacitance probes	Agreed with Takahama and Kato (1980)	Ambrosini <i>et al.</i> (2002)

2.4.3 Heat transfer through falling films

Heat transfer analysis in liquid film flow without an interfacial shear was only carried out in early investigations of this field. The present literature on heat transfer of falling films is mainly focused on two-phase flow with the presence of interfacial shear that enhances the heat and mass transfer processes. The large amount of literature written for such applications will not be considered here, as it is not applicable to the system being analysed in this thesis.

An analytical treatment for the heat transfer through laminar falling liquid films over a flat plate was reported by Bird *et al.* (2002) as given in Eqn. 2.19. The analysis was restricted to smooth laminar flow and based upon the film thickness solutions developed by Nusselt (1923) as given in Eqn. 2.11. A further assumption was made for film flow

with only short contact times between the film and plate so that the fluid temperature changes appreciably only in the immediate vicinity of the wall.

$$\bar{h}_{film} = \frac{3}{2}k \frac{1}{\Gamma(4/3)(9\beta^* H)^{1/3}} \quad (2.19)$$

where: H is the height of the plate (m),

$\Gamma(4/3) = 0.89297$ is a gamma function,

$$\beta^* = \mu k / (\rho^2 C_p g \delta).$$

Wilke (1962) developed a number of empirical mean Nusselt number correlations that can be used to estimate the heat transfer coefficient in a falling film heat exchanger. Wilke conducted measurements for liquid film heating (single-phase film without concurrent gas stream) over the outer surface of a vertical tube (diameter of 42 mm and 2.4 m long) using glycol/water mixtures in varying concentrations (0, 16, 55.5, 77.1 and 95% glycol). These correlations were developed in similar way to forced convection for the three flow regimes observed to occur in the film for $5.4 < Pr < 210$:

$$\text{For } Re_f < 1600, \quad \bar{Nu}_{film} = 0.2456 \left(\frac{Re_f}{4} \right)^{8/15} Pr^{0.344} \quad (2.20)$$

$$\text{For } 1600 < Re_f < 3200, \quad \bar{Nu}_{film} = 0.00448 \left(\frac{Re_f}{4} \right)^{6/5} Pr^{0.344} \quad (2.21)$$

$$\text{For } Re_f > 3200, \quad \bar{Nu}_{film} = 0.0264 \left(\frac{Re_f}{4} \right)^{14/15} Pr^{0.344} \quad (2.22)$$

The mean film thickness for laminar flow at $Re_f < 1600$ was determined using Nusselt's correlation while for $Re_f > 1600$, it was calculated using empirical correlation developed by Brauer (1956) as given in Eqn. 2.17.

2.5 SUMMARY

The literature review has shown that heat exchanger penalty on the system performance could be evaluated using mathematical modelling. To predict the amount of heat

transfer across the heat exchanger, heat transfer coefficients on the hot side of the heat exchanger and the natural convection coefficients on the tank side are required.

Mantle heat exchangers

In response to the realisation that theoretical heat transfer calculations for flow between parallel plates were of limited application to mantle heat exchanger designs due to the complexity of flow and heat flux distribution, researches have tended to focus directly on the problem of heat transfer in specific mantle heat exchanger configurations. The majority of the reported mantle side heat transfer correlations were developed for buoyancy driven flows in wide vertical mantles, and mixed convection flows in horizontal mantles with annular spacings of 5-10 mm. However, there is no publication on the mantle design where forced convection is dominant as proposed in this thesis. As a result, the measurement program and CFD modelling commenced in this project will provide detailed investigations for forced convection dominated conditions in the mantle.

Falling film heat exchangers

The falling film heat exchanger proposed in this thesis is a new concept for solar water heating application. Although the liquid film thickness is of importance in the heat transfer calculation, the literature review has indicated that it is not straightforward and the knowledge of film flow is usually restricted due to the presence of waves at the free surface. In this chapter, selected previous studies carried out in estimating the free falling film thickness were presented. For heat transfer problems involving falling film flows without an adjoined gas stream, there have not been any publications that correlate the heat transfer rate except the simple analytical solutions and early experimental attempts (Wilke, 1962). Most of the work in this field has focused on two-phase flow problems. In order to quantify the thermal performance of the falling film heat exchanger in this study, direct temperature measurements will be needed to determine the falling film heat transfer coefficient that can be implemented into a transient system simulation program, such as TRNSYS, to predict the long-term performance of a solar water heater incorporating a collector-loop heat exchanger.

- CHAPTER 3 -

EXPERIMENTAL APPARATUS AND TECHNIQUES

3.1 INTRODUCTION

The preceding chapter has presented a literature survey of the types of flows and heat transfer phenomena that occur in the mantle heat exchanger and the falling film heat exchanger proposed in this thesis. In this chapter, the experimental techniques used to examine the heat transfer characteristics of both novel collector-loop heat exchangers are outlined.

The first set of experiments aims to investigate the detailed flow and heat transfer processes in the mantle heat exchanger for a range of operation conditions. The studies were carried out based on:

- *Laboratory-scale measurements:* Mantle-tanks were tested under controlled conditions and detailed wall temperature measurements were made to determine the hot and cold side heat transfer coefficients. The indoor measurements were also used to determine the heat exchanger overall UA_{hx} .
- *Flow visualisation:* A scale model of a rectangular mantle was constructed to investigate the flow field in a mantle using dye-trace flow visualisation and optical velocity measurements using Particle Image Velocimetry. The details of the instrumentation and image acquisition procedures for this analysis are presented.

The second set of experiments aims to characterise the performance of falling film heat exchangers, with and without an advanced flow controller. Firstly, heat transfer coefficients for the heat exchanger were evaluated through a series of steady flow tests.

Secondly, effects of the switching controller operation on the system performance were investigated.

3.2 MANTLE HEAT EXCHANGER PERFORMANCE MEASUREMENTS

An indoor experimental arrangement as illustrated in Fig. 3.1a was setup to evaluate the overall heat transfer characteristics of the mantle heat exchanger and for the purpose of heat transfer coefficient measurements in the heat exchanger covering a range of mantle flow rates and thermal boundary conditions. The mantle was constructed with an annular spacing of 3 mm wrapped around the bottom half of a 270 L stainless steel tank. In order to access the inner surface of the core tank, the mantle-tank was specially constructed in two halves (Fig. 3.1b) for the laboratory-scale experiments. The interface between the top and bottom half of the tank was sealed using a gasket and bolts after thermocouples were attached on the inner wall of the mantle heat transfer surface. The tank was insulated with 150 mm thick polyester blanket.

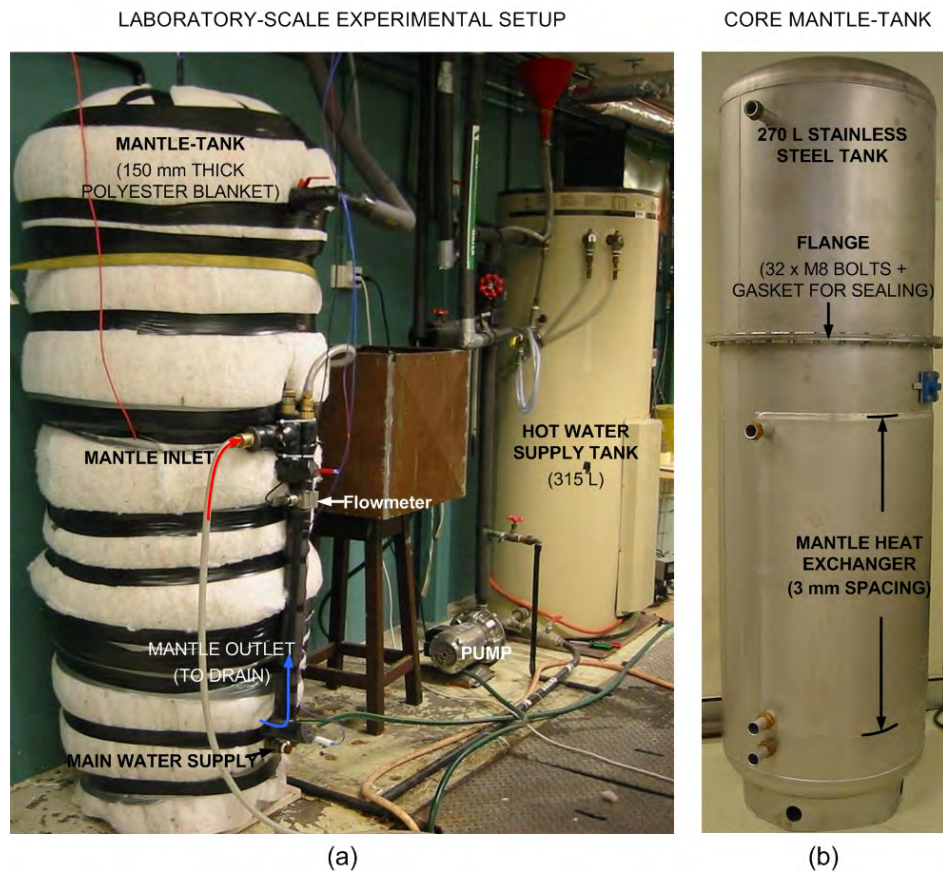


Fig. 3.1 (a) Indoor thermal measurement test rig. (b) The core of a narrow gap mantle heat exchanger and storage tank.

In the indoor experiments, hot water was supplied to the hot side of the heat exchanger from a 315 L conventional hot water tank as the heat source, simulating the heat output from a typical 3.6 m² solar collector array over a clear day. The simulated heating pattern was achieved by heating up a conventional hot water supply tank (315 L) from a cold start (approximately 20°C) using two 2.4 kW in-tank electric heating elements located at the bottom of the tank.

A schematic diagram of the indoor experimental setup is illustrated in Fig. 3.2 together with the location of instruments installed for the tests. For the tank temperature stratification and detailed wall temperature measurements, ten T-type thermocouples were fitted at different levels inside the core of the tank (Fig. 3.2) and additional 16 T-type thermocouples with nominal diameter of 0.7 mm were mounted on the tank side of the wall of the heat exchanger surface (Fig. 3.3). The use of fine thermocouples for the wall temperature measurements was to provide fast response time and to minimise any disturbances to the natural convective flow inside the tank. A thin layer of thermally conductive compound TIC-7500 was applied onto each thermocouple bead, and sealed by a thin piece of aluminium tape to ensure good thermal contact with the wall. The inlet and outlet temperatures and flow rate of the hot water through the heat exchanger were also monitored. All thermocouples were calibrated against a platinum resistance thermometer for a temperature range from 10 to 70°C at 5°C intervals. For the thermocouples attached on the tank side of the wall of the heat exchanger surface, a second test was performed by mixing the volume of the mantle to a uniform temperature using a temperature-controlled water bath. Variations between thermocouples were observed to be $\pm 0.2\text{K}$. The mantle flow rate was measured using a calibrated low-flow turbine flow meter OMEGA FTB9510. The flow meter was calibrated by comparing its frequency output with the measured water volumes over a time interval.

3. EXPERIMENTAL APPARATUS AND TECHNIQUES

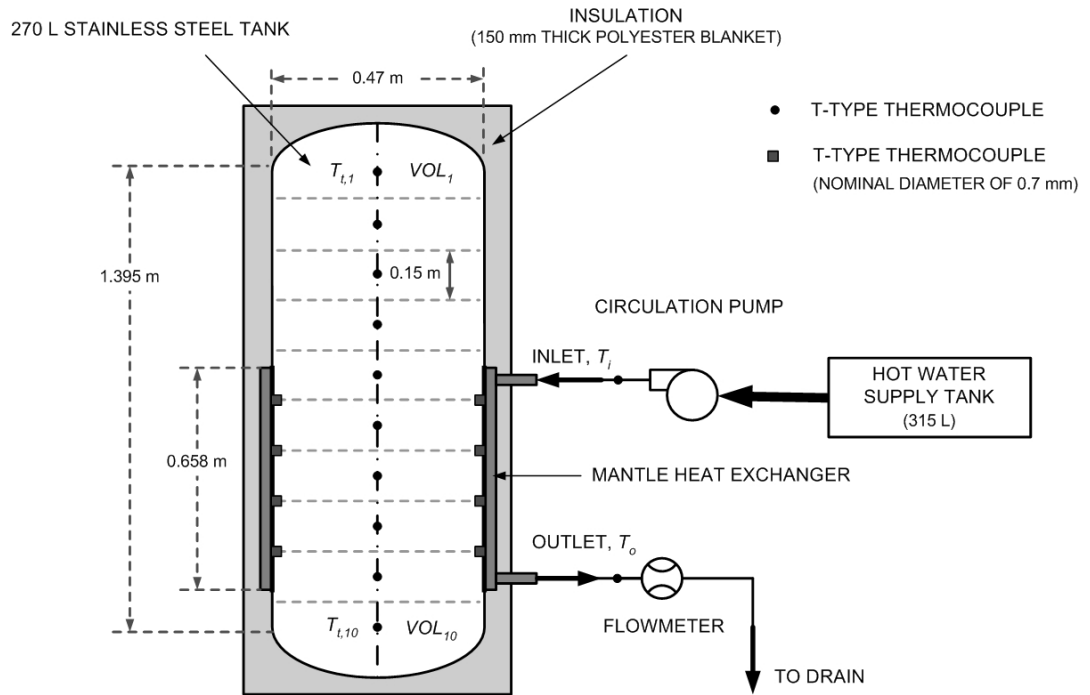


Fig. 3.2 Schematic diagram of monitoring points for laboratory-scale thermal measurements in the core of the mantle-tank.

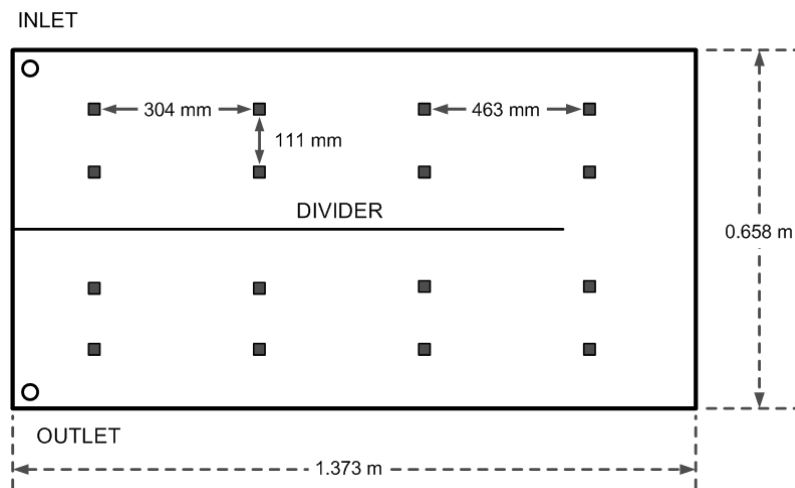


Fig. 3.3 Schematic diagram of monitoring points on the mantle wall.

3. EXPERIMENTAL APPARATUS AND TECHNIQUES

A data acquisition system (Fig. 3.4) was set up to collect data from sensors and was controlled by a data-logging program. All signals were scanned through differential channels in a DT500 datataker and two expansion modules, and were recorded on a PC through a serial communication port RS232 as one minute averages. Note that the solid-state relays and pyranometer shown in Fig. 3.4 were only used for outdoor measurements of a falling film system.

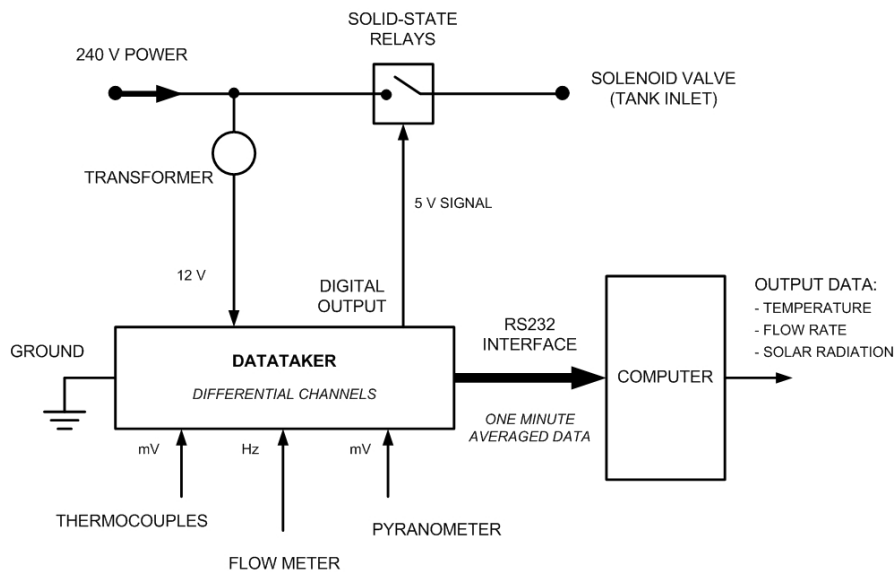


Fig. 3.4 Schematic diagram of the data acquisition system.

3.3 FLOW VISUALISATION IN RECTANGULAR MANTLES

For flow analysis in the mantle heat exchanger with a two-pass flow arrangement, a scaled rectangular mantle enclosure was used as a simplified geometry to facilitate flow visualisation by dye tracing and Particle Image Velocimetry (PIV) techniques. The aim of this experiment was to investigate the influence of the mantle spacing on the flow pattern and heat transfer. Apart from flow investigations, temperature distributions across the simplified mantle were also monitored during the heat up cycles. The flow fields and temperature measurements obtained from experiments were used to examine the validity of the numerical model (presented in Chapter 5).

3.3.1 Experimental Setup

A clear Perspex rectangular mantle enclosure mounted on one wall of a rectangular tank was constructed to allow flow visualisation with the dye tracing and a laser sheet illuminating the flow in the mid-plane of the mantle. Fig. 3.5 illustrates the construction of the experimental rig used for flow measurements. The test unit consists of a rectangular mantle (0.436 x 0.34 m) made of 12 mm thick Plexiglas (Perspex) with inlet and outlet ports (diameter of 8 mm, length of 30 mm), mounted on a 3 mm thick galvanised steel rectangular tank. Three mantle spacings of 3.5, 10 and 30 mm were investigated in this study. The interface between the mantle and the metal tank wall was sealed using a gasket held by 32 bolts around the mantle sides and along the divider.

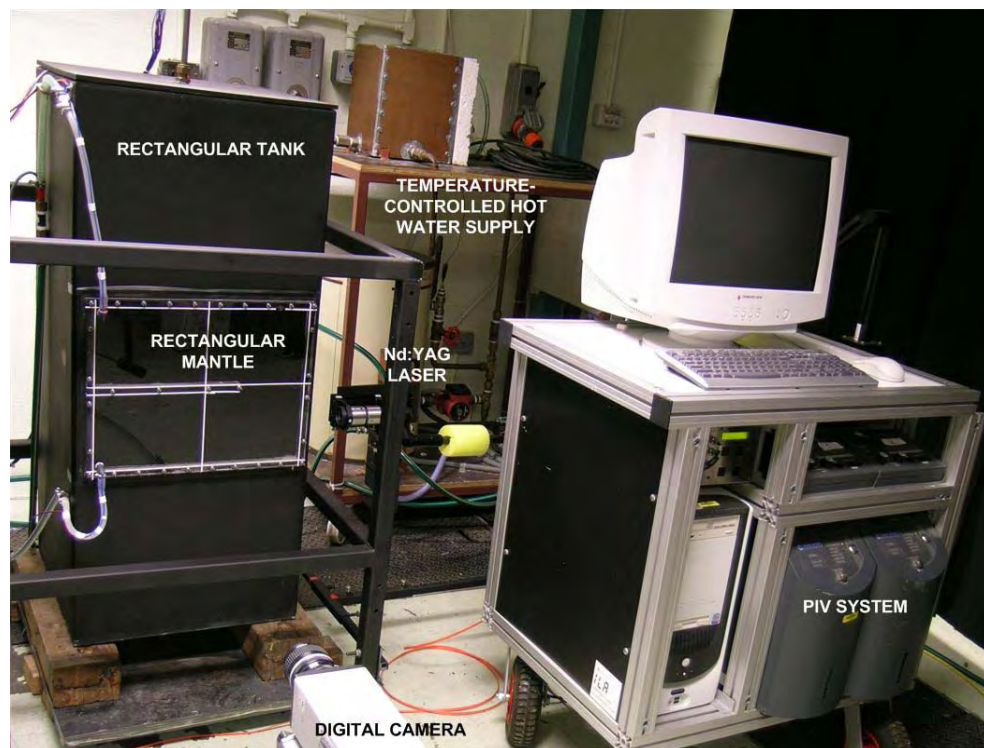


Fig. 3.5 Flow visualisation test rig for PIV measurements.

3. EXPERIMENTAL APPARATUS AND TECHNIQUES

Throughout the tests, the mantle inlet temperature was set to be approximately 10 K higher than the pre-conditioned tank temperature, representing the instantaneous heating pattern of a real solar water heater operation. Hot water was circulated through the mantle from a pumped temperature-controlled water heater in a closed-loop. To monitor the temperatures in the rectangular mantle-tank, thermocouples were located both in the mantle circuit, in the core tank (Fig. 3.6a) and twelve thermocouples were also brazed on the tank side of the mantle wall to ensure good thermal contact (Fig. 3.6b). All the thermocouples were calibrated against a platinum resistance thermometer for temperatures from 10 to 60°C at 5°C intervals. The flow rate was measured by a calibrated turbine flow meter OMEGA FTB2001 in the range of 0.5 to 5 L/min. All readings were recorded as one minute average on a PC via a DT500 datataker and an expansion module.

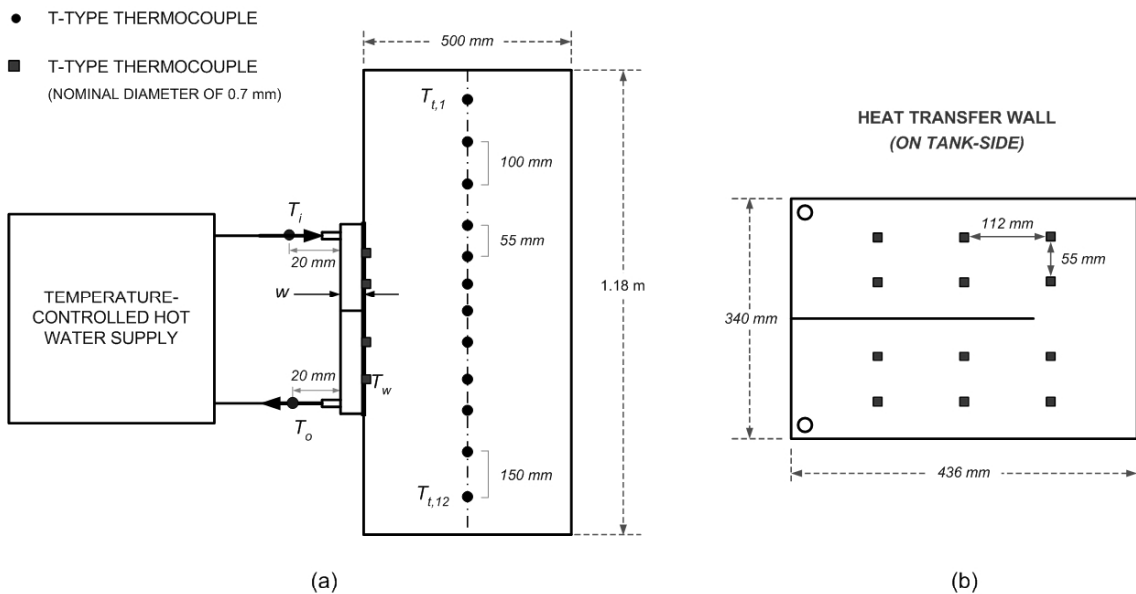


Fig. 3.6 Schematic diagram of monitoring points for flow visualisation experiments, (a) rectangular mantle-tank, (b) on the tank side of the wall of the mantle surface.

3.3.2 Dye Tracing

The first flow visualisation experiment was performed using methyl blue dye to form streak lines showing the flow field. The dye was injected into the mantle gap from both sidewalls using hyperdermic stainless steel tubes with an inner diameter of 0.42 mm (Fig. 3.7). The tubes were inserted into the mantle through 1 mm holes drilled through the centre of the spacers on the sides and then sealed by silicon. To obtain better contrast with the dye, the metal tank surface on the mantle heat transfer wall was painted white. In the 3.5 mm gap mantle, the dye trace could be clearly visualised since the flow was almost two-dimensional.

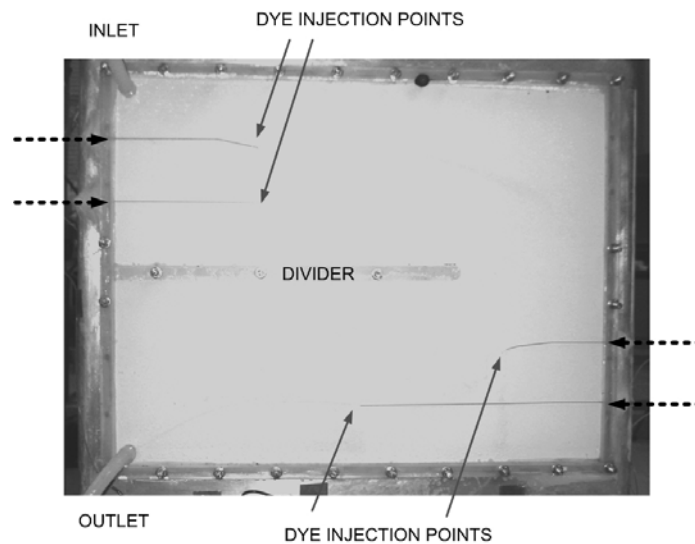


Fig. 3.7 Dye injection points.

3.3.3 Particle image velocimetry (PIV) measurements

As the mantle gap was widened, flow visualisation using colour dye tracing could not be performed due to the mixing of the dye caused by the three-dimensional buoyancy driven flow within the gap. Thus, Particle Image Velocimetry (PIV) technique was used to measure the velocity field in mantles with spacings of 10 and 30 mm as outlined in the following section.

3.3.3.1 PIV technique

Particle Image Velocimetry (PIV) is a non-intrusive and indirect optical flow measurement technique that gives an instantaneous local velocity vector-map over a two-dimensional (planar 2D-PIV) illuminated plane. The basic concept of the PIV technique is to illuminate small tracer particles added to the flow by means of a dual-pulsed laser. The time interval between pulses depends on the mean flow velocity. The successive images of the particle position are recorded via a digital CCD camera. The recorded images are then divided into small sub-areas, which are referred to as interrogation areas. A statistical cross-correlation method is performed between the images to evaluate the local velocity based on the displacement of the particles and the known separation time between the recorded images.

3.3.3.2 PIV measurement setup

The commercial PIV system which was used to perform the flow measurements consists of a light source generation device (dual pulse Nd:YAG lasers), a synchronisation unit, image acquisition device (digital CCD camera) and evaluation software for post-processing. The typical planar PIV flow measurement setup and the velocity evaluation technique (described in Section 3.3.3.3) are illustrated in Fig. 3.8.

Seeding particles

The seeding particles for the PIV image acquisition have to be carefully selected based on the nature of the flow and the working medium. In this study, neutral density PSP Polyamide seeding particles (Dantec Dynamics) with a mean diameter of 20 μm were used as a best compromise to avoid significant discrepancies between working fluid (water) flow and particle motion due to density difference while providing sufficient light scattering for the camera to capture the seeding particles. Approximately 5 g of 20 micron seeding particles was mixed with 70 litres of water in the hot water supply tank to achieve a medium image density for the PIV measurements.

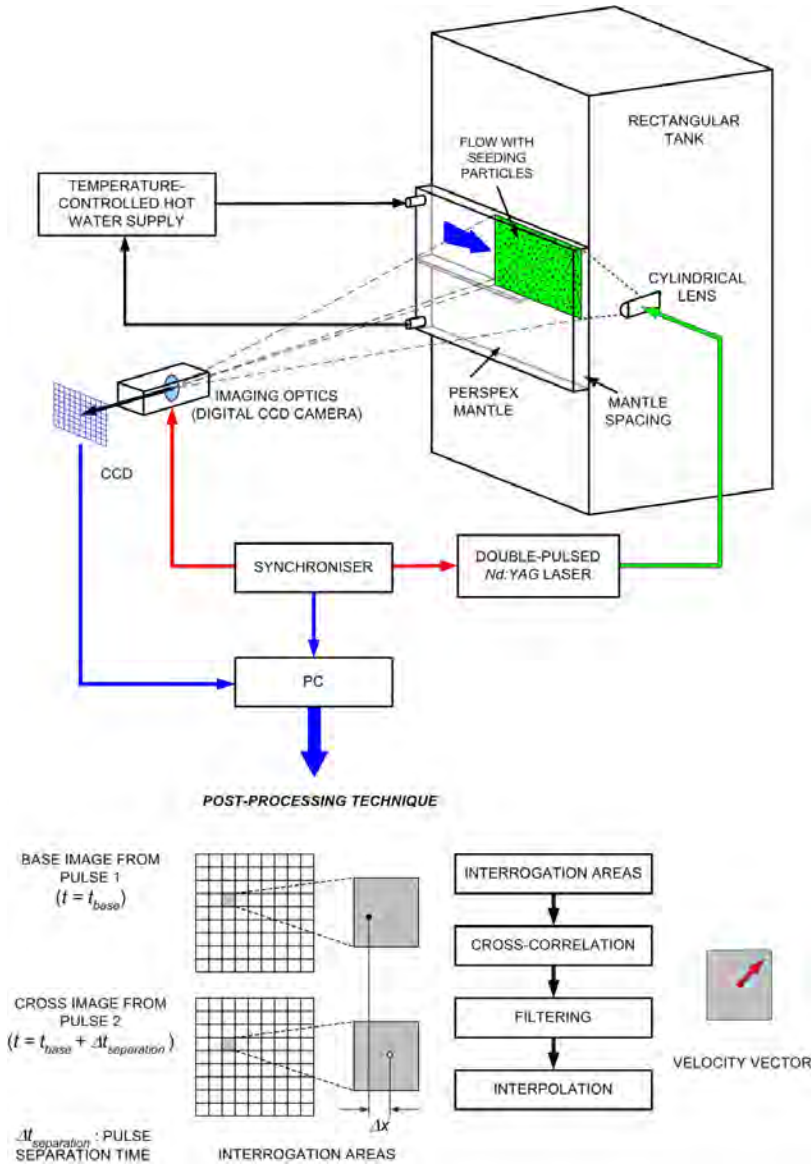


Fig. 3.8 Experimental arrangement for Particle Image Velocimetry (PIV) measurements, showing the instrumentation, test rig and an overview of cross-correlation method to generate the velocity vector-map on the measuring plane.

Dual pulse Nd:YAG lasers

The light pulses used to illuminate the tracer particles over the measuring plane in the mantle were generated by a double-pulsed Nd:YAG (Neodym:Yttrium-Aluminium-Garnet) laser system from New Wave Research (Gemini). This double-pulsed laser system consists of two laser heads in which the Nd:YAG rod is pumped within its laser head chamber with energy by a flash lamp to generate infrared radiation (1064 nm) with high energy of 120 mJ per pulse. During the pumping process, a closed-loop water-

cooling system is activated simultaneously to maintain an acceptable YAG rod temperature. The system incorporates an optical shutter called a Q-switch so that the lasers can be controlled precisely to generate more than one pulse. In order to provide visible laser beams at wavelength of 532 nm, a second harmonic generator made of a KTP crystal is integrated in the system. These visible laser beams are then focused to produce thin laser light sheets to illuminate the seeding particles. In this study, the pair of light sheets was aligned carefully with the mid-plane of the mantle parallel to the heat transfer wall. The first particle image from the first laser pulse is usually known as the base image and the second as the cross image. To prevent unnecessary reflections of the light sources, the metal tank walls were painted matt black for PIV measurements.

Digital CCD camera

The light scattered by the seeding particles in the measuring plane is captured by a digital camera (SensiCam) with a built-in CCD chip, and transferred to a PC via a fibre optic cable (maximum transfer rate of 132 Mbyte/s). The CCD (Charged-Coupled-Device) chip is a light-sensitive circuit that consists of a matrix of rectangular sensing elements. Each individual sensing element referred to as a pixel converts the captured optical image into electric signals. The camera used in this PIV measurement provides a resolution of 1280 x 1020 pixels with a 50 mm focal-length optical lens. In order to increase the image resolution, the rectangular mantle was divided into four-quarter measurement areas (approximately 218 x 165 mm for each section). The camera was positioned at a distance of approximately 1.1 m from the measurement plane, resulting in a resolution of approximately 5.8 pixels per mm for both vertical and horizontal coordinates.

Synchronizer

In order to avoid unwanted overlapping between images, the synchronizer in the PIV system is a timing device to coordinate precisely the time sequence of the laser flash lamps and its Q-switches and the camera. In this PIV measurement, double-frame images of illuminated particles in the flow were captured at a rate of 4 double exposures per second which was set in the synchronizer.

3.3.3.3 Cross-correlation techniques

The double-pulsed planar PIV system used in this study generates two light pulses at a time separation to produce a double-exposed pairs of illuminated particle images. The local velocity mapping can be obtained from the raw images through a statistical cross-correlation method. The statistical evaluation of PIV recordings at medium image density evaluates two fundamental parameters of the particles: displacement and time. The flow domain is subdivided into small interrogation areas showing the particle image locations. Between two successive particle images for each interrogation spot, the statistically determined correlation peak in the interrogation area is used to represent the average displacement of the particles (Refer to Raffel *et al.* (1998) for the mathematical details). As the pulse separation time is known, the local velocity for each interrogation area can be determined by the ratio of the measured particle displacement between successive light pulses and the pulse separation time.

Interrogation area

For cross-correlation PIV evaluation, the typical sizes of the interrogation area are 16 x 16, 32 x 32 and 64 x 64 pixels. Ideally, a small interrogation area is recommended in order to produce a good resolution velocity vector in flow regions with complex mixing or high velocity gradient. However, it is only valid provided sufficient number of seeding particles is in each interrogation area. When applying small interrogation area size with a sparse particle distribution, it can cause an empty area with missing velocity value which is called an outlier. The identified outliers are required to be interpolated from the neighbouring grids. For the PIV measurements presented in this work, an interrogation area size of 32 x 32 pixels corresponding to 5.5 x 5.5 mm was selected to provide reasonable resolution with minimal outliers in the measuring plane. In order to improve the resolution, interrogation separation of approximately half the interrogation area size was applied so that neighbouring interrogation areas are 50% overlapped to each other.

Pulse separation time

Since there is no absolute rule to determine the best pulse separation time for particular flow measurements, the time interval between the illuminated frames for each image pair has to be optimised iteratively depending on the flow velocities being measured. When large pulse separation time is used, the particle displacement may exceed the interrogation area and no particle will be illuminated twice (so-called as loss of pairs). In order to compensate for the loss of image pairs, a shorter pulse separation time should be used however, it will directly reduce the particle displacement and hence the measurement accuracy. Alternatively, increasing the size of the interrogation area with consideration of sufficient image resolution can also offset the loss of pairs. For the PIV measurements over the mid-plane of the rectangular mantle enclosure, trial measurements were performed to determine the optimum pulse separation time that gave minimal outliers over the measuring plane for each case. The typical pulse separation times for velocity measurements in the 10 mm and 30 mm gap mantles are 12 ms and 15 ms respectively for an inlet flow rate of 1 L/min.

3.4 FALLING FILM SYSTEM MEASUREMENTS

This section outlines the construction and experimental techniques used to assess the performance of a falling film heat exchanger.

3.4.1 Construction of falling film heat exchanger

The construction of the falling film heat exchanger and tank is shown in Fig. 3.9. The falling film heat exchanger consists of a 1.2 m long core tube with inner diameter of 197 mm down the centre of a water storage tank. The core tube is spirally welded and internally grit blasted (Fig. 3.10). To establish the flow as a thin film over the top inner surface of the core tube, a flow distributor is installed at top of core tube. The flow distributor consists of four distributor nozzles to initiate the inlet flow into four paths as shown in Fig. 3.11a. The flow impinges onto the tube wall and then falls down as a thin liquid film through a 0.5 mm gap for each nozzle (Fig. 3.11b).

3. EXPERIMENTAL APPARATUS AND TECHNIQUES

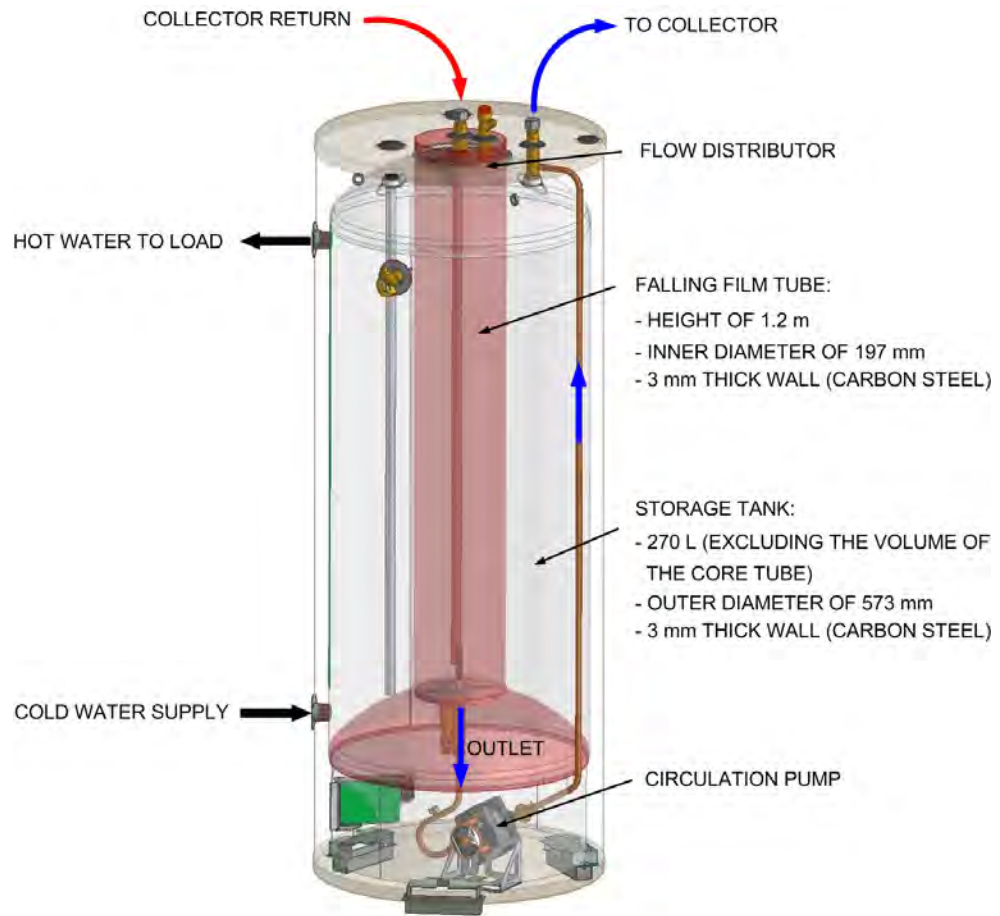


Fig. 3.9 Construction of falling film heat exchanger and storage tank.

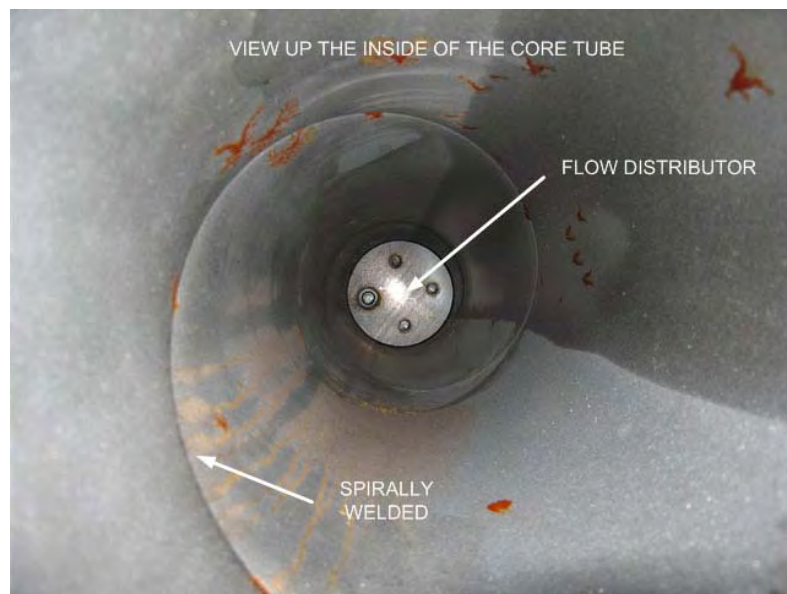


Fig. 3.10 View up the inside of the core tube.

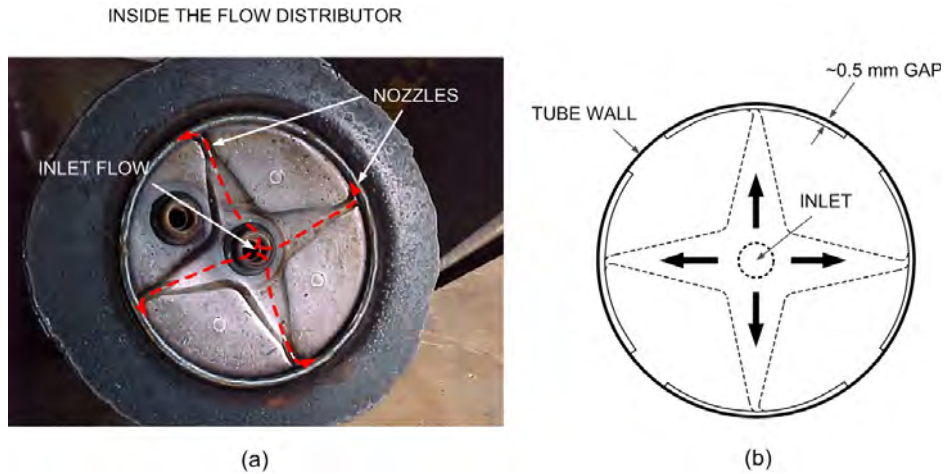


Fig. 3.11 (a) Photograph showing the distributor nozzles. (b) Sketch of the flow distributor.

3.4.2 Steady flow test rig for falling film

To evaluate the performance of a pumped-circulation solar domestic water heater with a falling film tank, tests were carried out under outdoor conditions in Sydney, Australia. The falling film tank was coupled to a flat plate collector array (3.6 m²) and 20% propylene glycol/water mixture was used as the working fluid in the closed collector-heat-exchanger loop. At the bottom of the core tube, a 200 mm depth of glycol mixture was used to avoid cavitation in the pump located at the outlet of the core tube.

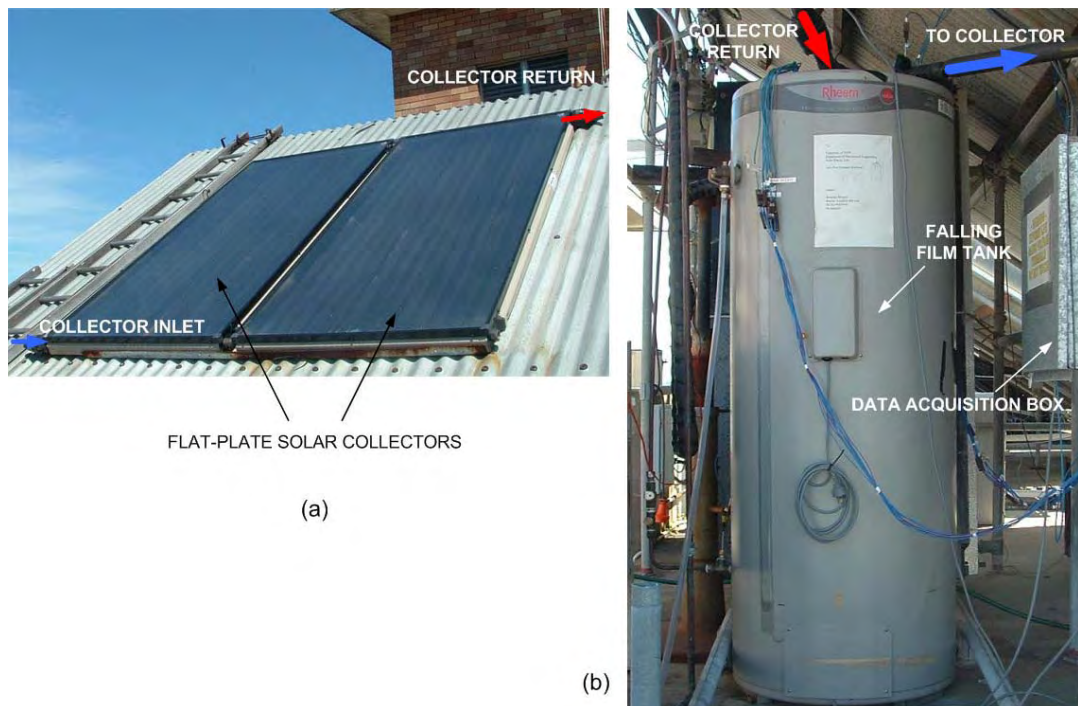


Fig. 3.12 Outdoor performance test rig, (a) flat plate solar collector array, (b) falling film tank.

Nine T-type thermocouples were fitted in the core of the storage tank and an additional nine T-type thermocouples were brazed on the tank side of the wall of the heat exchanger so that the heat exchanger heat transfer coefficients could be determined. The inlet and outlet temperatures and flow rate of the hot glycol mixture circulating through the heat exchanger were also monitored. Thermocouples located at the heat exchanger inlet and outlet ports were calibrated against a platinum resistance thermometer for a temperature range from 10 to 80°C at interval of 5°C. As the rest of the thermocouples were pre-installed in the tank core and on the outer wall of the core tube during tank construction, these thermocouples could only be calibrated by pump-circulating the tank core water through an external loop fitted with calibrated thermocouples for a temperature range from 30 to 70°C. During the calibration process, the insulated tank was isolated from the collector-loop and the core water was pre-conditioned at the required temperature level. The collector loop flow rate was measured by a calibrated turbine flow meter OMEGA FTB9510 in the range of 0.275 to 5 L/min. The flow meter was calibrated by comparing frequency output with the measured water volumes over a time interval. All readings were recorded on a PC via a DT800 datataker set to scan through all differential channels and downloaded one minute averaged readings. The schematic diagram of the experimental setup and locations of thermocouples are shown in Fig. 3.13.

Initially, measurements of thermal conditions in the falling film tank system were carried out with a conventional differential pump controller for heat up cycles from an initially cold tank (approximately 20°C in the early morning) and for different constant collector flow rates under clear sky conditions. The falling film tank was coupled to two copper flat-plate collectors. Measurements of the heat transfer coefficient in the falling film and the natural convection coefficient on the tank side of the heat exchanger were also performed based on steady flow tests. As the falling film tube extends from the top to the bottom of the storage tank, it is possible that cooler collector return may de-stratify the hot water in the top portion of the tank. The effect of degradation of tank stratification for the system with a differential pump controller was investigated through the daily performance tests. In these tests, the hot water tank setup was retained while the copper collectors were replaced by steel collectors with higher thermal mass so that energy can be collected when the pump is turn off.

3. EXPERIMENTAL APPARATUS AND TECHNIQUES

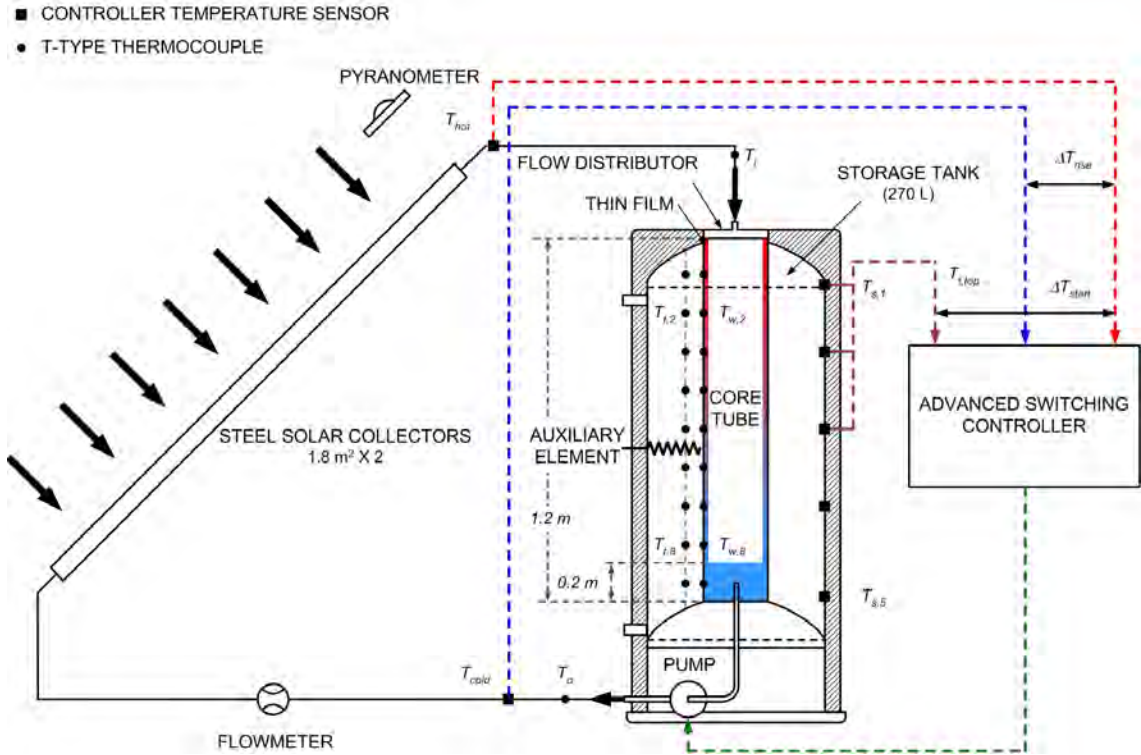


Fig. 3.13 Schematic diagram of monitoring points in the falling film system with a collector flow rate controller.

3.4.3 Collector flow rate controller

To overcome possible de-stratification, a collector flow rate controller was integrated to vary the flow rate to ensure a high collector return temperature relative to the top of the tank. Measurements of thermal conditions in the prototype of the falling film system were carried out with an advanced collector flow rate controller. Controller temperature sensors were fitted in the collector outlet (hot sensor, T_{hot}) and heat exchanger outlet (cold sensor, T_{cold}), and at the outer wall of the top half of the tank ($T_{t,top}$). The collector flow rate can be varied depending on the temperature rise (ΔT_{rise}) across the collector loop. When there is available solar energy from the collector, the controller switches on the pump. At the start of the heating process, the pump operates with the maximum flow rate to flood the collector loop and then changes to a fixed ΔT_{rise} of approximately 10 K by varying the pump flow rate. If the ΔT_{rise} drops to less than 3K or the temperature difference between the collector outlet and the tank top (ΔT_{start}) is less than 5 K (under weak solar radiation conditions), the pump is turned off and the collector

3. EXPERIMENTAL APPARATUS AND TECHNIQUES

fluid is drained back to the core tube. At the same time, the non-filled steel collectors are heated up under stagnation conditions by the solar radiation and store the energy until the circulation pump is turned on again when the ΔT_{start} reaches 6 K. The controller sequences used in the falling film system also ensure a high collector return temperature relative to the top of the tank (ΔT_{start} approximately of 6 K) in order to maintain the thermal stratification in the storage tank. The switching controller algorithm is illustrated in Fig. 3.14.

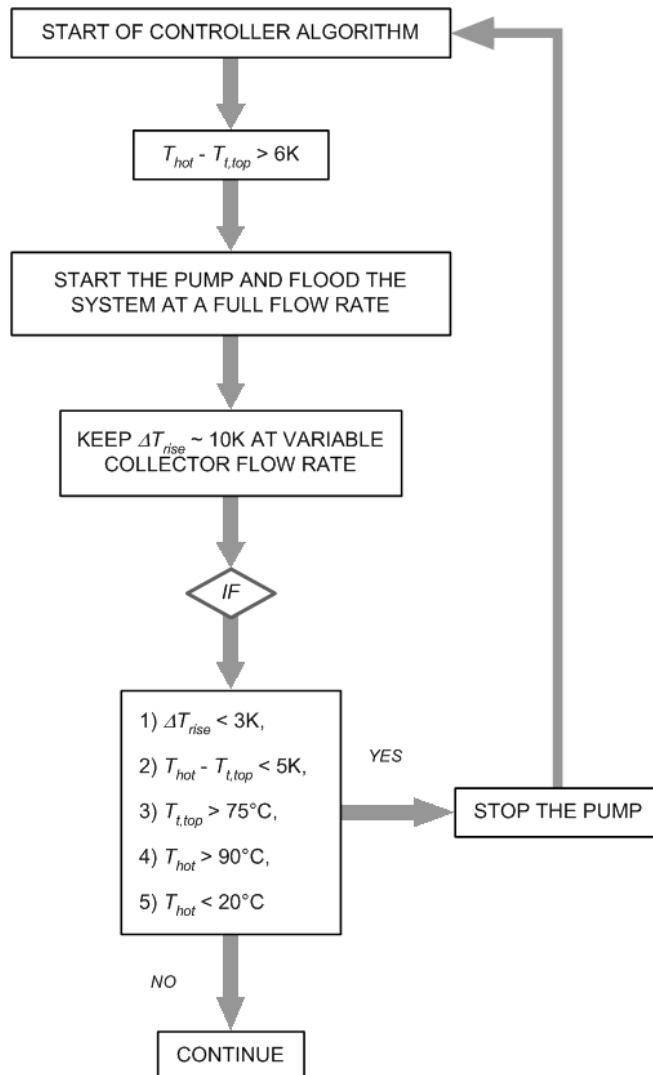


Fig. 3.14 Flow chart of the collector flow rate controller operation used in the falling film systems.

3.5 SUMMARY

The first part of this chapter outlined the experimental procedures used to measure the heat transfer in mantle heat exchangers with a two-pass flow arrangement, including thermal measurements in the core of the mantle-tank and flow visualisation in the rectangular mantle enclosure. The results obtained from flow visualisation experiments and thermal measurements will be presented in Chapter 5 and 6 respectively.

In the second part of this chapter, experimental techniques used to characterise a falling film heat exchanger were discussed, including measurements of heat transfer coefficients, daily performance and an overview of the collector flow rate controller operation sequences. The detailed analysis of falling film systems will be presented in Chapter 7. In the next chapter, aspects of numerical modelling used in this thesis will be presented.

- CHAPTER 4 -

NUMERICAL SIMULATION TECHNIQUES

4.1 INTRODUCTION

One of the important parts of the thesis is to investigate the convective heat transfer in the mantle heat exchangers and falling film heat exchangers. As the net heat transfer rate across the heat exchanger is highly dependant on the flow regime on the hot side and the natural convection circulation on the tank side (cold side) of the heat exchanger, it is necessary to understand the heat flux distribution over the heat transfer wall. Although experimental approaches detailed in Chapter 3 provide average heat transfer data, the detailed measurements are always restrictive, as placing instruments in the flow may disturb the flow behaviour. Therefore, detailed investigation of the flow structure and heat transfer processes in the mantle heat exchanger was performed using the commercial computational fluid dynamics (CFD) package, FLUENT in parallel to the experiments. In this thesis, only the mantle heat exchanger was studied using CFD simulations. For the falling film heat exchanger, numerical simulation was not undertaken as the presence of complicated wave phenomena at the free surface of the thin film would be difficult to simulate using CFD.

The basic theory behind CFD and aspects of numerical modelling that were applied to model mantle heat exchangers are described in this chapter. It includes the governing equations of motion, the turbulence model, fluid properties, discretisation method, solution procedure and mesh independence study.

4.2 FUNDAMENTALS OF CFD

CFD is a design tool involving predictions of fluid flow and heat transfer related to the physical phenomena by means of computer-based simulation. The principle concept of CFD is to solve the conservation of mass (continuity) equation, momentum equation and energy equation by discretisation of the governing equations on the small control volumes in the flow domain. For laminar and incompressible (e.g. water in this study) flow involving heat transfer with a gravitational body force, the fundamental governing equations are expressed as follows:

- Continuity equation:

$$\frac{\partial \rho}{\partial t} + \nabla \cdot (\rho \vec{v}) = 0 \quad (4.1)$$

- Momentum equation:

$$\frac{\partial}{\partial t} (\rho \vec{v}) + \nabla \cdot (\rho \vec{v} \vec{v}) = -\nabla p + \nabla \cdot (\mu \nabla \vec{v}) + \rho \vec{g} \quad (4.2)$$

- Energy equation:

$$\frac{\partial}{\partial t} (\rho E) + \nabla \cdot (\rho E \vec{v}) = -\nabla p \vec{v} + \nabla \cdot (k \nabla T) \quad (4.3)$$

where: E is the specific total enthalpy (J/kg),

\vec{g} is the gravitational force vector (m/s²),

k is the thermal conductivity (W/mK),

p is the static pressure (kg/ms²),

ρ is the density (kg/m³),

t is the time (s) which is only applicable for time-dependent simulation,

T is the temperature (K),

\vec{v} is the fluid velocity vector (m/s),

μ is the dynamic viscosity (kg/ms).

4.3 TURBULENCE MODELLING

In mantle heat exchangers, it was found that jet impingement from the inlet induced a region of localised turbulent mixing around the inlet region although the rest of the mantle flow is laminar (Refer to Chapter 5 and 6 for further details). The turbulence dissipation due to inlet jet impingement is more significant in narrow gap mantles, causing a stagnant heating region around the inlet that may not be captured properly by the laminar model. Thus, the shear-stress transport (SST) κ - ω turbulence model (Menter, 1994) in FLUENT was used to simulate the turbulent flow around the mantle inlet and low Reynolds number flow in the mantle away from the inlet. The SST model provides improved predictions of the standard κ - ε model and κ - ω model for low Reynolds number flows. Although the standard κ - ε model (Launder and Spalding, 1972) is the most widely used and validated model for turbulent flow, it is more valid for high Reynolds number bulk flow (flow away from walls). While the standard κ - ω model (Wilcox, 1998) incorporates modifications for low-Reynolds number effects and flow near the wall provided that the mesh resolution in the near-wall region is fine enough. In general, the SST κ - ω model combines the best features of the standard κ - ε model and κ - ω model to account for flow in both the near-wall and far-field zones with the introduction of a blending function.

$$\text{SST model} = F_1 (\kappa\text{-}\omega \text{ model}) + (1-F_1)(\kappa\text{-}\varepsilon \text{ model}) \quad (4.4)$$

where: F_1 is the blending function. At the wall, F_1 is in order of one whereas F_1 is zero in the far-field region.

Additionally, the standard definition of the turbulent viscosity as a function of the kinetic energy of turbulent fluctuations and turbulence eddy frequency in the κ - ω model has been modified in the SST model to account for the transport of the principle turbulent shear stress. Further details on the SST κ - ω model and its mathematical expressions are given in FLUENT (2005).

The SST turbulence model was applied for all CFD simulations with the following parameters:

- A turbulence intensity of 0.5 % was estimated in the inlet pipe which reflects the low turbulence range of Reynolds number (typically $2000 < Re_i < 5000$ in this study). Generally, turbulence intensities above 10 % are considered high (FLUENT, 2005).
- The characteristics length for the turbulence model was the mantle spacing, as the maximum size of the large eddies is restricted by the mantle spacing.

4.4 FLUID PROPERTIES

For the CFD simulations of mantle heat exchangers reported in this thesis, all the fluid properties are assumed to be constant except the density and viscosity. The fluid viscosity for all cases is modelled in terms of temperature. In order to obtain faster numerical convergence, the fluid density in the flow domain is modelled with the Boussinesq approximation instead of temperature dependent density. This model computes the fluid density as a constant value in all governing equations, except for the buoyancy term in the momentum equation:

$$(\rho - \rho_o)g \approx -\rho_o\beta(T - T_o)g \quad (4.5)$$

where: ρ_o is the constant density of the flow (kg/m^3) at T_o ,

T_o is the operating temperature ($^{\circ}\text{C}$),

β is the thermal expansion coefficient ($1/\text{K}$).

This approximation is accurate as long as changes in actual density with temperature are small. For the forced-flow narrow gap mantles, buoyancy forces do not play a significant role in the flow field. As a result, the use of the Boussinesq approximation in the simulations will not cause a significant effect on the predictions of heat transfer in the mantle.

4.5 DISCRETISATION AND SOLUTION PROCEDURES

4.5.1 Discretisation of equations

FLUENT incorporates a control-volume method (or finite volume) to convert the governing equations into a form of discretised equations at each control volume or cell in the computational domain. The discretised equations are then solved numerically. In fluid flow problems where convection is more dominating than diffusion, the properties at a cell face are highly influenced by values at the upstream cell. In this study, the second-order upwind differencing scheme is used for all simulations. This approach has the ability to identify the flow direction and offers second-order accuracy in which properties at cell faces are computed using a multidimensional linear reconstruction technique (Barth and Jespersen, 1989). The face value is computed using the following expression (FLUENT, 2005):

$$\phi_f = \phi + \nabla\phi \cdot \vec{\Delta s} \quad (4.6)$$

where: ϕ_f is the cell face value,

ϕ is the cell-centered value,

$\nabla\phi$ is the gradient in the upstream cell,

$\vec{\Delta s}$ is the displacement vector from the upstream cell centroid to the face centroid.

4.5.2 Pressure-velocity coupling

In solving the transport equations, the pressure and velocity terms are highly coupled as both velocity and pressure distributions are initially unknown and there is no separate equation that relates pressure and velocity. To promote convergence, a number of algorithms have been developed to iteratively resolve the coupling. The most common method is called SIMPLE. This method is iterative by guessing an initial value for the pressure field, and applying a pressure-correction equation to determine the correct pressure field for the momentum equations. The resulting velocity field should satisfy the continuity equation. In FLUENT, an improved version of SIMPLE is also available, which is called as SIMPLEC. SIMPLEC has the same basic steps as SIMPLE, however

the discretisation of momentum equations contains more terms, resulting in higher accuracy. In this study, SIMPLEC pressure-velocity coupling is adopted for all simulations.

4.6 GRID DEPENDENCE

In solving fluid dynamics and heat transfer problems using the CFD technique, grid refinement evaluation is essential in order to minimise the number of grid points and computational effort while resolving the behaviour of the real problem with an acceptable degree of accuracy. CFD modelling with a dense mesh would be preferable in producing an accurate numerical solution, however it requires extensive computing power and dramatically increases the computational time. In order to solve time-consuming problems, optimum number of grid points has to be used for the simulation domain. In addition, fine resolution of mesh in regions with high temperature or velocity gradients is necessary. Grid dependency check for all numerical models developed in this study is performed by comparing the total heat transfer rate across the mantle heat exchanger obtained from different mesh sizes. The results are presented in Chapter 5 for a scaled rectangular mantle model, and in Chapter 6 for a cylindrical mantle-tank model and a steady-state mantle model isolated from the tank.

4.7 SUMMARY

Numerical modelling of the flow and heat transfer in mantle heat exchangers are presented in Chapters 5 and 6. A comparison of the measured and simulated flow field and heat transfer rate in a scaled rectangular mantle heat exchanger is reported in Chapter 5. This chapter serves primarily as a validation of the numerical modelling study. In Chapter 6, the numerical modelling of a full-scale mantle heat exchanger on a cylindrical tank is performed by considering the transient nature of the flow. A simplified steady-state isolated mantle model that can be used for parametric studies is also developed.

- CHAPTER 5 -

FLOW IN RECTANGULAR MANTLES

5.1 INTRODUCTION

Experimental and numerical studies have been undertaken to investigate the flow and heat transfer in mantle heat exchangers with a two-pass flow arrangement. As it was difficult to use flow visualisation in a mantle on a cylindrical tank, a scaled rectangular mantle enclosure was used as a simplified model for the flow analysis. The experimental data presented in this chapter includes flow fields visualised using dye tracing, optical planar-PIV and heat transfer for isothermal tank conditions. Three-dimensional flow simulations with the same geometry as the tested unit were also performed using the commercial CFD package FLUENT. The numerical results were compared qualitatively and quantitatively against the experimental data.

5.2 FLOW VISUALISATION

A rectangular mantle enclosure mounted on one wall of a rectangular tank as illustrated in Fig. 5.1 was constructed as a simplified geometric representation of a cylindrical mantle-tank. This approach allows flow visualisation to be conducted using dye tracing and Particle Image Velocimetry (PIV) measurements. Mantle spacings of 3.5, 10 and 30 mm were tested. These are referred to as narrow, medium and wide gap mantles. In this study, flow fields over the mid-plane of the mantles were recorded 40 minutes after the start of the heating process. In order to simulate typical heating patterns in a solar water heater application, a pumped temperature controlled water heater was used to circulate hot water through the rectangular mantle. For each heat-up test, the mantle heat exchanger operated and started from an isothermal tank condition with a constant

5. FLOW IN RECTANGULAR MANTLES

inlet flow rate. The thermal boundary conditions used for the flow analysis in different mantle spacings are shown in Table 5.1.

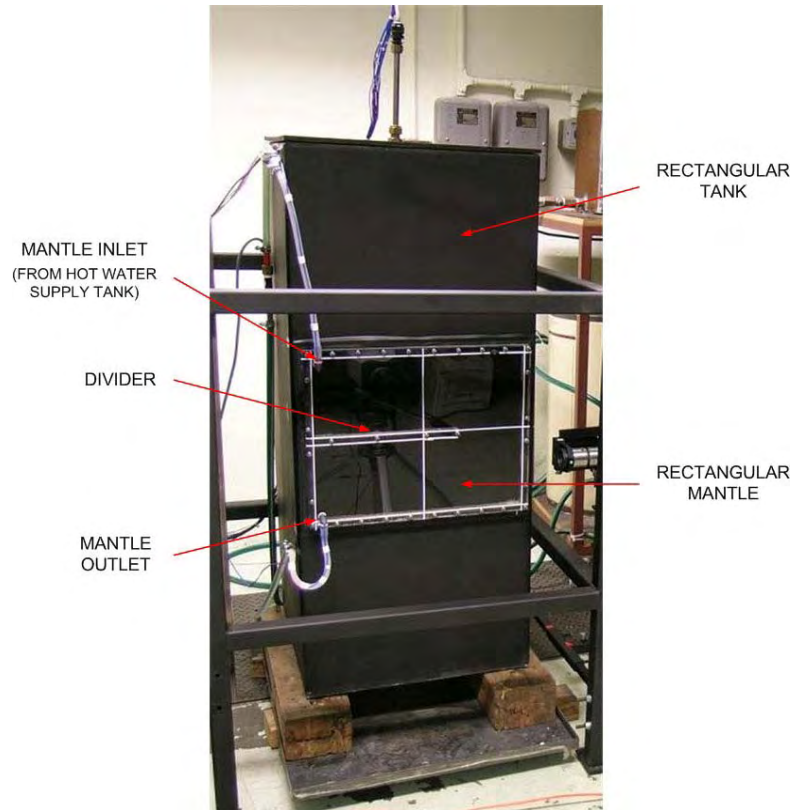


Fig. 5.1 Flow visualisation test rig.

Table 5.1 Representative thermal boundary conditions used in experiments.

CASE	MANTLE GAP (mm)	FLOW RATE (L/min)	MANTLE INLET TEMPERATURE (°C)	TANK TEMPERATURE
1	3.5	1	50	39°C (initially isothermal)
2	3.5	0.56	50	39°C (initially isothermal)
3	3.5	1	37	40°C at the top and 20°C at the bottom (initially stratified)
4	3.5	0.56	37	40°C at the top and 20°C at the bottom (initially stratified)
5	10	1	50	40°C (initially isothermal)
6	30	1	50	40°C (initially isothermal)
7	30	0.54	50	40°C (initially isothermal)

5.2.1 Narrow gap mantle: Dye tracing

Flow visualisation experiments for a 3.5 mm gap rectangular mantle were performed using dye injected into the mantle gap to show the flow direction. A photograph of the dye injection result for a hot inlet test with an initially isothermal tank (39°C), inlet temperature of 50°C and simulated collector loop flow rate of 1 L/min is shown in Fig. 5.2. As the flow in the narrow gap mantle is almost two-dimensional, good flow visualisation could be achieved. The dye streak lines indicate that the hot inlet stream spreads uniformly throughout the flow path of the heat exchanger without significant effect of buoyancy. The flow in the narrow gap mantle is laminar ($Re_d = 348$) and governed by forced convection. The thermal conditions used in this case simulated solar water heater operations during tank charging mode under full solar radiation conditions.

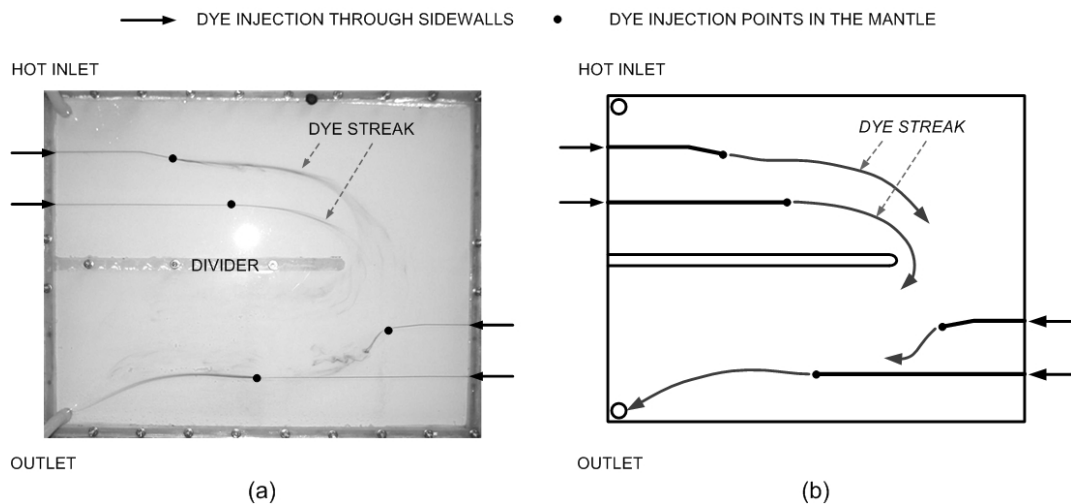


Fig. 5.2 Flow structure in the mid-plane of a 3.5 mm gap mantle for a constant inlet flow rate of 1 L/min and temperature of 50°C from an initially isothermal tank (39°C), (a) photograph of the dye injection result, (b) sketch of dye streak lines and injection points.

When the tank is stratified and the inlet temperature (37°C) is equal to the mean tank temperature adjacent to the mantle volume, the flow field in the narrow gap mantle obtained from dye tracing is shown in Fig. 5.3. In this case, the cooler inlet flow drops to its thermal equilibrium level which leads to most of the heat transfer occurring in the

5. FLOW IN RECTANGULAR MANTLES

bottom half of the mantle. This flow behaviour represents solar water heater operation in late afternoon after the tank is almost fully charged.

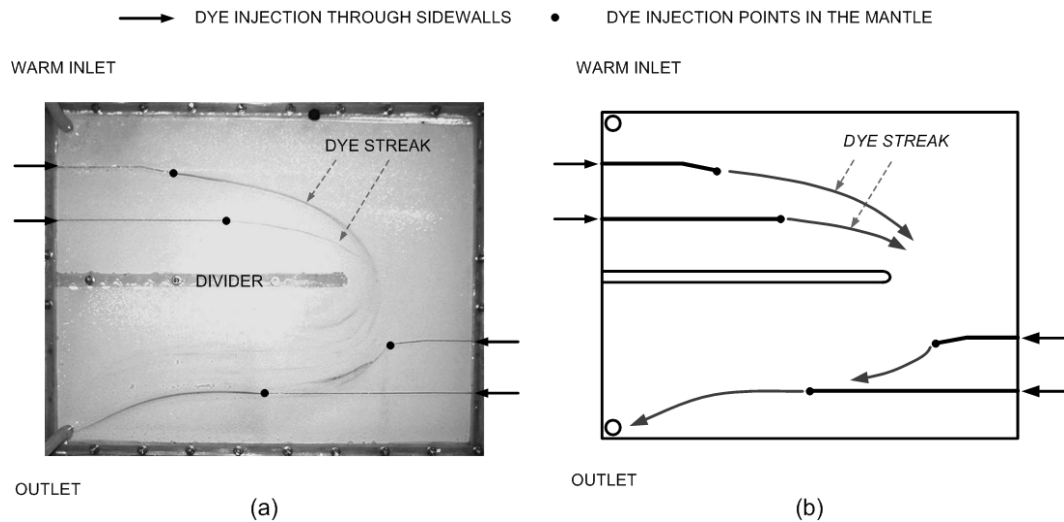


Fig. 5.3 Flow structure in the mid-plane of a 3.5 mm gap mantle for a constant inlet flow rate of 1 L/min and temperature of 37°C from an initially stratified tank (40°C at the top and 20°C at the bottom), (a) photograph of the dye injection result, (b) sketch of dye streak lines and injection points.

The effect of inlet flow rate on the flow pattern in a narrow gap rectangular mantle was also examined for the same thermal boundary conditions as for Fig. 5.2. For low flow ($Re_d = 187$), Fig. 5.4 shows that the hot inlet flow spreads out over the mantle due to the increased influence of buoyancy in the top of the mantle before being directed towards the bottom half of the mantle. In this case, the flow could be in the region of transition to mixed convective flow. For the warm inlet test with a low flow rate shown in Fig. 5.5, similar flow behaviour can be observed as in Fig. 5.3 in which the cooler inlet flow falls more directly to the bottom half of the mantle.

5. FLOW IN RECTANGULAR MANTLES

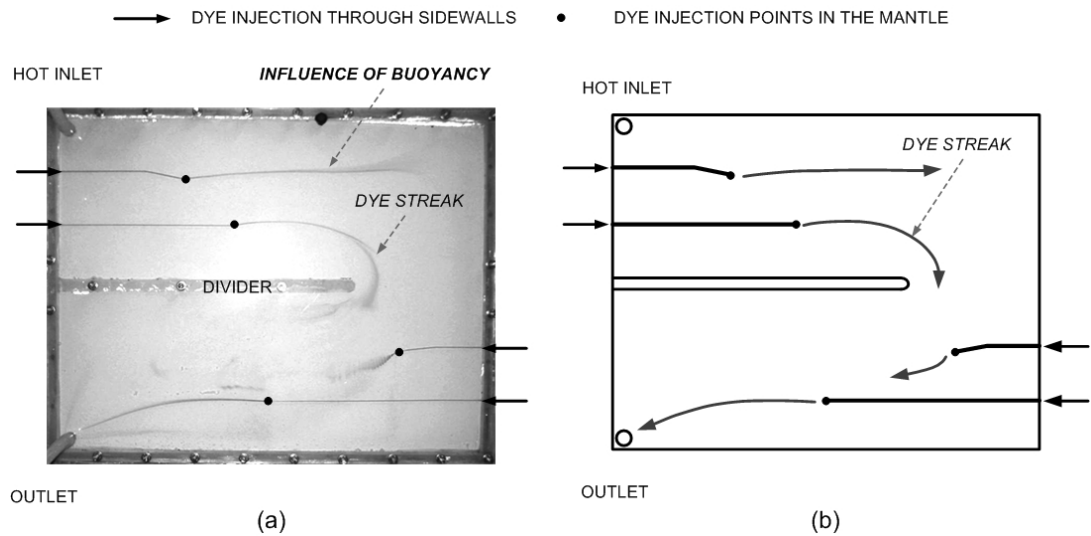


Fig. 5.4 Flow structure in the mid-plane of a 3.5 mm gap mantle for a constant inlet flow rate of 0.56 L/min and temperature of 50°C from an initially isothermal tank (39°C), (a) photograph of the dye injection result, (b) sketch of dye streak lines and injection points.

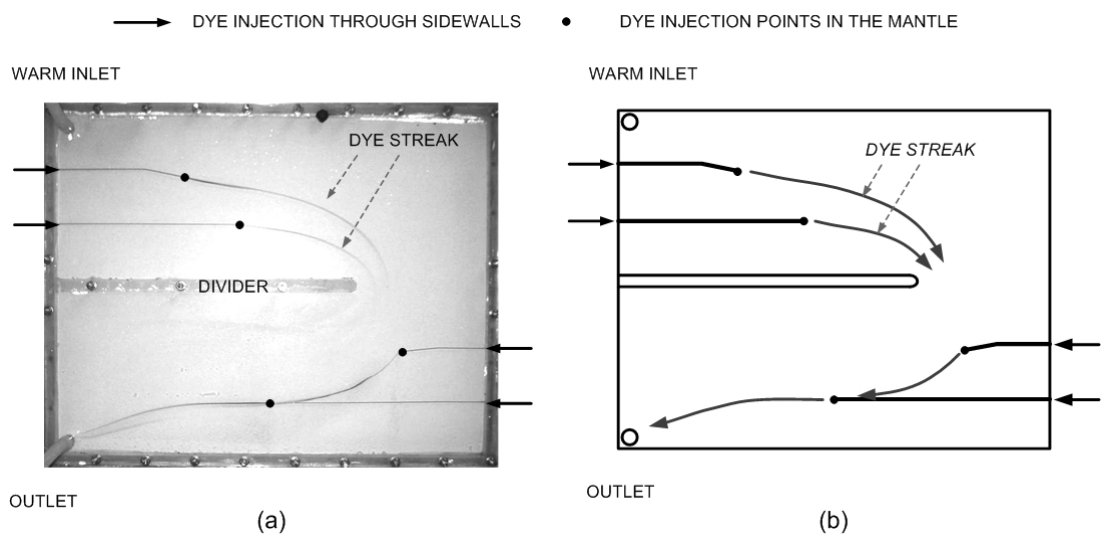


Fig. 5.5 Flow structure in the mid-plane of a 3.5 mm gap mantle for a constant inlet flow rate of 0.56 L/min and temperature of 37°C from an initially stratified tank (40°C at the top and 20°C at the bottom), (a) photograph of the dye injection result, (b) sketch of dye streak lines and injection points.

5.2.2 Medium and wide gap mantles: Particle Image Velocimetry (PIV)

When the mantle spacing is increased above 3.5 mm, it was difficult to visualise the flow field with dye due to mixing of the dye caused by buoyancy effects in the wider

flow path. Therefore, the velocity field in 10 and 30 mm gap mantles was measured using Particle Image Velocimetry (PIV). For PIV measurements, the image capture method and statistical cross-correlation method used to generate a velocity vector-map were detailed in Chapter 3. In order to achieve a good resolution of the flow tracer particle image, the rectangular mantle was divided into four measurement areas (Fig. 5.6a). Fig. 5.6b shows a PIV image-recording window over the mid-plane of the first quarter section of a 10 mm gap mantle, showing the instantaneous locations of the 20-micron Polyamide particles in the flow.

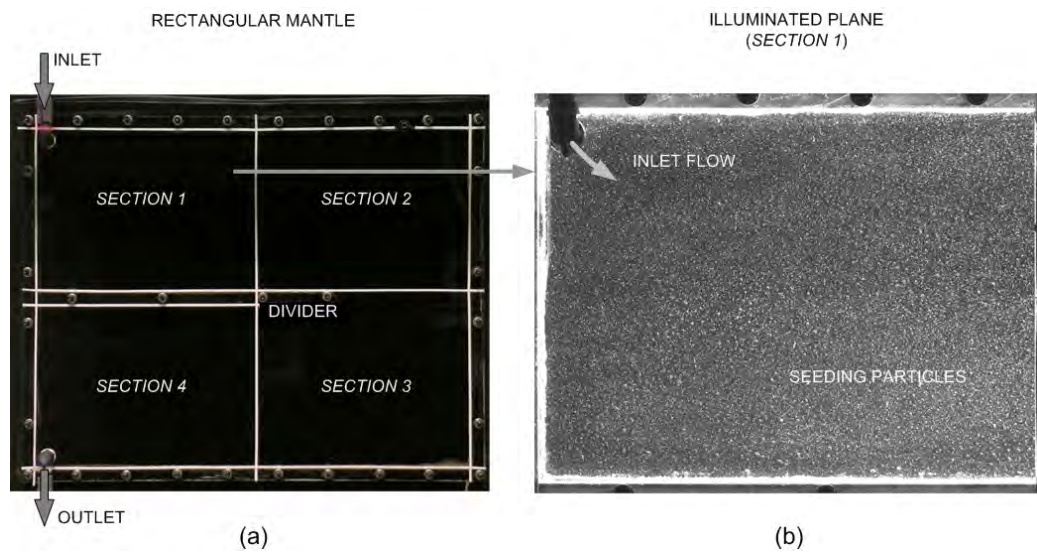


Fig. 5.6 (a) PIV measurement area in the mid-plane of the mantle enclosure, showing the quarter sub-sections, (b) instantaneous locations of the seeding particles over the first quarter of the mantle recorded during one of the dual laser pulse illuminations.

The velocity vector-map in the mid plane of a 10 mm gap mantle is shown in Fig. 5.7a. This velocity field was obtained by cross-correlating and averaging 40 pairs of images captured at sampling interval of 0.25 s with a 12 ms interval between each image pair. For an initially isothermal tank (40°C), inlet temperature of 50°C and flow rate of 1 L/min, the flow in the 10 mm gap mantle changes from being evenly spread as observed in the narrow gap mantle (Fig. 5.2a) into a mixed convective situation with buoyancy forces normal to the forced flow direction. Even though the bulk flow is laminar ($Re_d = 340$, $Ra_d = 1.26 \times 10^6$), the inlet stream impinging on the back wall coupling with the effect of buoyancy induces a region of localised turbulent circulation within the gap

near the inlet port. As a result, the small three-dimensional re-circulation cells near the inlet were unable to be captured due to the random motion of the seeding particles.

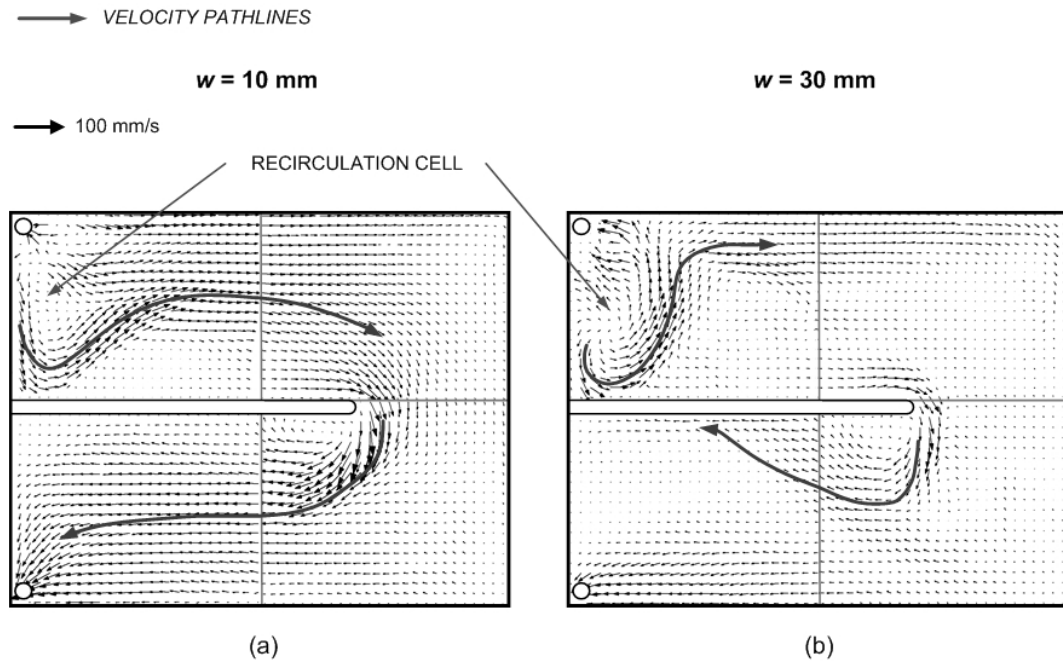


Fig. 5.7 Velocity vector-map and pathlines showing flow structure in the mid-plane mantle obtained from PIV measurements for a flow rate of 1 L/min and from an initially isothermal tank (40°C) with inlet temperature of 50°C , (a) mantle gap of 10 mm, (b) mantle gap of 30 mm.

In the 30 mm gap mantle for the same thermal boundary conditions and flow rate as for Fig. 5.7a, the flow is no longer two-dimensional or approximating to the duct-like flow behaviour. It can be observed in Fig. 5.7b that most of the hot inlet flow rises to the top 20% of the mantle section and the effect of localised natural convective circulation becomes significant. This velocity vector-map was obtained by averaging 40 pairs of images with a time interval between the base and cross images of 15 ms. The selection of longer pulse separation time was to capture the lower velocity seeding particles within the wide spacing.

As the inlet flow rate is decreased, the buoyancy induced flow becomes much more pronounced in the wider gap mantle as shown in Fig. 5.8. Most of the inlet flow stream rises to the very top of the mantle and then makes its way down to the second flow path. This flow field is very similar to that observed by Knudsen (2004) for a 33 mm gap

single-pass rectangular mantle (0.75 x 0.4) using PIV for hot inlet conditions (Fig. 5.9). In the single-pass mantle, there is a reverse circulation flow associated with buoyancy in the top section of the mantle, such a flow reversal is not observed in the two-pass configuration.

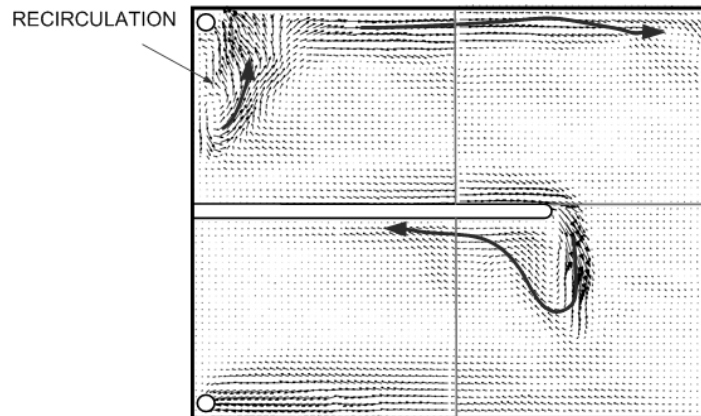


Fig. 5.8 Velocity vector-map and pathlines showing flow structure in the mid-plane of a 30 mm gap mantle obtained from PIV measurements for a flow rate of 0.5 L/min and from an initially isothermal tank (40°C) with inlet temperature of 50°C.

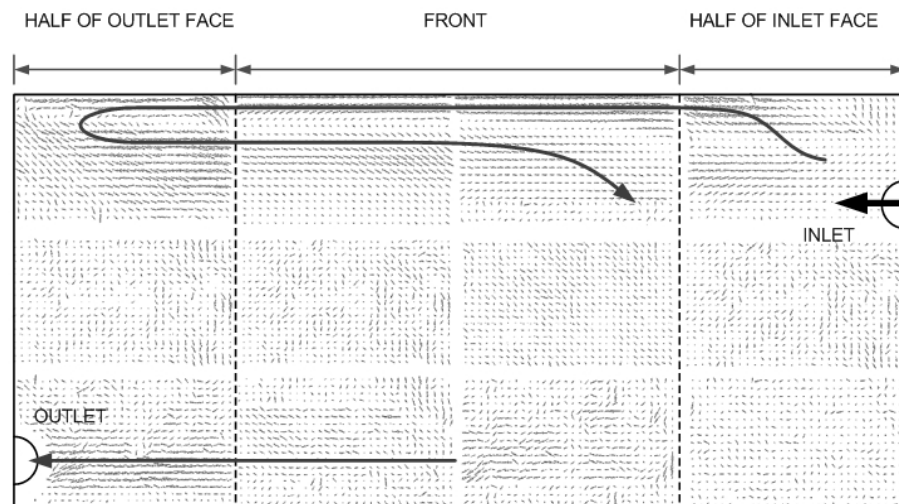


Fig. 5.9 Flow field in the mid plane of a 33 mm wide gap vertical mantle with a single-pass flow arrangement for a flow rate of 0.45 L/min and inlet temperature of 50°C (adapted from Knudsen, 2004).

5.3 CFD MODELLING IN RECTANGULAR MANTLES

5.3.1 Computational domain

This section describes the CFD model used to simulate the detailed flow and heat transfer in a rectangular mantle heat exchanger. Three-dimensional flow simulations of rectangular mantles for spacings of 3.5, 10 and 30 mm with the same dimensions as the experimental rigs were performed for steady-state conditions. For each simulation, the inlet temperature and flow rate from the indoor experiments were specified as inputs to the CFD model. As it is computationally expensive to model the entire mantle-tank configuration, the measured tank temperature and mean tank side heat transfer coefficient (Eqn. 5.1) determined from the measurements were specified (Fig. 5.10) on the inner heat transfer wall to represent the natural convection circulation inside the tank.

$$\bar{h}_t = \frac{\dot{Q}}{A(\bar{T}_{w,t} - \bar{T}_t)} \quad (5.1)$$

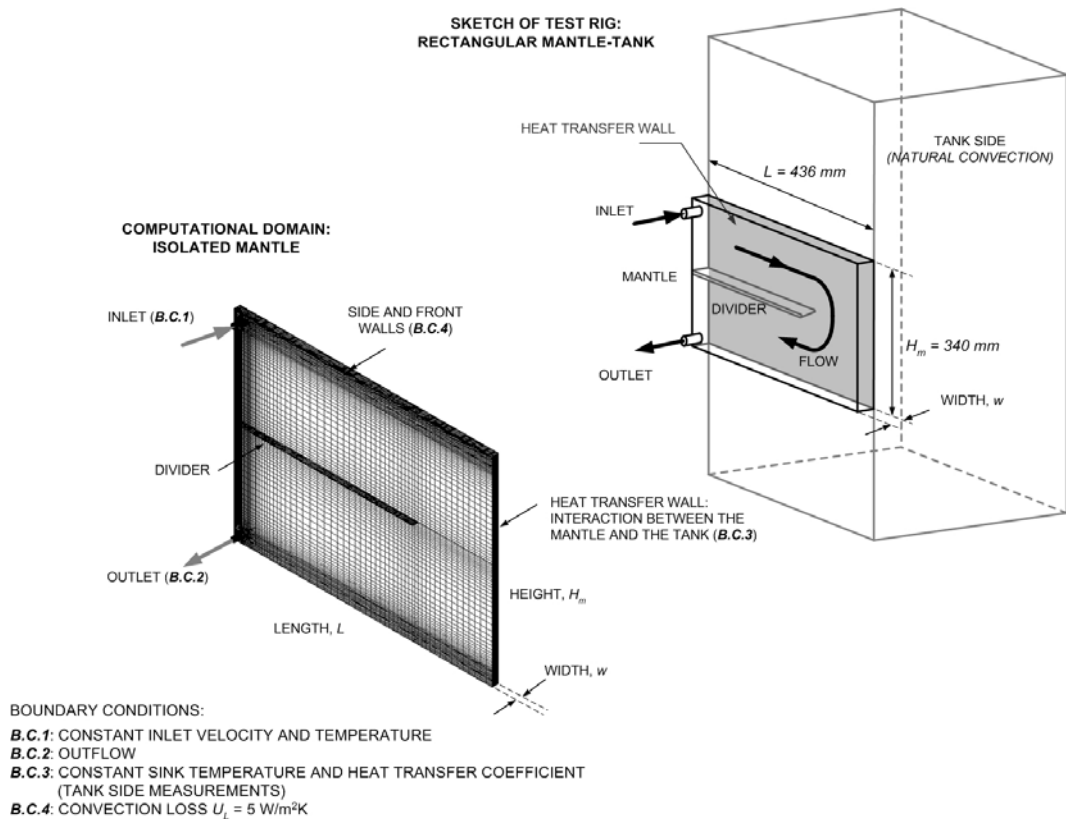


Fig. 5.10 Computational domain used in CFD simulations, showing the mesh and boundary conditions of the isolated mantle section.

The number of computational grid points used in each domain for different mantle gaps is shown in Table 5.2. A uniform mesh was used except in regions around the inlet and outlet ports where high resolution and non-uniform grids were used. In high temperature and velocity gradients near the heat transfer wall on the mantle side, 40% of the total grid points in the direction of the mantle width were concentrated in this high gradient region for all models.

Table 5.2 Number of computational points in the numerical models for different gap mantles.

MODEL	MANTLE GAP (mm)	NUMBER OF MESH POINTS	GRID DISTRIBUTION (LENGTH x HEIGHT x WIDTH)
1	3.5 (Narrow gap)	250,560	103 x 120 x 20
2	10 (Medium gap)	300,000	103 x 120 x 24
3	30 (Wide gap)	324,720	103 x 120 x 26

Although the main flow within the mantle gap is laminar, jet impingement near the inlet induced turbulent circulation around the inlet port in most cases. Therefore, a SST $k-\omega$ turbulence model was used throughout the CFD simulations to account for the localised turbulence mixing around the inlet port. Details of the SST $k-\omega$ turbulence model and parameters used in the modelling were discussed in Chapter 4. For the buoyancy term in the governing equations, the Boussinesq approximation was applied for all simulations in order to achieve faster numerical convergence. This approximation is valid in this numerical study as the temperature difference across the scaled rectangular mantle is less than 5 K.

5.3.2 Grid dependence of numerical models

In order to have sufficient number of grid points for solving the flow and heat transfer in rectangular mantles, a grid-sensitivity check was performed by doubling the mesh size given in Table 5.2. The parameter of interest used for examining the mesh sensitivity of the CFD model is the total heat transfer rate across the mantle. Table 5.3 shows that there is no significant difference in the total heat transfer rate between the

two grid sizes. Hence, the typical grids for mantle spacings of 3.5, 10 and 30 mm are mesh independent.

Table 5.3 Comparison of total heat transfer rate between typical grid and finer grid models.

SPACING (mm)	CONDITIONS	\dot{Q} (W) TYPICAL GRID	\dot{Q} (W) FINER GRID	% DIFFERENCE
3.5	1 L/min, $T_i = 50^\circ\text{C}$	252.4	253.0	0.20
10	1 L/min, $T_i = 50^\circ\text{C}$	234.6	234.7	0.04
30	0.54 L/min, $T_i = 50^\circ\text{C}$	184.3	189.4	2.70

5.4 VALIDATION OF NUMERICAL MODEL

Three experimental cases covering three distinct convective flow conditions were simulated numerically using the commercial CFD simulation package:

- Forced flow in a 3.5 mm gap mantle
- Buoyancy driven flow in a 30 mm wide mantle
- Mixed convective flow in a 10 mm gap mantle

To evaluate the validity of the CFD model, numerical results obtained from the CFD simulations were compared against the experimental data. The numerical simulations also provide further insight into the convective flow structure for different mantle spacings.

5.4.1 Flow in narrow gap mantles: CFD vs dye tracing

The experimental and simulated flow fields in the mid-plane of a 3.5 mm gap rectangular mantle are compared in Fig. 5.11a and b for an isothermal tank (39°C), inlet temperature of 50°C and flow rate of 1 L/min. In this narrow gap mantle where forced convection dominates, the experiment flow visualisation and CFD simulation results are in good agreement; both showing the hot inlet stream spreading evenly throughout the passageways in the mantle.

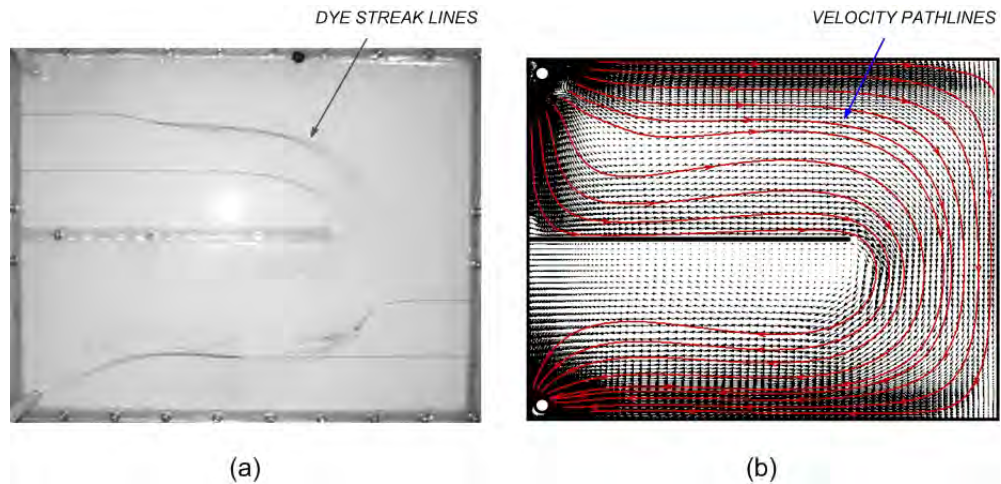


Fig. 5.11 Flow field in the mid plane of a 3.5 mm gap rectangular mantle for an isothermal tank (39°C), inlet temperature of 50°C and flow rate of 1 L/min ($Re_d = 348$) (a) photograph of the dye injection result, (b) CFD velocity vector-map and its pathlines.

Even though the bulk of the flow is laminar ($Re_d = 348$) and uniform within the flow path, the hot incoming stream impinging onto the back wall of the mantle causes a region of high velocity jet-like flow at the inlet corner of the mantle as observed in the simulated velocity contours shown in Fig. 5.12. Dye tracing of localised circulation flow could not be performed due to the fast dispersion of the dye.

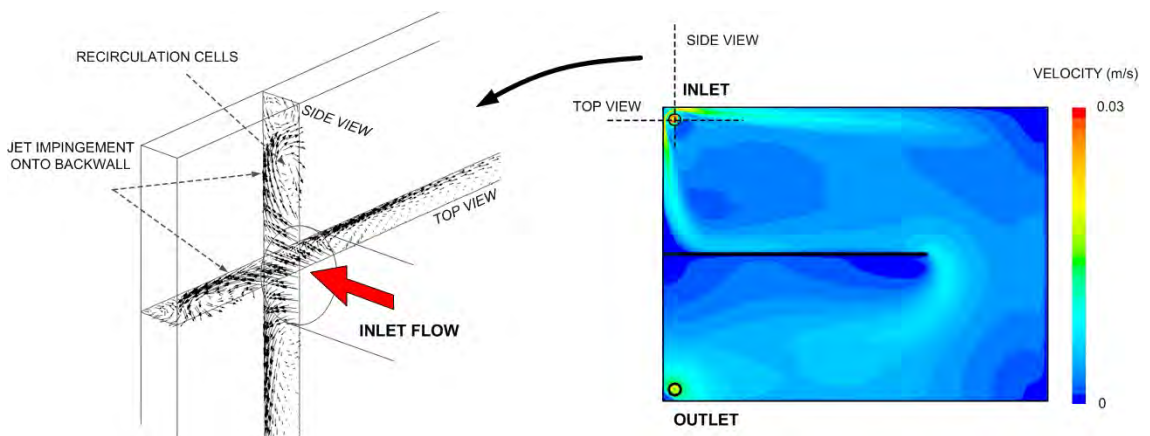


Fig. 5.12 CFD velocity vector at the inlet corner (left) and the velocity contours (right) in the mid plane of a 3.5 mm gap rectangular mantle.

The corresponding simulated temperature contour in the mid-plane of the mantle is shown in Fig. 5.13. The results reveal that the mantle fluid temperature is more uniform for forced convection dominated flow conditions in the narrow gap mantle. CFD prediction also indicates that approximately 4% of the total heat transfer takes place in the jet impingement region adjacent to the inlet port (2% of total mantle area).

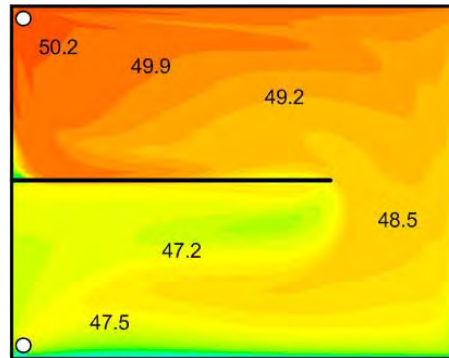


Fig. 5.13 Simulated temperature contours in the mid-plane ($^{\circ}\text{C}$) of a 3.5 mm gap rectangular mantle with an isothermal tank (39°C), inlet temperature of 50°C and flow rate of 1 L/min ($Re_d = 348$).

5.4.2 Flow in wide gap mantles: CFD vs PIV

When the mantle width is increased to 30 mm, the flow is no longer two-dimensional and the effect of buoyancy becomes significant resulting in more complex re-circulation flow paths. For the case with stronger buoyancy in a 30 mm wide gap mantle with a low inlet flow rate of 0.54 L/min, the velocity vector-maps obtained from PIV measurements and numerical simulation are in reasonably good qualitative agreement (Fig. 5.14 a and b). Within the wider gap, both PIV and CFD results indicate that the hot inlet stream initially drops down approximately 120 mm from the inlet port and then rises to the top of the mantle due to buoyancy effect. This stream flows along the top 20% of the mantle and then makes its way down to the second flow path of the mantle. In the second pass of this wider gap mantle a similar buoyancy induced flow can be observed particularly near the corner of the divider. It is important to note that the mantle used for the experiments consisted of a rounded-off edge divider whereas a flat edge divider (non-thickness wall) was adopted in the CFD model. For the rounded-off

edge divider configuration (Fig. 5.14a), the flow is driven slightly further down from the divider before rising towards the top of the second flow-pass by buoyancy forces compared to that of a flat edge divider configuration (Fig. 5.14b). Three-dimensional re-circulation cells are also visible in regions underneath the inlet port and the corner of the divider.

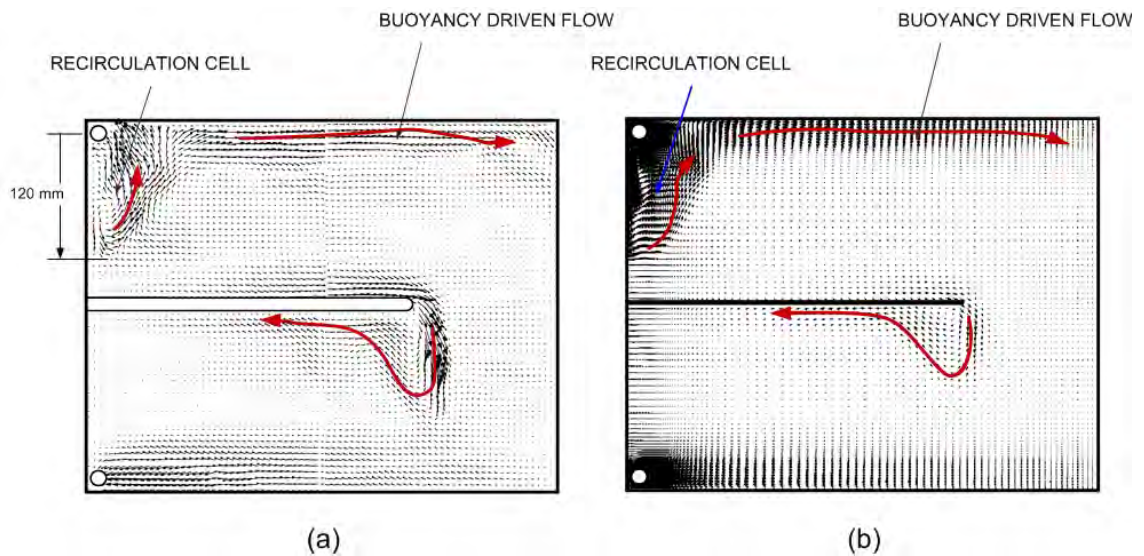


Fig. 5.14 Flow field in the mid plane of a 30 mm gap rectangular mantle for an isothermal tank (40°C), inlet temperature of 50°C and flow rate of 0.54 L/min, (a) PIV velocity vector-map and its streamlines, (b) CFD velocity vector-map and its streamlines.

A comparison of the velocity profile along a vertical line through the mid-plane of the mantle (200 mm from the inlet side) obtained from steady-state turbulence simulation and PIV measurements is shown in Fig. 5.15. The CFD simulation predicted approximately 10% higher peak velocity of the hot buoyant flow in the mantle top (interest region) than the PIV measurements. Due to the limitation of seeding particles per interrogation area in PIV measurements, averaging the velocity values between the adjacent interrogation areas would result a slightly lower mean values. In general, the predicted velocity profile shows reasonably quantitative agreement with the PIV measurements.

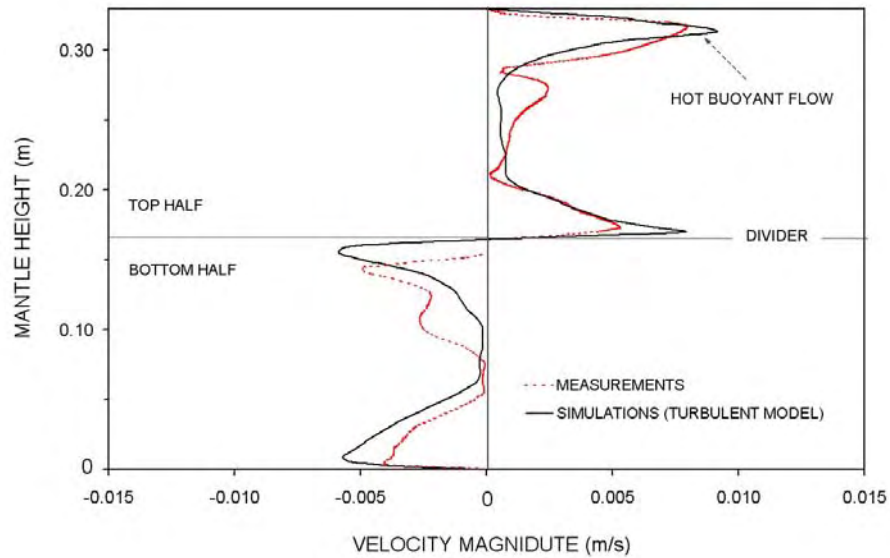


Fig. 5.15 Velocity profiles across a vertical line in the mid-plane and at 0.2 m from the sidewall near the inlet for the same conditions as in Fig. 5.14 obtained from PIV measurements and CFD simulation.

Fig. 5.16 shows the corresponding simulated temperature contours on the centre plane of the mantle for the 30 mm gap rectangular mantle. CFD results show that the mantle fluid stratifies over the height of the mantle therefore most of the heat transfer takes place in the top section of the mantle.

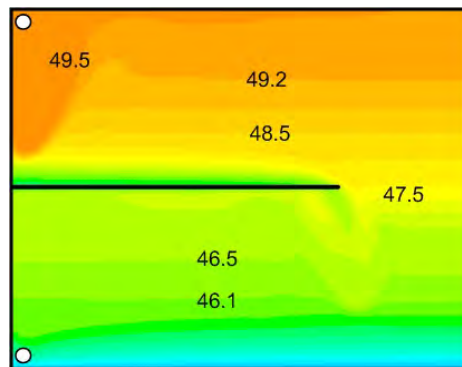


Fig. 5.16 Predicted temperature contours in the mid-plane ($^{\circ}\text{C}$) of a 30 mm gap rectangular mantle with an isothermal tank (40°C), inlet temperature of 50°C and flow rate of 0.54 L/min.

As buoyancy forces play an important role in the flow field and heat transfer in wider gap mantles, simulations using the Boussinesq approximation were compared to

temperature dependent solution as shown in Fig. 5.17. It is seen that the heat flux as a function of mantle height is the same for simulations using the Boussinesq approximation and temperature dependent property model. The validity of the Boussinesq approximation in modelling the flow and heat transfer process in the natural convection-dominated wide mantle is also due to the small temperature gradient across the mantle.

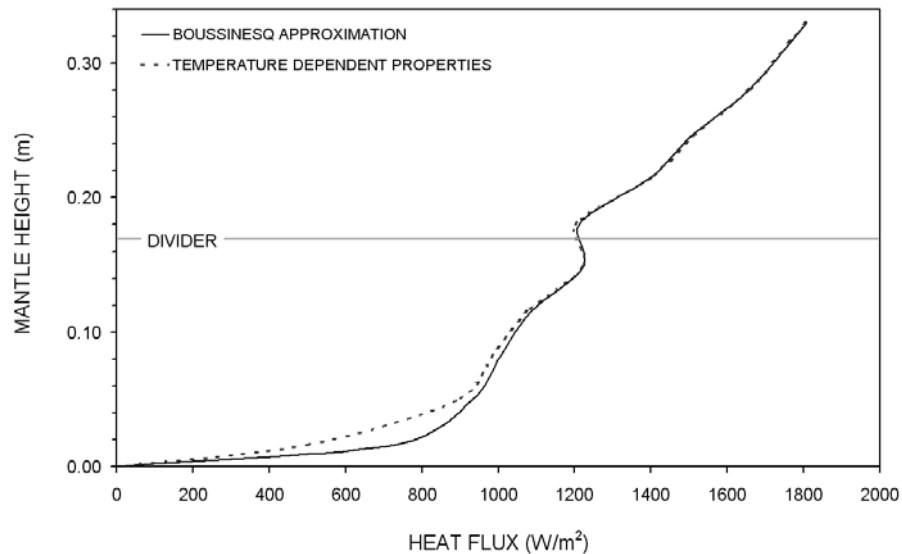


Fig. 5.17 Heat flux as a function of height for a 30 mm gap mantle with the same conditions as in Fig. 5.14, obtained from CFD model using the Boussinesq approximation and temperature dependent property model

5.4.3 Flow in medium gap mantles: CFD vs PIV

The transition between forced and natural convective flow in a rectangular mantle has also been investigated. In such a transitional regime, the flow in the mantle changes from being evenly spread into a conjugate or mixed convective situation involving a coupling of the inertia and buoyancy forces. Fig. 5.18a and b show a qualitative comparison between measured and predicted velocity vector-maps in the mid-plane of a 10 mm gap mantle for a flow rate of 1 L/min. For the numerical simulations, only the turbulence model with the Boussinesq approximation was considered. The hot incoming stream impinges on the back wall of the mantle and then distributes the flow through the mantle passageways influenced by buoyancy. The hot buoyant flow tends

to rise to the top of the mantle normal to the inertia driven flow before making its way towards the outlet. This flow behaviour is also known as orthogonal mixed convection.

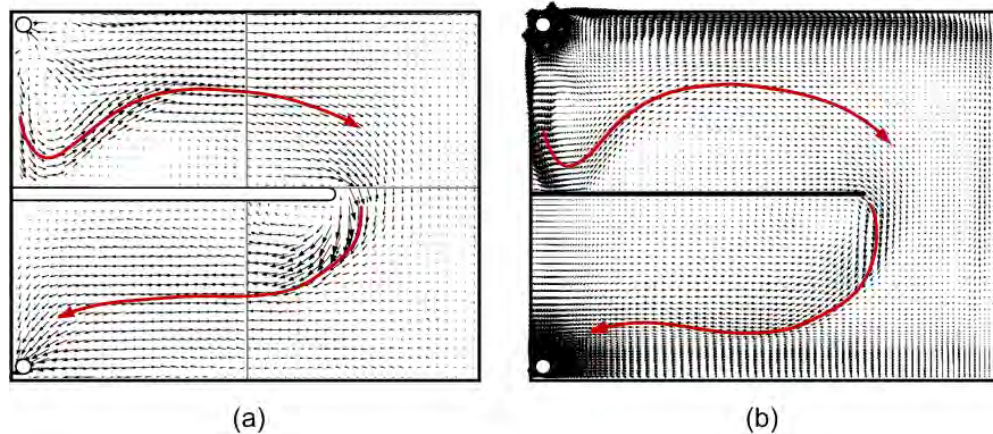


Fig. 5.18 Flow field in the mid plane of a 10 mm gap rectangular mantle for an isothermal tank (40°C), inlet temperature of 50°C and flow rate of 1 L/min, (a) PIV velocity vector-map and its streamlines, (b) CFD velocity vector-map and its streamlines.

The predicted velocity profile along a vertical line through the mid-plane of the mantle (200 mm from the inlet side) obtained from steady-state turbulence simulation is compared to PIV measurements in Fig. 5.19. For the mixed convection flow conditions in a 10 mm gap mantle, the predicted velocity profile shows good quantitative agreement with the PIV measurements in the top half of the mantle except in the very top region, and tends to overestimate the measurements in the bottom half of the mantle. A negative velocity in Fig. 5.19 means that the flow is towards the outlet port. In the very top section of the mantle, the high velocity jet-like flow due to inlet impingement could not be captured correctly due to the limitation of seeding particles per interrogation area in this high velocity gradient region. Furthermore, it is generally not possible to optimise the measurements using the same pulse separation time for every velocity gradient over the measuring plane. For the second pass of the mantle, the numerical results tend to overestimate the measured velocity magnitude. This is thought to be due to the influence of different divider edge between the test unit and CFD model.

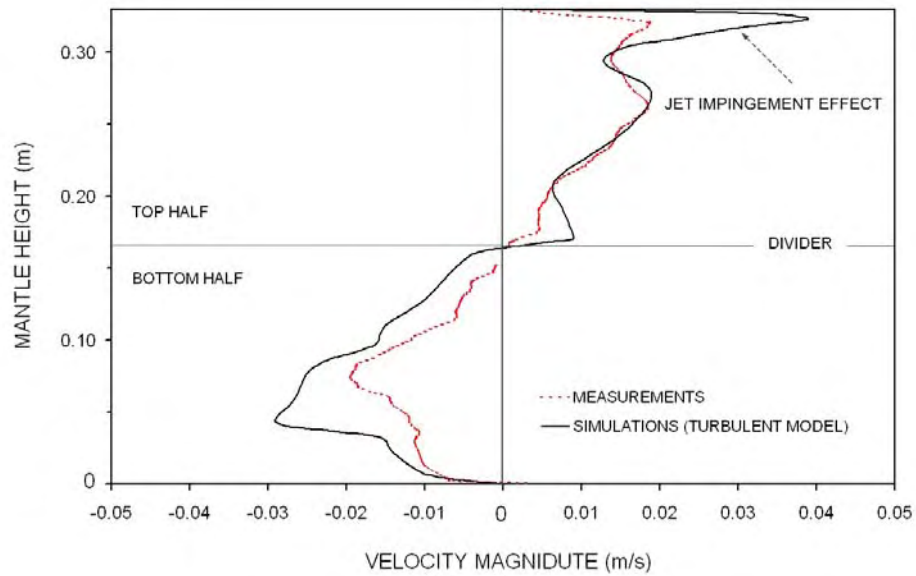


Fig. 5.19 Velocity profiles across a vertical line in the mid-plane and at 0.2 m from the sidewall near the inlet for the same conditions as in Fig. 5.18 obtained from PIV measurements and CFD simulation.

The CFD simulated temperature contours in the mid-plane of the 10 mm gap mantle is shown in Fig. 5.20. The hot incoming fluid is first driven down from the inlet but rises to the top section of the mantle with the influence of buoyancy before making its way towards the outlet.

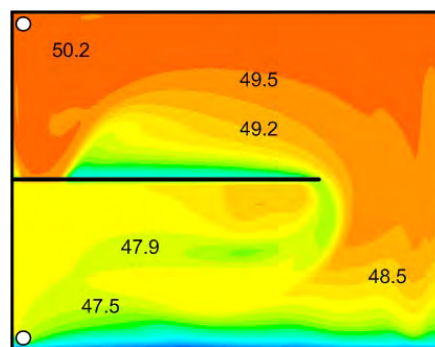


Fig. 5.20 Predicted temperature contours in the mid-plane (°C) of a 10 mm gap rectangular mantle with an isothermal tank (40°C), inlet temperature of 50°C and flow rate of 1 L/min.

5.4.4 Heat transfer: CFD vs experiments

Part of the validation procedure is to compare the measured and simulated net heat transfer rate (\dot{Q}) across the mantle heat exchanger as shown in Fig. 5.21. The net heat transfer rate can be evaluated using the mass flow rate (\dot{m}) and temperature change between the mantle inlet (T_i) and outlet (T_o) as follows:

$$\dot{Q} = \dot{m}c_p(T_i - T_o) \quad (5.2)$$

The results obtained from simulations are within 5% of the measured heat transfer rate for mantle spacings of 3.5, 10 and 30 mm covering a range of thermal boundary conditions. The good agreement between the numerical simulations and measurements for both the flow field and the heat transfer rate show that the CFD simulations can be used for parametric studies of the performance of mantle heat exchangers.

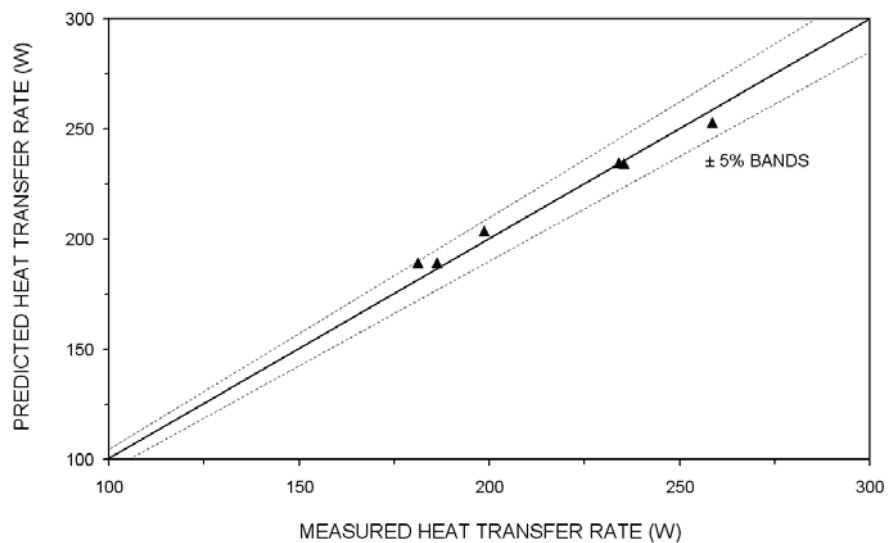


Fig. 5.21 A comparison of measured and simulated net heat transfer rate across the scaled mantle heat exchanger.

5.5 SUMMARY

The steady state flow structure and heat transfer in a simplified rectangular mantle heat exchanger have been investigated through a series of flow visualisation experiments including dye tracing, PIV measurements and CFD simulations for mantle spacings varying from 3.5 mm to 30 mm. In a narrow gap mantle of 3.5 mm, the bulk flow was mainly dominated by forced convection. As the mantle gap was increased, the flow in the mantle was gradually influenced by buoyancy forces directing the hot inlet stream towards the top section of the mantle.

The simulated flow structure and heat transfer rate in the laboratory-scale rectangular mantle enclosures were in good agreement with the measured conditions. The agreement between the CFD simulations and measurements provides some confidence in the use of commercial CFD simulation package to study the heat transfer characteristics of mantle heat exchangers.

- CHAPTER 6 -

HEAT TRANSFER IN NARROW GAP MANTLE HEAT EXCHANGERS

6.1 INTRODUCTION

In this chapter, the performance of narrow gap mantle heat exchangers is evaluated. The investigations are divided into four parts as follows:

- Results from controlled indoor experiments were used to quantify tank stratification and overall heat transfer coefficient-area product (UA_{hx}) of the heat exchanger. Measurements of the heat transfer coefficients for the heat exchanger are also presented.
- Two CFD models were developed to provide detailed understanding of the operation characteristics of the heat exchanger.
- Both measured and simulated data were used to develop non-dimensional heat transfer correlations as a function of dependent variables for the heat exchanger. These empirical correlations are required in the TRNSYS model for predicting the long-term system performance which will be discussed in Chapter 8.
- Heat transfer for larger heat exchanger size, initially preheated tank conditions and other mantle spacings are presented.

6.2 MEASUREMENTS OF HEAT EXCHANGER CHARACTERISTICS

The thermal performance of a narrow-gap mantle-tank for use in a pumped system was measured under controlled indoor conditions. Details of the core of the mantle-tank are given in Table 6.1. In this indoor experiment, steady flow of hot water as the heat source was supplied with the inlet temperature varying in the manner expected in a solar water heater application. Simulated flow rates of 2, 2.7 and 3.8 L/min for the hot side of the heat exchanger were used. The details of the experimental setup, instrumentation and controlled indoor heating technique are given in Chapter 3. In this section, the characteristics of the mantle heat exchanger were evaluated under two heating patterns:

- heat-up from a cold start representing a full tank recovery mode,
- heat-up from a half charged tank.

Table 6.1 Details of mantle-tank tested under controlled indoor conditions.

STORAGE TANK	
Tank volume (L)	270
Volume of water above top of mantle (L)	115
Volume of water below bottom of mantle (L)	37.4
Tank height (m)	1.5
Material	Stainless steel
Wall thickness (m)	0.0016
MANTLE	
Spacing (m)	0.003
Mantle height (m)	0.658
Heat transfer area (m ²)	0.903

To quantify the performance of the mantle heat exchanger for use in a solar water heater, it is necessary to investigate thermal stratification in the storage tank and the rate of change of the thermal energy accumulated in each segment of the tank. The heat transfer rate to each tank volume can be calculated by the equation:

$$\dot{Q}_{vol_i} = \rho V_i C_p \frac{dT_{t,i}}{dt} \quad (6.1)$$

where $dT_{t,i}$ is the temperature difference for tank element i measured over a ten-minute period (dt). The positions of measured tank core temperatures and the volume of each tank element are given in Table 6.2.

Table 6.2 Positions of measuring points and volume of each segment in the tank (Fig. 6.1).

TEMPERATURE MEASURING POINT	DISTANCE FROM THE TANK BOTTOM (m)	TANK ELEMENT	VOLUME (L)
$T_{t,1}$	1.45	Vol 1	31
$T_{t,2}$	1.30	Vol 2	26
$T_{t,3}$	1.15	Vol 3	26
$T_{t,4}$	1.00	Vol 4	26
$T_{t,5}$	0.85	Vol 5	26
$T_{t,6}$	0.70	Vol 6	26
$T_{t,7}$	0.55	Vol 7	26
$T_{t,8}$	0.40	Vol 8	26
$T_{t,9}$	0.25	Vol 9	26
$T_{t,10}$	0.10	Vol 10	31

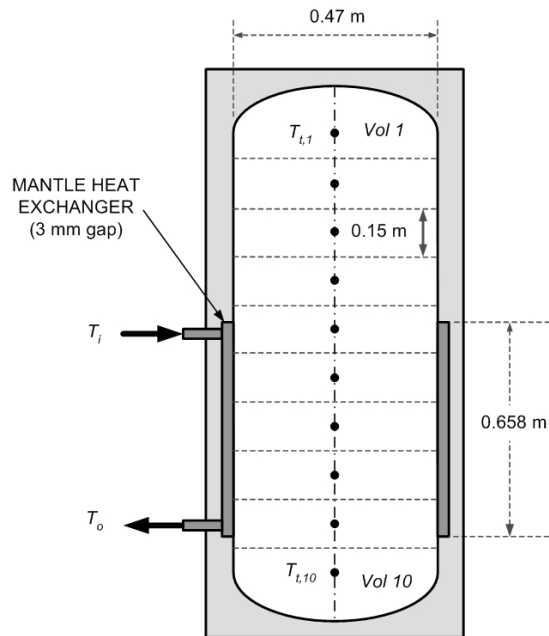


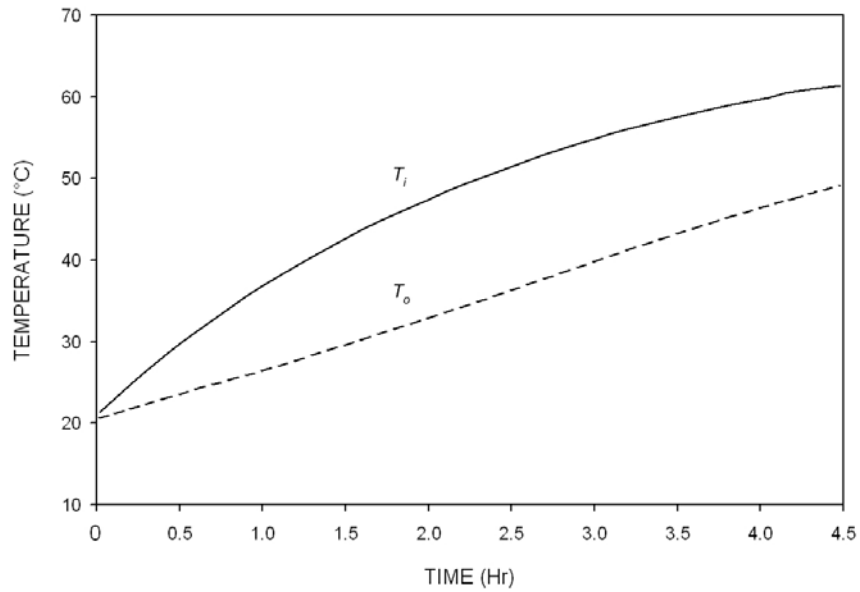
Fig. 6.1 Measuring points and tank elements.

6.2.1 Charging conditions

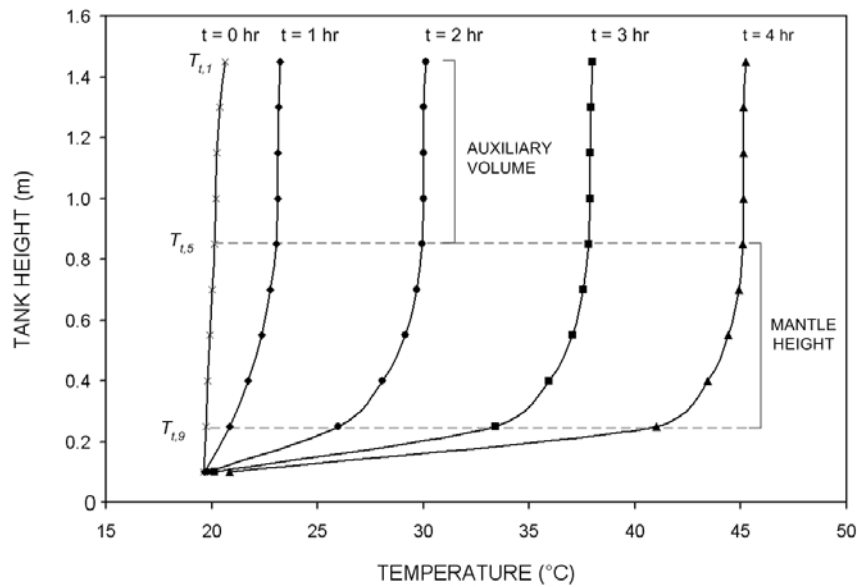
The cold start tests were first conducted in a full tank recovery mode (charging mode) representing typical operations of a solar domestic hot water system under clear sky conditions. In this case, the collector return temperature is always higher than the tank temperature adjacent to the top section of the mantle. Hot water draw-off and auxiliary heat input to the storage tank were not considered in these tests.

Tank stratification

The temperature of the heat exchanger inlet and outlet are shown in Fig. 6.2a, and the tank stratification is shown in Fig. 6.2b for a cold start test with a constant flow rate of 2 L/min on the hot side of the heat exchanger. At the initial heat-up stage, the tank temperature rises slowly which coincides with low mantle inlet temperature for system operating in the early morning. This slow start-up condition is also due to the high water viscosity at low temperature (less than 30°C), resulting in weak buoyancy driving force within the tank. As the tank is heated, a temperature gradient of 5 K can be observed within the depth adjacent to the heat exchanger, while the top section of the tank remains fully mixed throughout the heat-up cycle. This indicates that only minimal tank stratification is achieved. The cold water below the bottom of the heat exchanger is not affected by natural convection circulation in the tank. During the dynamic charging mode, the temperature difference between the heat exchanger outlet, T_o (Fig. 6.2a) and the adjacent tank element, $T_{t,9}$ (Fig. 6.2b) heated by the mantle heat exchanger is less than 5 K. This indicates that the heat exchanger in the collector loop is able to return the fluid close to the tank bottom temperature so that the collector could operate with an inlet temperature close to lowest temperature in the tank.



(a)



(b)

Fig. 6.2 Temperatures observed during a heat-up cycle from a cold start with a constant flow rate of 2 L/min, (a) inlet and outlet temperatures of the mantle, (b) tank core temperatures.

Heat transfer rate

The heat transfer rate to each tank element during the cold start test is shown in Fig. 6.3 using Eqn. 6.1. It can be seen that most of the heat is transferred to the water above the top half of the mantle during the initial heat-up stage ($t = 1$ hr). As the tank is heated further ($t = 2$ hr), heat is transferred uniformly to each tank element adjacent to the

mantle and above the mantle. The heat transfer process starts taking place at the tank portion adjacent to the bottom of the mantle heat exchanger when the tank is fully charged ($t = 4$ hr).

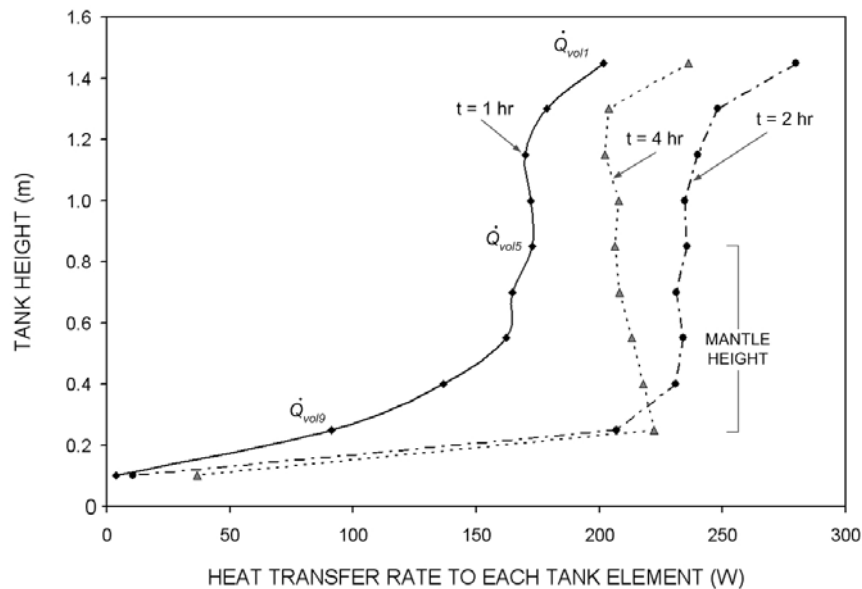


Fig. 6.3 Heat transfer rate to each element of the tank for an initially cold tank condition for a simulated collector flow rate of 2 L/min.

6.2.2 Preheated tank conditions

Another typical operation of a solar domestic hot water system is that the top half of the tank is pre-heated by an in-tank electric boosting element under cloudy conditions, and subsequently the system operates. In such instance, only the bottom half of the tank would be heated by solar input through the collector-heat-exchanger circuit.

Tank stratification

Fig. 6.4 presents measured tank temperature stratification for a half tank recovery mode with a flow rate of 2 L/min on the hot side of the heat exchanger ($\sim 52^\circ\text{C}$ at the auxiliary section and $\sim 20^\circ\text{C}$ at the bottom half of the tank). Throughout the first hour of heating, the temperature in the portion of the tank adjacent to the mantle rises quickly as the natural convection circulation is only confined within this portion of the tank. Due to the steep temperature gradient separating the hot and cold zones, the penetration of the boundary layer flow could be blocked by the stagnant hot layer in the top half of the

tank. When the temperature in volume 5 of the tank ($T_{t,5}$) reaches the stagnant hot layer in the auxiliary volume ($T_{t,4}$) as seen in Fig. 6.4, the flow and heat transfer process inside the tank may become more complicated due to the mixing natural convective flow between these tank layers. However, the mixing process does not significantly influence the temperature in the top portion of the tank above these mixing layers.

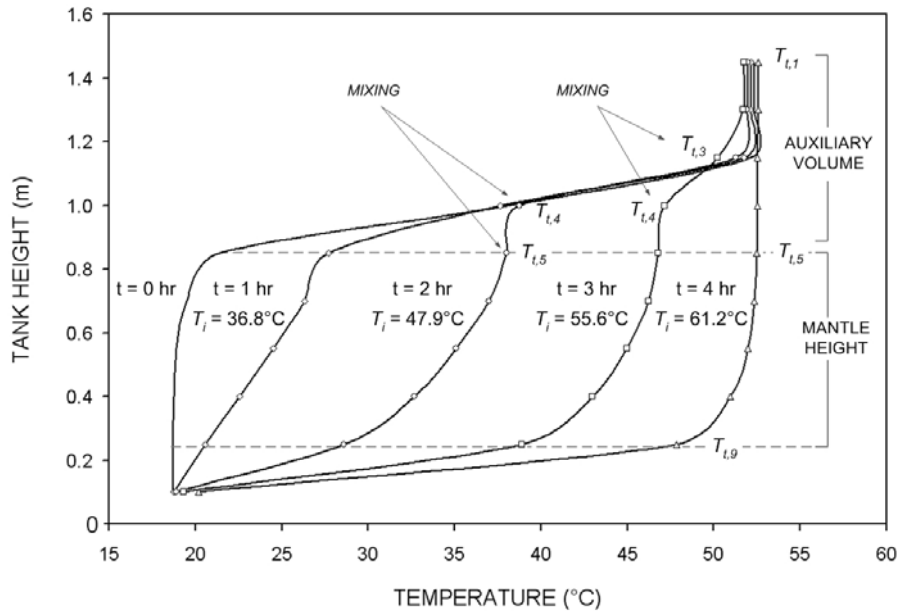


Fig. 6.4 Tank temperatures for a heat-up cycle from a pre-conditioned stratified tank condition (52-20°C) with a simulated collector flow rate of 2 L/min.

Heat transfer rate

For the tests with initially stratified conditions, the heat transfer rate to each element of the tank is shown in Fig. 6.5 using Eqn. 6.1. At the beginning of heating process, heat from the mantle is first transferred to the top portion of the solar preheat volume in the tank and a small amount of heat is conducted from the hot layer. As the tank is heated further, most of the heat transfer takes place at the bottom half of the section of the tank adjacent to the heat exchanger. In Fig. 6.5, it can be observed that there is an undesirable negative rate of heat transfer in volume 4 of the tank caused by the mixing when the tank temperature $T_{t,5}$ reaches $T_{t,4}$. This results in heat being transferred from the hot top layers to lower cooler layers.

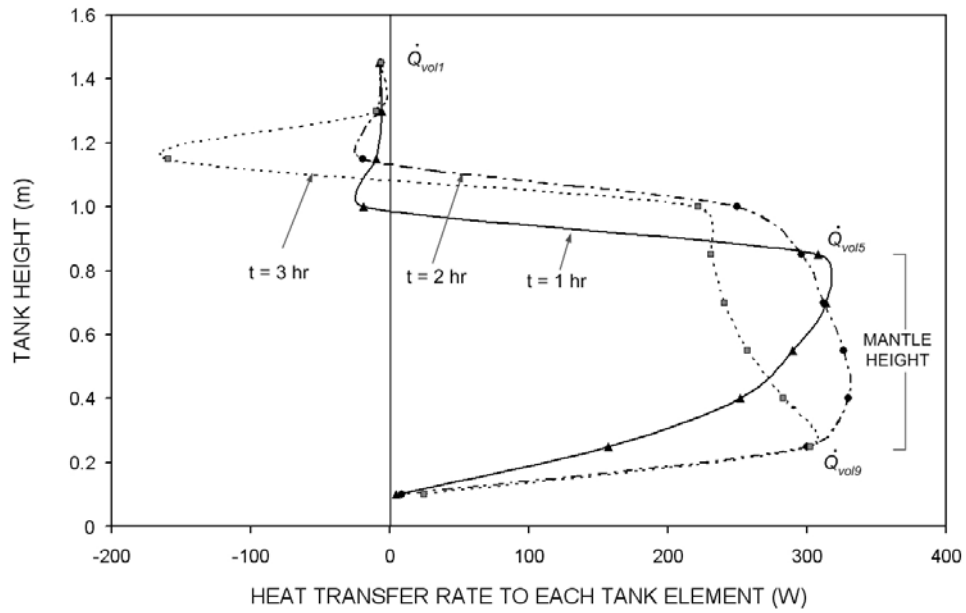


Fig. 6.5 Heat transfer rate to each element of the tank for an initially preheated tank condition for a simulated collector flow rate of 2 L/min.

6.3 OVERALL HEAT TRANSFER PERFORMANCE

In this section, overall heat transfer coefficient-area product (UA_{hx}) for the narrow gap mantle heat exchanger under full tank recovery operation mode is reported in order to characterise the overall heat transfer performance of the heat exchanger.

6.3.1 Heat transfer coefficients

Heat transfer between the hot collector fluid in the mantle heat exchanger and the potable water in the storage tank is governed by convective heat transfer on the hot side of the heat exchanger, conduction through the tank wall and natural convection circulation inside the tank. The mean convective heat transfer coefficients (\bar{h}) for the two convection processes in the mantle heat exchanger were determined using Eqns. 6.2 and 6.3 based on the measured inner wall temperatures and the tank core temperatures. Assuming one-dimensional heat transfer and isothermal wall boundary conditions, the overall heat transfer coefficient-area product (UA_{hx}) of the heat exchanger can be defined in terms of individual thermal resistances (Eqn. 6.4).

$$\text{On the mantle side, } \bar{h}_m = \frac{\dot{Q}}{A(\bar{T}_m - \bar{T}_{w,m})} \quad (6.2)$$

$$\text{On the tank side, } \bar{h}_t = \frac{\dot{Q}}{A(\bar{T}_{w,t} - \bar{T}_t)} \quad (6.3)$$

$$\frac{1}{UA_{hx}} = \frac{1}{\bar{h}_m A} + R_{wall} + \frac{1}{\bar{h}_t A} \quad (6.4)$$

where: A is the available heat transfer area of the mantle heat exchanger (m^2),

$\bar{T}_{w,t}$ is the measured averaged inner wall temperature on the tank side ($^{\circ}\text{C}$),

$\bar{T}_{w,m} = \frac{\dot{Q}t_w}{k_w A} + \bar{T}_{w,t}$ is the wall temperature on the mantle side of the wall ($^{\circ}\text{C}$),

t_w, k_w are the thickness (m) and thermal conductivity (W/mK) of the tank wall.

Fig. 6.6a and b show the heat transfer coefficients on the mantle side and tank side of the heat exchanger for cold tests with mantle flow rates of 2 and 2.7 L/min. For an inlet flow rate of 2 L/min, the heat transfer coefficient on the mantle side was found to be 600 $\text{W}/\text{m}^2\text{K}$ (Fig. 6.6a) while the heat transfer coefficient on the tank side varied from 200 to 400 $\text{W}/\text{m}^2\text{K}$ (Fig. 6.6b) due to the change of viscosity with temperature. The results obtained from cold tests with a mantle flow rate of 2 L/min show that the heat transfer coefficient on the mantle side is a factor of 1.5 times higher than that on the tank side. When the mantle flow rate is increased to 2.7 L/min, the mantle side heat transfer coefficient increases possibly due to the impingement effect near the inlet and better flow distribution across the mantle at high flow rate. Even though higher mantle side heat transfer coefficients could be achieved at flow rates above 2 L/min, the tank side heat transfer coefficient remains essentially unchanged (Fig. 6.6b) and as a result the limiting factor on the performance of the mantle heat exchanger is primarily the natural convection in the storage tank.

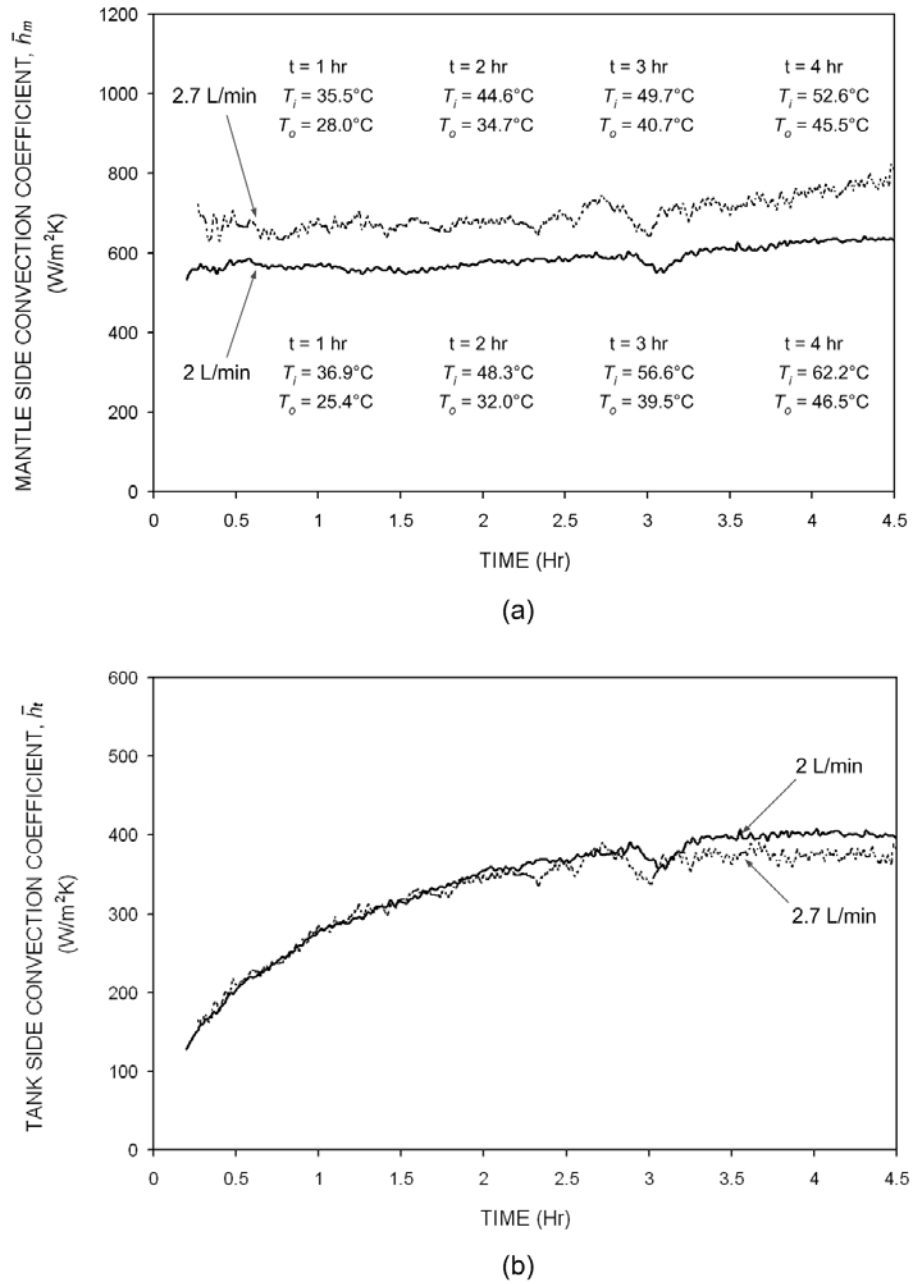


Fig. 6.6 Heat transfer coefficients for cold start tests with flow rates of 2 and 2.7 L/min, (a) mantle side, (b) tank side.

6.3.2 Overall heat exchanger UA_{hx}

Heat exchanger overall heat transfer coefficient-area product (UA_{hx}) associated with individual thermal resistances can also be conventionally defined as in Eqn. 6.5 based on the log-mean temperature difference between the hot and cold fluids (ΔT_{lm}) in the heat exchanger. This approach is only valid for a counter-flow heat exchanger where

both fluids flowing in opposite directions. For cross-flow and multi-pass heat exchangers, a correction factor (F) less than unity has to be accounted for in Eqn. 6.5 so that the heat exchanger UA_{hx} can be determined using the counter-flow approach. For the mantle heat exchangers in this study, the flow in the mantle circulates circumferentially around the tank into two-pass. Flow paths in this two-pass mantle design are perpendicular to the natural convection driven flows in the inner tank, hence it is operating as a cross-flow and two-pass heat exchanger. Assuming the mantle heat exchanger as one shell and two tube passes conventional type heat exchanger, the UA_{hx} correction factors for the heat-up tests are approximated based on the mantle inlet (T_i) and outlet (T_o) temperatures and the highest ($T_{t,5}$) and lowest ($T_{t,9}$) tank core temperatures. Note that there is no significant difference between $T_{t,5}$ and tank top temperature as the tank is well-mixed above the mantle.

$$UA_{hx} = \frac{\dot{Q}}{\Delta T_{lm}} \quad (6.5)$$

$$UA'_{hx} = FUA_{hx} \quad (6.6)$$

$$\Delta T_{lm} = \frac{(T_i - T_{t,5}) - (T_o - T_{t,9})}{\ln \left(\frac{(T_i - T_{t,5})}{(T_o - T_{t,9})} \right)} \quad (6.7)$$

where: F is the correction factor for cross-flow heat exchanger,

$T_i, T_o, T_{t,5}, T_{t,9}$ are the mantle inlet and outlet temperatures and temperatures in volumes 5 and 9 of the tank ($^{\circ}\text{C}$).

The variation of the overall heat exchanger UA'_{hx} during a cold test with an inlet flow rate of 2 L/min was found to be 150-213 W/K (Fig. 6.7) based on log-mean temperature difference with a correction factor of 0.95 (obtained from Incropera and DeWitt, 1996). The primary cause of the UA'_{hx} variation is due to the change of viscosity with temperature on the tank side. Fig. 6.7 also shows a comparison of the mantle heat exchanger UA_{hx} values evaluated using Eqns. 6.4, 6.5 and 6.6. The results indicate that the heat exchanger UA_{hx} with a correction factor matches to the heat exchanger UA_{hx} values determined in terms of individual thermal resistances using Eqn. 6.4. It is

assumed that the log-mean temperature difference method with a correction factor is applicable to the study here.

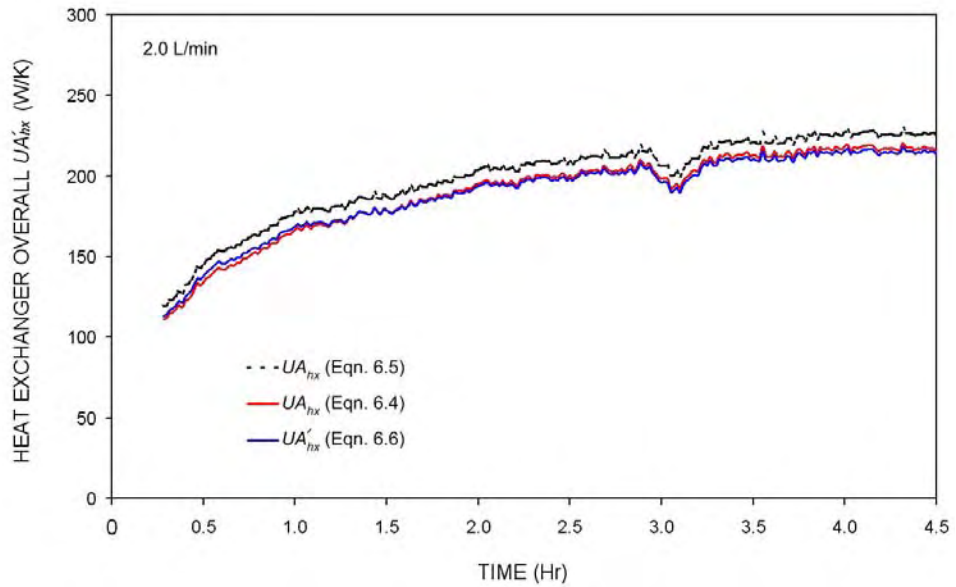


Fig. 6.7 Overall heat transfer coefficient-area product (UA'_{hx}) with a correction factor of 0.95 for the mantle heat exchanger (3 mm gap, 0.903 m^2 heat transfer area and 270L storage tank) during a heat-up cycle with an inlet flow rate of 2 L/min. Also shown are the UA_{hx} values evaluated using Eqns. 6.4 and 6.5.

The heat transfer characteristics of the narrow gap mantle heat exchanger for flow rates of 2.7 L/min and 3.8 L/min were also examined and compared to the 2 L/min case. Although the mantle side heat transfer coefficient increases with flow rate, the overall UA'_{hx} value of the heat exchanger was found to be very similar due to the limitation of natural convection heat transfer in the storage tank (Fig. 6.8).

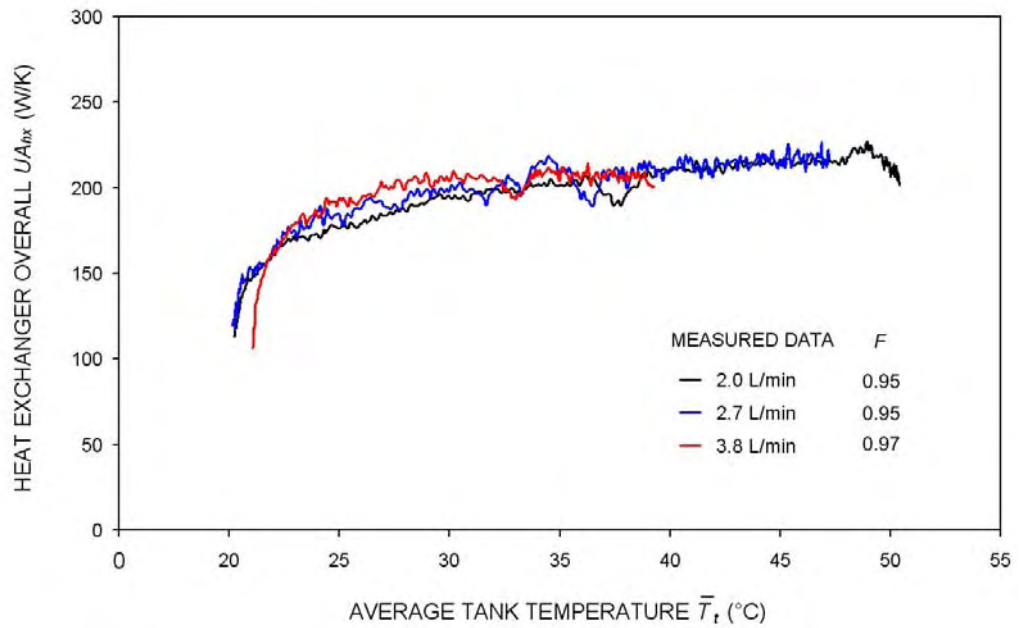


Fig. 6.8 Overall heat transfer coefficient-area product (UA'_{hx}) for mantle heat exchanger (3 mm gap, 0.903 m^2 heat transfer area and 270L storage tank) during heat-up cycles with flow rates of 2, 2.7 and 3.8 L/min.

6.4 MANTLE HEAT EXCHANGER MODELLING

6.4.1 Computational domains

This section describes numerical models for investigating detailed heat transfer in a narrow gap mantle heat exchanger using a commercial CFD package, FLUENT. In this study, two numerical models were developed:

Transient model: Full mantle-tank

The experiments were first simulated numerically by taking into account of the time-dependent natural convective flow on the tank side. A three-dimensional CFD model of a mantle heat exchanger coupled with a storage tank was developed with the same dimensions as the prototype unit. The computational domain was simplified by modelling the dome-shaped walls at the top and the bottom of the tank as flat walls, whereas the rest of mantle-tank volume remained the same as the prototype unit. In order to allow structured mesh to be used inside the tank volume, a very small diameter cylinder of 2 mm was located at the centre of the tank which would appear as a line in

the computational domain. High concentration mesh was used in the high temperature gradient regions near the heat transfer wall between the mantle and the storage tank. A total of 397,154 grid points were used in the computational domain within the mantle gap and the inner tank.

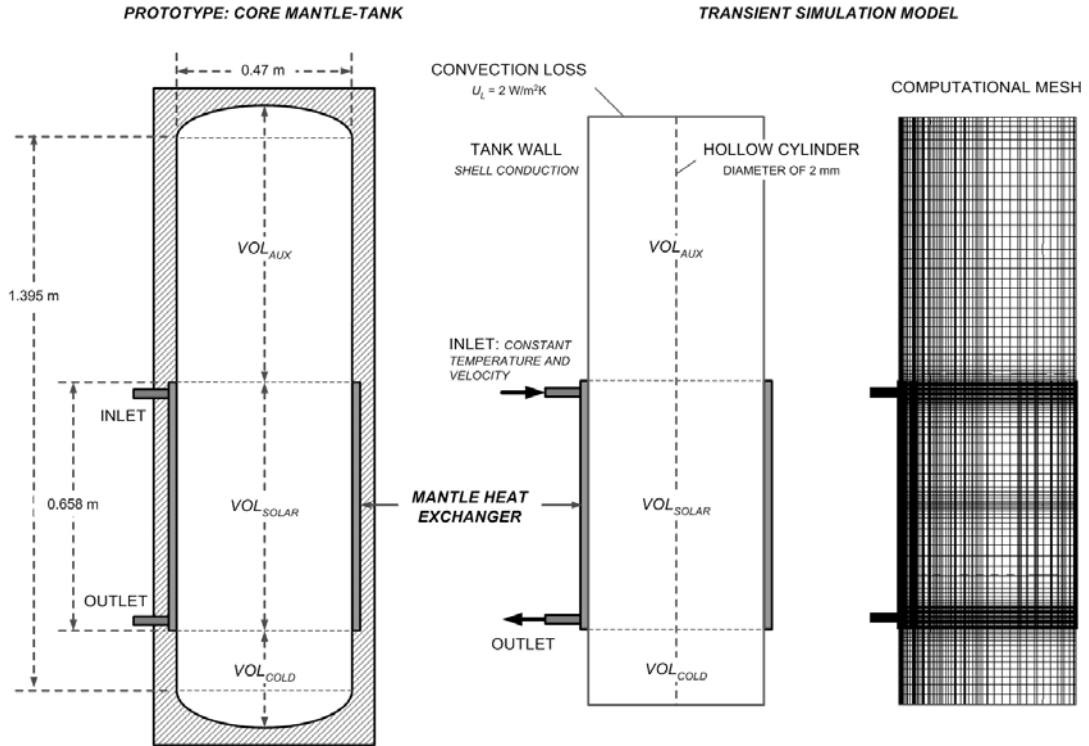


Fig. 6.9 CFD computational domain of a mantle-tank for time-dependent simulations.

Ideally, simulating the entire heat up cycle from a cold start with the mantle inlet temperature being increased in a manner that simulates the solar input should be carried out. However, this approach is impractical due to the excessive computing power required. Therefore, simulating several snapshots of the experimental data over 20 minute periods of heating process for each test was undertaken. The typical running time for each simulation was approximately 3 weeks. For each simulation, the inlet temperature and flow rate from the indoor experiments were specified as inputs to the CFD model. On the tank side, the temperature profile along the tank height was initialised based on the measured data. Heat loss from the tank was modelled using a constant convective heat transfer coefficient on the outer surfaces of the tank. All physical properties of water were assumed to be constant except the density in the buoyancy term (Boussinesq approximation) in order to obtain faster numerical

convergence. The time step in the transient simulations was set to 0.5 seconds. To account for localised turbulence mixing around the inlet, a SST $k-\omega$ turbulence model was used. Details of the SST $k-\omega$ turbulence model and parameters used in the modelling were presented in Chapter 4.

Steady-state model: Unwrapped mantle isolated from the tank

For parametric studies of the flow and heat transfer processes in mantle heat exchangers, a simple computational model is required due to the constraint of computing power. Thus, an unwrapped mantle model isolated from the storage tank (Fig. 6.10) was developed by specifying the tank temperature profile and average heat transfer coefficient on the inner heat transfer wall to represent the time-dependent natural convective flow inside the tank. These boundary conditions are used to compute the heat flux while solving the transport equations in the mantle domain. The effects of wall curvature on the flow and heat transfer in horizontal mantle heat exchangers have been shown to be negligible by Rosengarten *et al.* (2001) for the case of mixed convection. For the forced convection dominated conditions in narrow-gap mantle, the cylindrical mantle can be represented by the unwrapped mantle as a simplified geometry. Throughout the simulations, SST $k-\omega$ turbulence model and Boussinesq approximation were used.

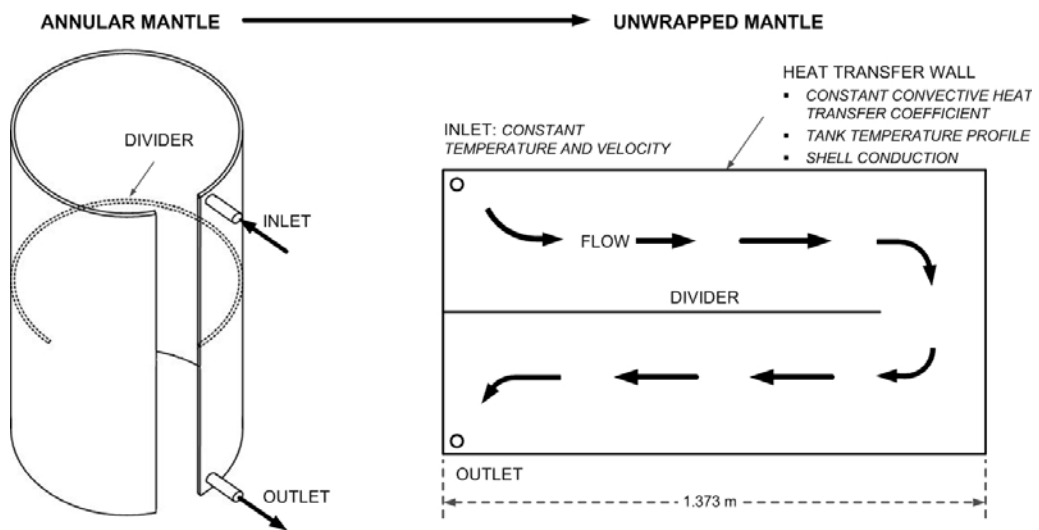


Fig. 6.10 Computational domain of a mantle heat exchanger isolated from the storage tank.

6.4.2 Grid refinement

In order to have sufficient number of grid points for solving the flow and heat transfer in mantle (steady-state model) particularly near the inlet jet impingement region and the high temperature gradient near the heat transfer wall, a mesh sensitivity check was undertaken by comparing the numerical results for different mesh sizes. The parameter of interest used for examining the mesh sensitivity of the CFD model is the total heat transfer rate using Eqn. 5.2 based on the mass flow rate and temperature difference across the mantle. Three different mesh sizes of the unwrapped mantle model were developed: a coarse mesh model with 30,492 grid points, a medium mesh model with 139,904 grid points and a fine mesh model with 526,464 grid points. The number of computational grid points in each model is given in Table 6.3.

Table 6.3 Number of computational points in the three models.

MODEL	NUMBER OF MESH POINTS	GRID DISTRIBUTION (LENGTH x HEIGHT x WIDTH)
I (COARSE MESH)	30,492	51 x 56 x 10
II (MEDIUM MESH)	139,904	76 x 88 x 20
III (FINE MESH)	526,464	129 x 128 x 30

Fig. 6.11 shows the total heat transfer rate across a 3 mm gap mantle heat exchanger obtained from CFD simulations for three different mesh sizes. It can be seen that the total heat transfer rate for Model II with medium mesh size is similar to that of Model III with fine mesh size for all three operating conditions. When the mesh of the mantle domain is coarser (Model I), a significant difference in the total heat transfer rate between Model I and III can be noticed due to insufficient grid points to resolve the flow and heat transfer in the mantle heat exchanger.

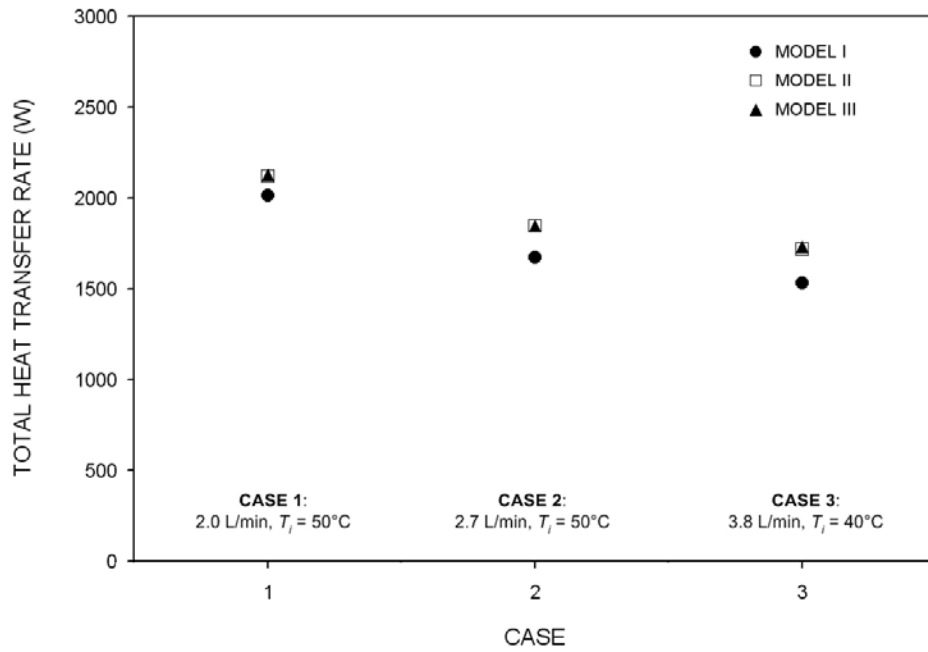


Fig. 6.11 Grid refinement check of total heat transfer rate in a 3 mm mantle heat exchanger for different mesh sizes as given in Table 6.3 and for three different operating conditions.

In the full mantle-tank model, the mesh of the cylindrical mantle domain is the same as the unwrapped mantle model which has been shown to be grid independent. On the tank side of the heat exchanger, a grid independent check was not performed due to time constraints, however dense mesh was used in the high gradient region near the wall (109,060 mesh points in the 5 mm region near the wall).

6.4.3 Validation of numerical models

In order to examine the validity of the CFD simulation models used for heat transfer studies in mantle heat exchangers, simulated results were compared with experimental data. Fig. 6.12 shows a comparison of numerical and experimental evaluation of the total heat transfer rate based on the mass flow rate and the temperature differences across the mantle heat exchanger using Eqn. 5.2. The numerical results obtained from both time-dependent and steady-state simulations show good agreement with the measurements to within $\pm 5\%$.

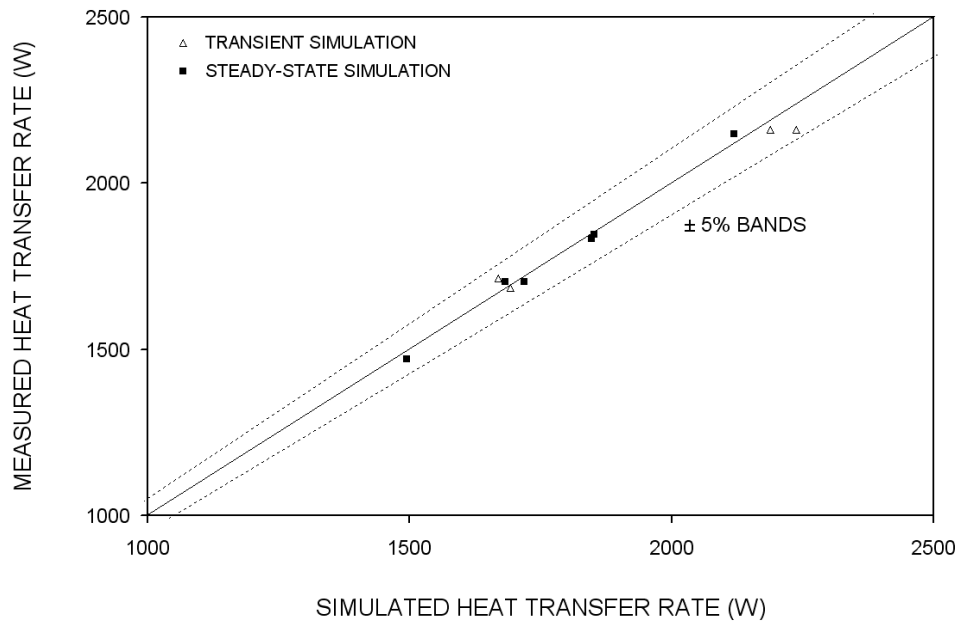


Fig. 6.12 Comparison of simulated and measured heat transfer rate across the narrow gap mantle heat exchanger.

A comparison of tank temperature stratification between experiments and time-dependent simulations is shown in Fig. 6.13 for a snapshot of the cold start test with an inlet temperature of 50°C and flow rate of 2 L/min. The numerical simulations were initialised with the measured tank temperature profile represented by the dotted line in Fig. 6.13. At the start of each simulation, circulation flow inside the tank was not considered therefore a minor delay in the natural convection circulation in the tank is expected. As observed in Fig. 6.13, the predicted tank temperature stratification (solid lines) is in reasonable agreement with the measured temperature profiles (dots) for each heating stage over 20 minutes simulation time. At the very bottom of the tank, the simulated temperature is higher than the measured temperature as the mass of water at the bottom of the dome-shaped of the storage tank was not included in the CFD model.

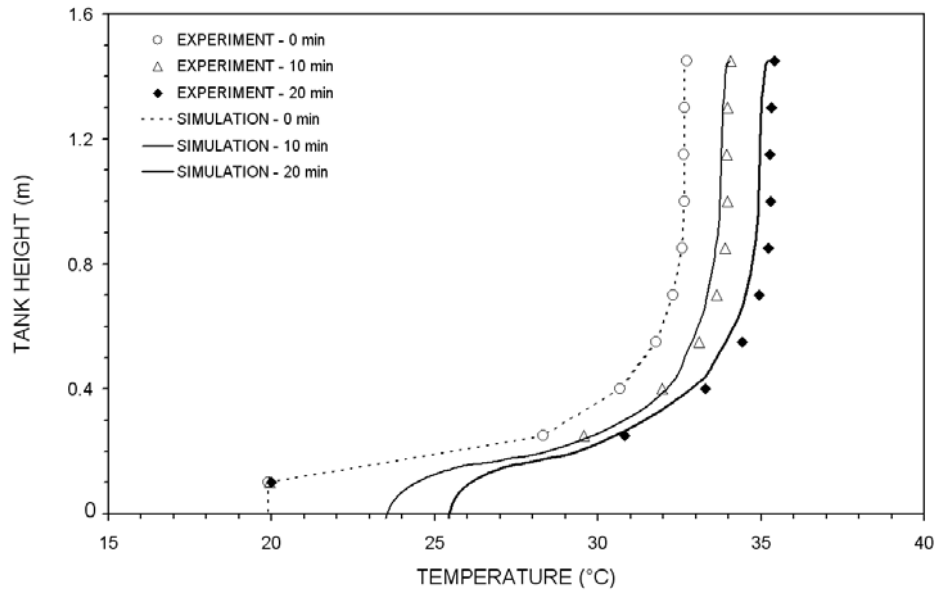


Fig. 6.13 Simulated and measured core temperature distribution along the height of the storage tank for a mantle inlet temperature of 50°C and flow rate of 2 L/min.

6.4.4 Flow and heat flux distribution

In this section, the steady-state simulation model was used to examine the influence of inlet flow rate on the flow structure, temperature distribution and heat flux in a 3 mm gap mantle. In the simulations, the average heat transfer coefficient on the tank side of the heat transfer surface was specified to be 360 W/m²K (from measurements) with tank temperature stratification of 26-32°C.

Fig. 6.14a shows the simulated velocity contours together with pathlines, indicating both magnitude and direction of the mantle flow for an inlet flow rate of 2 L/min (inlet Reynolds number, $Re_i = 3173$) and inlet temperature of 50°C. It can be observed that the hot inlet stream impinges onto the back wall inducing a region of high velocity jet-like flow at the inlet corner of the mantle. This jet impingement effect results in higher heat transfer around the inlet. Apart from the inlet region, the mantle flow ($Re_d = 318$ based on hydraulic diameter) spreads evenly across the passageways without significant effect of buoyancy forces. A region of small re-circulation flow at the end of the divider, dead regions in the corners away from the inlet and outlet ports, and suction from the outlet are also visible. The corresponding temperature contours in the mid plane and heat flux distribution over the mantle surface are shown in Fig. 6.14b and c

respectively; both reflecting the inlet jet impingement effect and uniform flow distribution for forced convection flow conditions in the narrow gap mantle. By comparing the heat transfer in the region around the inlet (0.027m^2) with the total heat transfer rate, approximately 6% of the total heat transfer takes place in the jet impingement region opposite the inlet port.

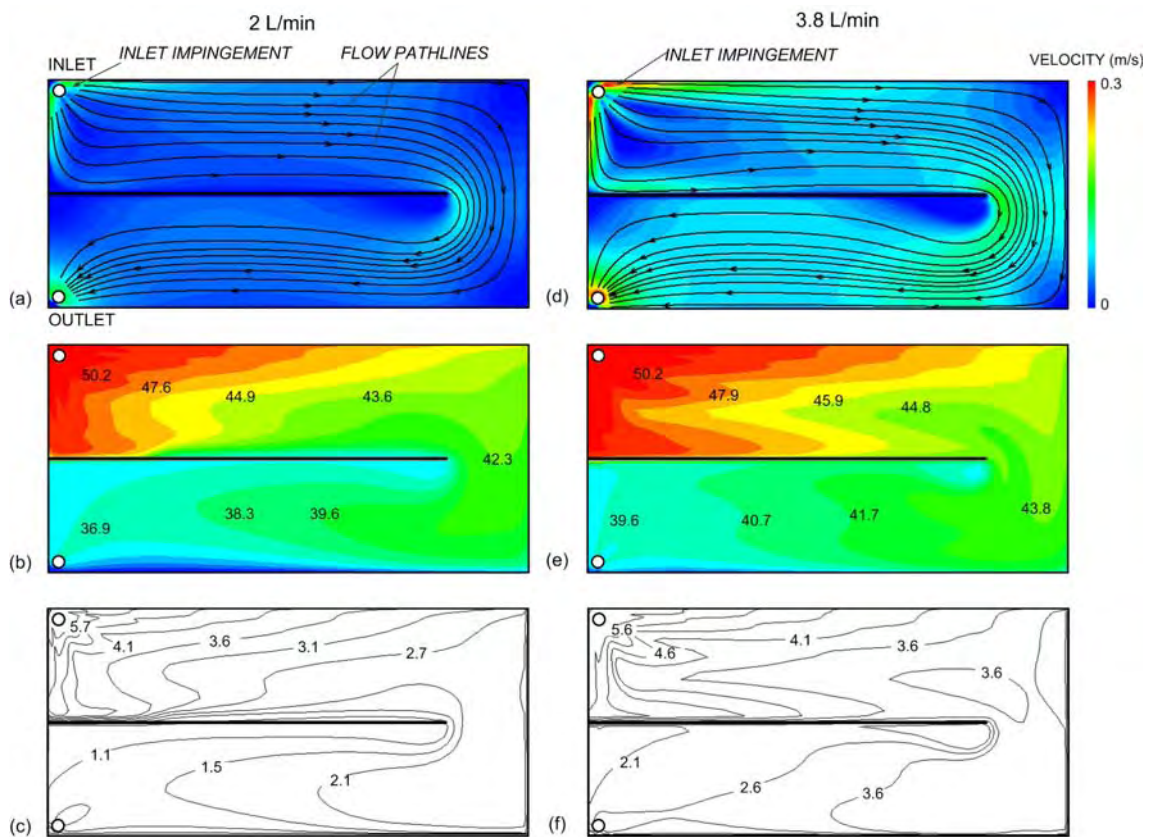


Fig. 6.14 CFD simulations for a 3mm gap mantle with an inlet temperature of 50°C , (a) simulated velocity contours (m/s) and pathlines in the mid plane of the mantle for an inlet flow rate of 2 L/min, (b) temperature contours ($^\circ\text{C}$) in the mid plane of the mantle, (c) heat flux contours (kW/m^2). (d) Simulated velocity contours (m/s) and pathlines in the mid plane of the mantle for an inlet flow rate of 3.8 L/min, (e) temperature contours ($^\circ\text{C}$) in the mid plane of the mantle, (f) heat flux contours (kW/m^2).

The effect of inlet flow rate on the flow pattern in the narrow-gap mantle was examined for the same thermal boundary conditions as for the 2 L/min case. For an inlet Reynolds number of 5665, the high velocity impingement on the back wall adjacent to the inlet becomes more significant (Fig. 6.14d) and spreads the hot stream over the inlet

quarter of the mantle (Fig. 6.14e). For the higher flow rate, approximately 33% of the total heat transfer takes place in the inlet quarter of the mantle. Away from the inlet region, the temperature and heat flux over the heat exchange surface distribute more evenly at high inlet flow rates (Fig. 6.14f).

CFD simulations were also used to provide heat transfer data of different mantle fluid and heat exchanger size. Results are presented in non-dimensional numbers in the following sections.

6.5 NON-DIMENSIONAL HEAT TRANSFER ANALYSIS

To model the annual performance of a solar water heater incorporating a mantle heat exchanger, predictions of the heat transfer coefficient in the mantle and the natural convection coefficient on the tank side of the heat exchanger are required in order to compute the heat transfer across the heat exchanger. In solar simulation programs such as TRNSYS TYPE60, modelling of detailed flow and heat transfer process as a function of the geometry of the heat exchanger does not exist. Applying the conventional heat exchanger effectiveness method in characterising a mantle heat exchanger is also not applicable as the natural convection flow rate on the tank side is usually unknown. As an alternative, empirical heat transfer correlations can be developed to predict the heat transfer as a function of dependent variables. To generalise the physical quantities obtained from experiments and CFD simulations, non-dimensional correlations were used.

6.5.1 Mantle-side heat transfer correlation

The majority of the reported heat transfer correlations on the mantle side of the heat exchanger were developed for buoyancy driven flows in wide mantles (spacing from 20 to 35 mm) with significantly higher heat flux distribution in the top section of the mantle (Shah and Furbo, 1998; Furbo and Knudsen, 2005). For forced convection dominated conditions in narrow gap mantles and correspondingly uniform heat flux distribution, the heat transfer rate essentially depends on the collector flow rate and fluid properties.

The two standard ways of correlating forced convection heat transfer process for duct flow such as a narrow gap mantle are:

$$\overline{Nu} = C Re_d^a Pr^b \quad (6.8)$$

or alternatively,

$$\overline{Nu} \sim f(x^*) \quad (6.9)$$

where: *Nusselt number*, $\overline{Nu} = \frac{\overline{h}d_h}{k} = \frac{\dot{q}d_h}{k\Delta T}$ (6.10)

Reynolds number, $Re_d = \frac{\dot{m}d_h}{\mu A_c}$ (6.11)

Prandtl number, $Pr = \frac{c_p \mu}{k}$ (6.12)

Dimensionless thermal entrance length, $x^* = \frac{x}{d_h Re_d Pr}$ (6.13)

C , a and b shown in Eqn. 6.8 are the coefficients that can be determined from experimental data for forced convection heat transfer. This functional form is also well known in correlating Nusselt number for turbulent flow in a duct (e.g. Colburn equation).

On the other hand, Eqn. 6.9 is a standard form of correlating the Nusselt number as a function of dimensionless thermal entrance length for a laminar duct flow, which takes into account for the developing region along the flow length. Due to the complicated jet impingement flow around the mantle inlet, the characteristic of thermal entry length in the mantle is not obvious (local heat transfer will be discussed in Section 6.5.1.5). Furthermore, there appears to be a region of localised turbulent flow around the inlet due to the jet impingement. For these reasons, the heat transfer data for the narrow gap mantle obtained from both the experimental measurements and CFD simulations are correlated in an exponential function of Reynolds and Prandtl numbers as given in Eqn. 6.8. To be consistent with the duct flow analogy, the characteristic length of the mantle is based on the hydraulic diameter ($d_h = 2w$).

6.5.1.1 Effect of flow rate

Fig. 6.15 shows the mean Nusselt number determined from experiments and CFD simulations (red points) in the 3 mm gap mantle heat exchanger as a function of Reynolds number covering a wide range of temperature differences at flow rates of 2, 2.6 and 3.8 L/min. The range of Reynolds numbers presented in Fig. 6.15 corresponds to the collector flow rate limits of a typical pumped-circulation solar water heater. In the same figure, the dotted line represents the theoretical laminar fully developed Nusselt number ($Nu = 4.86$) between parallel plates with boundary conditions of 3rd kind (Shah and London, 1978).

In the lower regime of Reynolds number, it can be seen that the mean Nusselt number is approaching the asymptote of laminar fully developed forced-flow Nusselt number. Both experimental measurements and CFD simulations (Fig. 6.15) also reveal that the mean Nusselt number increases with increasing Reynolds number. The dependency of the heat transfer process on the flow could be attributed by the inlet impingement. As the inlet flow rate is increased, the turbulent mixing due to impingement could extend over one quarter of the mantle (observed in Section 6.4.4), hence increasing the heat transfer coefficient. Although the heat transfer would be enhanced at higher flow rate, minimal thermal stratification in the storage tank is expected as a trade-off to the system performance, therefore no further investigation for flow rate above 3.7 L/min was carried out. In general, the results shown in Fig. 6.15 suggest that Reynolds number is the most significant parameter for correlating heat transfer in a narrow gap mantle heat exchanger.

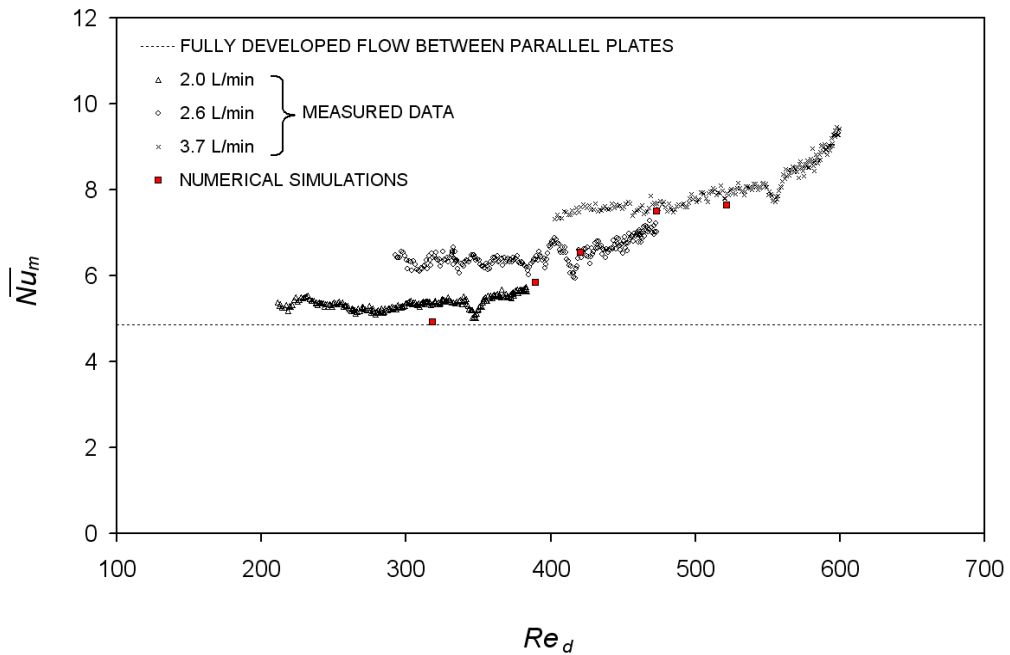


Fig. 6.15 Measured and simulated mean Nusselt number in a narrow gap mantle as a function of Reynolds number. Also shown is the laminar fully developed forced flow Nusselt number for flow between parallel plates.

6.5.1.2 Effect of fluid properties

All data points presented in Fig. 6.15 were obtained using pure water as the working fluid with Prandtl number in the range of 3 to 7. In practice, a 20% propylene glycol/water mixture with higher Prandtl number (7-12) and viscosity is typically used in the collector-heat-exchanger loop in order to provide effective freeze protection for solar water heaters. In this section, the influence of fluid properties of 20% propylene glycol mixture on the heat transfer in a 3 mm gap mantle is investigated based on numerical simulations. The CFD cases presented in Fig. 6.15 were re-simulated using the thermal properties for 20% propylene glycol mixture (Appendix B) while retaining all boundary conditions. By utilising propylene glycol mixture as the mantle fluid, the lower range of Reynolds numbers shown in Fig. 6.15 is extended. In Fig. 6.16, it can be seen that the higher viscosity of propylene glycol mixture decreases the Reynolds number by approximately a factor of two as compared to pure water with the same boundary conditions. There appears to be an asymptotic Nusselt number of 4.86 being

approached in the lower regime of Reynolds number. In this regime, the Nusselt number in the mantle is no longer dependent on the Reynolds number.

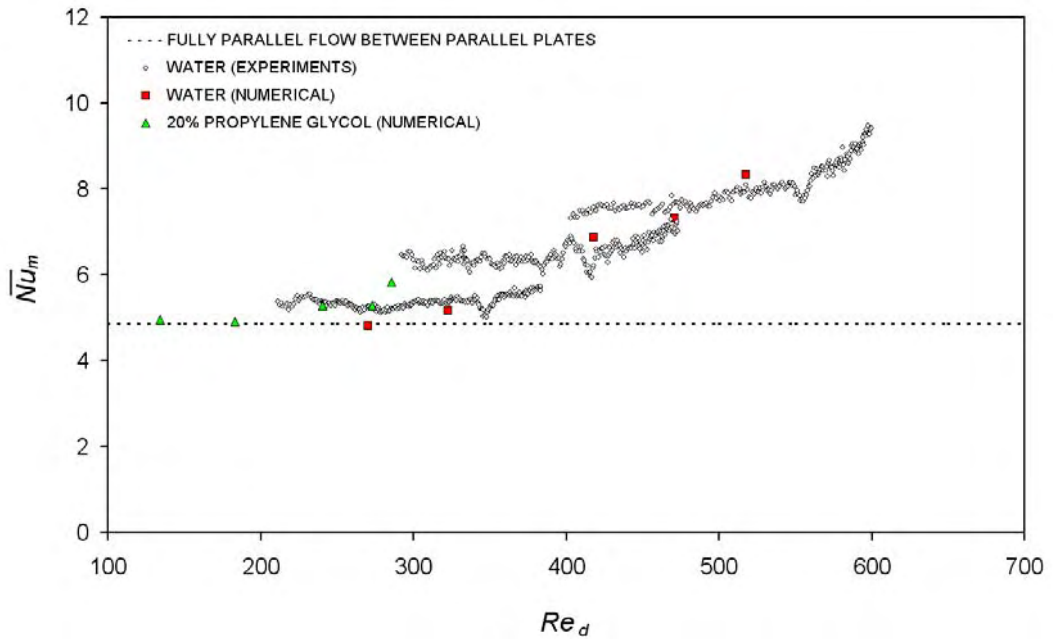


Fig. 6.16 Mean Nusselt number in a 3 mm gap mantle as a function of Reynolds number from experiments and numerical simulations with water as mantle fluid, and numerical simulations with 20% propylene glycol/water mixture as mantle fluid.

6.5.1.3 Effect of buoyancy

To examine the potential effect of buoyancy on heat transfer in a narrow gap mantle, the ratio Gr_d/Re_d^2 was used to indicate the relative magnitude of natural and forced convection components. If Gr_d/Re_d^2 is of the order of one, the heat transfer in the mantle is governed by mixed convection which is the coupling of inertia and buoyancy forces. In Fig. 6.17, both measured and simulated data indicates that the influence of natural convection on the heat transfer in the 3 mm gap mantle heat exchanger is negligible for all operating conditions reported in this study although some of the data points fall in the transitional zone between forced and mixed convection. Hence, the inclusion of Grashof number or Rayleigh number for correlating heat transfer in a narrow gap mantle heat exchanger is unnecessary for highly forced convection-dominated conditions.

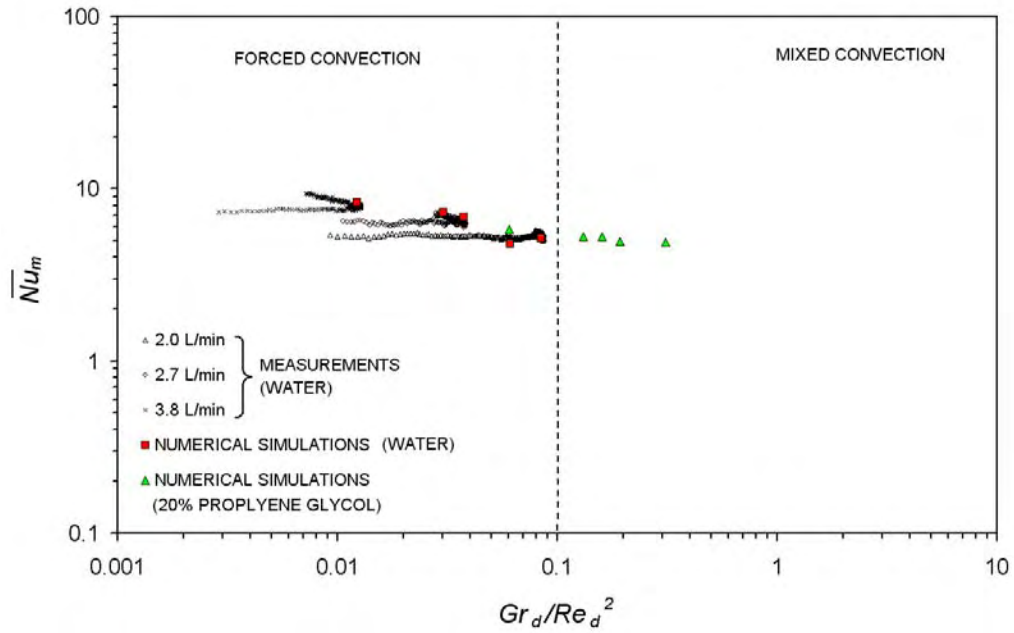


Fig. 6.17 Buoyancy and forced convection zones in a narrow gap mantle heat exchanger.

6.5.1.4 Development of mean Nusselt number correlation

In this study, the evaluation of the heat transfer across the mantle heat exchanger covering a wide range of Prandtl number was not performed, therefore the scaling of $Nu \sim Pr^{0.33}$ for duct flow was adapted. When the results ($Re_d > 200$) shown in Fig. 6.16 replotted as $\overline{Nu}_m/Pr^{0.33}$ against Re_d in Fig. 6.18, this dependence correlates fairly well for all results and the dependency on the Reynolds number is now known. This assumption is applicable as most of the working fluids in the collector-heat-exchanger loop are water or mixture of propene glycol/water with $3 < Pr < 12$. Additionally, the primary parameter for correlating the heat transfer data is essentially the Reynolds number for a forced convection situation.

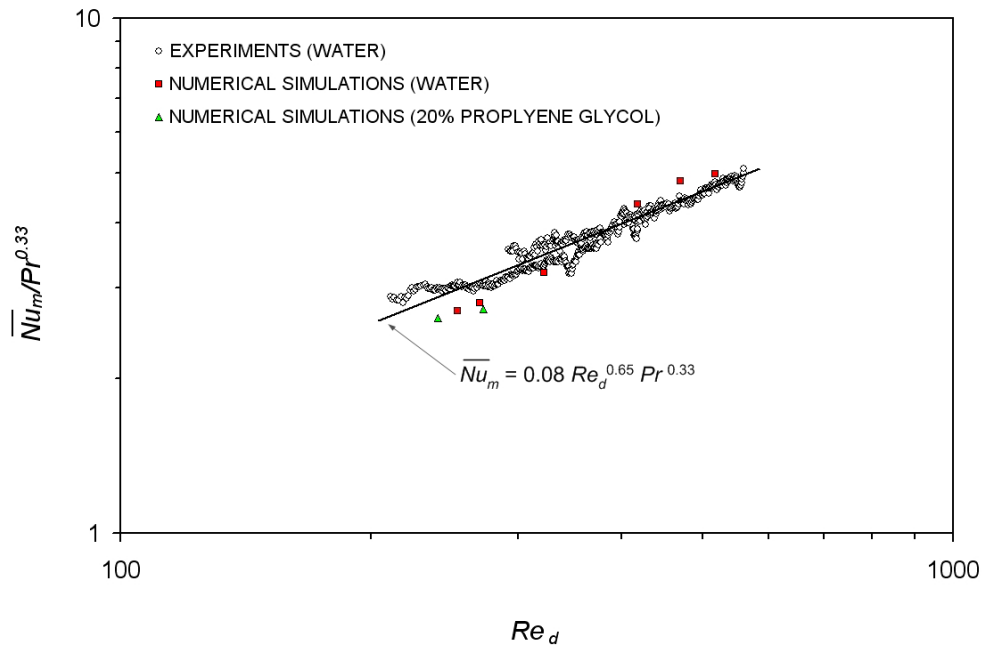


Fig. 6.18 Measured and simulated mean Nusselt number divided by $Pr^{0.33}$ against Reynolds number in the narrow gap mantle.

A general functional relation of mean Nusselt number ($Re_d > 200$) for forced convection dominated conditions in a mantle was developed from a regression-fit to the experimental and simulated data as given in Eqn. 6.14.

$$\overline{Nu}_m = 0.08 Re_d^{0.65} Pr^{0.33} \quad (6.14)$$

Fig. 6.19 shows that the measured and simulated data are within 10% of the predicted values using Eqn. 6.14 for $200 < Re_d < 600$ with properties calculated at the average between mantle fluid and wall temperatures. In the lower regime of Reynolds number where an asymptotic Nusselt number of 4.86 is approached, the absolute critical Reynolds number for the mantle is not known however a Nu value of 4.86 is assumed when Eqn. 6.14 gives a value less than the asymptote Nusselt number.

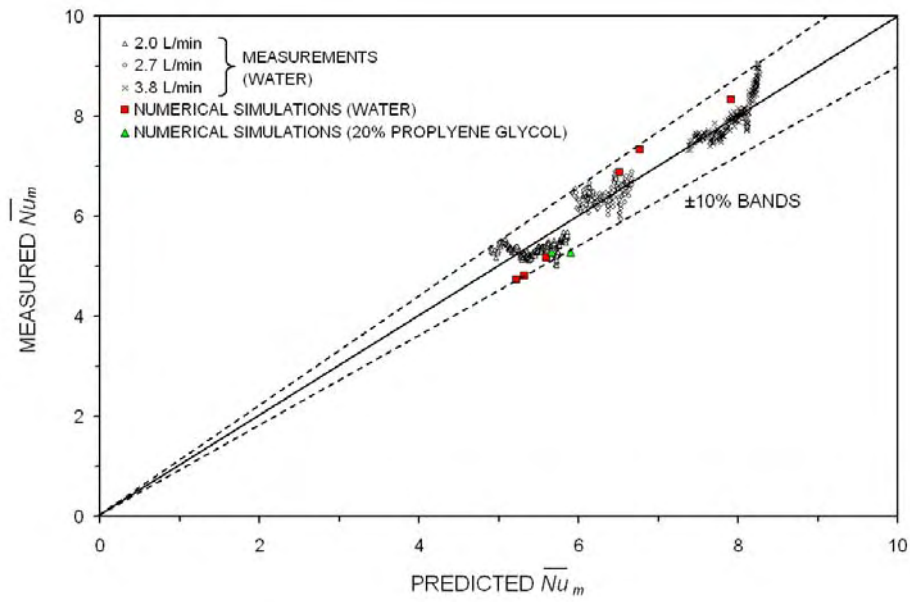


Fig. 6.19 Measured and predicted (Eqn. 6.14) Nusselt numbers for different flow rates.

6.5.1.5 Local heat transfer in developing flow

In practice, the flow in a narrow gap mantle is neither hydrodynamically nor thermally developed. A correlation of laminar developing forced convective heat transfer between parallel plates with boundary conditions of 3rd kind by Mercer *et al.* (1967) that could be applied to flow in a narrow gap mantle is given in Eqn. 2.8 (Refer to Chapter 2). This was used by Baur *et al.* (1993) to model the performance of a 20 mm gap vertical mantle heat exchanger for use in a pumped system. To match the measured results, they found that a correction factor of approximately 1.8 had to be applied to the standard parallel plate heat transfer correlation. The reason for the higher heat transfer coefficient was thought to be due to mixing induced by the higher velocities near the inlet port and mixed convection in the mantle gap. In this study, the local Nusselt number as a function of the flow length obtained from numerical simulations is illustrated in Fig. 6.20 and compared with Mercer's correlation. The local Nusselt number was evaluated as following:

$$Nu_x = \frac{h_x d_h}{k} = \frac{\dot{q}_x d_h}{k \Delta T_{m,x}} \quad (6.15)$$

where subscript x represents the coordinate in the flow length. The local heat transfer coefficients in Eqn. 6.15 were based on the log-mean temperature difference between the mantle fluid and the wall to be consistent to Mercer's approach.

At low Reynolds number of 270 as seen in Fig. 6.20, the local Nusselt numbers are in reasonable agreement with Mercer's correlation and the data approaches the asymptote laminar fully-developed forced-flow Nusselt number except in the small region around the inlet where jet impingement occurred. For higher Reynolds numbers, Mercer's correlation tends to underestimate the local Nusselt numbers on the mantle side. This is thought to be due to the influence of inlet jet impingement causing a laminar-transitional flow in the mantle gap. Moreover, the heat transfer coefficient on the mantle side of the heat transfer surface for approximately uniform heat flux would be larger than the uniform temperature heat transfer correlation developed by Mercer *et al.* (1967).

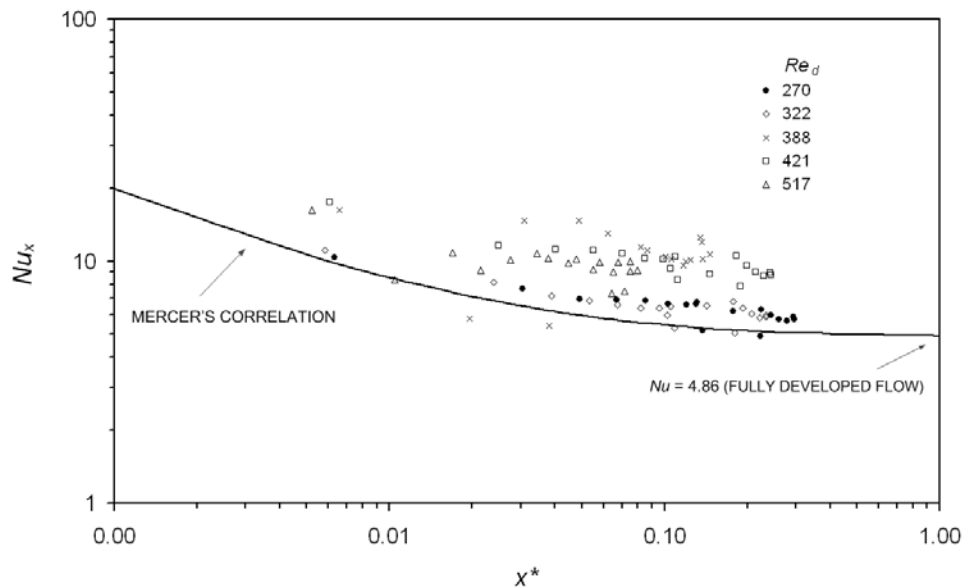


Fig. 6.20 Numerically obtained local Nusselt number as a function of thermal entrance length for a 3 mm gap mantle heat exchanger plotted with the standard laminar developing flow between parallel plates.

6.5.2 Tank side heat transfer correlation

For natural convection circulation on the tank side of the mantle, the mean heat transfer coefficient can be represented in the following standard non-dimensional form:

$$\overline{Nu}_t = \frac{\overline{h}_t H}{k} = C Ra_H^n \quad (6.16)$$

where: Rayleigh number, $Ra_H = \frac{g\beta(\overline{T}_w - \overline{T}_t)H^3}{\nu^2} Pr$ (6.17)

C and n shown in Eqn. 6.16 are the coefficients determined from measurements. The natural convection boundary layer on the inner wall of the storage tank is assumed to extend up to the height of the mantle where heat is being transferred.

Fig. 6.21 shows the mean Nusselt number obtained from experiments for different mantle flow rates together with prediction from empirical Nusselt number correlations for free convection on an isothermal vertical flat plate (Incropera and DeWitt, 1996) as given in Eqn. 6.18 and 6.19.

For laminar flow, $Nu = 0.59 Ra^{0.25}$, $Ra < 10^9$ (6.18)

For turbulent flow, $Nu = 0.1 Ra^{1/3}$, $10^9 \leq Ra \leq 10^{13}$ (6.19)

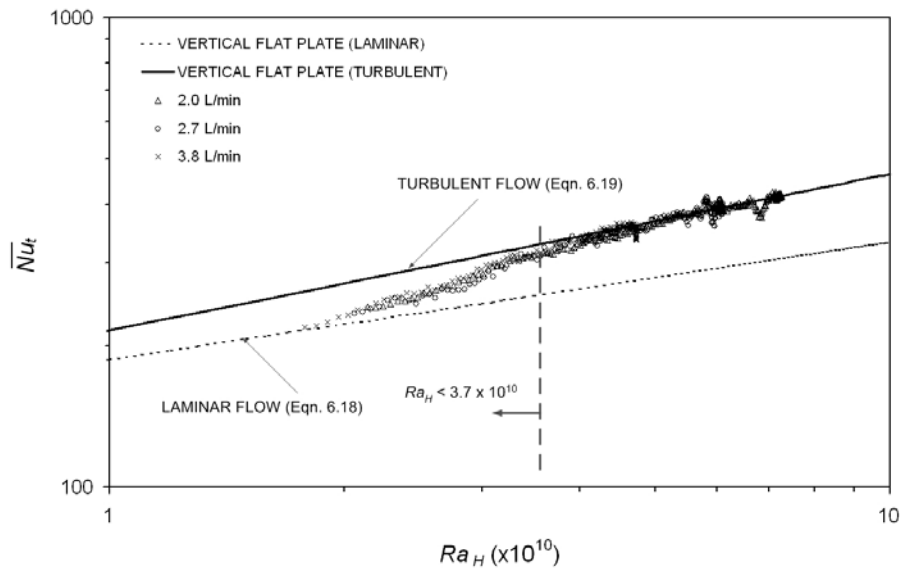


Fig. 6.21 Comparison of measured tank side mean Nusselt number and empirical laminar and turbulent isothermal vertical flat plate functions.

The flow on the tank side of the mantle surface is observed to be turbulent with Rayleigh number (Ra_H) in the low range of turbulent natural convection conditions. In this region of operation, the measured tank side mean Nusselt number matches the

correlation for turbulent free convection on a flat plate given in Eqn. 6.19 at Rayleigh number above 3.7×10^{10} , but overestimates the heat transfer on the tank side by 10-15% at the start of heating for lower Rayleigh number conditions (below 3.7×10^{10}). The lower heat transfer on the tank side is due to the high water viscosity at low temperatures (less than 30°C in this region where $Ra_H < 3.7 \times 10^{10}$), resulting in weak buoyancy driving force within the tank. As observed in Fig. 6.21, the measured data for this operating region is in transition region between the laminar and turbulent flow. A best fit to the data is given as follows:

$$Nu = 0.001Ra^{0.52}, \quad 10^{10} \leq Ra \leq 3.7 \times 10^{10} \quad (6.20)$$

Note that the coefficients in Eqn. 6.20 are only applicable for a storage tank incorporating a narrow gap mantle heat exchanger. Fig. 6.22 shows that most of the measured data lies within 10% of the predicted values using Eqn. 6.20 for $3.7 \times 10^{10} < Ra_H < 7 \times 10^{10}$ and Eqn. 6.19 for $10^{10} < Ra_H < 3.7 \times 10^{10}$.

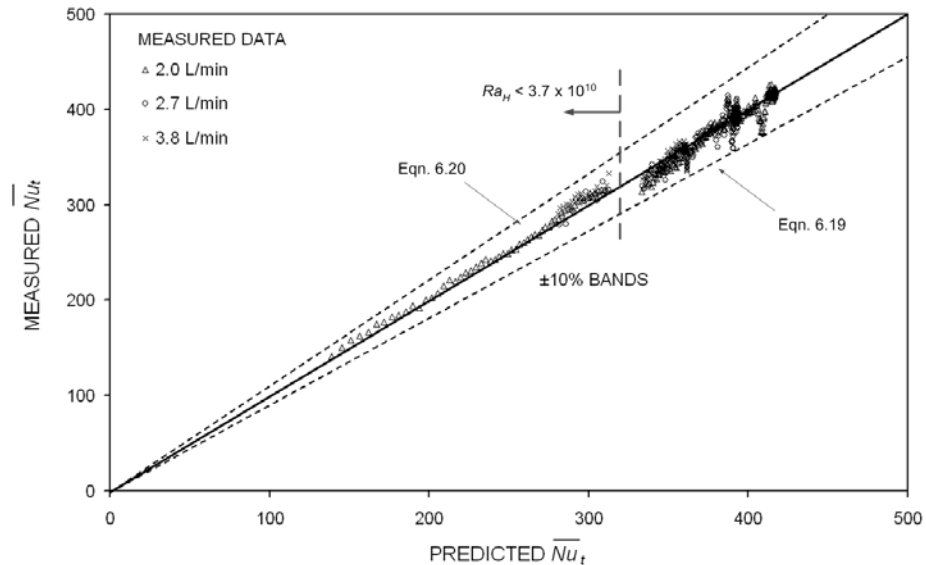


Fig. 6.22 Comparison of measured and predicted (Eqn. 6.19 and 6.20) tank side Nusselt number.

6.6 EFFECT OF HEAT EXCHANGER SIZE

In the preceding sections, the heat transfer characteristics of the narrow gap mantle heat exchanger were evaluated based on a 270 L mantle-tank with a mantle spacing of 3 mm and heat transfer area of 0.903 m^2 . Another mantle-tank with a larger mantle heat

transfer area and storage tank capacity (315L tank, 1.13 m² mantle heat transfer area, 0.826 m mantle height and 3 mm mantle gap) was also tested in the laboratory under controlled indoor conditions. Both of the small and larger mantle heat exchangers are used for domestic solar water heaters with an in-tank electric boosting element, therefore the mantle height is only wrapped around the bottom half of the storage tank just below the boosting element in order to avoid degradation of tank stratification.

For a flow rate of 2 L/min on the hot side of the heat exchanger, the overall UA'_{hx} with a correction factor of 0.91 (obtained from Incropera and DeWitt, 1996) for the larger heat exchanger was found to be 182 W/K to 257 W/K (Fig. 6.23) which is approximately 13% higher than that of the reference mantle-tank with a smaller heat transfer area of 0.903 m². This result scales directly with the area ratio of the mantle heat exchanger surface in the 270L and 315L tanks. Measurements of the wall temperature for determining the heat transfer coefficients on the mantle side and tank side were not performed for the 315L mantle-tank. However snapshots of the heat-up cycles for flow rates of 2, 3 and 3.7 L/min were simulated using the full mantle-tank CFD model to determine the mean wall temperature over the mantle surface.

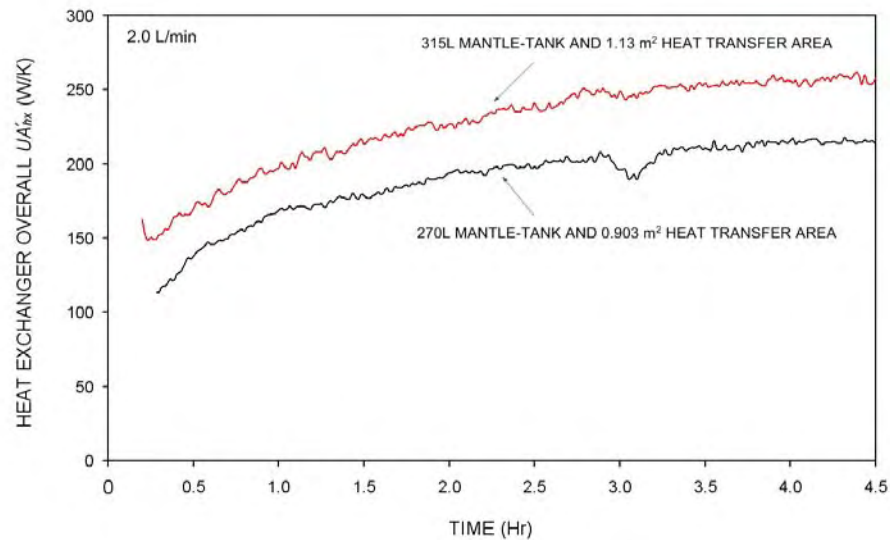


Fig. 6.23 Overall heat transfer coefficient-area product (UA'_{hx}) for the 270L mantle-tank (0.903 m² heat transfer area) and 315 L mantle-tank (1.13 m² heat transfer area) during heat-up cycles with a flow rate of 2 L/min evaluated using log-mean temperature difference with correction factors of 0.95 and 0.91 respectively (Incropera and DeWitt, 1996).

Fig. 6.24 shows a comparison of mean mantle-side Nusselt number obtained from the CFD simulations and predictions using Eqn. 6.14 for the 315 L mantle-tank. It can be seen that the predicted values for the larger mantle agree with the mean Nusselt number from CFD simulations to within 10%. For forced convection dominated conditions in the narrow gap mantle with more uniform flow and heat flux distribution, the influence of the mantle heat exchanger dimensions may not be significant, except the mantle spacing (Section 6.8).

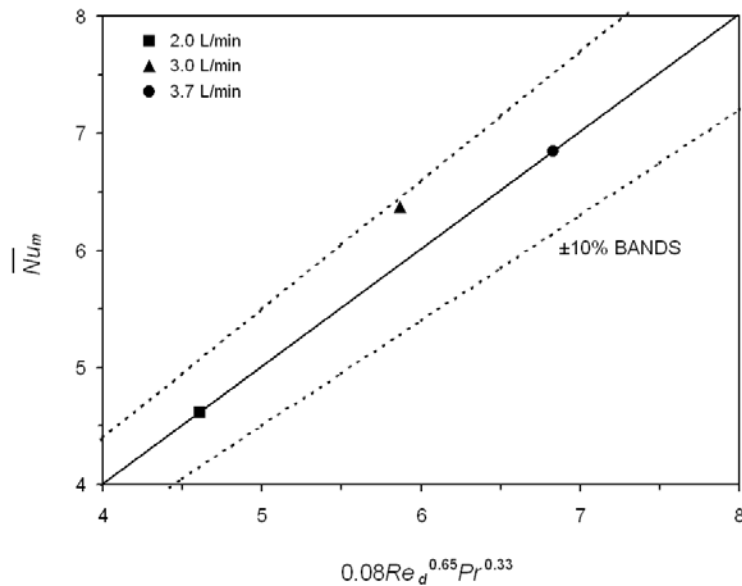


Fig. 6.24 Mantle-side Nusselt numbers from CFD simulations and predicted using Eqn. 6.14 for a narrow gap mantle heat exchanger with heat transfer area of 1.13 m^2 with different flow rates.

On the tank side of the heat exchanger, the mean Nusselt number from CFD simulations show good agreement with the turbulent free convection on a flat plate given in Eqn. 6.19 (Fig. 6.25). The scaling between the overall heat transfer coefficient with the available heat transfer area suggests that there are no significant differences between the small and larger heat exchangers.

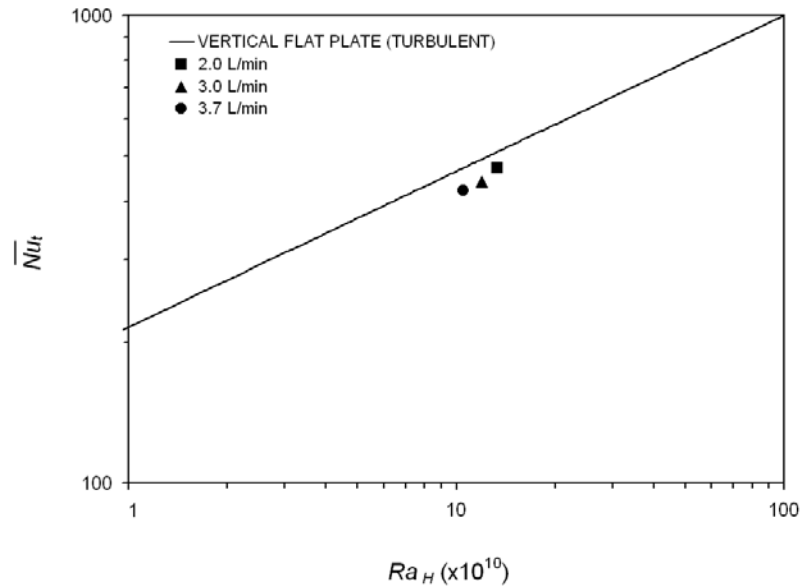


Fig. 6.25 Comparison of tank side Nusselt number from CFD simulations for a narrow gap mantle heat exchanger with heat transfer area of 1.13 m^2 and empirical turbulent isothermal vertical flat plate function (Eqn. 6.19).

6.7 PREHEATED TANK CONDITIONS

When the mantle heat exchanger operates from an initially preheated top half of the tank with a steep temperature gradient separating the hot and cold zones, the heat transfer process is more complex and could be influenced by the mixing natural convective flow between these tank layers and the influence of conduction.

Fig. 6.26 shows a comparison of the mean mantle heat transfer coefficient (\bar{h}_m) based on the averaged measured wall temperature for the preheated tank case and cold start case for a flow rate of 2 L/min. At the start of the heating process, the heat transfer coefficients for both operation modes are similar. As the heating progresses, \bar{h}_m for the preheated tank conditions increases, with larger values than the cold start tests, and decreases when the tank is well-mixed. One of the reasons for this could be due to transient effects of mixing of the boundary layer flow on the tank side of the mantle wall with the hot upper preheated layer. Due to the mixing, heat could be transferred from the hot upper layer in the tank to cooler section as reported in Section 6.2.2 and as a result, tank wall at the top of the mantle would be pre-heated. If the average

temperature over the entire mantle surface is used to calculate the heat transfer coefficient, this effect would result in a smaller temperature difference between the mantle fluid and wall and hence the apparent \bar{h}_m values increases. To examine this effect, the average surface temperature was determined from thermocouple readings over the bottom two-third of the mantle where approximately 80% of the heat transfer takes place. This modified mantle side heat transfer coefficient is similar to the characteristic of a full recovery cold start (Fig. 6.26).

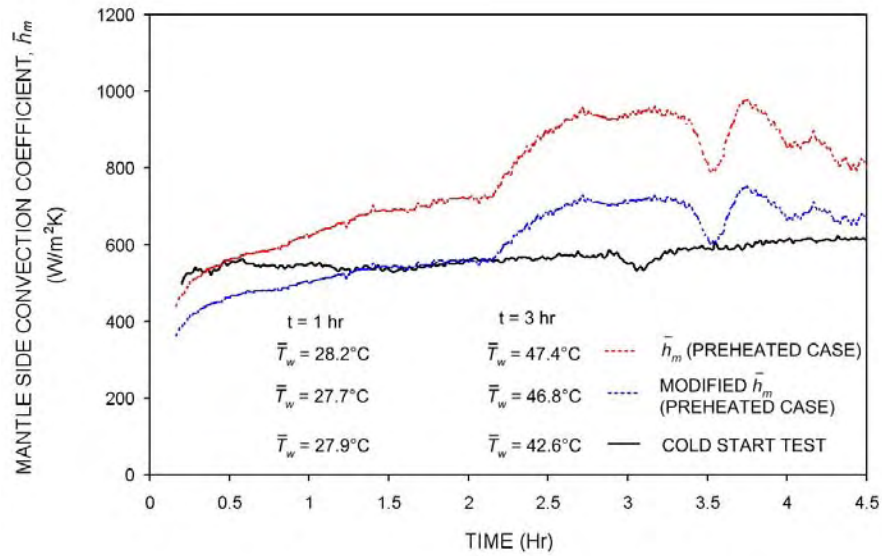


Fig. 6.26 Mantle-side heat transfer coefficient during heat-up cycle with a flow rate of 2 L/min from an initially stratified tank conditions and compared to the cold start tests.

The corresponding heat transfer coefficient on the tank side (\bar{h}_t) as shown in Fig. 6.27 was also calculated based on the difference between the average temperature over the bottom two-thirds of the mantle surface on the tank side and its adjacent average tank temperature ($T_{t,6}$ to $T_{t,9}$). The modified \bar{h}_t values for the preheated case show similar characteristics to that of the full recovery cold start operation mode. This is only one of the influences that may be affecting the mantle heat exchanger operation with a steep temperature gradient in the storage tank. More specific analysis for this limiting operation mode is necessary, but is beyond the scope of this project.

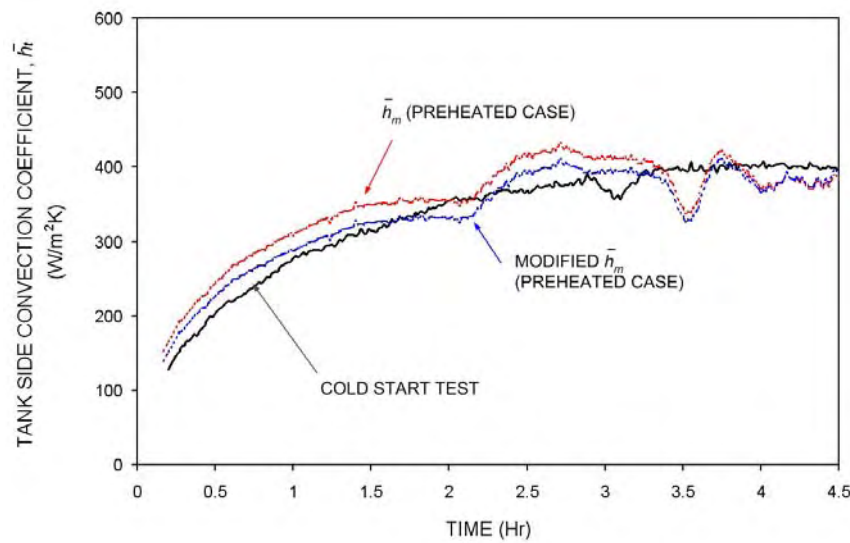


Fig. 6.27 Tank-side heat transfer coefficients during heat-up cycle with a flow rate of 2 L/min from an initially stratified tank conditions and compared to the cold start tests.

6.8 OTHER MANTLE SPACINGS

Flow visualisation experiments in a scaled rectangular mantle presented in Chapter 5 showed that the flow in a mantle changes markedly depending on the mantle spacing. As the mantle spacing increases, buoyancy effects start to prevail and as a consequence, the mantle flow changes significantly. This section presents the variation of convective heat transfer for mantle spacings of 3, 10 and 30 mm. For the purpose of the parametric study, two research mantle-tanks with mantle gaps of 10 and 30 mm were tested under controlled indoor conditions with the same setup as for the 3 mm gap mantle tank (Refer to Chapter 3). Each system was operated from a cold start with an inlet temperature varying in the manner expected in a solar water heater application. The experimental data is presented in non-dimensional form.

To account for the effect of buoyancy on heat transfer in different width mantles and operating conditions, the Nusselt number is divided by the Reynolds number raised to the power of 0.65 (regression-fit coefficient for forced convection flow in Eqn. 6.14), and replotted against the ratio Gr_d/Re_d^2 , which is a general parameter to determine the relative contribution of forced and natural convection. In the pure forced convection region at Gr_d/Re_d^2 less than 0.1, the heat transfer is independent on the natural

convection for all operating data obtained for the 3 mm gap mantle. Attention has been paid to this forced convection regime in this study.

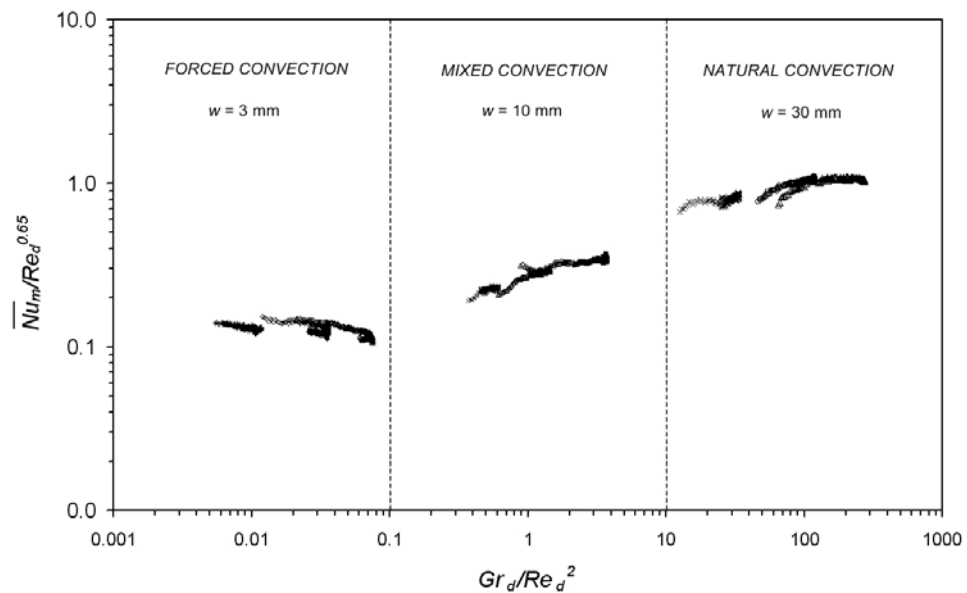


Fig. 6.28 The influence of mantle spacing on the Nusselt number.

As the mantle spacing is increased buoyancy starts to become significant and the Nusselt number is no longer purely dependent on Reynolds number. Coupling of inertia and buoyancy driven convective heat transfer was found for a mantle gap of 10 mm with the ratio Gr_d / Re_d^2 in the range 0.1 to 10. It can be seen that there is a significant difference in the way the data correlates for different mantle spacings in this regime. Further investigations are needed in order to understand the heat transfer processes in mixed convection operating conditions.

When the mantle spacing is increased to 30 mm that is close to the typical European single-pass mantle design (Knudsen, 2004), the natural convection heat transfer becomes significant at Gr_d / Re_d^2 larger than 10. It is important to note that for free convection dominated conditions in wide gap mantle heat exchangers the heat flux is significantly higher in the top section of the mantle due to the localised buoyancy effect. In such a mantle configuration, localised heat transfer correlations for buoyancy driven flows have been developed by Knudsen (2004).

It is not surprising that the development of a general heat transfer correlation as a function of mantle gap ranging from forced-dominated flow in a narrow gap to buoyancy induced flow in a wider gap is not straightforward and generally not available. Changes in mantle spacing significantly influences the flow and heat transfer process in a mantle. Thus, mantle spacing is not considered as a scaling factor in Eqn. 6.14.

6.9 SUMMARY

The heat transfer characteristics of a narrow-gap mantle heat exchanger (with a two-pass flow arrangement) were investigated under controlled indoor conditions with the inlet temperature varying in a manner expected in a solar water heater application. Measurements showed that the tank is well mixed above the level of the heat exchanger. For the preheated case with a steep temperature gradient separating the hot and cold zones, the mixing between the boundary layer flow and the stagnant hot layer in the top half of the tank could result in heat being transferred from the hot top layers to lower cooler layers. The overall heat transfer coefficient-area product (UA_{hx}) for the narrow gap mantle heat exchanger was found to be 150-213 W/K. For forced convection dominated flow conditions in a narrow gap mantle, the overall heat transfer coefficient was found to be primarily limited by the tank side free convection.

The influence of inlet flow rate on the flow and heat flux distribution in a narrow gap mantle was investigated using CFD simulations. As the inlet flow rate is increased, the simulated results showed that inlet jet impingement on the back wall adjacent to the inlet induces a region of localised turbulent flow. Except for the impingement region near the inlet, approximate uniform flow and heat flux distribution within the mantle gap was observed in narrow gap mantles.

The heat transfer data obtained from measurements and CFD simulations were generalised in the form of a non-dimensional correlation. On the mantle side of the heat exchanger, the results revealed that the heat transfer rate essentially depends on flow rate and fluid properties. For Reynolds number below 200 the data approached the fully

developed Nusselt number of 4.86 for laminar flow between parallel plates. For Reynolds number above 200, an empirical Nusselt number correlation was developed in terms of Reynolds and Prandtl numbers.

For natural convection circulation on the tank side of the heat exchanger, the measured tank side mean Nusselt number agreed well with correlations of turbulent free convection on a flat plate, except for lower Rayleigh number conditions (below 3.7×10^{10}). A correlation was developed from a regression-fit to the measured data in the transition region between the laminar and turbulent flow which occurs at the beginning of the day for typical solar water heater application.

The measured performance of a larger mantle heat exchanger was found to match the heat transfer correlation developed from the smaller test heat exchanger. These correlations will be implemented in Chapter 8 in the solar simulation program TRNSYS to model the annual performance of a solar water heater incorporating a mantle heat exchanger.

- CHAPTER 7 -

CHARACTERISTICS OF FALLING FILM HEAT EXCHANGERS

7.1 INTRODUCTION

The preceding chapters have presented detailed investigations of the flow and heat transfer processes in mantle heat exchangers. In this chapter, the evaluation of falling film heat exchangers, which is the second heat exchanger in this thesis, is presented.

The investigations are divided into three parts as follows:

- Thermal measurements for constant collector flow rate were first carried out to quantify the heat transfer characteristics and tank thermal stratification of the heat exchanger. Measurements of the heat transfer coefficients for the heat exchanger are also presented.
- The falling film system is intended to operate with an advanced switching controller that modulates the collector flow rate, so that thermal stratification in the tank can be maintained. The results from the variable flow rate tests using this controller are presented for two heating cases from a cold start and initially stratified tank to determine the influence of the controller strategy on the system performance.
- Flow visualisation experiments were conducted to qualitatively determine the wetted area of the thin film under typical operating conditions. Non-dimensional analysis on the total heat transfer rate of the heat exchanger was performed and empirical correlations were developed as a function of flow rate and fluid properties.

7.2 THERMAL MEASUREMENTS FOR CONSTANT FLOW RATE

The heat transfer characteristics of a falling film heat exchanger for use in a pumped-circulation solar water heater have been examined through three heat-up tests with a constant collector flow rate under clear sky conditions. The specifications of the core of the falling film-tank are given in Table 7.1. The results obtained from the steady flow tests have been used to quantify the thermal performance of the heat exchanger and to develop heat transfer correlations. In each test, the system was operated from a cold start representing the full recovery mode in the tank under clear day conditions. Instantaneous auxiliary heat added to the tank contents and water draw-off during the day were not considered in these tests. Steady collector flow rates of 1.6, 2.6 and 3.6 L/min were used. For all steady flow tests, tank temperature stratification, outer wall temperature of the core tube and heat exchanger inlet and outlet temperatures were measured. The details of the experimental setup and instrumentation are given in Chapter 3.

Table 7.1 Specifications of the falling film-tank tested under outdoor conditions.

STORAGE TANK	
Tank volume (L)	270
Tank height (m)	1.21
Tank wall material	Carbon steel
Tank wall thickness (m)	0.003
Tank contents	Water
FALLING FILM TUBE	
Inner diameter (m)	0.197
Height (m)	1.21
Tube wall material	Carbon steel
Tube wall thickness (m)	0.003
Working fluid	20% propylene glycol/water mixture

7. CHARACTERISTICS OF FALLING FILM HEAT EXCHANGERS

To quantify the performance of the falling film heat exchanger for use in solar water heating applications, it is of interest to investigate thermal stratification in the storage tank and the rate of change of the thermal energy accumulated in each segment of the tank. The heat transfer rate to each tank volume can be calculated by the equation:

$$\dot{Q}_{vol i} = \rho V_i C_p \frac{dT_{t,i}}{dt} \quad (7.1)$$

The change in measured temperature ($dT_{t,i}$) for tank volume i is over a ten-minute period (dt). The positions of measured tank core temperatures and the volume of each segment are given in Table 7.2.

Table 7.2 Positions of measuring points and volume of each segment in the tank (Fig. 7.1).

TEMPERATURE MEASURING POINT	DISTANCE FROM THE TANK BOTTOM (m)	TANK ELEMENT	VOLUME (L)
$T_{t,1}$	1.185	<i>Vol 1</i>	16.7
$T_{t,2}$	1.040	<i>Vol 2</i>	32.3
$T_{t,3}$	0.895	<i>Vol 3</i>	32.3
$T_{t,4}$	0.750	<i>Vol 4</i>	32.3
$T_{t,5}$	0.605	<i>Vol 5</i>	32.3
$T_{t,6}$	0.460	<i>Vol 6</i>	32.3
$T_{t,7}$	0.315	<i>Vol 7</i>	32.3
$T_{t,8}$	0.170	<i>Vol 8</i>	32.3
$T_{t,9}$	0.025	<i>Vol 9</i>	16.7

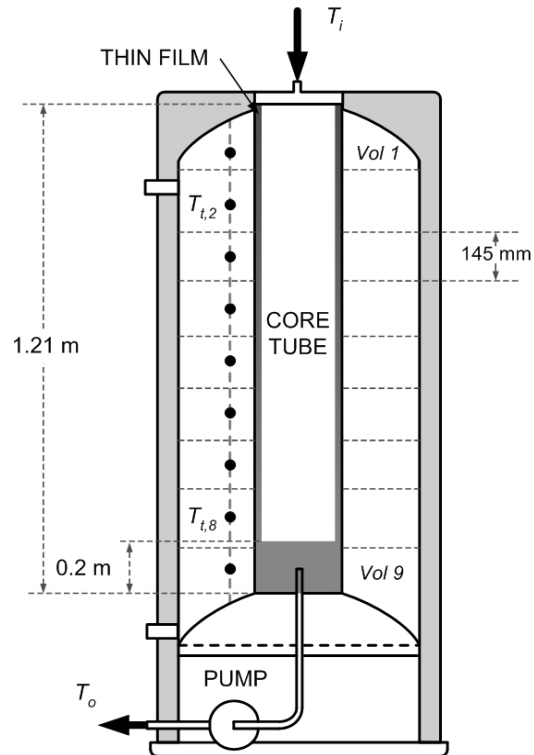
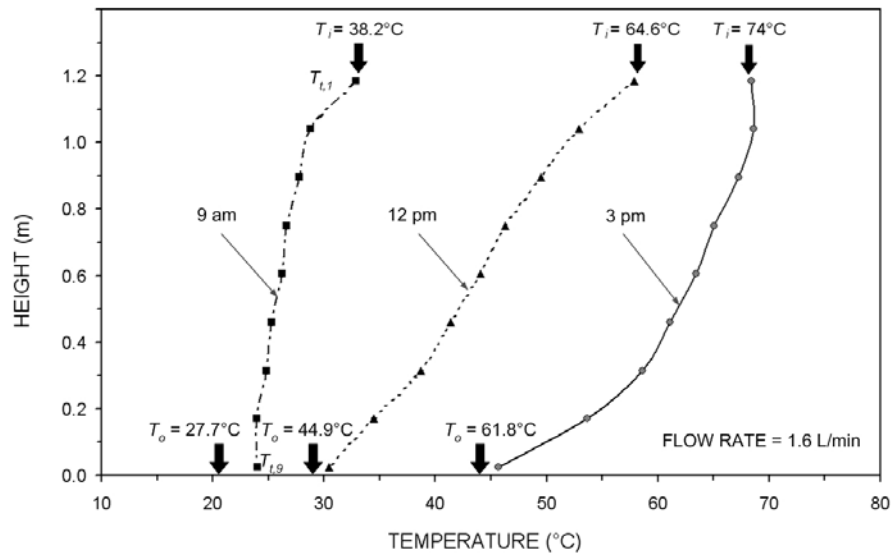


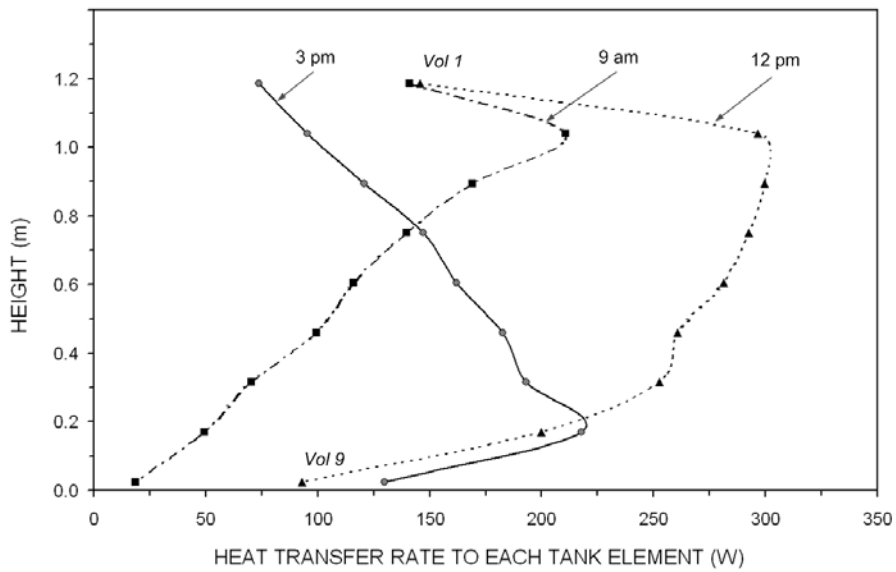
Fig. 7.1 Measuring points and tank elements.

Tank stratification and heat transfer rate

Fig. 7.2a displays the variation of measured tank temperature for a steady flow test of 1.6 L/min. A large temperature gradient of 28 K in the tank can be observed at noon for a system started from a cold tank (25°C). In the late afternoon, thermal stratification continues to be maintained with the top half of the tank being heated to the desired load temperature of 60-70°C. As the falling film tube extends from the top to the bottom of the storage tank, heat can be transferred along the full height of the tube to the adjacent tank contents. The rate of heat transfer to each volume in the tank core during the heat-up cycle is shown in Fig. 7.2b calculated using Eqn. 7.1. It can be noticed that most of the heat is transferred to the top half of the tank in the morning thus promoting thermal stratification in the tank. As the tank is fully charged in the late afternoon, the heat transfer process starts taking place at the bottom portion of the tank as seen in Fig. 7.2b. In the same figure, the lower heat transfer rate at the very top portion of the tank may be attributed to heat loss to the surroundings through the tank top and outlet.



(a)



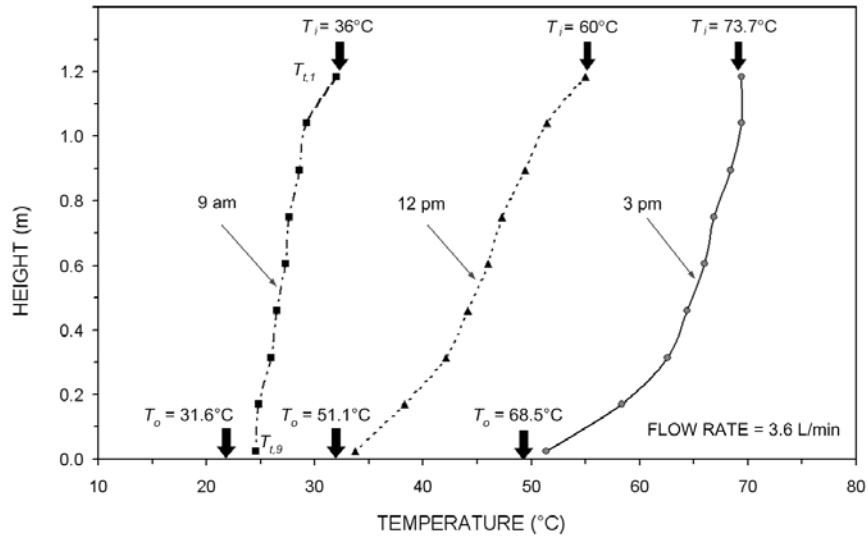
(b)

Fig. 7.2 Steady flow test data for a collector flow rate of 1.6 L/min, (a) measured tank temperature stratification, (b) heat transfer rate to each element of the tank.

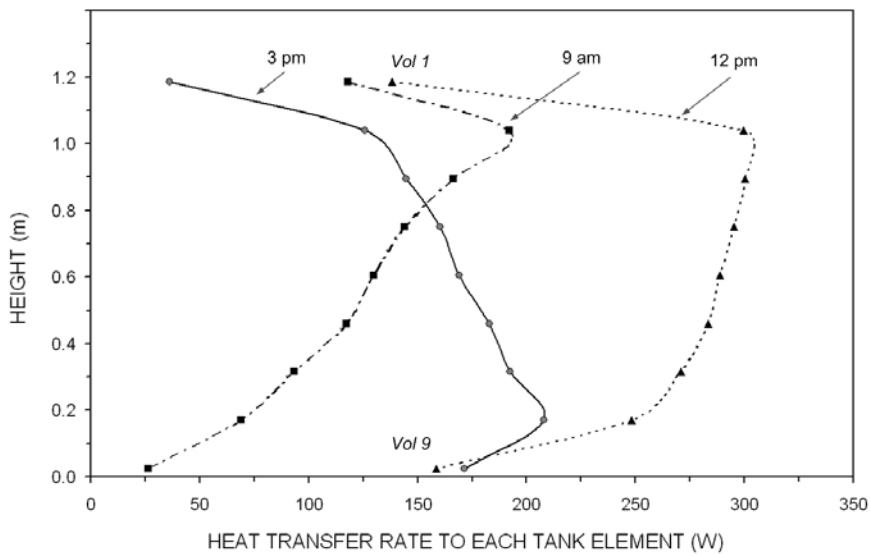
The influence of the collector flow rate on the tank stratification and heat transfer rate is shown in Fig. 7.3 for a constant flow rate of 3.6 L/min. The results show that thermal stratification in the tank (Fig. 7.3a) can be promoted even at higher flow rate on the falling film side of the heat exchanger. For higher flow rates, a more uniform heat flux distribution along the tube would be expected. This is evident in Fig. 7.3b which shows

7. CHARACTERISTICS OF FALLING FILM HEAT EXCHANGERS

that the heat transfer rate to each tank element is only varying within 250-200 W from volume 2 to 8 during the noon period. In the late afternoon when the tank is fully charged, the heat transfer process starts taking place at the bottom portion of the tank.



(a)



(b)

Fig. 7.3 Steady flow test data for a collector flow rate of 3.6 L/min, (a) measured tank temperature stratification, (b) heat transfer rate to each element of the tank.

For both cases, the heat exchanger inlet temperature is always higher than the tank top temperature corresponding to the ideal heating pattern under clear sky conditions. However, as the falling film tube covers the full height of the storage tank, there is a risk of degradation of thermal stratification when the collector return temperature is cooler than the tank top temperature. The hot layer stored in the top half of the tank can be extracted to the cooler collector fluid, which will decrease the system performance. This indicates that a tank with a heat exchanger covering the full tank height is not recommended in practice. As such, the heat exchanger inlet could be fitted in the mid height region of the core tube, however only half of the available heat transfer area can be utilised. Alternatively, to overcome de-stratification, a switching controller could be implemented that is able to modulate the collector flow rate to ensure a high collector return temperature relative to the top of the tank.

7.3 ADVANCED CONTROLLER STRATEGY

With the integration of a switching controller, it is anticipated that it will be possible to maintain stratification in the tank by modulating the collector flow rate in accordance to the following variables:

- Temperature difference between the collector return and the top half of the tank (ΔT_{start}) to be greater than 6 K so that there is always positive heat input to the tank,
- Temperature rise across the collector (ΔT_{rise}) to be greater than 10 K.

The flow rate is controlled by pulsing the pump on or off. The details of the operating sequences of the collector flow rate controller are given in Chapter 3. The characteristics of the falling film system incorporating a collector flow rate controller were evaluated under two heating patterns: heat-up from a cold start (charging condition) and from an initially stratified tank (preheated condition) with temperature of 52°C in the top half and 25°C in the bottom half of the tank.

7.3.1 Charging conditions

The falling film tank with a collector flow rate controller was first operated from a cold start under clear sky conditions. In this test, auxiliary heat added to the tank contents and water draw-off from the tank was not considered. Fig. 7.4 shows the switching controller sequences with varying collector flow rates during the heat-up cycle. When there is available solar energy from the collector in the early morning, the pump operates with the maximum flow rate to ‘flood’ the collector loop at the start of the system operation. The pump start threshold is when the collector temperature is 6 K above the tank top temperature. Throughout the system operation, the nominal power applied to the circulation pump is controlled by the switching controller in order to maintain a fixed ΔT_{rise} of approximately 10 K with varying collector flow rates. During the noon period, it can be seen that the pump operates with a maximum flow rate of 3.1 L/min in order to transfer the largest possible amount of heat that is available in the collectors to the tank. When the tank is fully charged in the late afternoon, the collector flow rate is decreased to ensure a high collector return temperature relative to the top of the tank ($\Delta T_{start} \sim 6$ K). This could avoid any possibility of the hot layer stored in the tank being extracted by the cooler collector fluid in the falling film tube.

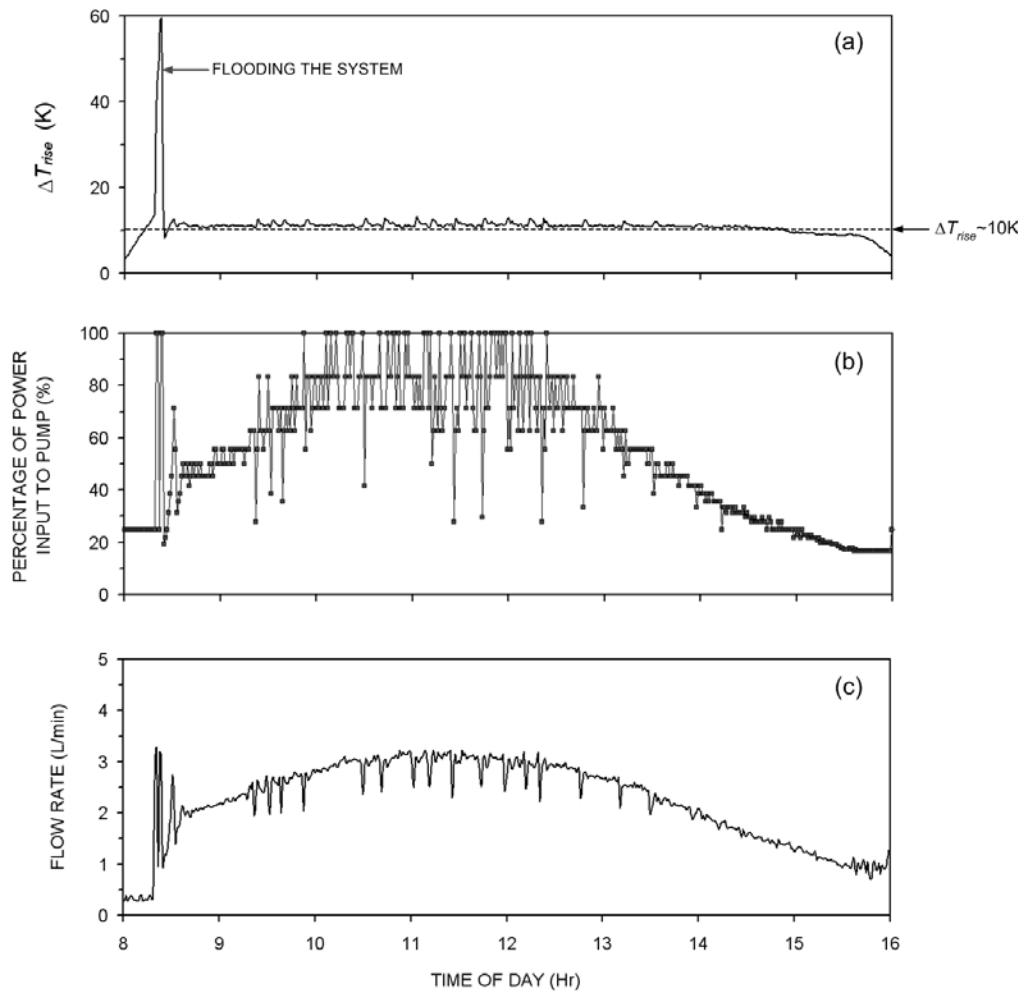
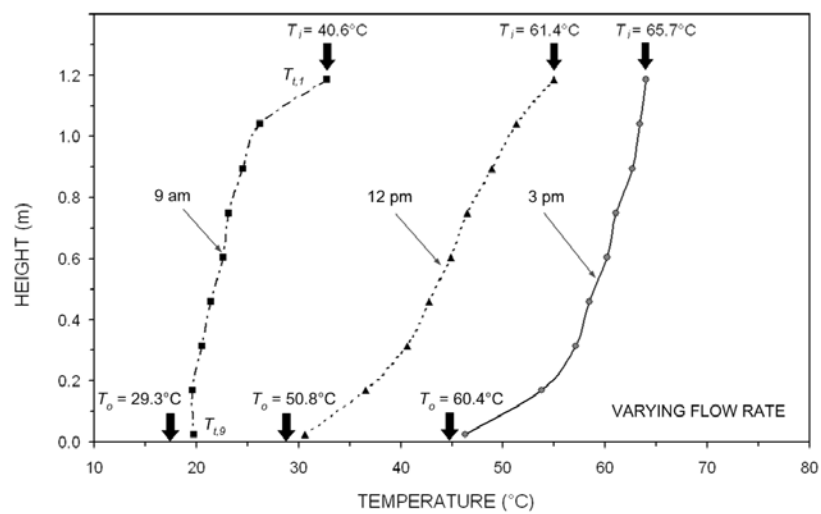


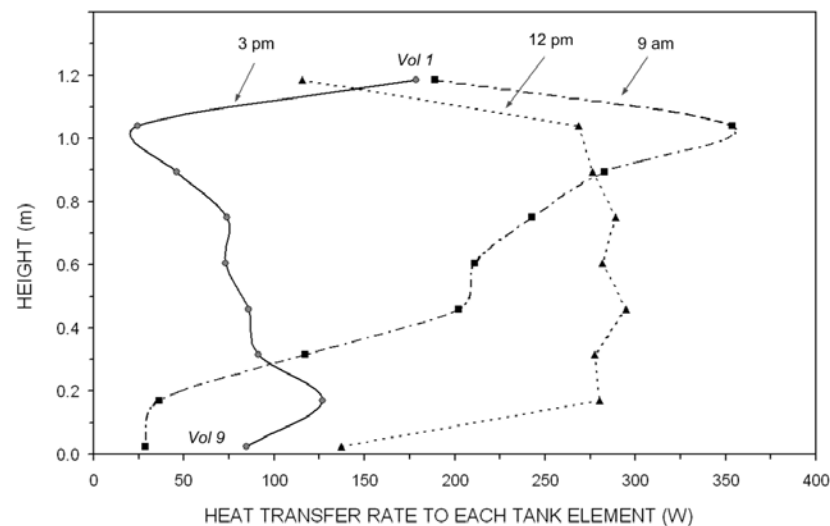
Fig. 7.4 Daily performance test of a falling film system with a switching controller from a cold start under clear sky conditions, (a) temperature rise across the collector loop, (b) percentage of power input to pump, (c) collector flow rate.

Fig. 7.5a shows the variation of the measured tank temperature stratification throughout the heat-up cycle. It can be also seen that the collector return or heat exchanger inlet temperature is always approximately 6 K higher than the average temperature of the tank top. Comparing the constant flow rate and variable flow rate tests, similar tank temperature stratification can be noticed when the system operates under clear sky conditions. This is because the collector return is always higher than the tank temperature thus the possibility of de-stratification in the tank is eliminated. The rate of heat transfer to each volume in the tank core during the heat-up cycle is shown in Fig. 7.5b. In the beginning of the heating process, most of the heat is transferred to the top portion of the tank for a collector flow rate of 2 L/min. When the collector flow rate is

modulated to the maximum value of 3.1 L/min during the solar noon period, heat is transferred uniformly from the thin liquid film in the heat exchanger tube to each adjacent segment of the tank as shown in Fig. 7.5b. When the tank is fully charged in the late afternoon, the system operates only at low collector flow rate below 1.5 L/min and as a consequence, a small amount of energy is delivered to the bottom portion of the tank. The concept behind the integration of a collector flow rate controller in falling film systems is to maintain the tank stratification under weak solar radiation conditions, which will be presented in the following sub-section.



(a)



(b)

Fig. 7.5 Varying flow test data for a falling film system with an advanced switching controller, (a) measured tank temperature stratification, (b) heat transfer rate to each element of the tank.

7.3.2 Preheated conditions

For typical operation of a solar water heater, the top half of the tank may be heated by an electric boosting element or the tank may be stratified under clear sky conditions in the morning, and the system subsequently operates under cloudy conditions in the afternoon. In this case, the hot layer in the top half of the tank could be de-stratified by the cooler collector fluid.

Fig. 7.6 shows the collector flow rate controller sequences for a falling film system operating from an initially preheated tank ($\sim 52^\circ\text{C}$ at the top half and $\sim 25^\circ\text{C}$ at the bottom half) under cloudy conditions. The corresponding solar radiation levels showing the cloudy sky conditions during the test is displayed in Fig. 7.6a. In such instance, the temperature difference between the collector return and the tank top (ΔT_{start}) drops below 6 K (Fig. 7.6b) and the pump is turned off and the collector fluid drains back to the core tube. At the same time, the empty steel collectors are heated up under stagnation conditions by the weak solar radiation and store the energy until the circulation pump is turned on when the ΔT_{start} reaches 6 K again. The percentage of pump drive and the collector flow rate are shown in Fig. 7.6c and d respectively. It is noted that the nominal power input to the pump below 20% represents the pump being off. When the pump is off, the collector fluid is draining back to the falling film tube by gravity as represented by a low flow rate (less than 1 L/min) shown in Fig. 7.6d. Fig. 7.6e shows that the tank top temperature is not influenced by the cooler collector return due to the operation of the switching controller.

7. CHARACTERISTICS OF FALLING FILM HEAT EXCHANGERS

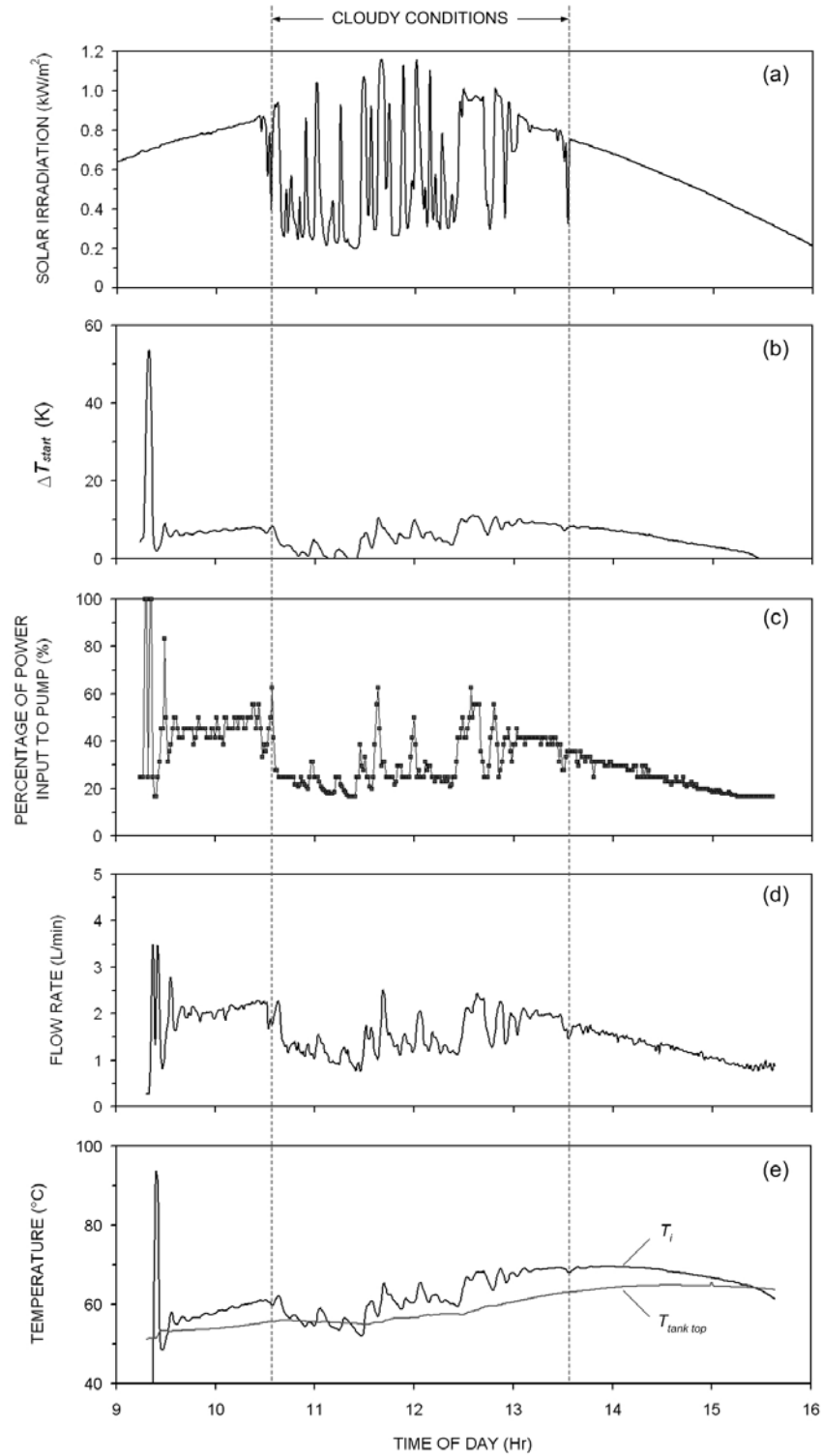
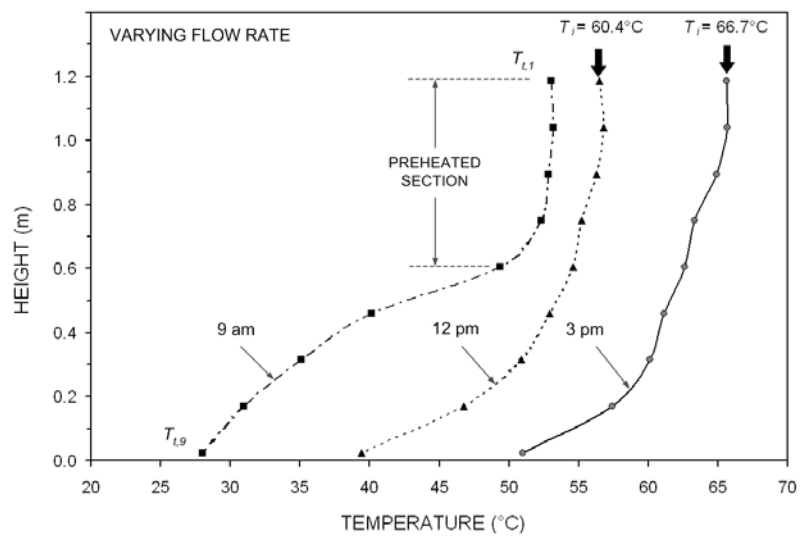


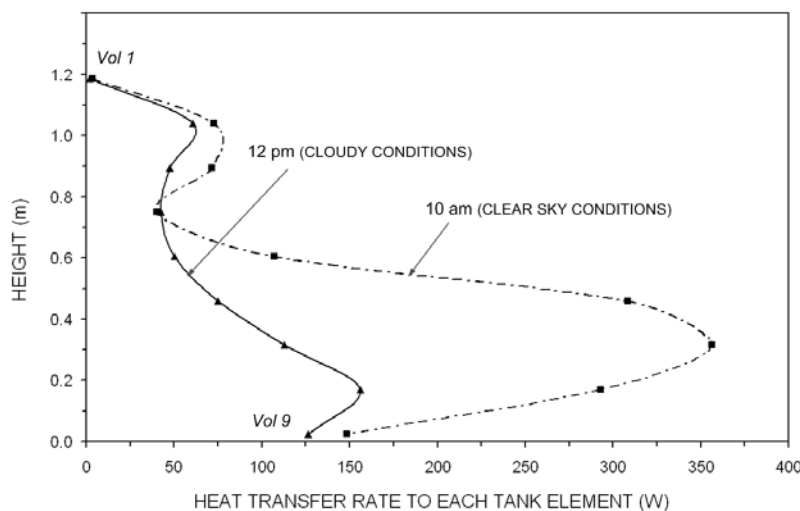
Fig. 7.6 Daily performance test of a falling film system with a controller operating under cloudy conditions starting from an initially stratified tank, (a) solar radiation, (b) temperature difference between the collector return and the top half of the tank, (c) percentage of power input to pump, (d) collector flow rate, (e) heat exchanger inlet and tank top temperatures.

7. CHARACTERISTICS OF FALLING FILM HEAT EXCHANGERS

Throughout the heat-up cycle for the preheat test, Fig. 7.7a shows that thermal stratification in the tank can be maintained for a falling film system operating with a switching controller. The corresponding energy increase rate for each volume in the tank is shown in Fig. 7.7b. It can be noticed that most of the heat is transferred to the bottom half of the tank just below the preheated section under both clear sky conditions in the beginning of the test with a collector flow rate of 2 L/min and cloudy conditions during the noon period.



(a)



(b)

Fig. 7.7 Preheated test data for a falling film system with an advanced switching controller, (a) measured tank temperature stratification, (b) heat transfer rate to each element of the tank.

7.4 OVERALL HEAT TRANSFER CHARACTERISTICS

In this section, the overall heat transfer coefficient and area product (UA_{hx}) for the falling film heat exchanger is reported in order to quantify the performance of the heat exchanger. Brief descriptions of heat exchanger overall UA_{hx} were given in Chapter 6. Since the collector fluid is falling downward as a thin film over the inner surface of the heat exchanger tube opposing the buoyancy driven upward flow in the tank, the falling film heat exchanger UA_{hx} can be determined using Eqn. 7.2 based on the log-mean temperature difference assuming as applied to a counter-flow heat exchanger.

$$UA_{hx} = \frac{\dot{Q}}{\Delta T_{lm}} \quad (7.2)$$

$$\Delta T_{lm} = \frac{(T_i - T_{t,2}) - (T_o - T_{t,8})}{\ln \frac{(T_i - T_{t,2})}{(T_o - T_{t,8})}} \quad (7.3)$$

where positions of the temperatures in Eqn. 7.3 can be referred to Fig. 7.1.

Assuming one-dimensional heat transfer and isothermal wall boundary conditions, the overall UA_{hx} value of the falling film heat exchanger can be defined in terms of individual thermal resistances across the heat exchanger as the equation:

$$\frac{1}{UA_{hx}} = R_{film} + R_{wall} + R_{tank} \quad (7.4)$$

$$\text{On the falling film side, } R_{film} = \frac{1}{\bar{h}_{film} A_{film}} = \frac{(\bar{T}_{film} - \bar{T}_{w,film})}{\dot{Q}} \quad (7.5)$$

$$\text{On the tank side, } R_{tank} = \frac{1}{\bar{h}_{tank} A_{tank}} = \frac{(\bar{T}_{w,tank} - \bar{T}_{tank})}{\dot{Q}} \quad (7.6)$$

where: A_{film} , A_{tank} are the area wetted by the film over the inner surface of the heat exchanger tube and the total outer surface of the core tube on the tank side (m^2). Note that the area wetted by the falling film may not be the same as the area on the potable water side of the heat exchanger,

$\bar{h}_{film}, \bar{h}_{tank}$ are the film side and the tank side mean heat transfer coefficients (W/m²K),

$\bar{T}_{film}, \bar{T}_{tank}, \bar{T}_{w,film}, \bar{T}_{w,tank}$ are the averaged temperatures of the thin film, tank, inner and outer walls of the falling film tube respectively (°C).

The variation of the overall heat transfer coefficient and area product for the heat exchanger during a heat up test with a constant flow rate of 2.6 L/min is shown in Fig. 7.8. The UA_{hx} values for the falling film heat exchanger without an advanced switching controller were found to be 150-200 W/K under full recovery mode from a cold start.

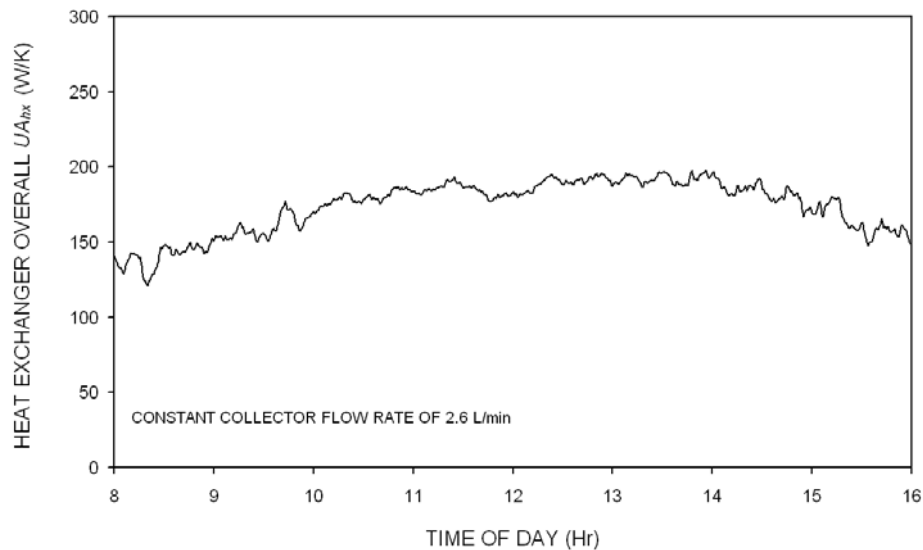


Fig. 7.8 Overall heat transfer coefficient and area product (UA_{hx}) for the falling film heat exchanger during heat-up cycles with a flow rate of 2.6 L/min.

The corresponding thermal resistances on the film side and tank side were determined using Eqn. 7.5 and 7.6 respectively through detailed measurements of the outer wall temperature of the falling film tube. As shown in Fig. 7.9, the thermal resistance of the film side (R_{film}) was found to vary from 0.0035 to 0.002 K/W before the noon period, and approach a constant value of 0.002 K/W as the tank is charged further. The cause of the variation in the falling film R_{film} is primary due to the change in film thickness due to variation of viscosity with temperature. It is also evident in Fig. 7.9 that the thermal resistance on the tank side (R_{tank}) is approximately a factor of 1.5 times higher

than on the falling film side. The thermal resistance contributed by the 3 mm thick carbon steel wall can be neglected compared to the convection heat transfer processes. As a result, the limiting factor on the performance of the heat exchanger is primarily the natural convection circulation in the storage tank.

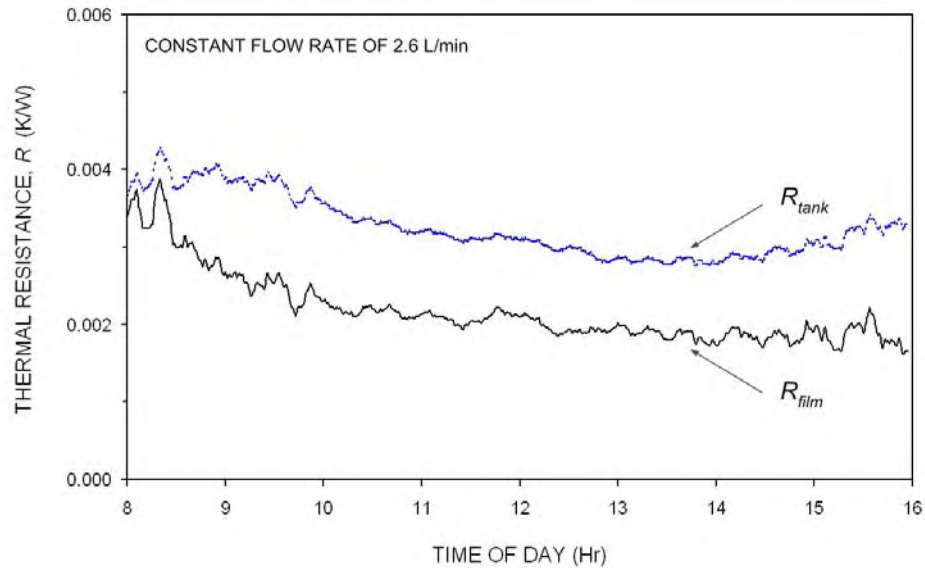


Fig. 7.9 Falling film and tank side thermal resistance for a heat exchanger operating from a cold start with a flow rate of 2.6 L/min.

Effect of flow rate on heat exchanger UA_{hx} : Steady flow tests

Measurements of the heat transfer characteristics were conducted for constant flow rates of 1.6 and 3.6 L/min. Comparison of the heat exchanger overall UA_{hx} for different collector flow rates is shown in Fig. 7.10. The heat transfer characteristic for different flow rates were found to be very similar over the anticipated application flow rate range of 1.6 to 3.6 L/min. This is primary due to the natural convection heat transfer process in the storage tank that limits the heat flow from the thin liquid film through the tube wall.

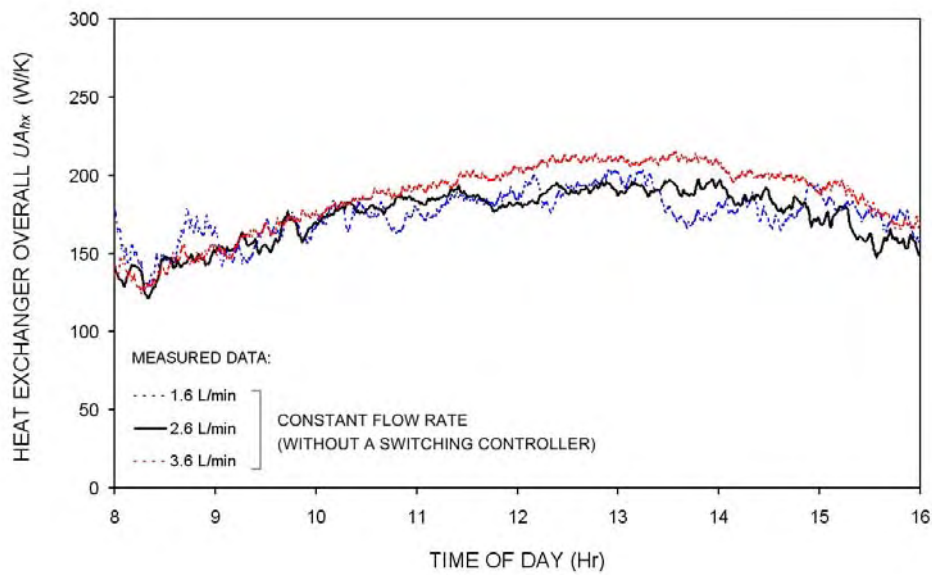


Fig. 7.10 Overall heat transfer coefficient and area product (UA_{hx}) for falling film heat exchanger for flow rates of 2, 2.6 and 3.6 L/min.

Comparison of UA_{hx} for system with and without an advanced controller

For a falling film heat exchanger system operating with a switching controller that modulates the collector flow rate in response to changes of collector output, the heat exchanger UA_{hx} was also found to be in a range of 150-200 W/K (Fig. 7.11) which is the same as observed in the steady flow tests (Fig. 7.10). The only difference in UA_{hx} values between the two modes of operation is at the end of the heat-up cycle when the tank is fully charged. A drop of 30% in heat exchanger overall UA_{hx} for system operating with a switching controller can be noticed. In that heating period, the collector flow rate of the falling film system is modulated down to approximately 1.3 L/min which may result in a smaller wetted area over the surface of the heat exchanger tube. Visual observations of the wetting extent in the falling film tube will be presented in Section 7.5.

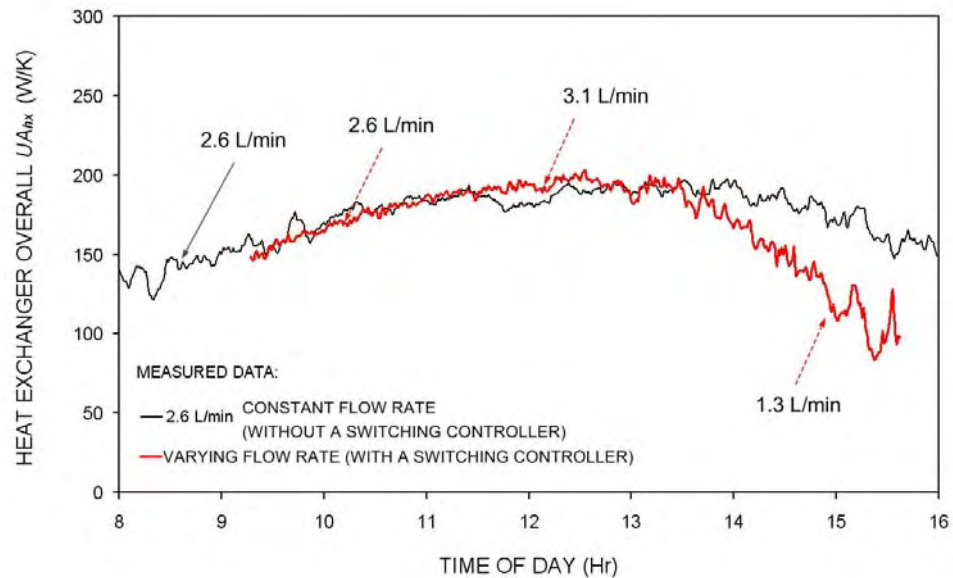


Fig. 7.11 Overall heat transfer coefficient and area product (UA_{hx}) for falling film heat exchanger with an advanced controller that varies the collector flow rate during the heat-up cycle test.

7.5 FILM FLOW BEHAVIOUR

As the falling film may not cover the entire heat exchanger tube circumference, the tube surface wetted by the film flow has to be known in order to determine the heat transfer coefficient on the falling film side of the heat exchanger. The wetting behaviour of falling films on the inner surface of the heat exchanger tube is difficult to quantify as it is influenced by parameters, such as film-feeding system at the inlet, surface roughness, film flow rate, fluid properties etc. In this section, results from visual evaluation of the film wetting extent over the inner surface of the heat exchanger tube are presented for typical operating flow rates of 2 and 3.4 L/min and inlet temperatures of 24°C and 50°C. A research unit of the falling film tube with the same dimensions as the prototype unit was used for these observations. The core tube was isolated from the tank and heat transfer to the potable water was not taken into account. 20% propylene glycol/water mixture was used as the working fluid for all experiments. The flow distributor configuration fitted at the top of the heat exchanger tube is shown in Fig. 7.12 and the detailed description of this distributor is given in Chapter 3.

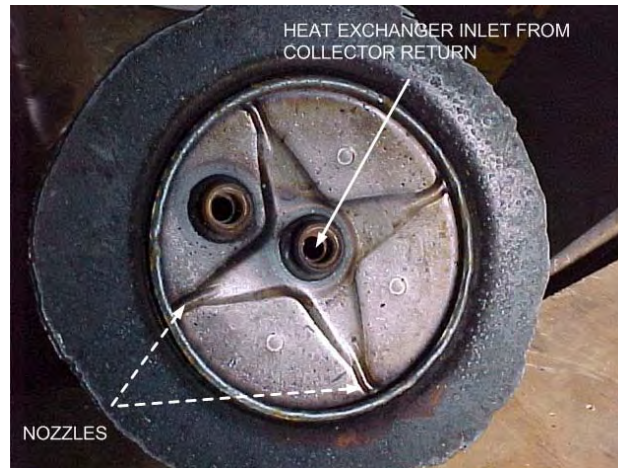
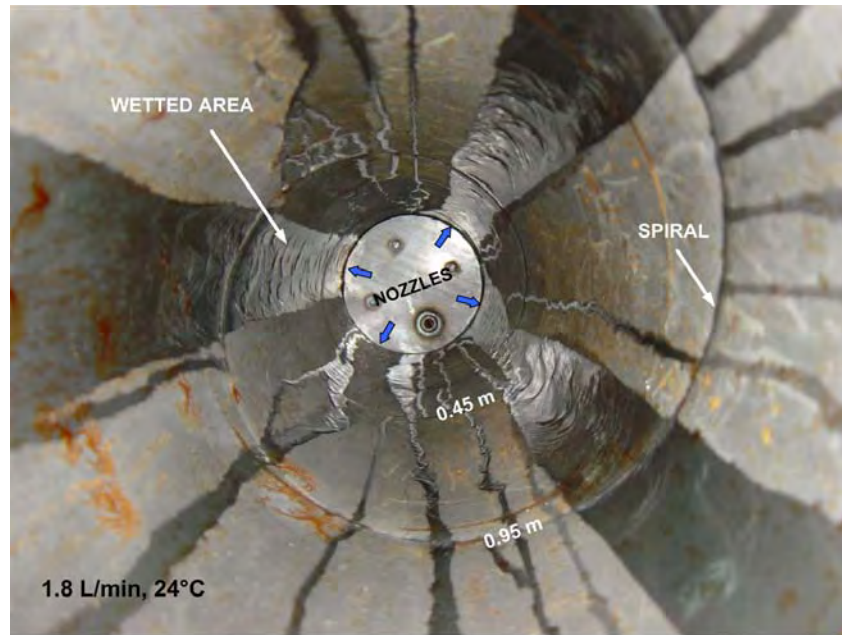
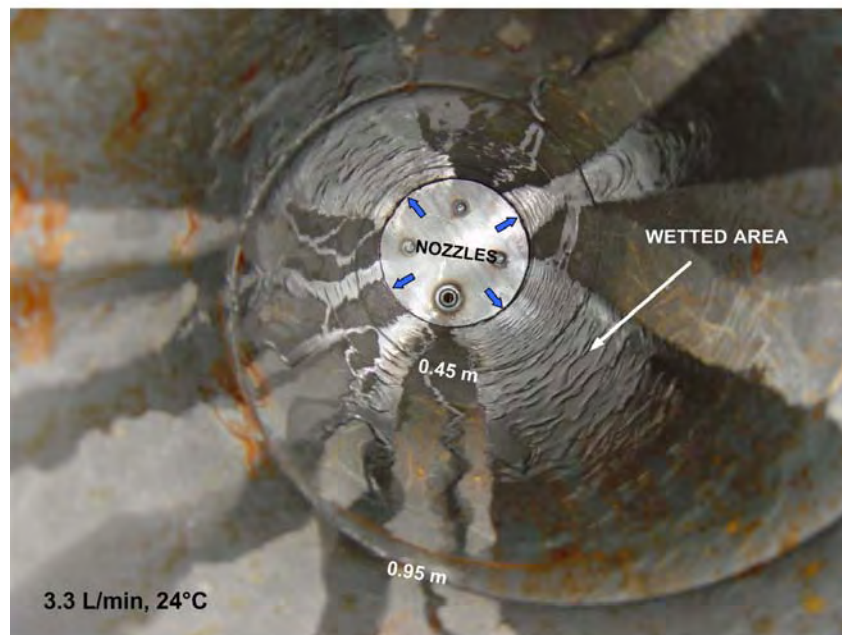


Fig. 7.12 Flow distributor used in prototype of a falling film tank tested in this thesis.

Fig. 7.13a shows the film flow pattern and wetted area observed in the view up the core tube at inlet temperature of 24°C and for a flow rate of 1.8 L/min. It can be seen that the falling film does not wet the whole inner surface of the tube for low film velocity. This would probably explain the decrease in overall UA_{hx} when the collector flow rate is modulated down to 1.3 L/min (Fig. 7.11). The poor wetted area of the tube observed in Fig. 7.13a could be due to the high viscosity and surface tension of the glycol solution at low film temperature of 24°C. When the flow rate is increased to 3.3 L/min (Fig. 7.13b), the wetted area increases compared to that lower flow rate. Both photographs in Fig. 7.13a and b also indicate the presence of waves in the film however the thin film remained in contact to the wall. In the photos, it can also be seen that the small gap between the spirally welded walls did not disturb the film flow. The film-wetting phenomena in Fig. 7.13 correspond to a system operating from a cold start in the early morning.



(a)



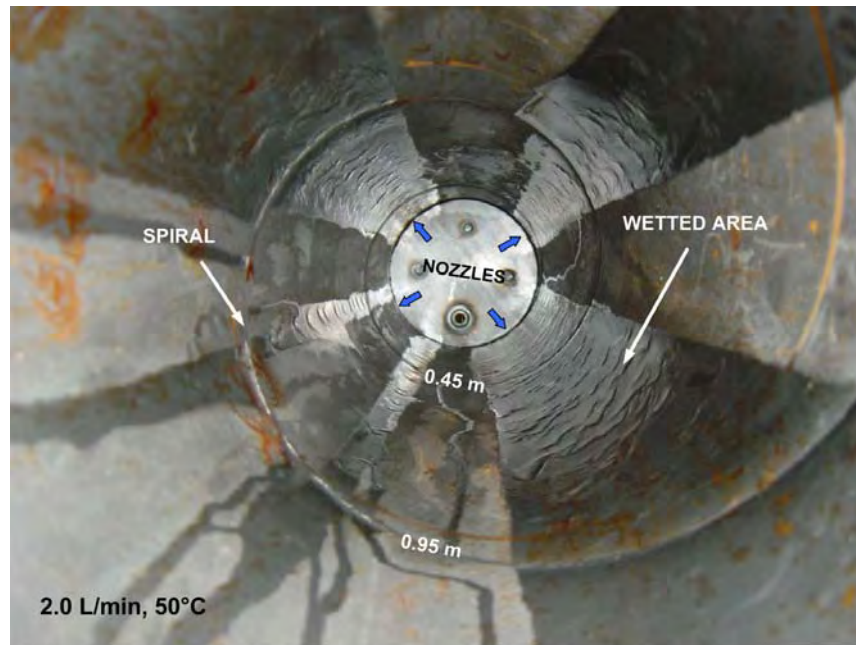
(b)

Fig. 7.13 Photos looking up the heat exchanger tube, (a) flow rate of 1.8 L/min and inlet temperature of 24°C, (b) flow rate of 3.3 L/min and inlet temperature of 24°C.

A second set of photographs in Fig. 7.14 show the film flow and wetted area for an inlet temperature of 50°C with flow rates of 2 and 3.4 L/min. As viscosity and surface tension of the glycol mixture decrease with temperature, the falling film is visibly wetting a larger fraction of the tube surface and smoother films are observed compared

7. CHARACTERISTICS OF FALLING FILM HEAT EXCHANGERS

to that observed at low film temperature (Fig. 7.13). The increase in flow rate from 2 L/min to 3.4 L/min has only a small effect on surface wetting. The film flow patterns in Fig. 7.14 correspond to a system operating under tank charging mode during the noon period.



(a)



(b)

Fig. 7.14 Photos looking up the heat exchanger tube, (a) flow rate of 2 L/min and inlet temperature of 50°C, (b) flow rate of 3.4 L/min and inlet temperature of 50°C.

Based on the photos taken of the falling film in the heat exchanger tube, the wetted area was evaluated qualitatively to be approximately half of the total tube surface. It should be noted that this approximation is only valid for the heat exchanger tube with the film distributor design shown in Fig. 7.12. In further production of falling film tubes with different distributor design, the wetting extent will have to be investigated for each configuration.

7.6 FILM THICKNESS

Due to the presence of complicated wave phenomena at the free surface of the film, attempts to correlate film thickness taking into account of wave formation and instability is still an on-going research topic by many investigators as mentioned in Chapter 2. In this study, the film thickness in the falling film heat exchanger was evaluated using an analytical expression developed by Nusselt (1923) for a smooth surface and laminar flow as given in Eqn. 7.6. Several assumptions are made in this analysis of film thickness:

- The film is assumed to cover half of the inner surface of the core tube.
- The flow is fully developed and laminar ($200 < Re_f < 1000$) although a wavy film was observed. Ambrosini *et al.* (2002) has shown that the film thicknesses agreed reasonably with Nusselt's correlation for laminar wavy film flows at Re_f less than 1000 over a flat plate for temperatures of 20 to 70°C.
- The drag effect at the free surface of the film caused by the air in the tube is neglected due to the small viscosity of air compared with that of the film liquid.

Under these assumptions the relation between film thickness and flow rate for fully developed conditions (Nusselt, 1923) is:

$$\delta = \left(\frac{3\mu Q}{\rho g b^*} \right)^{1/3} \quad (7.7)$$

where b^* is half of the circumference of the falling film tube to allow for 50% wetting. The dimensionless film Reynolds number (Re_f) is defined by Eqn. 7.8 based on the hydraulic diameter ($d_h=4\delta$) of the film and volumetric flow rate.

$$Re_f = \frac{4\rho Q}{\mu b^*} \quad (7.8)$$

For the application flow rate range of 2 to 3 L/min, the film Reynolds number varies from 200 to 900 depending on the film temperature. The fully developed film thickness is approximately 0.2 to 0.4 mm determined using Eqn. 7.7.

7.7 HEAT TRANSFER CORRELATIONS

To model the annual performance of a solar water heater incorporating a falling film heat exchanger, prediction of the heat transfer coefficient in the falling film and the natural convection coefficient on the tank side of the heat exchanger are required. A sketch of one-dimensional convective heat transfer across a falling film heat exchanger is shown in Fig. 7.15.

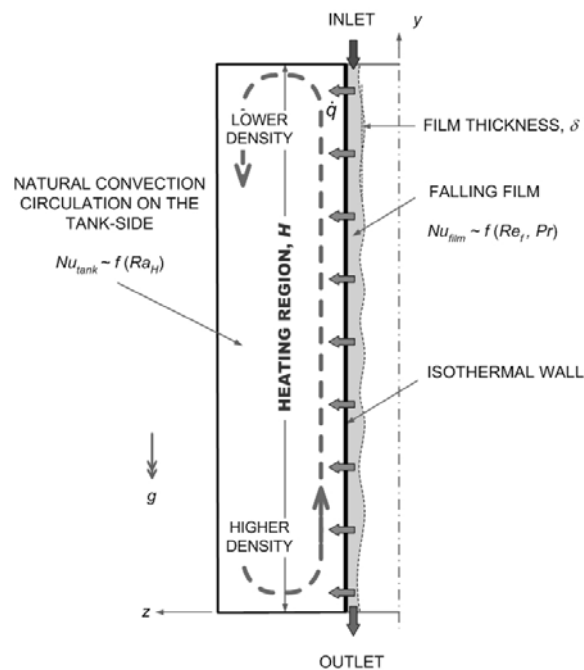


Fig. 7.15 Sketch of one-dimensional heat transfer across a falling film heat exchanger.

7.7.1 Film side convection heat transfer

In determining the film side mean heat transfer coefficient (\bar{h}_{film}), it is usually assumed that the entire tube surface is wetted. The assumption of fully wetted area over the heat exchanger tube may lead to an under estimate of film side heat transfer coefficient. In

this study, half of the inner surface of the heat exchanger tube was assumed to be wetted by the thin falling film as evaluated qualitatively in Section 7.5. Non-dimensional relations of mean heat transfer coefficient for correlating experimental data were developed based on the mean temperature of the heat transfer wall, collector flow rate, inlet and outlet temperatures and fluid properties.

7.7.1.1 Comparison of analytical solution and measurements

An analytical heat transfer coefficient expression (Bird *et al.*, 2002) given in Eqn. 2.19 (Refer to Chapter 2) for a liquid falling film over an infinite width flat plate with short contact times may be used as an approximation of the heat transfer rate in the falling film heat exchanger. The analytical solution was based upon the film thickness expression developed by Nusselt (1923) as given in Eqn. 7.7. Using the hydraulic diameter ($d_h=4\delta$) as the characteristic length, the analytical heat transfer coefficient expression (Eqn. 2.19) is redefined in terms of Nusselt number as follows:

$$\overline{Nu}_{film} = \frac{3}{2} \frac{1}{\Gamma(4/3)(9\beta^* H)^{1/3}} 4\delta \quad (7.9)$$

where: H is the height of the plate (m),

$\Gamma(4/3) = 0.89297$ is a gamma function,

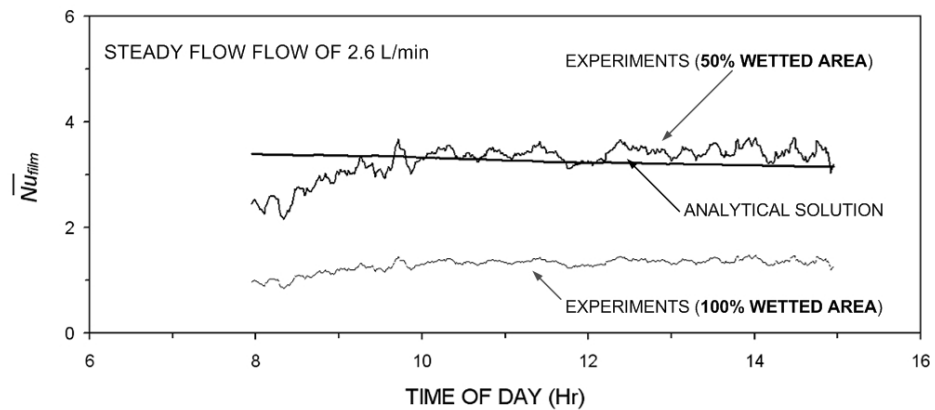
$$\beta^* = \mu k / (\rho^2 C_p g \delta).$$

A comparison of measured and analytical solutions (Eqn. 7.9) for the film side Nusselt number for steady flow rates of 2.6 and 3.6 L/min is shown in Fig. 7.16. The measured Nusselt number was determined for both 50% and 100% wetted area. It can be seen that the measured Nusselt number based on 50% wetted area (as observed in Section 7.5) is in reasonable agreement with the theoretical function in Eqn. 7.9. At the initial heating stage in the early morning, the analytical expression tends to overestimate the Nusselt number. This could be due to a smaller fraction of wetted area at lower film temperature as observed in Section 7.5. The enhancement mechanism of the rivulet flow at higher flow rate has not been investigated in this study due to experimental and numerical difficulties. However, the uncertainty due to this factor may be insignificant

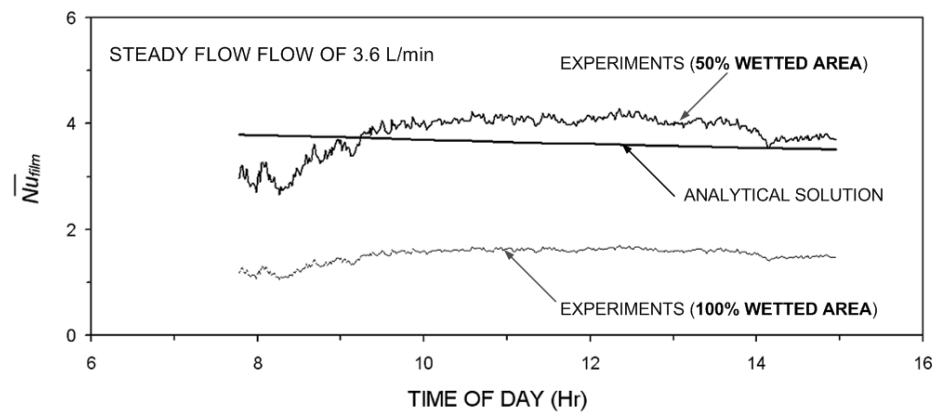
7. CHARACTERISTICS OF FALLING FILM HEAT EXCHANGERS

as the primary limiting thermal resistance of the heat exchanger is the natural convection process on the tank side.

It is noted that the analytical expression in Eqn. 7.9 only presents the physical quantities of the falling film with heat transfer i.e. the Nusselt number is primary a function of the film thickness. In this equation, although the film thickness is a function of Reynolds number, there is no explicit appearance of Reynolds number as is customary in Nusselt number correlations. Therefore, to be of practical utility and relevant to design calculations, it is desirable to develop a non-dimensional correlation in the customary form of $Nu = f(Re)$. This is discussed in the next section.



(a)



(b)

Fig. 7.16 Comparison between measured Nusselt number obtained from steady flow tests and analytical solution, (a) flow rate of 2.6 L/min, (b) flow rate of 3.6 L/min.

7.7.1.2 Non-dimensional correlation

Fig. 7.17 shows the mean Nusselt number determined from steady flow experiments on the falling film side as a function of film Reynolds number for a range of temperature differences at steady flow rates of 1.6, 2.6 and 3.6 L/min. The measured data was determined by assuming half of the inner surface of the falling film tube to be wetted. In Fig. 7.17, it is shown that the Reynolds number is in the laminar range ($Re_f < 1600$) and a dependency of Nusselt number on Reynolds number is also observed for all operating conditions. As the flow rate is increased, the heat transfer is enhanced by the increased convection effect due to the higher velocity film on the heat exchanger tube. Fig. 7.17 also shows that measured data for a system operating with a variable flow rate controller is consistent with the steady flow tests data covering the operating collector flow rates.

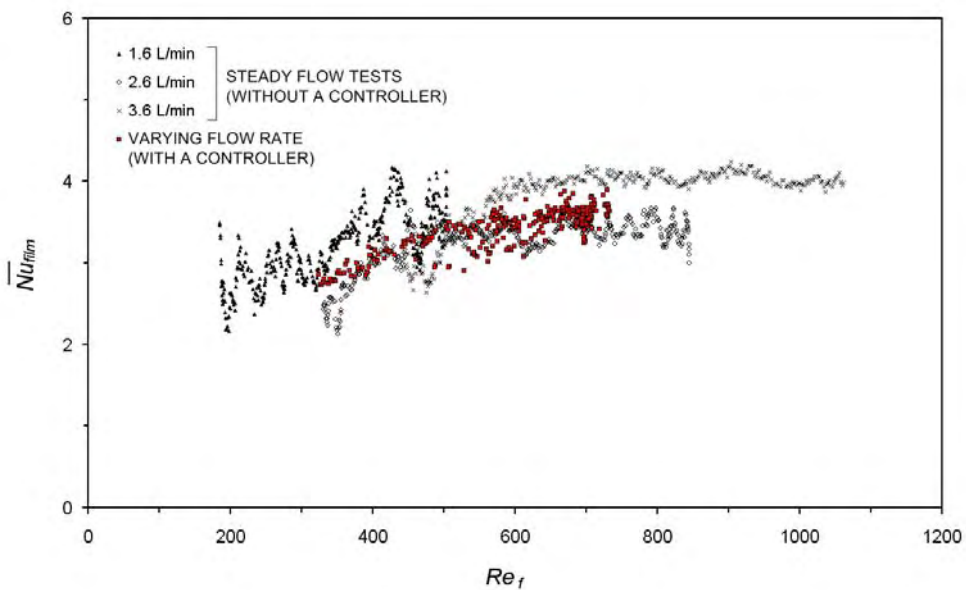


Fig. 7.17 Measured mean Nusselt number as a function of film Reynolds number in a falling film heat exchanger with and without a collector flow rate controller.

In general, the heat transfer data shows that the film Reynolds number is the most significant parameter for correlating heat transfer in the falling film heat exchanger. In this study, the standard correlation for forced convection flow over a vertical flat plate was used. When the results shown in Fig. 7.17 are plotted as $\overline{Nu}_{film} / Pr^{0.33}$ against Re_f in Fig. 7.18, this dependence correlates fairly well for all test results. In order to correlate

the measured data for current falling film heat exchanger design, a new Nusselt number and Reynolds number correlation was developed by regression-fit to the measured data as given in the following equation,

$$\overline{Nu}_{film} = 0.183 Re_f^{0.358} Pr^{0.33} \quad (7.10)$$

for $5 < Pr < 13$ and $200 < Re_f < 1000$, with properties calculated at the average of the film and wall temperatures (20% propylene glycol/water mixture). Note that the non-dimensional correlation is only applicable for the falling film tube tested in this study with assumption of 50% wetted area. The dependency of different film distributor and tube designs was not investigated here as different designs may result in different film wettability.

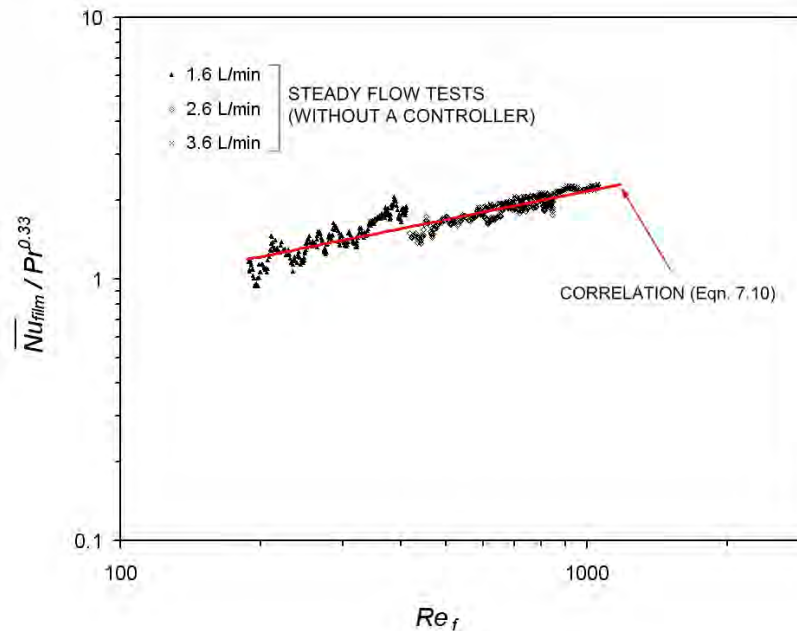


Fig. 7.18 Measured mean Nusselt number divided by $Pr^{0.33}$ against Reynolds number in a falling film heat exchanger.

7.7.1.3 Applicability of steady flow correlation

Fig. 7.19 shows that the measured mean Nusselt number for a falling film system operating on three different sunny days with collector flow rate being modulated by an advanced switching controller agrees well with the Nusselt number obtained using Eqn. 7.10. The comparison shows that the empirical expression developed from steady flow measurements predicts the film side heat transfer coefficient for most of the operating

conditions with an accuracy of 10%. The scattered data in Fig. 7.19 represents the system operating in the early morning or late evening when the collector flow rates are typically lower than 1.5 L/min.

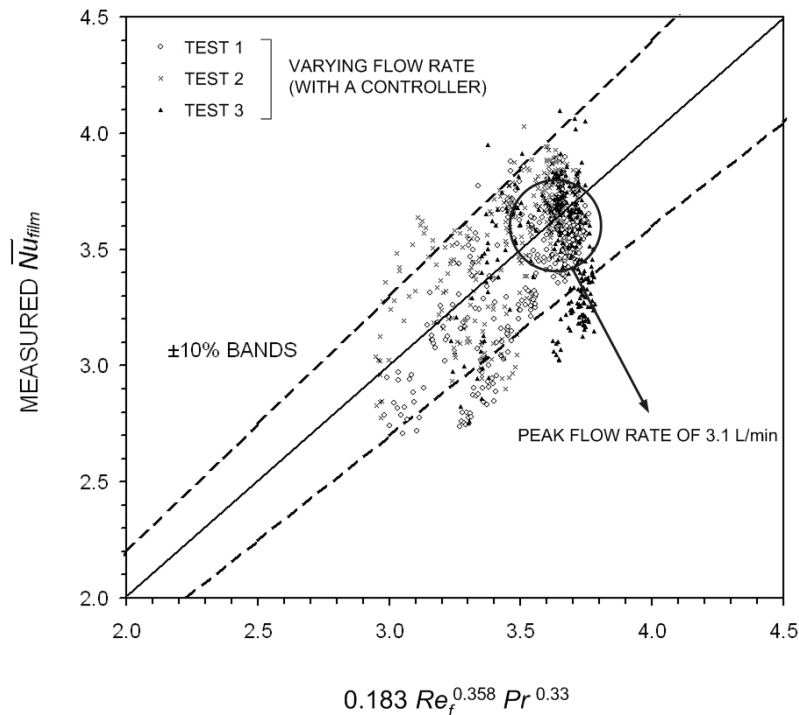


Fig. 7.19 Measured and predicted (Eqn. 7.10) Nusselt number for a falling film system operating with a collector flow rate controller.

7.7.2 Correlation of tank side natural convection heat transfer

On the tank side, the flow is driven by buoyancy forces which distribute the heat over the height of the tank. The standard means of correlating natural convection heat transfer processes is to relate the non-dimensional Nusselt number (Nu) to the Rayleigh number (Ra). The variation of measured mean Nusselt number (\overline{Nu}_{tank}) with Rayleigh number (Ra_H) based on the tank height during heat up cycle tests is shown in Fig. 7.20. The heat transfer coefficient on the tank side of the outer surface of the falling film heat exchanger is observed correspond with turbulent flow conditions. Natural convective heat transfer between the tank wall and the tank contents can be approximated by the vertical isothermal flat plate correlation (Incropera and DeWitt, 1996) for turbulent flow:

$$\overline{Nu}_{tank} = 0.1Ra_H^{1/3}, \quad 10^9 \leq Ra_H \leq 10^{13} \quad (7.11)$$

As seen in Fig. 7.20, the measured data is in reasonable agreement with the standard turbulent correlation in the range $10^{11} \leq Ra_H \leq 10^{12}$.

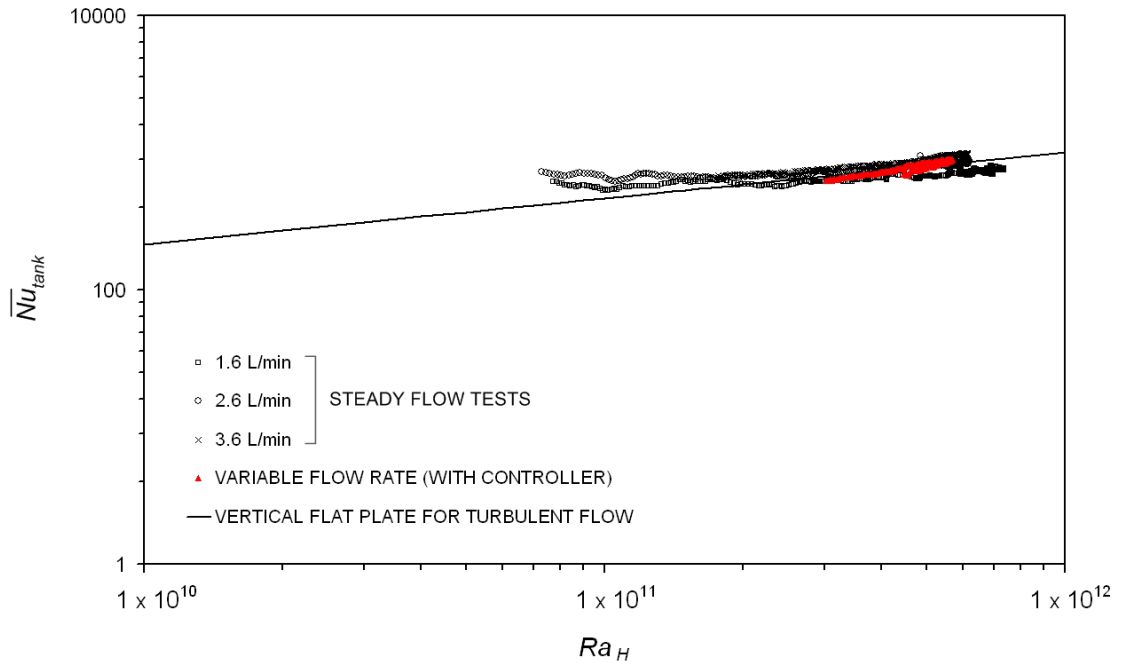


Fig. 7.20 Comparison of measured mean Nusselt number on the tank side of the falling film heat exchanger and standard turbulent isothermal vertical flat plate function.

7.8 SUMMARY

This chapter outlined the characterisation of the performance of falling film heat exchangers for use in pumped-circulation solar water heaters. The investigations were based on measurements from outdoor product tests and the following conclusions are obtained:

- Measurements from steady flow tests showed that large degree of thermal stratification in the storage tank could be obtained for full recovery operation mode.
- As the falling film tube covers the full height of the storage tank, there is a risk of degradation of thermal stratification when the collector return temperature is cooler than the tank top temperature. With the integration of a switching controller that

modulates the collector flow rate measurements show that thermal stratification can be maintained when the system operates under cloudy conditions.

- The overall heat transfer coefficient-area product (UA_{hx}) for the falling film heat exchanger with and without a switching controller was found to be 150-200 W/K. Although the falling film side heat transfer coefficient is comparatively high, the factor limiting the performance of the heat exchanger is primarily the buoyancy driven circulation in the storage tank.
- Based on visual observations of the wetting extent of the falling film, the wetted area was qualitatively determined to be approximately half of the total tube surface for the heat exchanger tube with the film distributor design tested in this study.
- On the falling film side of the heat exchanger, the film thickness was evaluated using an analytical expression (Nusselt, 1923) for a smooth laminar film. A non-dimensional Nusselt number correlation was developed in terms of Reynolds and Prandtl numbers, from a regression-fit to measured data. The empirical expression developed from steady flow measurements was able to predict the film side heat transfer coefficient for a system operating with a switching controller to within an accuracy of 10%.
- For natural convection circulation on the tank side of the heat exchanger, the measured tank side mean Nusselt number agreed well with the correlation for turbulent free convection on a flat plate.

Both film side and tank side heat transfer correlations will be implemented in Chapter 8 in the solar simulation program TRNSYS to model the annual performance of a solar water heater incorporating a falling film heat exchanger. It should be noted that the dependency of the film wettability on the system performance was not investigated in this study, however the uncertainty due to this factor may be insignificant as the primary limiting thermal resistance of the heat exchanger is the natural convection process on the tank side. The effect of the wetting extent on the annual performance of a falling film system will be presented in Chapter 8 using TRNSYS.

- CHAPTER 8 -

SYSTEM MODELLING

8.1 INTRODUCTION

The work in the previous chapters involved detailed investigations on the heat transfer characteristics of a mantle heat exchanger and a falling film heat exchanger. Convective heat transfer correlations for both types of solar collector-loop heat exchangers have been developed in Chapters 6 and 7 in order to predict the heat transfer rate across the heat exchanger. In this chapter, these empirical correlations are implemented into the standard one-dimensional storage tank model TYPE 60 in TRNSYS to simulate heating in mantle heat exchangers and falling film heat exchangers. The complete systems are modelled and compared to the performance of a direct system under representative meteorological weather data and for daily and seasonal load conditions specified in the Australian Standard AS4234 (1994).

8.2 MODELLING SOLAR WATER HEATERS

There have been many types of solar water heater products ranging from simple thermosyphon systems to pumped-circulation systems with or without a heat exchanger. The design of these systems depends on the climate, common plumbing practices and solar market considerations in different countries. The long-term performance of solar water heaters can be predicted by means of mathematical models with representative meteorological data and short-term experimental data for the solar collector performance. Individual component tests are carried out to characterise each component of the system i.e. solar collector efficiency, heat loss coefficient for the storage tank, thermal resistances of heat exchanger etc. These test results are then implemented in a mathematical model such as TRNSYS to compute the input-output

performance of each sub-system. Without conducting long-term performance tests that are usually costly, the influences of operating conditions, such as different weather data, load or demand profile, operating set points or component modifications, on the long-term performance of a system can be predicted. This technique is also adopted in Australian Standard AS4232 to evaluate ratings for solar water heater products.

Models of heat exchangers in hot water storage tanks are generally available in solar simulation programs such as TRNSYS (Klein *et al.*, 2001), MantlSim (Furbo and Berg, 1990) and TSOL (Valentin, 2004). The concepts behind these models are quite different. TRNSYS is the most widely used commercial transient solar simulation program and can be used to model a variety of system designs. To describe thermal stratification in the tank, the TRNSYS standard storage tank model (TYPE 60) uses one-dimensional vertical discretisation approach to divide the tank domain into a number of small fixed elements. Based on an energy balance that accounts for all energy flows into or out of each node, the temperature variation inside the storage tank can be determined. If there is a temperature inversion in the node adjacent to the fixed heat exchanger inlet, the fluid is mixed with the appropriate nodes above and below until the inversion is eliminated. The heat exchanger model is an option available with the multiple node stratified tank model. The model is empirical and requires mathematical correlations of the heat transfer coefficient to predict the heat transfer rate across the heat exchanger by solving the one-dimensional energy balance equation at each tank node containing the heat exchanger. This routine was originally written for immersed coil heat exchangers by Newton (1995), however it can be modified to include new heat transfer correlations that suit each particular heat exchanger configuration. TSOL is another commercially available solar simulation program that consists of pre-programmed system models. This program does not allow users to enter their own empirical data for particular components of the system. In this study the standard TYPE 60 routine in TRNSYS was modified to accommodate the empirical correlations for both proposed heat exchangers as presented in the following section.

8.3 ONE-DIMENSIONAL HEAT EXCHANGER MODEL

This section first presents a brief introduction of the standard stratified storage tank model TRNSYS TYPE 60. The primary difference between the mantle heat exchanger and falling film heat exchanger models and the standard TYPE 60 model is the heat transfer correlations for convection heat transfer on either side of the heat exchanger.

8.3.1 Standard TYPE 60 model

The heat exchanger option in the TYPE 60 model is written in general with the tank side heat transfer coefficient specified in standard Nusselt number and Rayleigh number form (Eqn. 8.1) where the coefficients C and n can be specified to accommodate the experimental data.

$$Nu = CRa^n \quad (8.1)$$

On the pumped circulation side of the heat exchanger, the heat transfer coefficient is modelled using standard pipe flow correlations. The model initially divides the heat exchanger into elements with equal height to the adjacent tank nodes and energy balance is solved for each element separately. As the outlet temperature of the heat exchanger is initially unknown, the heat transfer rate of the heat exchanger is solved iteratively until the outlet temperature matches the convergence criterion.

At each time step, the change in the internal energy in each tank segment taking into account of all possible energy flows into and out of a node is illustrated in Fig. 8.1. An example of the node energy balance equation associated with all energy flows is given in Eqn. 8.2. In this equation, only certain terms are included in solving the energy balance for particular tank node. For example, heat transfer from the heat exchanger is only solved for the tank segments containing a heat exchanger. The auxiliary heat input from the electric heating element only occurs in the top portion of the tank to maintain the desired load temperature.

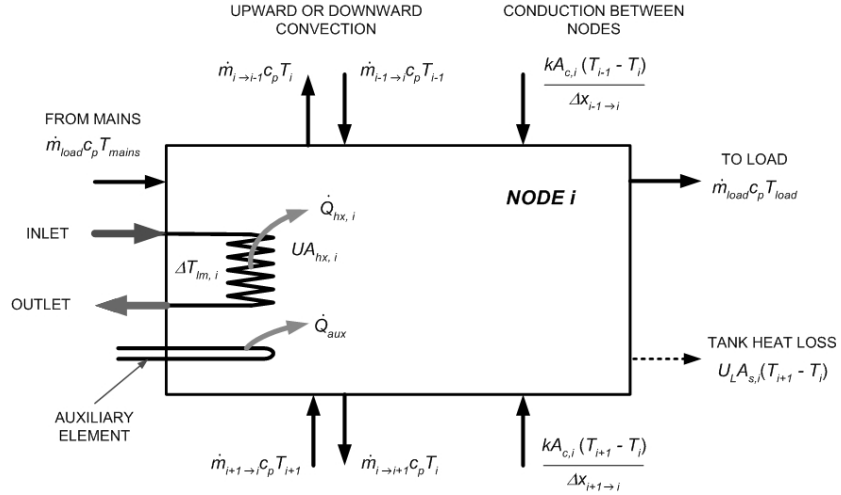


Fig. 8.1 Heat balance computation in each tank segment of the TYPE 60 TRNSYS model.

Net energy into node i = Conduction from adjacent nodes – Heat loss from the tank +
 Convection from adjacent nodes + Auxiliary energy input +
 Convection from load flow + Heat input across the heat
 exchanger

$$\begin{aligned}
 (M_i c_p) \frac{dT_i}{dt} = & \frac{kA_{c,i}}{\Delta x_{i+1 \rightarrow i}} (T_{i+1} - T_i) + \frac{kA_{c,i}}{\Delta x_{i-1 \rightarrow i}} (T_{i-1} - T_i) - U_L A_{s,i} (T_i - T_a) + \\
 & \dot{m}_{i \rightarrow i-1} c_p T_i - \dot{m}_{i-1 \rightarrow i} c_p T_{i-1} + \dot{m}_{i+1 \rightarrow i} c_p T_{i+1} - \dot{m}_{i \rightarrow i+1} c_p T_i + \dot{Q}_{aux} + \\
 & \dot{m}_{load} c_p T_{mains} + \dot{m}_{load} c_p T_{load} + UA_{hx} \Delta T_{lm,i}
 \end{aligned} \quad (8.2)$$

8.3.2 Modifications of TYPE 60 model and verification

In this study, the standard TRNSYS TYPE 60 tank model described in Section 8.3.1 has been modified to model a mantle heat exchanger and a falling film heat exchanger for use in pumped circulation solar water heaters. The convective heat transfer correlations for the inside and outside of the heat exchanger in the TYPE 60 routine were modified to implement the new non-dimensional heat transfer correlations developed in this thesis for both mantle heat exchanger and falling film heat exchanger. The well-established TYPE 60 routine for modelling tank stratification is retained. The modified models are verified by comparing predicted performance with measured performance.

8.3.2.1 Mantle heat exchanger model

Fig. 8.2a shows a sketch of a one-dimensional mantle-tank model. The storage tank was divided into multiple equal height elements with the mantle elements and the tank wall divided at the same height as the tank elements. On the mantle side, control volumes of each node in the mantle are not used due to the very low mass of fluid in the collector loop side. The convective heat transfer coefficient is estimated from the non-dimensional correlation (Eqn. 6.14). A thermal resistance circuit representing the heat transfer in each tank node containing a heat exchanger in the model is shown in Fig. 8.2b.

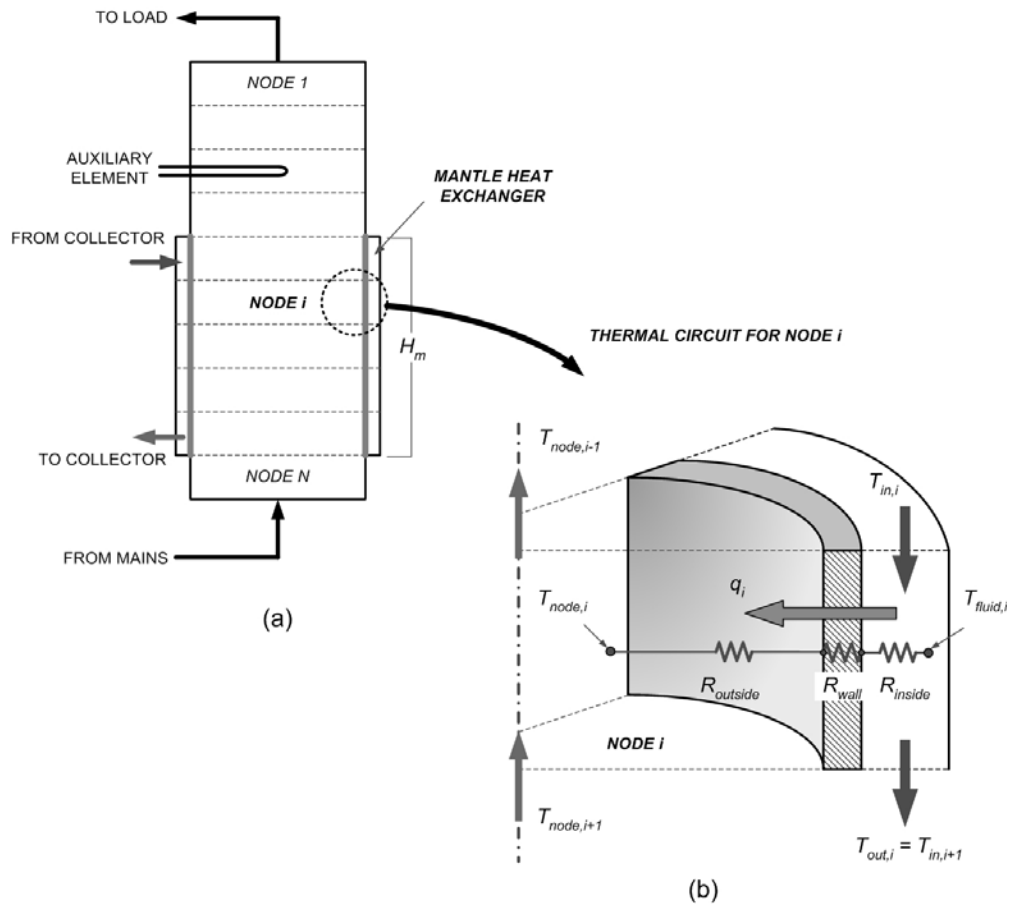


Fig. 8.2 (a) Schematic of one-dimensional model of a mantle heat exchanger, (b) thermal circuit diagram of a tank element.

In each tank node, the heat transfer in the heat exchanger element is defined as:

$$\dot{Q}_{hx,i} = UA_{hx,i} \Delta T_{lm,i} \quad (8.3)$$

To compute the heat transfer, the overall UA_{hx} value associated with the heat transfer resistances across the heat exchanger needs to be determined as follows:

$$\frac{1}{UA_{hx,i}} = R_{inside,i} + R_{wall,i} + R_{outside,i} \quad (8.4)$$

The convection resistance (R_{inside}) inside the mantle heat exchanger is calculated using the following equation:

$$R_{inside,i} = \frac{1}{h_{inside,i} A_i} = \frac{kNu_{inside}}{d_h A_i} \quad (8.5)$$

where $Nu_{inside} = 0.08 Re_d^{0.65} Pr^{0.33}$

The overall thermal resistance of the solid wall is given by:

$$R_{wall,i} = \frac{t_w}{k_{wall} A_i} \quad (8.6)$$

The convection resistance for the natural convection on the outside of the mantle heat exchanger on the tank side ($R_{outside}$) is computed as:

$$R_{outside,i} = \frac{1}{h_{outside,i} A_o} = \frac{kNu_{outside}}{H_m A_o} \quad (8.7)$$

where $Nu_{outside} = 0.1 Ra^{1/3}$

Tank temperature stratification

To examine the accuracy of the one-dimensional heat transfer model of the mantle heat exchanger, tank temperature stratification predicted by the TRNSYS model and measured from experiments were compared for heat up cycles from cold start and preheated tank with a flow rate of 2 L/min. In TRNSYS simulations, the tank was initialised at the measured temperature profile and the mantle inlet temperature and flow rate from the indoor experiments were specified as inputs to the TRNSYS model.

Fig. 8.3 shows a comparison of the simulated and measured temperature profiles for a cold start test. The standard stratified TRNSYS tank routine predicts less tank stratification. At the beginning of the heating process, some discrepancies can be observed in the tank adjacent to the bottom half of the mantle. This could be attributed to the mixing algorithm in TRNSYS where the fluid is mixed with the nodes above or below until any temperature inversion is eliminated. As the heating progresses, reasonable agreement between the simulated and measured data was obtained with all the simulation results slightly under-estimate at the top and over-estimate at the bottom of the tank compared to the experimental data. In reality, the buoyancy induced boundary layer flows penetrate along the tank wall and transfer heat to its equilibrium level, resulting in promotion of thermal stratification in the storage tank. This phenomenon is not accounted for in the standard TRNSYS TYPE 60 stratified tank routine. Although auto temperature seek mode is available for direct systems in TRNSYS to predict tank stratification, the routine is not implemented in modelling the stratification in a closed tank enclosure without direct mixing from the collector loop.

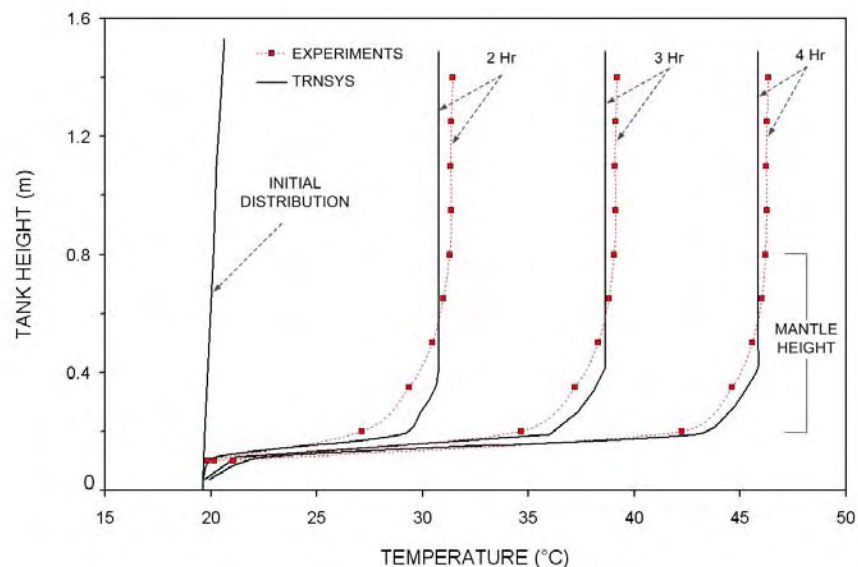


Fig. 8.3 Comparison of measured and simulated temperature distributions in the tank for a heat-cycle from a cold start with a flow rate of 2 L/min.

The comparison between the simulation results and experiments for an initially stratified tank is presented in Fig. 8.4. For this heating case, good comparison is evident with the undisturbed preheated top section of the tank and similar temperature

profile over the depth of the mantle to the experiments. Discrepancies can be noticed when mixing occurs between the hot layer and its adjacent layer. This complicated mixing phenomena is not accounted for in the TRNSYS model.

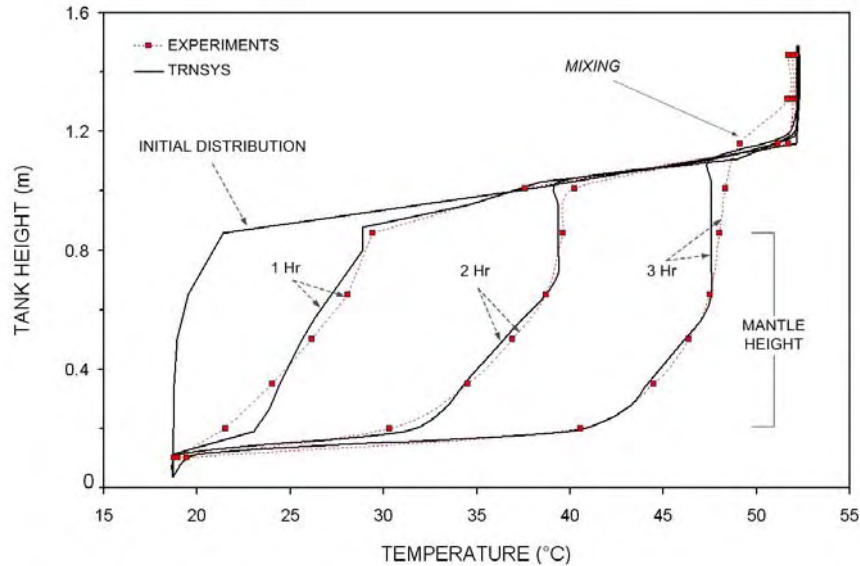


Fig. 8.4 Comparison of measured and simulated temperature distributions in the tank for a heat-up cycle from an initially stratified condition with a flow rate of 2 L/min.

8.3.2.2 Falling film heat exchanger model

This section describes the one-dimensional heat transfer model for a falling film tank, other components of the system such as advanced switching controller are presented in Section 8.4.2. Fig. 8.5a illustrates the falling film tank model in which the storage tank is divided into multiple equal height elements. The corresponding thermal resistance circuit representing the heat transfer for each tank node containing a heat exchanger is shown in Fig. 8.5b. In each tank node, the procedures for determining the heat transfer in the falling film heat exchanger are the same as for the mantle heat exchanger model defined in Eqns. 8.3-8.7. The only difference between the mantle heat exchanger and falling film heat exchanger models is the implementation of different heat transfer correlations on either side of the heat exchanger surface (Eqn. 8.4) and modelling the thermal capacitance of the pool of fluid in the bottom of the falling film tube.

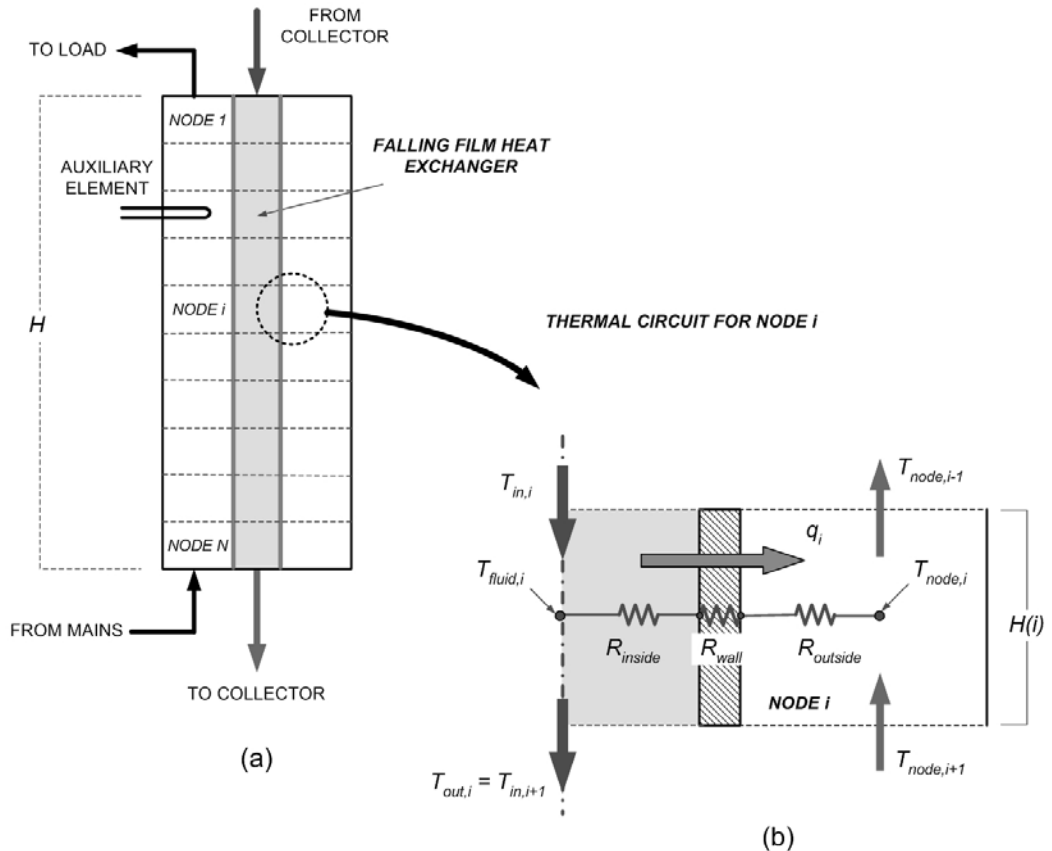


Fig. 8.5 (a) Schematic of one-dimensional model of a falling film heat exchanger, (b) thermal circuit diagram of a tank element.

The heat transfer from the collector fluid to the tank contents takes place in two sections of the falling film tube. Most of the heat is transferred from the thin liquid film to the tank (tank height from 0.2 to 1.2 m) while a small amount of heat is transferred from the pool of liquid in the bottom 200 mm depth. A pool of fluid must be retained in the bottom of the falling film tube to avoid pump cavitation. Two heat exchanger models were used in the TRNSYS TYPE 60 stratified tank routine to represent the film heating and pool heating in the bottom of the tube (Fig. 8.6). The heat transfer from the falling film is modelled on the basis of the non-dimensional correlation of the experimental measurements implemented into TYPE 60 routine. Heat transfer from the pool at the bottom of the tube is modelled using a TYPE 4 mixed tank routine coupled to a second heat exchanger. The outlet of the first heat exchanger model (falling film heating) is the heat source for the TYPE 4 tank model while the load from the TYPE 4 model is circulated to the second heat exchanger in the storage tank model. The volume of the TYPE 4 tank is used to model the thermal capacitance of the pool.

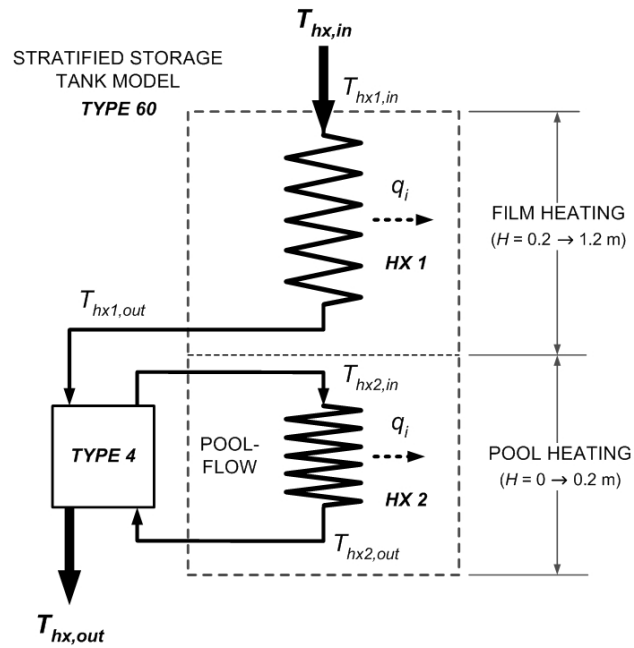
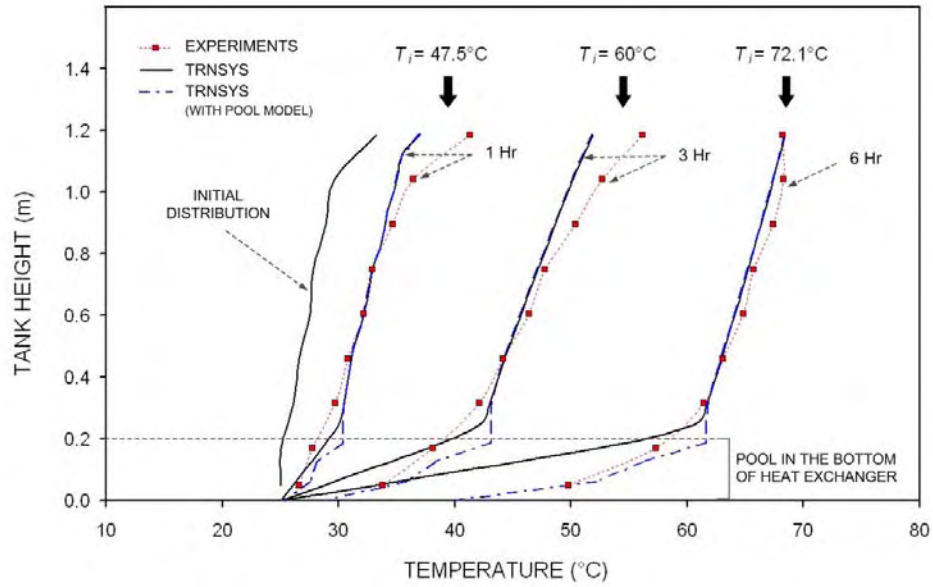


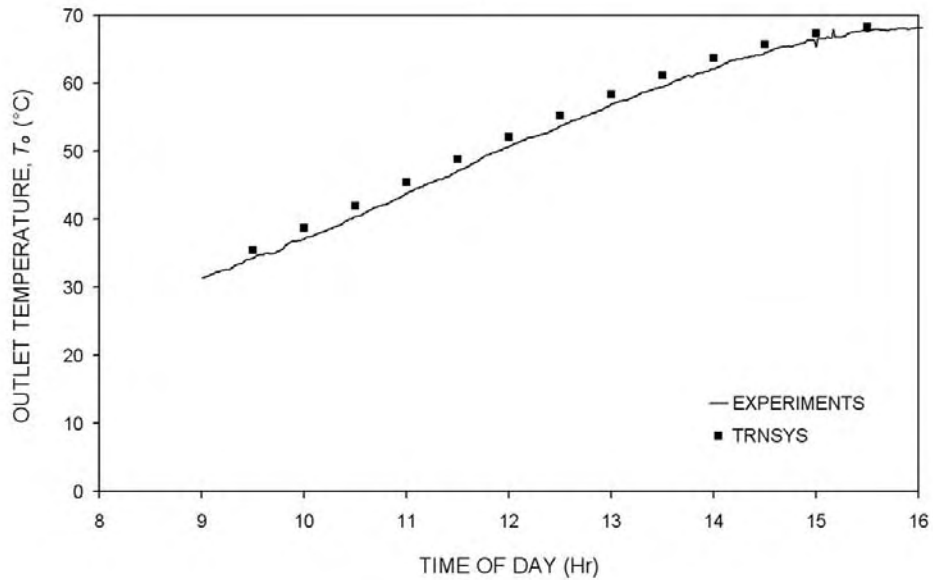
Fig. 8.6 Falling film heat exchanger model.

Tank temperature stratification

The accuracy of the one-dimensional heat transfer model of the falling film heat exchanger was examined to determine if heat exchanger model is able to predict the formation of thermal stratification in the tank. A comparison of tank temperature stratification between measurements and predictions of the falling film heat exchanger model with or without pool heating in the tube bottom is shown in Fig. 8.7a for heat up cycles from cold start with a constant flow rate of 2.6 L/min. In TRNSYS simulations, the tank was initialised at the cold start measured temperature profile, and the inlet temperature and flow rate on the hot side of the heat exchanger from experiments were specified as inputs to the TRNSYS simulations. As seen in Fig. 8.7a, the temperature distributions in the tank predicted from both falling film heat exchanger models are in good agreement with the experiments throughout the heat up cycle. During the initial stages of the simulation, the falling film model tends to underestimate the measured tank top temperature. The higher tank top temperature in the experiments was probably due to jet impingement of the inlet flow onto the tube wall. The heat exchanger model with the TYPE 4 mixed tank and secondary heat exchanger in the depth of the pool in the bottom of the heat exchanger has good agreement with measured temperature conditions in the bottom of the tank.



(a)

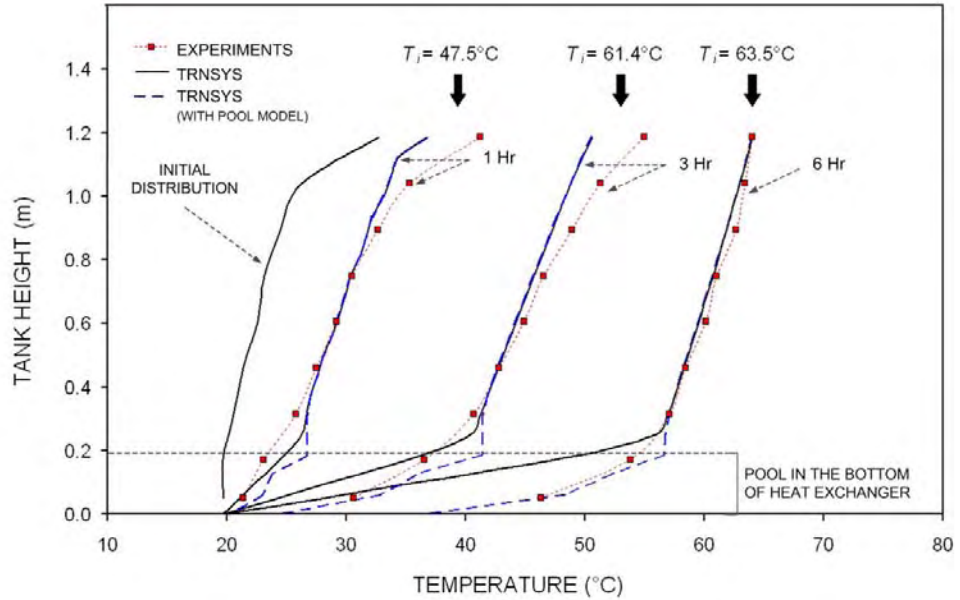


(b)

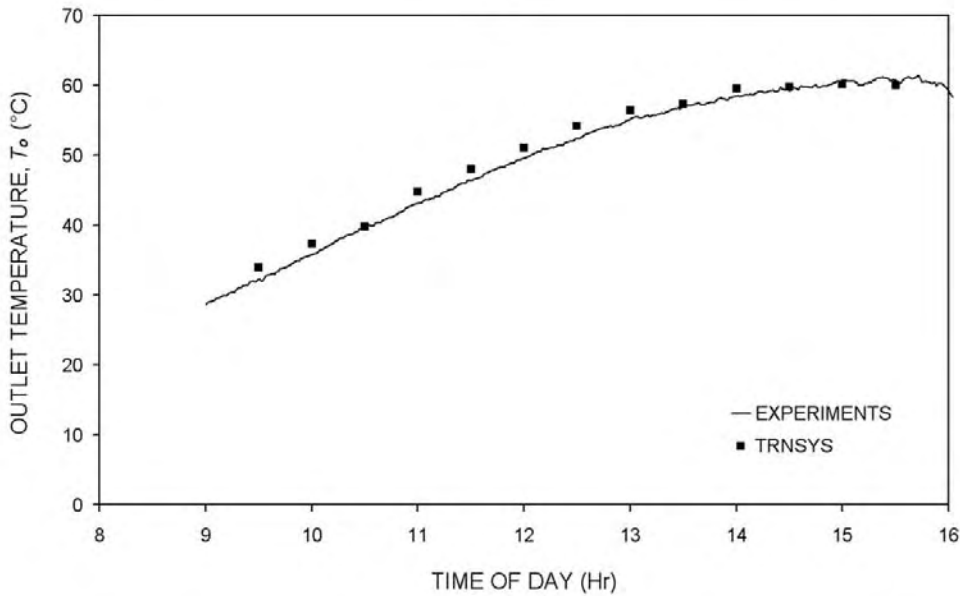
Fig. 8.7 Comparison of measured and simulated temperatures for a falling film heat exchanger operated from a cold start with a constant flow rate of 2.6 L/min, (a) temperature distribution in the tank, (b) heat exchanger outlet temperature.

Fig. 8.8a shows a comparison of tank temperature stratification between the outdoor measurements and predictions from the falling film heat exchanger model with and without the pool fluid heat exchanger in the tube bottom for heat up cycles with varying heat exchanger inlet flow rate. In the simulations, the measured flow rates were

specified as inputs to the heat exchanger models. Good agreement in tank thermal stratification between the TRNSYS predictions and measurements is observed in Fig. 8.8a. During the initial stages of the simulation, the falling film models underestimate the tank top temperature as found in Fig. 8.7a.



(a)



(b)

Fig. 8.8 Comparison of measured and simulated temperatures for a falling film heat exchanger operated from a cold start with varying collector flow rate modulated by a switching controller, (a) temperature distribution in the tank, (b) heat exchanger outlet temperature.

8.4 COMPLETE SOLAR WATER HEATER MODELS

The good agreement between the experimental and TRNSYS results has confirmed the validity of the one-dimensional heat transfer models for both the mantle heat exchanger and the falling film heat exchanger to predict tank stratification. In this section, complete TRNSYS system models for both heat exchangers are developed and descriptions of each major component are presented.

8.4.1 Solar water heater with a mantle heat exchanger

Fig. 8.9 shows a schematic diagram of a complete solar domestic water heater model incorporating a mantle-tank (modified TYPE 60) with an in-tank auxiliary heating element located above the mantle. The storage tank model is divided into 20 equal-volume elements with the mantle elements divided at the same height as the tank elements. During daytime, the solar thermal energy gained in the collector array is determined based on the collector efficiency correlation and weather data. The heat transfer rate across the heat exchanger is predicted using the empirical correlations and tank temperature stratification is computed by solving the energy balance equation for each node for each time step as detailed in Section 8.3.1. When the heat exchanger does not supply enough energy to the tank to maintain the load set temperature, the electric auxiliary element located above the mantle is turned on. The circulation pump is modelled using a TYPE 3 routine together with a standard on/off differential controller model (TYPE 2) to control the fluid flow through the solar collector loop depending on the collector outlet and heat exchanger outlet temperature. In typical solar water heater applications, hot water in the top portion of the tank is drawn off to the domestic load and the replacement water from mains enters to the bottom of the tank simultaneously. In the TRNSYS simulation, representative load patterns specified in AS4234 are used.

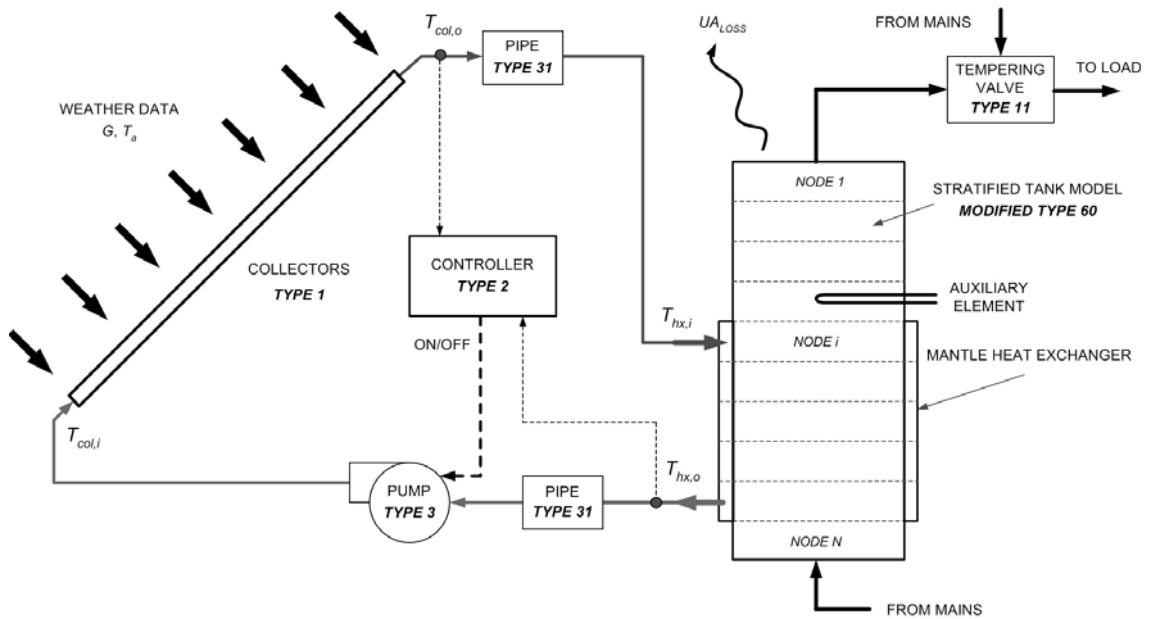


Fig. 8.9 Schematic of a TRNSYS model for a solar water heating system with a mantle heat exchanger.

8.4.2 Falling film system with an advanced controller

As mentioned in Chapter 7, a programmed switching controller is used to modulate the collector flow rate to ensure a high collector return temperature relative to the top of the tank, so that thermal stratification in the tank can be maintained. If the energy available in the collector loop does not meet the following requirements:

- Temperature difference of 6 K between the collector return and the top of the tank (ΔT_{start}) or,
- Temperature rise across the collector loop less than 10 K (ΔT_{rise}),

all collector fluid is drained back to the falling film tube. At the same time, the non-filled steel collectors are heated up under stagnation conditions and store the energy in the collector mass until the circulation pump is turned on again. A TRNSYS model for the complete falling film system with a collector flow rate controller and with an in-tank auxiliary heating element located above the top half of the tank was developed as illustrated in Fig. 8.10.

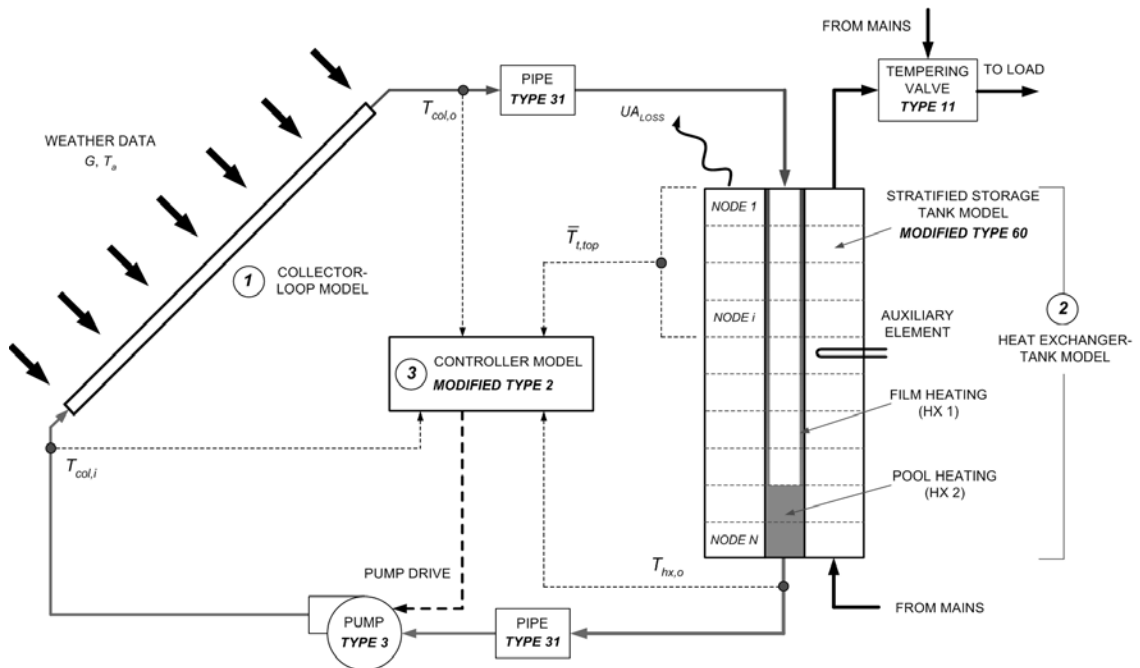


Fig. 8.10 Schematic of a TRNSYS model for a solar water heating system with a falling film heat exchanger.

Collector loop model

The standard TRNSYS TYPE 1 collector routine does not include the thermal mass of the collector and hence cannot model the energy stored in the collector during stagnation periods. The high mass steel flat-plate collectors used in this system store energy even under weak radiation conditions. To model the collector thermal mass, a TYPE 4 mixed tank model was coupled in parallel with the TYPE 1 collector model as shown in Fig. 8.11. The volume of the mixed tank in the TYPE 4 routine is equal to the collector thermal mass. A constant loop flow is maintained between the zero mass collector model and the zero heat loss tank model. When the pump is off, the energy gained from the TYPE 1 routine is stored in the TYPE 4 routine. This energy is accounted for in the computations when the pump is turned on again. This consideration of a zero mass collector model coupled to a zero loss tank is able to model both energy stored during the day when the pump turns off and the start-up and shut down energy losses at the start and end of the day.

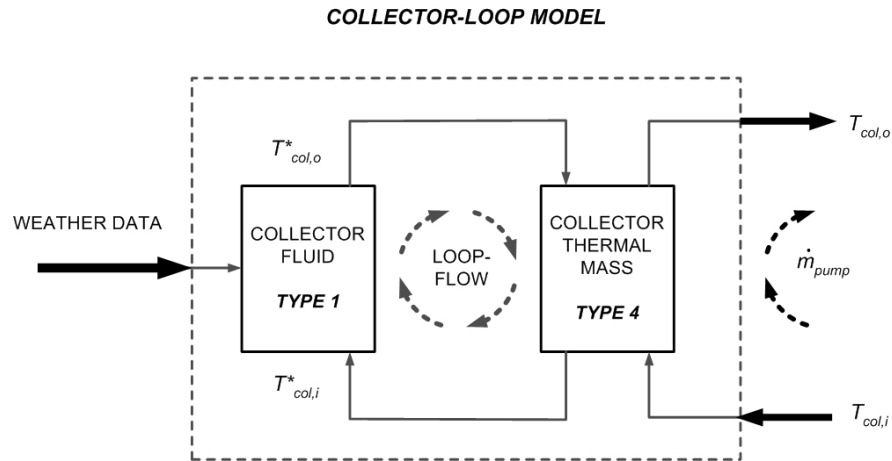


Fig. 8.11 Solar collector model accounting for collector thermal mass.

Heat exchanger and tank model

The heat transfer from the collector fluid to the tank contents takes place in two sections of the falling film tube:

- Falling film heating (above 0.2 m from the tube bottom),
- Pool heating (below 0.2 m in the tube).

Details of the falling film model were given in Section 8.3.2.2. The storage tank model (modified TYPE 60) is divided into 40 equal-volume elements with two heat exchanger models. The first heat exchanger model consists of heat transfer prediction from the thin liquid film to the tank using the empirical heat transfer correlations developed in this project. In the second heat exchanger model, the pool heating of the fluid in the 200 mm depth at the bottom of the falling film tube is accounted for by coupling a TYPE 4 mixed tank routine and a heat exchanger tube.

Advanced switching controller model

The majority of pumped systems use an on/off differential controller to control the fluid flow through the solar collector loop depending on the collector outlet and tank bottom temperatures. This conventional controller strategy can be modelled using standard TYPE 2 routine. For advanced switching controller strategy applied in falling film systems, the collector flow rate has to be modulated by the controller so that a fixed temperature rise across the collectors can be maintained. In this study, several

additional operating conditions for the advanced controller were included in a new controller routine. This controller generates an output control function γ_o that represents on or off by state values of ‘1’ or ‘0’ respectively. The new γ_o value is a function of the inputs 1 to 7. Limits to inputs 2, 3 and 7 are set by parameter 4, 2 and 3 respectively. The difference between the collector return temperature (input 1) and tank top temperature (input 7) is controlled in dead band ranges set by input 5 (upper limit) and input 6 (lower limit). For the standard TYPE 2 routine, the differential is taken between inputs 1 and 2 rather than inputs 1 and 7 as in the modified TYPE 2 routine.

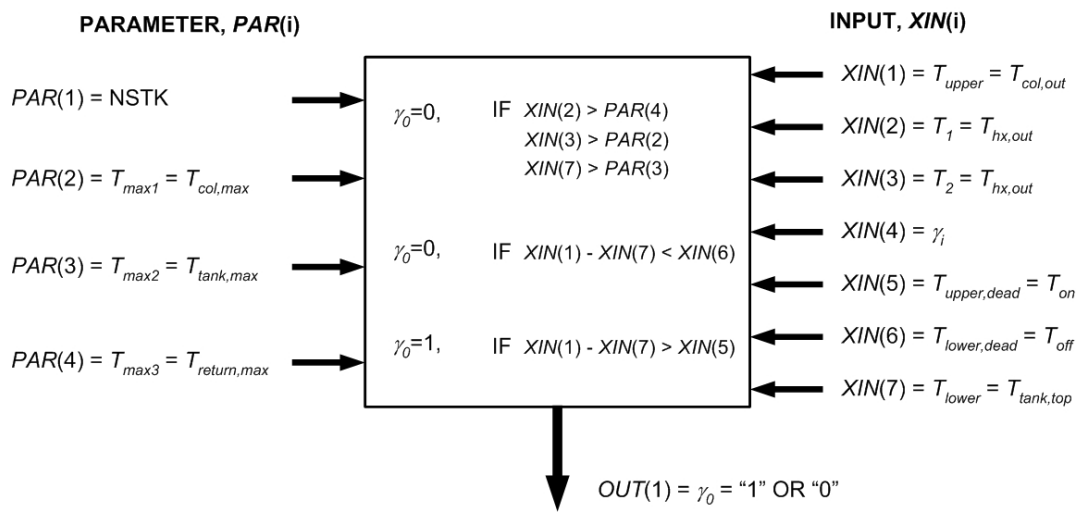


Fig. 8.12 Parameter setup for the modified TYPE 2.

Other components

When the heat exchanger does not supply enough energy to the tank to maintain the load set temperature, the electric auxiliary element located at the mid tank is turned on. An instantaneous gas booster model can also be modelled as the auxiliary source in the falling film model. The circulation pump is modelled using TYPE 3 routine together with the modified differential controller model to control the fluid flow through the solar collector loop depending on the collector outlet and heat exchanger outlet temperature. The varying collector flow rates are calculated based on the solar input and fixed temperature rise across the collector ($\Delta T_{rise} \sim 10$ K). Hot water drawn from the top portion of the tank to the domestic load is also modelled in the TRNSYS model based on daily and seasonal load conditions as specified in AS4234.

8.5 LOAD CYCLE SIMULATIONS

The long-term performance of pumped-circulation solar water heaters with the following configurations is evaluated:

- 1) Single mantle-tank system with in-tank electric boost,
- 2) Single falling film-tank system with in-tank electric boost,
- 3) Falling film system as a solar pre-heater in series with an instantaneous gas heater.

The predicted long-term performance is compared to that of a system with direct circulation from the collector to the storage tank (benchmark case). In all simulations, a typical 3.6 m² flat plate collector is modelled at 20° roof inclination facing north and coupled to a vertical-tank with 270L storage volume. The single-tank systems have an in-tank electric booster positioned at the mid-height of the tank. For systems operating as a solar pre-heater, the storage tank is coupled in series with an instantaneous gas heater. The main parameters used in the TRNSYS modelling are listed in Table 8.1 and Table 8.2.

Table 8.1 Solar collector parameters.

COLLECTOR	
Area (m ²)	3.6
Efficiency (High quality selective surface collector) <i>For mantle system</i>	$\eta = 0.804 - 4.6 \frac{(\bar{T} - T_a)}{G} - 0.0098 \frac{(\bar{T} - T_a)^2}{G}$
Efficiency (Steel collector) <i>For falling film system</i>	$\eta = 0.842 - 4.539 \frac{(\bar{T} - T_a)}{G} - 0.01337 \frac{(\bar{T} - T_a)^2}{G}$
Inclination angle	20°
Incident angle modifier, $K_{\tau} = 1 - b \left(\frac{1}{\cos \theta} - 1 \right)$	$b = 0.06$

8. SYSTEM MODELLING

Table 8.2 Solar water heater parameters:

(a) Direct-couple tank (benchmark case)

Tank volume (L)	270
Tank diameter (m)	0.47
Tank heat loss UA_L (W/K)	2.85
Cold inlet	Tank bottom
Material	Stainless steel
Electric booster location	0.778 m from bottom of tank
Thermostat location	0.878 m from bottom of tank
Collector return	0.728 m from bottom of tank
Solar pump stop temperature difference (K)	$T_{col,o} - T_{hx,o} < 2$

(b) Single mantle-tank

Tank volume (L)	270
Tank diameter (m)	0.47
Tank heat loss UA_L (W/K)	2.85
Cold inlet	Tank bottom
Material	Stainless steel
Wall thickness (m)	0.0016
Mantle spacing (m)	0.003
Mantle height (m)	0.658
Heat transfer area (m ²)	0.903
Working fluid	20% Propylene glycol/water mixture
Electric booster location	0.893 m from bottom of tank
Thermostat location	0.993 m from bottom of tank
Solar pump stop temperature difference (K)	$T_{col,o} - T_{hx,o} < 2$

8. SYSTEM MODELLING

(c) Single falling film-tank

Tank volume (L)	270
Tank height (m)	1.21
Tank heat loss UA_L (W/K)	3.65
Cold inlet	Tank bottom
Material	Carbon steel
Wall thickness (m)	0.003
Falling film tube inner diameter (m)	0.197
Falling film tube height (m)	1.21
Working fluid	20% Propylene glycol/water mixture
Electric booster location	0.731 m from bottom of tank
Thermostat location	0.831 m from bottom of tank
Solar pump stop temperature difference (K)	Refer to Fig. 3.14

To evaluate performance under different climatic conditions, the simulations in this chapter were modelled based on representative meteorological weather data for Sydney and Melbourne in Australia. The seasonal load patterns for both capital cities are specified in Australian Standard AS 4234 (1994) with peak winter energy delivery of 40 MJ/day in Sydney and 42 MJ/day in Melbourne. The hourly load pattern shown in Table 8.3 is used for the load-cycle simulations. The hourly load is the product of the peak load and seasonal and hourly load pattern factors.

Table 8.3 Hourly load pattern factor for annual performance assessment.

TIME	HOURLY LOAD PATTERN FACTOR
0700	0.15
0800	0.15
1100	0.10
1300	0.10
1500	0.125
1600	0.125
1700	0.125
1800	0.125

The performance of a single-tank solar water heater with in-tank electric boosting is assessed by comparing the monthly average solar contribution relative to a conventional electric water heater. The energy savings of the single-tank system were calculated as follows:

$$f_R = \frac{Aux_E - Aux_{S+E}}{Aux_E} = \frac{L + Q_{loss} - Aux_{S+E}}{L + Q_{loss}} \quad (8.8)$$

where: Aux_E is the energy consumption when a conventional water heating system is used,

Aux_{S+E} is the auxiliary energy consumption when a solar system is used,

L is the load energy (useful energy delivered),

Q_{loss} is the heat loss from a conventional water heating system.

The energy savings of a pre-heater in series with an instantaneous gas heater were calculated as follows:

$$f_R = \frac{Aux_G - Aux_{S+G}}{Aux_G} \quad (8.9)$$

where: Aux_G is the energy consumption when a standard instantaneous gas heater is used,

Aux_{S+G} is the amount of booster gas energy consumed when a solar pre-heater system is used in series with a gas booster.

8.6 LONG-TERM PERFORMANCE OF MANTLE HEAT EXCHANGER SOLAR WATER HEATERS

8.6.1 Comparison of different system configurations

Fig. 8.13 shows a comparison of auxiliary energy consumption between a pumped-circulation system incorporating a narrow gap mantle heat exchanger (3 mm mantle gap, 270 L tank) and a system with direct circulation between the collector and the storage tank (270 L) under representative weather data in Sydney Australia (latitude of -

34°). Both solar water heater models included an in-tank electric booster positioned above the top of the heat exchanger for the mantle-tank system and at the mid-height of the tank for the direct-coupled system. A typical collector flow rate of 2 L/min was used in the simulations. During the winter period in June, the monthly simulation results indicate that the mantle-tank system consumes 9% more auxiliary energy than a direct-coupled system with maximise thermal stratification. In Fig. 8.13, it can also be seen that the auxiliary energy consumption for a direct-coupled system increases if the storage tank is simulated using the fixed inlet option in standard stratified TYPE 60 routine. This is because the fixed inlet model is unable to simulate the maximal stratification in the tank when the inlet stream enters the tank as a mixing plume with fixed position.

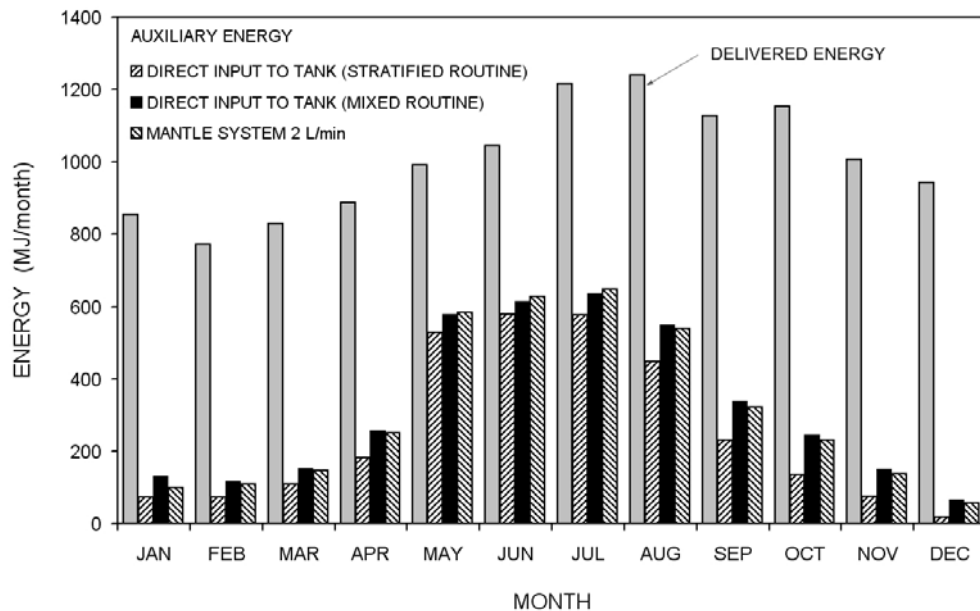


Fig. 8.13 Delivered energy and auxiliary energy of direct coupled and mantle heat exchanger solar water heaters in Sydney.

The monthly energy savings of a narrow-gap mantle system with an in-tank electric booster is compared to that of a direct-coupled system in Fig. 8.14. For the same collector flow rate of 2 L/min, the performance simulations show that the annual solar contribution for a standard domestic hot water demand in Sydney drops from 79% for a direct-coupled system to 73.3% for a system with a mantle heat exchanger in the collector loop. The decrease in system performance is due to the heat exchanger

penalty and reduced thermal stratification in the tank, however the loss of performance may be acceptable given the advantage of freeze protection that the mantle heat exchanger provides.

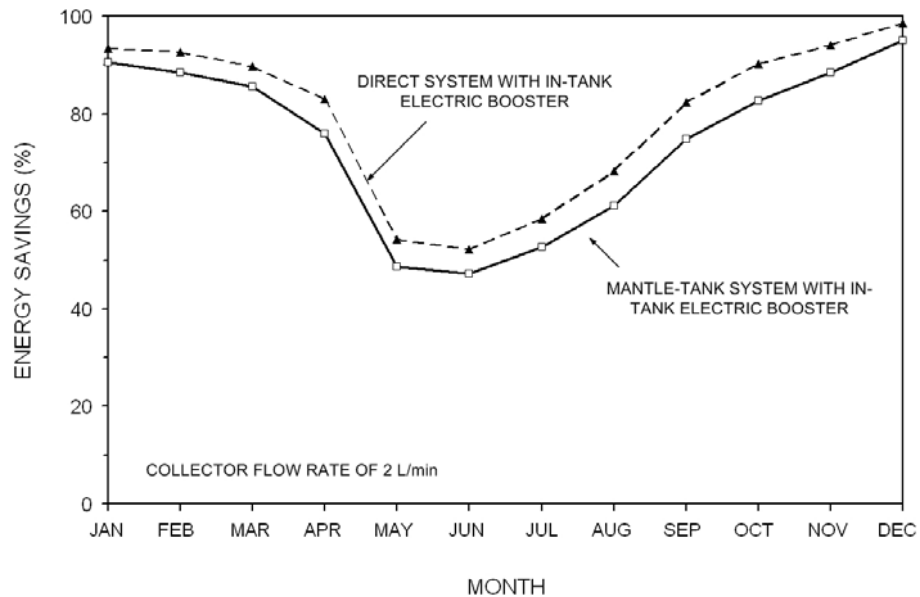


Fig. 8.14 Comparison of monthly energy savings of direct coupled and mantle heat exchanger solar water heaters in Sydney.

8.6.2 Effect of auxiliary element position

The long-term performance of three systems based on a narrow-gap mantle heat exchanger are simulated to evaluate possible interaction between the mantle heat exchanger and the position of the electrically heated layer above the mantle:

- The first system (base case system) consists of a mantle heat exchanger wrapped around the bottom half of the tank with the boost element located 50 mm above the mantle.
- The second system consists of a mantle wrapped around the bottom half of the tank with the boost element located in the tank at the level of the top of the mantle.
- The third system configuration considers a mantle heat exchanger extending over the full height of the storage tank, while retaining the position of the electric boost element in the tank as for the base case unit.

Comparing the monthly energy savings between systems 1 and 2, the simulation results in Fig. 8.15 show that the performance of a mantle heat exchanger can be slightly reduced if level of the boost element is lowered to the top of the mantle. For the mantle design covering the full tank height, a reduction of 12% in annual system performance (Fig. 8.15) is observed compared to a mantle located below the electric element. As the mantle top is located above the auxiliary heater, the mantle fluid will remove heat from the auxiliary heated part of the tank when the mantle inlet temperature is lower than the set temperature and hence decrease system performance. Therefore, mantle heat exchanger should not extend above the level of auxiliary heater.

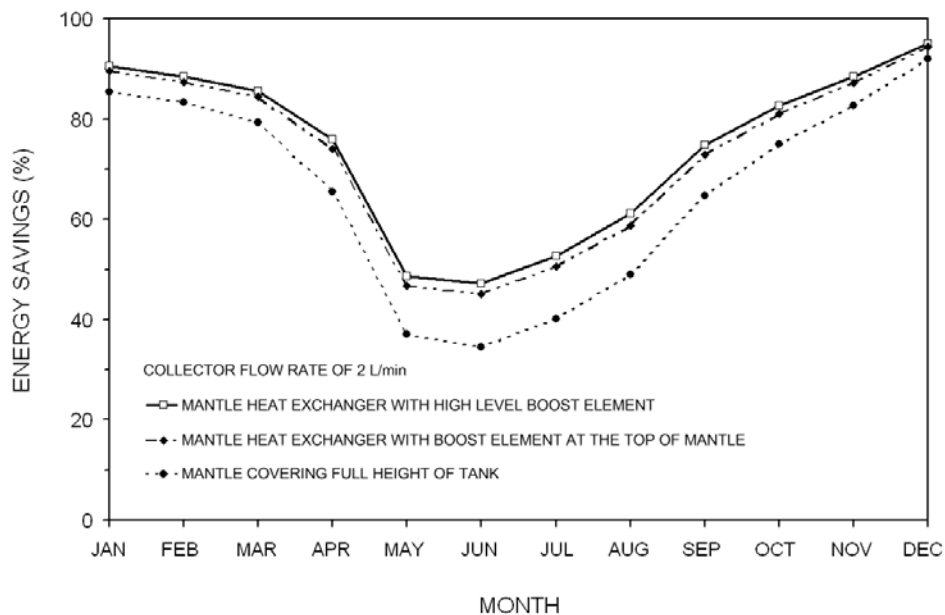


Fig. 8.15 Comparison of monthly energy savings of three mantle-tank systems based on different auxiliary element positions for operation in Sydney.

8.6.3 System size

Fig. 8.16 shows the long-term performance of a 270 L in-tank boost system with 2 collectors (base case system) and a 330 L system with 3 collectors for operation in Sydney. The 270 L system consists of a mantle heat transfer area of 0.903 m² while the 315 L system uses a larger mantle heat transfer area of 1.13 m². For a collector flow rate of 2 L/min, the annual solar contribution increases from 73.3% to 83.8% when the larger system is used.

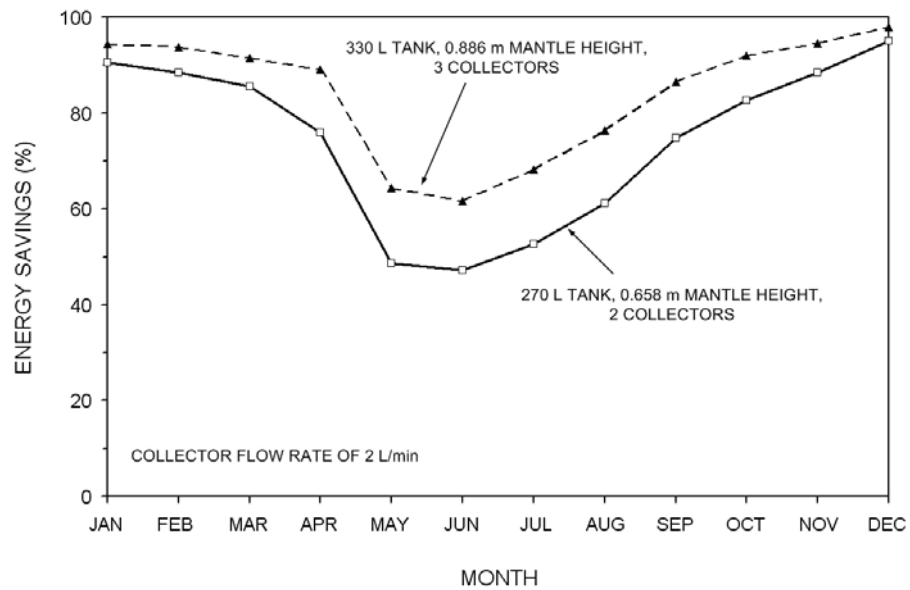


Fig. 8.16 Comparison of monthly energy savings of two mantle-tank system sizes in Sydney.

8.6.4 Comparison of performance in different climatic conditions

The long-term performance of a mantle-tank system operating in Melbourne (latitude of -38°) and Sydney (latitude of -34°) is shown in Fig. 8.17. The monthly energy savings during summer months is approximately 90% in both Sydney and Melbourne. During winter in June, the monthly energy saving in Sydney and Melbourne are 46.3% and 26% respectively due to the effect of in-tank electric boosting that reduces the solar preheat volume. As expected, the decrease in performance for systems installed in Melbourne is because of the relatively low solar irradiation level during winter in Melbourne and higher hot water demand. The performance simulation also shows that the annual energy saving for a direct-coupled system is approximately 8% higher than a mantle system in both Sydney and Melbourne.

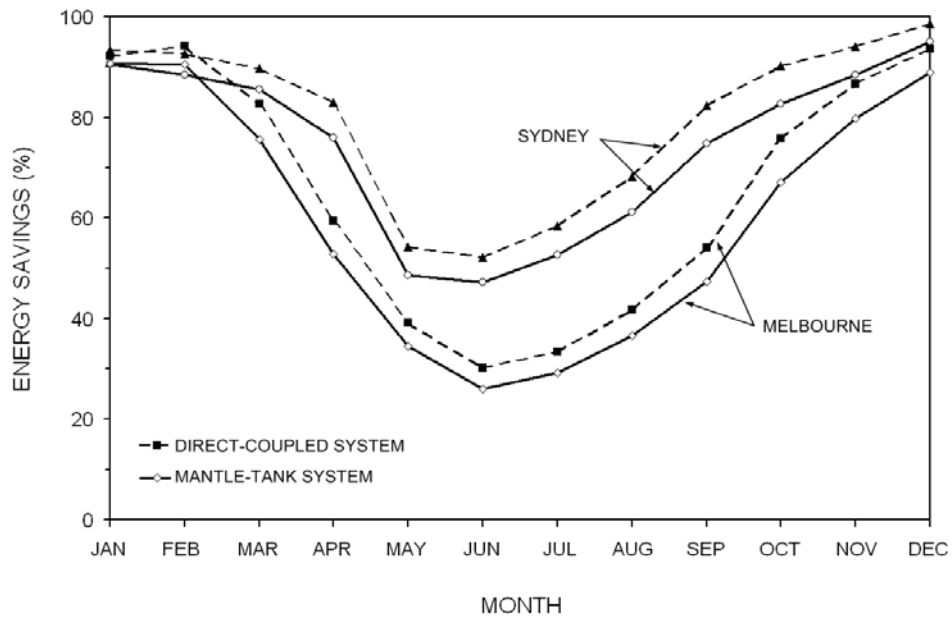


Fig. 8.17 Comparison of monthly energy savings of direct coupled and mantle heat exchanger solar water heaters in Sydney and Melbourne Australia.

8.7 LONG-TERM PERFORMANCE OF FALLING FILM SOLAR WATER HEATERS

8.7.1 Single-tank systems with in-tank boosting

In this section, the performance of a falling film system (270 L) with in-tank electric boosting (base case system) is compared to a typical direct-coupled system with in-tank boosting. The falling film system operates with a varying collector flow rate controlled by a switching controller depending on the collector temperature rise ($\Delta T_{rise} \sim 10\text{K}$) and tank temperature stratification ($\Delta T_{start} \sim 6\text{K}$). In the standard falling film tank, the collector return port is positioned at the top of the heat exchanger tube. The direct-coupled system (benchmark case) was simulated with a constant collector flow rate of 2 L/min and auto-peek inlet option was used in the simulation.

In Fig. 8.18, it can be seen that the monthly energy savings of a falling film tank system with in-tank electric boosting is lower than a direct-coupled system throughout the year. The performance simulations show that the annual solar contribution for a standard domestic hot water demand in Sydney drops from 79% for a direct-coupled system to

64% for a system with a falling film heat exchanger in the collector loop. During winter, the loss of performance for a falling film system with in-tank electric boosting is significant. When the falling film system operates under low solar radiation or transient cloudy sky conditions in winter, the circulation pump is frequently turned off due to insufficient available solar energy in the collector loop ($\Delta T_{rise} < 3\text{K}$). In such operation mode, the solar contribution for the system drops due to the switch from a solar-only system to an in-tank electric boosted system. The potable water in the auxiliary portion is heated by the in-tank electric booster. This would cause the collectors to operate at a higher temperature range as the system requires a high collector return temperature relative to the top of the tank to avoid de-stratification ($\Delta T_{start} \sim 6\text{K}$). The loss of performance may be acceptable given the cost advantage of the system as well as reliable freeze protection that the falling film heat exchanger provides.

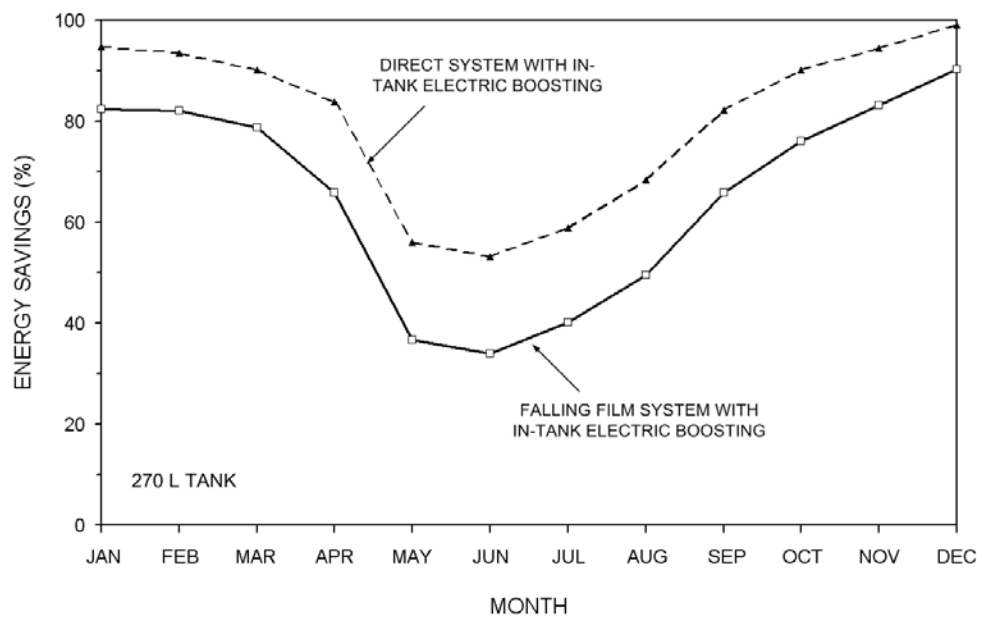


Fig. 8.18 Comparison of monthly energy savings of direct coupled and falling film solar water heaters with in-tank boosting in Sydney.

8.7.2 Solar pre-heater systems

The performance of a falling film system (270 L) with an in-line instantaneous gas heater was simulated for a standard domestic hot water demand in Sydney. In Fig. 8.19, it can be seen that a falling film tank system (270 L) with an in-line instantaneous gas heater performs better than the system with in-tank electric boosting during winter.

When the falling film tank is used as a solar pre-heater system, the auxiliary energy is supplied instantaneously to the load flow without reducing the solar storage volume. Improved thermal stratification in the storage tank as a result of removal of the in-tank booster could also improve the collector efficiency resulting in better system performance. As the instantaneous gas heater is usually expensive, a falling film system as a solar pre-heater with a smaller storage tank size (lower cost) may be an option to compensate for the cost of a gas booster if performance is not significantly reduced due to the use of the smaller tank. The performance simulations (Fig. 8.20) show that the annual solar contribution drops from 69% for the 270 L pre-heat tank to 65.3% for a 170 L pre-heat tank.

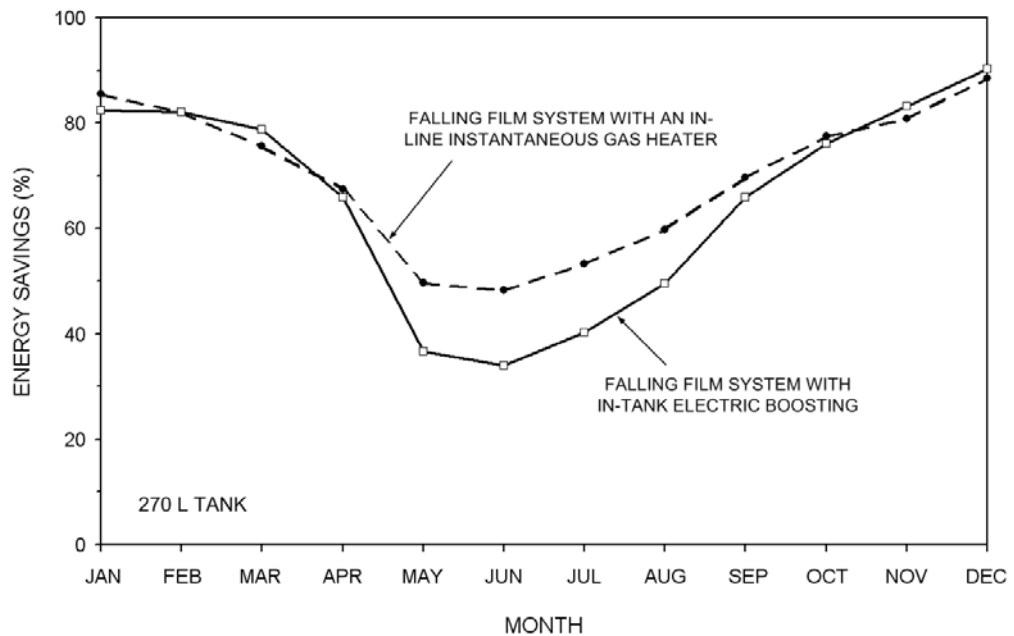


Fig. 8.19 Monthly energy savings of falling film solar water heaters with in-tank boosting or with an instantaneous gas heater in Sydney.

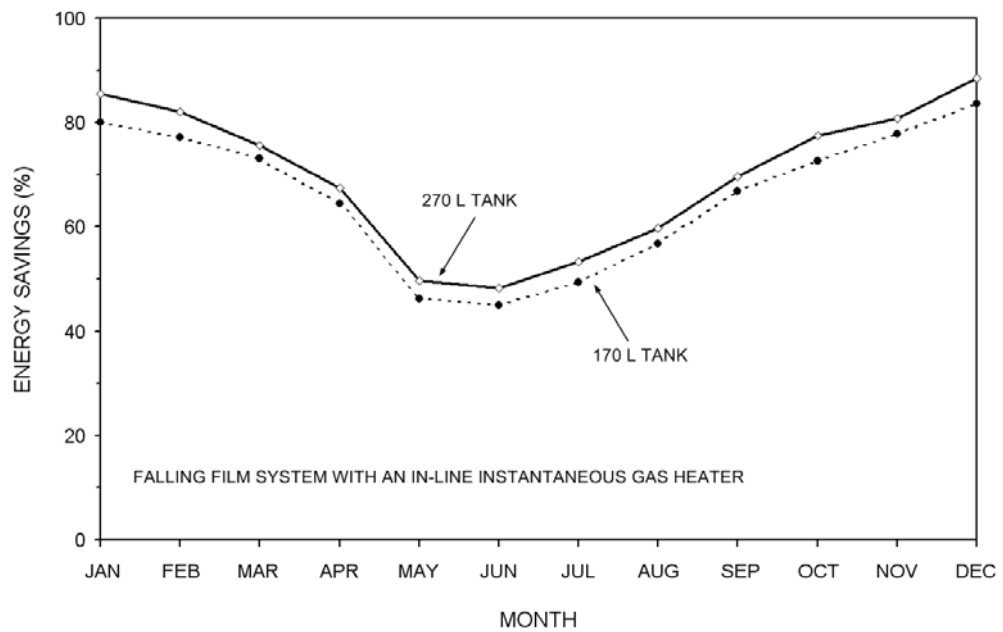


Fig. 8.20 Comparison of monthly energy savings of gas boosted falling film solar water heaters based on different heat exchanger sizes in Sydney.

8.7.3 Effect of advanced controller strategy

For a falling film system operating without a switching controller, the falling film heat exchanger transfers heat to all sections of the tank over the depth of the film established in the core tube. If the film is started at the top of the core tube, then heat may be extracted from the top of the tank while adding heat to the bottom of the tank. If an in-tank electric boosting element is used and located in the middle of the tank, the position of the film nozzles should ideally be set below the position of the electric element. As shown in Fig. 8.21, the simulated monthly energy savings of the falling film system (constant collector flow rate of 3 L/min, no advanced switching controller) for standard domestic hot water demand in Sydney are affected by the location of the film nozzles. The annual solar contribution of a falling film system with a top inlet but without a switching controller drops approximately 15% compared to a system with the film inlet located just below the auxiliary portion. This is primarily due to the fact that the cooler collector return fluid would degrade tank stratification when the falling film tube extends from the top to the bottom of the tank.

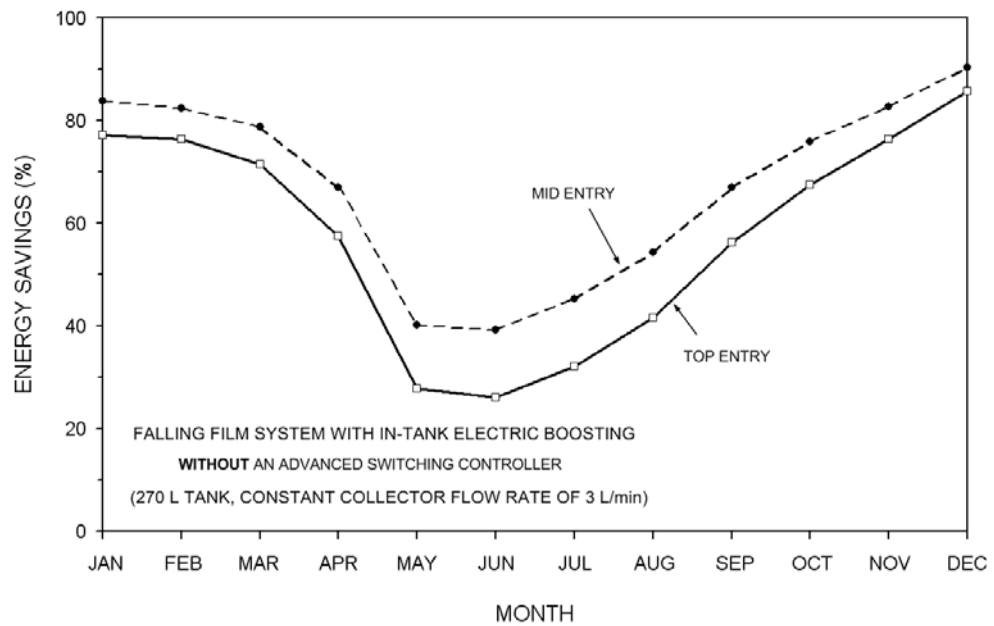


Fig. 8.21 Comparison of monthly energy savings of falling film solar water heaters with top or mid film nozzles positions operating without a collector flow rate controller in Sydney.

With the implementation of a switching controller that avoids tank de-stratification, the performance of a system with a top inlet configuration can be improved by 12% compared to a system without a switching controller (Fig. 8.22). In Fig. 8.23, the performance of two falling film systems with and without an advanced switching controller are compared. The film inlet for both systems is located just below the auxiliary portion, therefore de-stratification in the tank is eliminated. The simulation results show that there is insignificant influence of the advanced switching controller strategy for the system with mid-level-positioning of the falling film heat exchanger.

8. SYSTEM MODELLING

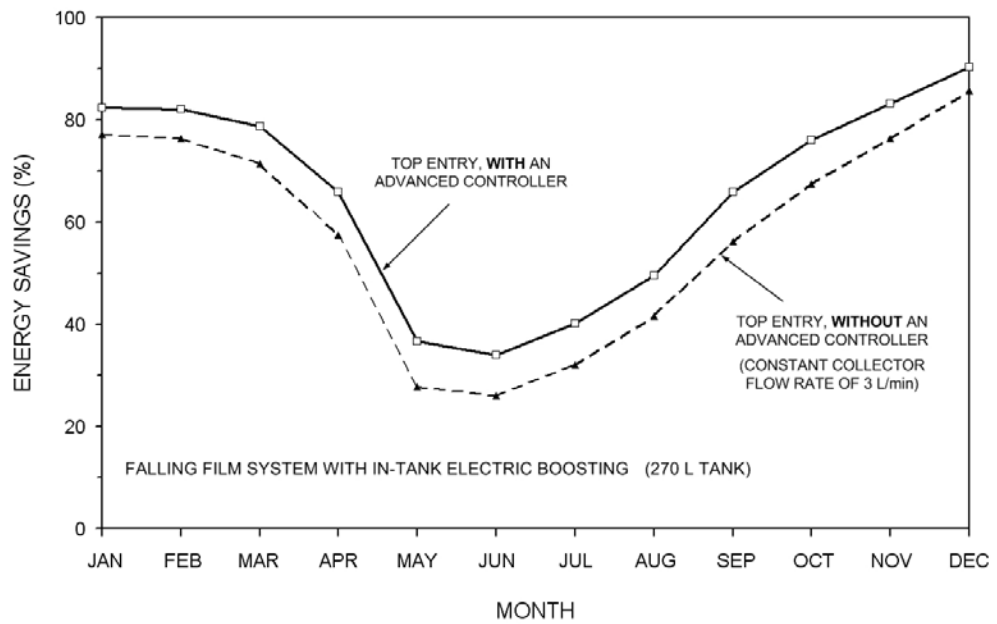


Fig. 8.22 Comparison of monthly energy savings of falling film solar water heaters for top entry operating with and without a collector flow rate controller in Sydney.

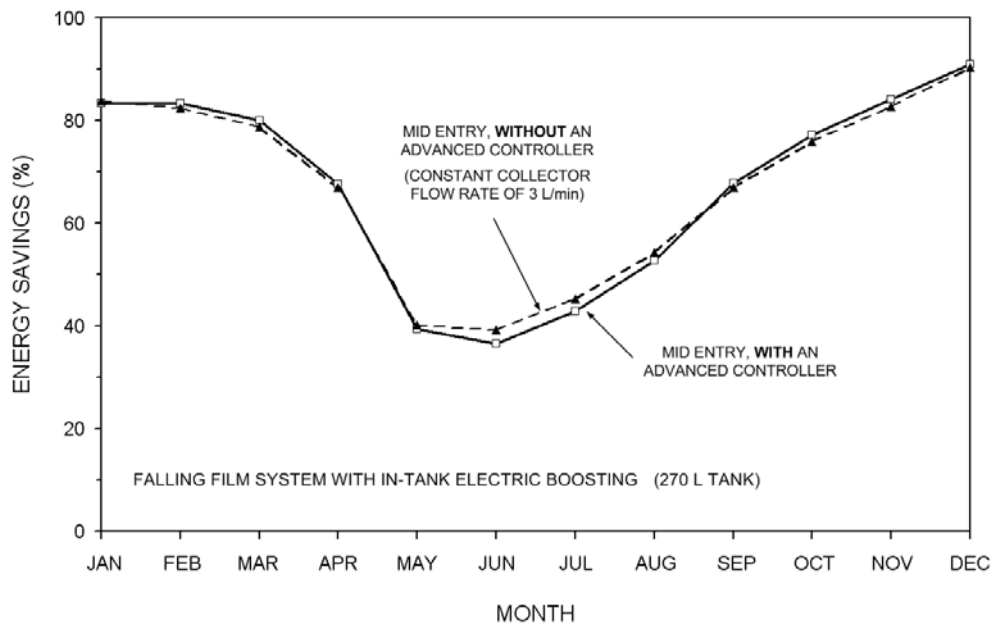


Fig. 8.23 Comparison of monthly energy savings of falling film solar water heaters for mid entry operating with and without a collector flow rate controller in Sydney.

8.7.4 Comparison of performance in different climatic conditions

The long-term performance of a falling film system either with in-tank boosting or in series with an instantaneous gas booster for operation in Melbourne (latitude of -38°) and Sydney (latitude of -34°) are shown in Fig. 8.24 and Fig. 8.25 respectively. For a falling film system with in-tank boosting operates in Sydney and Melbourne, the monthly energy savings in summer is approximately 80%. During the winter (May to July), the average monthly saving in Sydney is 37%, while in Melbourne the winter saving is only 15% due to the low solar radiation conditions and higher hot water demand.

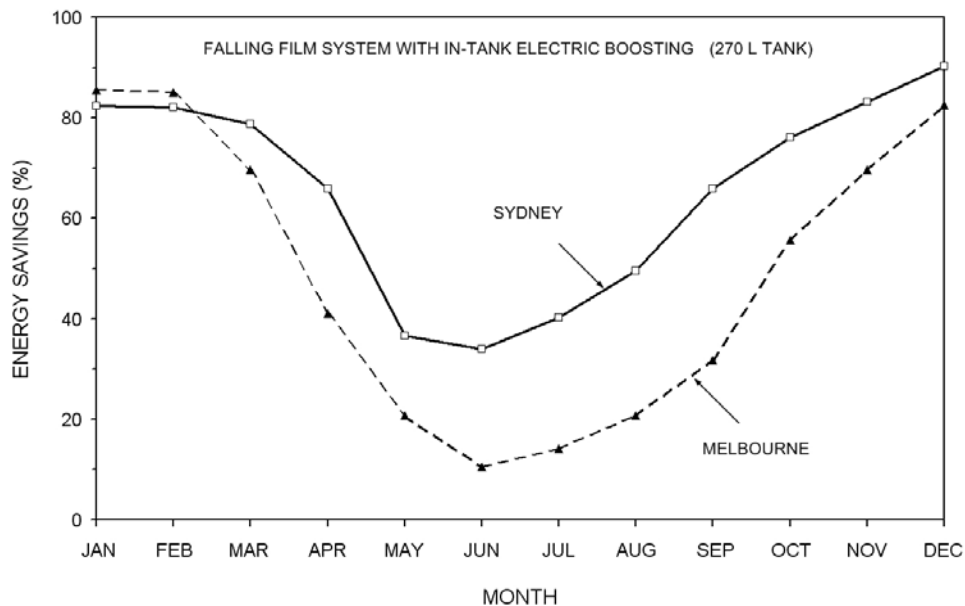


Fig. 8.24 Comparison of monthly energy savings of falling film solar water heaters with in-tank boosting in Sydney and Melbourne Australia.

For a falling film system in series with an instantaneous gas heater operates in Sydney or Melbourne, the monthly energy savings in summer is approximately 80%. During winter (May to July), the average monthly saving in Sydney is 50%, while in Melbourne it is 33%. Compared to the base case in-tank boosting system, the pre-heat tank falling film system performs substantially 47% better during the winter.

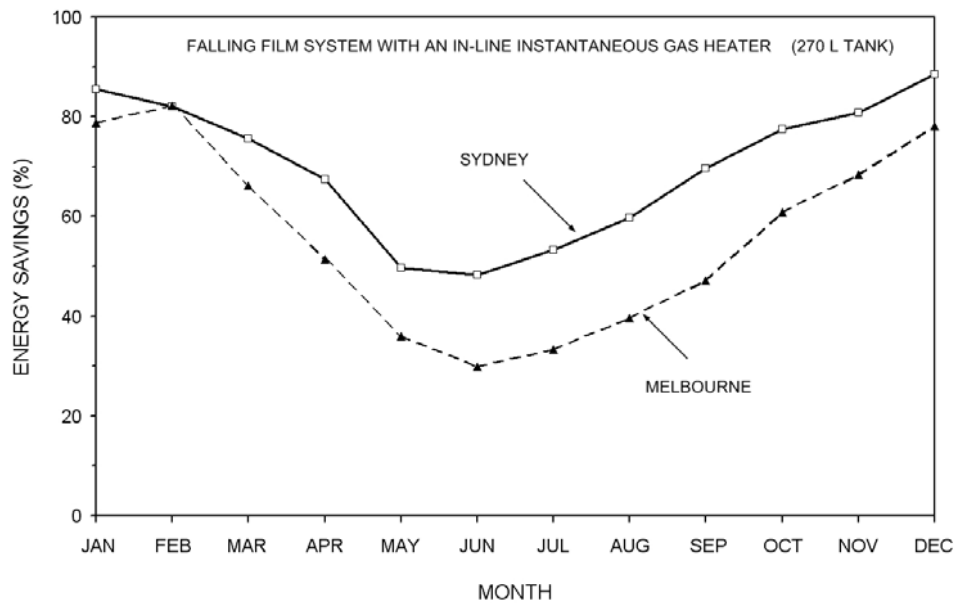


Fig. 8.25 Comparison of monthly energy savings of falling film solar water heaters with an instantaneous gas heater in Sydney and Melbourne Australia.

8.7.5 Effect of film wettability

Based on the visual evaluation presented in Chapter 7, the film in the prototype system evaluated in this study only covered approximately half of the inner surface of the heat exchanger tube. In this section, the influence of film wettability on the long-term performance of a falling film system is examined using TRNSYS simulations. The performance simulations show that the annual solar contribution for a standard domestic hot water demand in Sydney slightly increases from 64% for a half wetted falling film system to 65% for a fully wetted falling film system. The negligible influence of the film wettability on system performance is primary due to the limiting natural convection process on the tank side.

8.8 SUMMARY

The standard TRNSYS TYPE 60 stratified tank routine was extended to cover both the new heat exchangers investigated in this study by implementing new non-dimensional heat transfer correlations developed in Chapter 6 for narrow-gap mantle heat exchangers and Chapter 7 for falling film heat exchangers. For both mantle and falling film heat exchangers performance predictions using the modified TRNSYS TYPE 60 model are in good agreement with measurements in the prototype units.

To predict the long-term performance of solar water heaters incorporating either a mantle heat exchanger or a falling film heat exchanger, two system simulation models were developed for each system configuration. Features that have been added to TRNSYS are:

- New non-dimensional heat transfer correlations for both heat exchangers (modified TYPE 60),
- New differential controller routine developed for the advanced switching controller strategy applied in falling film systems for modulating the collector flow rate,
- The thermal capacitance of the high mass steel collectors used in the falling film system was modelled by coupling a zero mass collector model and a zero loss tank model for simulating both the energy stored in the collector during stagnation periods of the switching controller operation,
- The thermal capacitance of the pool in the bottom of the falling film tube was modelled using a zero loss tank coupled to a second heat exchanger.

The annual solar contribution of different system configurations was investigated based on representative meteorological weather data for Sydney and Melbourne in Australia. The seasonal load patterns for both capital cities specified in AS4234 with peak winter energy delivery of 40 MJ/day in Sydney and 42 MJ/day in Melbourne. The results are given in Table 8.4 and Table 8.5.

8. SYSTEM MODELLING

Table 8.4 Annual solar contribution of solar water heaters incorporating a mantle heat exchanger (3 mm spacing) in Sydney and Melbourne Australia.

NO.	PRODUCT CONFIGURATION	TANK SIZE (L)	MANTLE HEIGHT (m)	NO. COLLECTOR	LOCATION	ANNUAL f_R (%)
1	In-tank electric boosting	270	0.658	2	Sydney	73.3
2	In-tank electric boosting	270	0.658	2	Melbourne	57.6
3	In-tank electric boosting	330	0.886	3	Sydney	83.8
4	In-tank electric boosting	330	0.886	3	Melbourne	67.7

Table 8.5 Annual solar contribution of falling film solar water heaters in Sydney and Melbourne Australia.

NO.	PRODUCT CONFIGURATION	TANK SIZE (L)	LOCATION	ANNUAL f_R (%)
1	In-tank electric boosting	270	Sydney	64.0
2	In-tank electric boosting	270	Melbourne	46.9
3	Instantaneous gas boosting	270	Sydney	69.0
4	Instantaneous gas boosting	270	Melbourne	54.5
5	Instantaneous gas boosting	170	Sydney	65.3

- CHAPTER 9 -

CONCLUSIONS AND FUTURE WORK

9.1 OVERVIEW

This final chapter summarises research and concluding remarks on the results presented in the previous chapters. The work presented in this thesis involves evaluation of the performance of two innovative collector-loop heat exchangers for application in vertical-tank pumped-circulation solar water heaters. The heat exchangers evaluated are a narrow-gap mantle with two-pass flow arrangement and a falling film system modified from a standard gas hot water tank.

The methodology applied in this research is divided in three stages. Firstly, the heat exchangers were assessed by carrying out dynamic heat-up tests for a range of operating conditions. These experiments were aimed to quantify the overall heat exchanger UA_{hx} value and the effect of thermal stratification in the tank. Flow visualisation experiments and CFD modelling were also performed to provide detailed understanding of the operation characteristics of the heat exchangers. Secondly, to extend the TRNSYS program to cover the new heat exchanger designs, heat transfer coefficients on the collector-side and tank-side of these heat exchangers were determined to characterise the heat transfer rate of the heat exchangers as a function of dependent variables through detailed wall temperature measurements and CFD simulations. Thirdly, the heat transfer correlations developed for both types of heat exchanger have been implemented into full solar water heater simulation models in TRNSYS to predict the long-term performance of systems incorporating these heat exchangers for typical domestic hot water demand patterns. The concluding remarks on the results obtained are divided into three sections in Section 9.2.

9.2 CONCLUDING REMARKS

9.2.1 Mantle heat exchangers

The results obtained from flow visualisation and CFD modelling have shown that forced convection is dominant in narrow-gap mantles. Except for the impingement region near the inlet, approximate uniform flow and heat flux distribution was observed in narrow-gap mantles. As the mantle gap is increased, the flow in the mantle is gradually influenced by buoyancy forces directing the hot inlet stream towards the top section of the mantle.

From the prototype testing of a 270 L mantle-tank (base case system), measurements showed that for forced convection dominated flow conditions in a narrow-gap mantle the thermal resistance is primarily limited by the tank side convection. For such conditions the performance of a mantle heat exchanger depends on thermal stratification in the tank over the depth of the mantle.

The heat transfer data obtained from measurements and CFD simulations were generalised and collector loop side heat transfer coefficients were correlated by developing new Nusselt number versus Reynolds and Prandtl number correlations. In the lower Reynolds number range ($Re_d < 200$) the data approached the fully developed Nusselt number of 4.86 for flow between parallel plates. For natural convection circulation on the tank side of the heat exchanger, the measured mean Nusselt number agreed well with turbulent free convection on a flat plate, except for lower Rayleigh number conditions (below 3.7×10^{10}). A correlation was developed from a regression-fit to the measured data in the transition region between the laminar and turbulent flow that occurs at the beginning of the day.

For a larger mantle heat exchanger (315 L tank), the overall heat transfer coefficient was found to scale directly with the area ratio of the mantle heat exchanger surface in the 270 L and 315 L tanks.

9.2.2 Falling film heat exchangers

For a falling film system operating with a standard differential pump controller and steady collector flow rate, significant thermal stratification in the storage tank was observed. However, there is a risk of degradation of thermal stratification when the collector return temperature is cooler than the tank top temperature as the heat exchanger tube covers the full tank height. With the integration of an advanced switching controller to modulate the collector flow rate, measurements from preheated tank tests showed that thermal stratification can be maintained even under cloudy conditions. Measurements also showed that the falling film side thermal resistance is comparatively low and the factor limiting the performance of the heat exchanger is primarily the buoyancy driven circulation in the storage tank.

Visual evaluation of the wetting extent of the particular falling film system used in this investigation was undertaken in order to determine the mean heat transfer coefficient on the falling film side of the heat exchanger. For the prototype unit tested in this study, the wetted area was found to be approximately half of the total tube surface for typical operating conditions.

A Nusselt number correlation was developed in terms of Reynolds and Prandtl numbers, from a regression-fit to the measured data. The empirical expression developed from steady flow measurements was able to estimate the film side heat transfer coefficient for a system operating with a switching controller with an accuracy of 10%. On the tank side of the heat exchanger, measured free convective heat transfer coefficients were found to agree well with the standard flat-plate turbulent flow correlations.

9.2.3 Long-term performance

To predict the long-term performance of solar water heaters incorporating these heat exchangers, complete system simulation models were developed for each system configuration (base case system) by implementing new non-dimensional heat transfer correlations and with added features in TRNSYS.

Comparing two base case systems with a 270 L storage tank and in-tank electric boosting, the performance simulations showed that the annual solar contribution for a standard domestic hot water demand in Sydney drops from 79% for a standard direct-coupled system to 73.3% for a system with a mantle heat exchanger in the collector loop. The reduction in performance of mantle systems is due to reduced tank thermal stratification and the heat exchanger penalty. The simulated results also showed that mantle heat exchanger should not extend above the level of the auxiliary heater as the mantle fluid would remove heat from the auxiliary heated part of the tank when the mantle inlet temperature is lower than the set temperature and hence decrease system performance.

The long-term performance of two configurations of falling film systems was evaluated: as a single-tank system with in-tank boosting or as a solar pre-heater with an instantaneous gas booster. The findings are:

- 1) The winter energy savings obtained from load-cycle simulations for a single-tank system with in-tank electric boosting is lower than a standard direct-circulation system. The reduction in performance is because the system requires a high collector-return temperature relative to the top of the tank to avoid de-stratification, and as a consequence raising the collector operating temperature.
- 2) For the top film inlet design, the implementation of a switching controller into the falling film system is necessary as the performance simulations showed that the system without a switching controller has a 12% point reduction in winter performance due to de-stratification in the tank.
- 3) If the film inlet for the system is located just below the auxiliary portion therefore de-stratification in the tank is eliminated, the simulations results showed that there is insignificant influence of the advanced switching controller strategy for the system with mid-level-positioning of the falling film heat exchanger.
- 4) For a system operating as a solar pre-heater, the annual performance simulations showed that a 270 L falling film tank system with an in-line instantaneous gas heater out-performs the system with in-tank electric boosting during winter. This

could be due to improved thermal stratification in the storage tank as a result of removal of the in-tank booster resulting in better system performance.

In overall, the loss of performance for a falling film system is acceptable given the cost advantage of the system as well as reliable freeze protection that the falling film heat exchanger provides.

9.3 SUGGESTED FUTURE WORK

In this study, it was shown that narrow-gap mantle heat exchangers offer high heat transfer coefficient on the collector-loop side therefore the overall system performance is primarily limited by the tank side convection depending on degree of thermal stratification. To improve tank thermal stratification, a diffuser (Fig. 9.1) placing near the wall on the tank side of the heat exchanger would be used to promote thermal stratification in the tank. The use of a diffuser to promote tank stratification has been used in some immersed coil heat exchanger and external heat exchanger designs, but has not been applied to mantle-tanks. Further manufacturing considerations and heat transfer investigations on such mantle-tank configuration are needed.

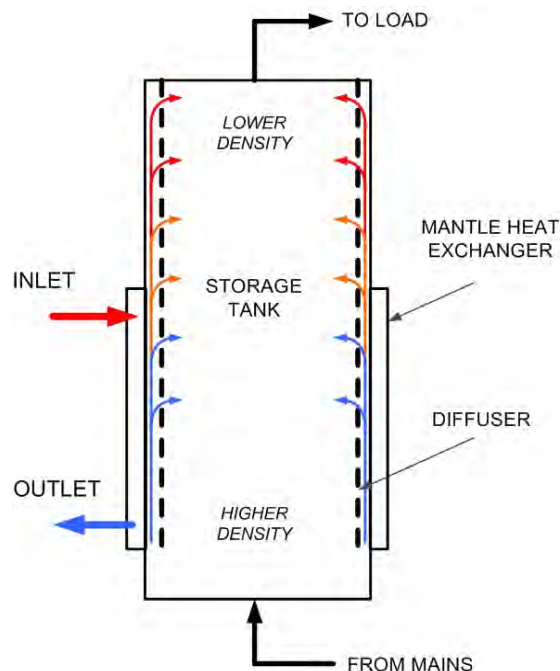


Fig. 9.1 Mantle-tank design with a diffuser inside the tank.

The work presented in this thesis revealed that falling film systems with in-tank electric boosting have lower winter performance due to the high collector return temperature required to avoid de-stratification of the boosted zone in the top of the tank. To overcome such problem, two sets of film distributors could be used, one fitted at the top of the heat exchanger tube and one fitted below the auxiliary element. The switching controller algorithm could select the level of entry depending on tank stratification and collector operating conditions. Alternatively, a side-arm auxiliary energy supply system could be used to improve the system performance due to significant thermal stratification in the storage tank as a result of removal of the in-tank booster, however this may increase the capital cost of the system.

Apart from further developments of physical systems, aspects that may offer scope for future research are:

- Develop heat transfer correlations for mantles covering the full height of the tank,
- Develop a general heat transfer correlations as a function of mantle gap ranging from forced-dominated flow in a narrow gap to buoyancy induced flow in a wide gap,
- The dependency of falling film side heat transfer coefficient on the film behaviour, such as wavy flow and wettability, for a range of falling film tube and film distributor designs.
- Develop simulation models with different parameter inputs for the purpose of system optimisation.

List Of References

Ambrosini, W., Forgione, N. and Oriolo, F., 2002, "Statistical characteristics of a water film falling down a flat plate at different inclinations and temperatures," *Int. J. Multiphase Flow*, Vol. 28, pp. 1521-1540.

AS4232, 1994, "Solar water heaters - Domestic and heat pump - Calculation of energy consumption," Standard Australia.

Barth, T.J and Jespersen, D., 1989, "The design and application of upwind schemes on unstructured meshed," Technical Report AIAA-89-0366, AIAA 27th Aerospace Sciences Meeting, Reno, Nevada.

Baur, J. M., Klein, S. and Beckman, W. A., 1993, "Simulation of water tanks with mantle heat exchangers," In *Proceedings, ASES Solar93*, pp. 286-291.

Beavers, G.S., Sparrow, E.M. and Magnuson, R.A., 1970, "Experiments on the breakdown of laminar flow in a parallel-plate channel," *Int. J. Heat Mass Transfer*, Vol. 13, pp. 809-815.

Benney, B.J., 1966, "Long waves in liquid films," *J. Math. Phys.*, Vol. 45, pp.150-155.

Berg, P., 1990, "Højtydende solvarmeanlæg med små volumenstrømme – teoretiske undersøgelser," Technical University of Denmark, Thermal Insulation Laboratory, Report 209.

Bird, R.B., Stewart, W.E. and Lightfoot, E.N., 2002, "Transport phenomena," John Wiley and Sons.

Brauer, H., 1956, "Strömung and Wärmeübergang bei Reiselfilme," *Ver. Deut. Ingr. Forschungsheft*, Vol. 457.

Brauner, N., 1987, "Roll wave celerity and average film thickness in turbulent wavy film flow," *Chemical Engineering Science*, Vol. 42, No. 2, pp. 265-273.

Brauner, N., 1989, "Modelling of wavy flow in turbulent free falling films," *Int. J. Multiphase Flow*, Vol. 15, No. 4, pp. 505-520.

Chang, H.C., 1994, "Wave evolution on a falling film," *Annu. Rev. Fluid Mech.*, Vol. 26, pp. 103-136.

Chu, K.J. and Dukler, A.E., 1974, "Statistical characteristics of thin, wavy films: part II. Studies of the substrate and its wave structure," *A.I.Ch.E.*, Vol. 20, pp. 695-706.

Drosos, E.I.P, Paras, S.V. and Karabelas, A.J., 2004, "Characteristics of developing free falling films at intermediate Reynolds and high Kapitza numbers," *Int. J. Multiphase Flow*, Vol. 30, pp. 853-876.

Farrington, R.B. and Bingham, C., 1986, "Testing and analysis of immersed heat exchangers," SERI/TR-254-2866, Golden, CO.

Feiereisen, T., Klein, S., Duffie, J. and Beckman, W., 1982, "Heat transfer from immersed coils," ASME 82-WA/Sol-18, Madison, University of Wisconsin.

Feind, K., 1960, "Strömungsuntersuchungen bei Gegenström von Reiselfilme und Gas in lotrechten Rohren," *Ver. Deut. Ingr. Forschungsheft*, Vol. 481.

FLUENT, 2005, Release FLUENT 6.2.16, FLUENT Inc., 10 Cavendish Court, Lebanon, NH03766, USA.

Fraser, K.F., Hollands, K.G.T. and Brunger, A.P., 1995, "An empirical model for natural convection heat exchangers in SDHW systems," *Solar Energy*, Vol. 55, pp. 75-84.

Fulford, G.D, 1964, "The flow of liquids in thin films," *Advanced Chemical Engineering*, Birmingham University, Vol. 5, pp. 151-236.

Furbo, S., 1993, "Optimum design of small DWH, low flow solar systems," In *ISES Solar World Congress*, Budapest, Hungary.

Furbo, S. and Berg, P., 1990, "Calculation of the thermal performance of small hot water solar heating systems using low flow operation," *North Sun 90*, Reading, UK.

Furbo, S. and Knudsen, S., 2005, "Heat transfer correlations in mantle tanks," In *ISES Solar World Congress*, Orlando, USA.

Harrison, S.J., 2005, "Passive heat exchanger anti-fouling for solar DHW systems," In *Proceedings of International Solar Energy Conference*, Orlando, USA.

IEA SHC, 2005, "Solar heating worldwide - Markets and contribution to the energy supply 2003".

Incropera, F.P. and DeWitt, D.P., 1996, "Introduction to heat transfer," John Wiley and Sons, 3rd.

Kakac, S., Shah, R.K. and Aung, W., 1987, "Handbook of single-phase convective heat transfer," John Wiley and Sons.

Kapitsa, P.L., 1948, *Zh. Eksperim. i Teor. Fiz.*, Vol. 18, pp. 3.

Karapantsios, T.D. and Karabelas, A.J., 1995, "Longitudinal characteristics of wavy falling films," *Int. J. Multiphase Flow*, Vol. 21, No. 1, pp. 119-127.

Klein, S.A *et al.*, 2001, "TRNSYS version 15 user manual," University of Wisconsin Solar Energy Laboratory.

Kline, S.J. and McClintock, F.A., 1953, "Describing uncertainties in single-sample experiments," *Mech. Eng.*, pp. 3.

Knudsen, S. and Furbo S., 2004, "Thermal stratification in vertical mantle heat exchangers with application to solar domestic hot water systems," *Applied Energy*, vol. 78, pp. 257-272.

Knudsen, S., Morrison, G.L., Behnia M., and Furbo, S., 2004, "Analysis of the Flow Structure and Heat Transfer in a Vertical Mantle Heat Exchanger," *Solar Energy*, vol. 78, pp. 281-289.

Knudsen, S., 2004, "Investigation and optimisation of heat storage tanks for low-flow SDHW systems," PhD thesis, Technical University of Denmark, Department of Buildings and Energy, Denmark.

Krantz, W.B. and Goren, S.L., 1971, "Stability of thin liquid films flowing down a plane," *Ind. Eng. Chem. Fund*, Vol. 10, pp. 91-101.

Launder, B.E. and Spalding, D.B., 1972, "Lectures in mathematical models of turbulence," Academic Press, London, England.

Menter, F.R., 1994, "Two-equation eddy-viscosity turbulence models for engineering applications," *AIAA Journal*, Vol. 32, pp. 1598-1605.

Mercer, W.E., Pearce, W.M. and Hitchcock, J.E., 1967, "Laminar forced convection in the entrance region between parallel flat plates," *ASME J. Heat Transfer*, Vol. 89, pp. 251-257.

Mertol, A., Place, W., Webster, T. and Greif, R., 1981, "Detailed loop model (DLM) analysis of liquid solar thermosiphons with heat exchangers," *Solar Energy*, Vol. 27, pp. 367-386.

Miller, J.A. and Hittle, D.C., 1995, "Experimental evaluation of a simulation model for wrap-around heat exchanger, solar storage tank," *Solar Engineering 1995, ASME Solar Energy Conference*, pp. 1117-1124.

Morrison, G.L., Nasr, A., Behnia, M. and Rosengarten, G., 1998, "Analysis of horizontal mantle heat exchangers in solar water heating systems," *Solar Energy*, Vol. 64, pp. 19-31.

Morrison, G.L., Rosengarten, G. and Behnia, M., 1999, "Mantle heat exchangers for horizontal tank thermosyphon solar water heaters," *Solar Energy*, Vol. 67, pp. 53-64.

Newton, B.J., 1995, "Modelling of solar storage tanks," M.S. Thesis, Department of Mechanical Engineering, University of Wisconsin-Madison.

Nusselt, W., 1923, *VDI (Ver. Deut. Ingr) Z.* 60, pp. 206.

Parent, M. G. H., Van Der Meer and Hollands, K. G. T., 1990, "Natural convection heat exchangers in solar water heating systems: theory and experiment," *Solar Energy*, Vol. 45, pp. 43-52.

Purdy, J. M., Harrison, S. J. and Osthuizen, P. H., 1998, "Thermal evaluation of compact heat exchangers in a natural convection application," In *Proceedings of the 11th International Heat Transfer Conference*, Kyongju, Korea, pp. 305-310.

Raffel, M., Willert, C.E. and Kompenhans, J., 1998, "Particle Image Velocimetry: A Practical Guide," Springer, New York.

Rosengarten, G., Morrison, G.L. and Behnia, M., 1999, "Some aspects concerning modelling the flow and heat transfer in horizontal mantle heat exchangers in solar water heaters," *Int. J. Energy Res.*, Vol. 23, pp. 1007-1016.

Rosengarten, G., Morrison, G.L. and Behnia, M., 2001, "Mixed convection in a narrow rectangular cavity with bottom inlet and outlet," *Int. J. Heat and Fluid Flow*, Vol. 22, pp. 168-179.

Shah, L.J. and Furbo, S., 1996, "Optimisation of mantle tanks for low flow solar heating systems," In *Proceedings EuroSun*, Freiburg, Germany, pp. 369-375.

Shah, L.J. and Furbo, S., 1998, "Correlation of experimental and theoretical heat transfer in mantle tanks used in low flow SDWH systems," *Solar Energy*, Vol. 64, pp. 245-256.

Shah, L.J., 1999, "Investigation and modelling of thermal conditions low flow SDHW systems," PhD thesis, Technical University of Denmark, Department of Buildings and Energy, Denmark.

Shah, L.J., Morrison, G.L. and Behnia, M., 1999, "characteristics of vertical mantle heat exchangers for solar water heaters," *Solar Energy*, Vol. 67, pp. 79-91.

Shah, L.J., 2000, "Heat transfer correlation for vertical mantle heat exchangers," *Solar Energy*, Vol. 69, pp. 157-171.

Shah, R.K. and London, A.L., 1978, "Laminar flow forced convection in ducts. A source book for compact heat exchanger analytical data," Academic Press.

Sparrow, E.M., 1955, "Analysis of laminar forced-convection heat transfer in entrance region of flat rectangular ducts," NACA TN3331.

Stephan, K., 1959, "Wärmeübertragung laminar strömender Stoffe in einseitig beheizten oder gekühlten ebenen Kanäken," *Chemie-Ing.-Techn.*, Vol. 32, pp. 401-404 .

Takahama, H. and Kato, S., 1980, "Longitudinal flow characteristics of vertically falling liquid films without concurrent gas flow," *Int. J. Multiphase Flow*, Vol. 6, pp. 203-215.

Trifonov, Y.Y. and Tselodub, O.Y., 1991, "Non-linear waves on the surface of a falling liquid film. Part 1. Waves of the first family and their stability," *J. Fluid Mech.*, Vol. 229, pp. 531-551.

Valentin, 2004, T*SOL Energies software.

Webb, D.R. and Hewitt, G., 1975, "Downwards co-current annular flow," *Int. J. Multiphase Flow*, Vol. 2, pp. 35-49.

Webster, T. L., Coutier, J. P., Place, J. W. and Tavana, M., 1987, "Experimental evaluation of solar thermosyphons with heat exchangers," *Solar Energy*, Vol. 38, pp. 219-231.

Wilcox, D.C., 1998, "Turbulence modelling for CFD," DCW Industries, Inc., La Canada, California.

Wilke, W., 1962, "Warmeübergang an Reiselfilme," V.D.I 490, *Forsch Hft* (In German).

Xinian, J., Zhen, T. and Junsheng, L., 1994, "Theoretical and experimental studies on sequential freezing solar water heater," *Solar Energy*, Vol. 53, pp. 139-146.

Yu, L.Q., Wasden, F.K., Duckler, A.E., Balakotaiah, V., 1995, "Nonlinear evolution of waves on falling films at high Reynolds numbers," *Phys. Fluids*, Vol. 7, pp. 1886-1902.

- Appendix A -

Uncertainty Analysis

This appendix presents the uncertainty analysis for heat transfer measurements.

A.1 Uncertainty in temperature measurement

All thermocouples (used for heat exchangers' inlet and outlet temperature measurements) were calibrated against a platinum resistance thermometer (Fluke SN143885) with an accuracy of $\pm 0.05^\circ\text{C}$ using a temperature-controlled water bath (EXTECH, Model 7312). The temperatures were scanned through differential channels in a datataker, and were recorded on a PC through a serial communication port RS232 as one minute averages. A linear-least-squares line of best fit was used to relate temperature sensor reading to the platinum resistance thermometer temperature. Typical error deviation observed in the mean least squares fitting procedures was $\pm 0.1^\circ\text{C}$. The overall temperature sensor error (ω_T) is a function of the platinum resistance thermometer error (ω_p) and the curve fitting error (ω_c):

$$\omega_T = f(\omega_c, \omega_p) \quad (\text{A.1})$$

This function can be approximated by

$$\begin{aligned} \omega_T^2 &= \omega_c^2 + \omega_p^2 \\ &= \pm 0.11K \end{aligned} \quad (\text{A.2})$$

After thermocouples were attached on the tank side of the wall of the mantle heat exchanger surface, a second test was performed by mixing the volume of the mantle to a uniform temperature using a temperature-controlled water bath. For the temperature range from 18°C to 55°C , variations between sensors were observed to be $\pm 0.2^\circ\text{C}$.

Thermocouples used for tank temperature measurements were calibrated against a platinum resistance thermometer using a temperature-controlled water bath. For the temperature range from 10°C to 70°C, variations between sensors were observed to be $\pm 0.11^\circ\text{C}$.

As thermocouples were pre-installed in the tank core and on the outer wall of the core tube of the falling film heat exchanger during tank construction, these thermocouples could only be calibrated by pump-circulating the tank core water through an external loop fitted with calibrated thermocouples for a temperature range from 30 to 70°C. During this checking process, the insulated tank was isolated from the collector-loop and the core water was pre-conditioned at the required temperature level. For the range of temperatures considered in the set of experiments, variations between sensors were observed to be $\pm 0.3^\circ\text{C}$.

A.2 Uncertainty in flow measurement

Two low-flow turbine flow meters (OMEGA FTB9510) were used in this study to measure the volume flow rate on the hot side of the heat exchanger, one used for the mantle heat exchanger (flow meter 1) and one used for the falling film heat exchanger (flow meter 2). Both flow meters were calibrated by comparing frequency output against measured water flow rate over a five-minute period at temperature of 25°C. The data were scanned through differential channels in a datataker, and were recorded on a PC through a serial communication port RS232 as one minute averages. A linear-least-squares line of best fit was used, by plotting frequency output proportional to the flow rate. Maximum error deviation observed in the mean least squares fitting procedures was ± 17 mL/min for the flow meter 1 and ± 13 mL/min for the flow meter 2.

A.3 Uncertainty analysis

The uncertainty analysis for heat transfer measurements is performed using the method proposed by Kline and McClintock (1953). The desired result is a function of the variables x_1, x_2, \dots, x_n as follows:

$$R = R(x_1, x_2, \dots, x_n) \quad (\text{A.3})$$

and the uncertainty of the desired result (w_R) is:

$$w_R = \left[\left(\frac{\partial R}{\partial x_1} w_1 \right)^2 + \left(\frac{\partial R}{\partial x_2} w_2 \right)^2 + \dots + \left(\frac{\partial R}{\partial x_n} w_n \right)^2 \right]^{1/2} \quad (\text{A.4})$$

where w_n is the uncertainty in the independent variables.

Uncertainty in total heat transfer rate

The equation for total heat transfer rate across the heat exchanger is:

$$\dot{Q} = \dot{m} c_p (T_i - T_o) = \dot{m} c_p \Delta T \quad (\text{A.5})$$

Using the method proposed by Kline and McClintock (1953) given in Eqn. A.4, the uncertainty in the total heat transfer rate measurements is defined as:

$$(\delta \dot{Q})^2 = \left(\frac{\partial \dot{Q}}{\partial \dot{m}} \delta \dot{m} \right)^2 + \left(\frac{\partial \dot{Q}}{\partial T_i} \delta T_i \right)^2 + \left(\frac{\partial \dot{Q}}{\partial T_o} \delta T_o \right)^2 \quad (\text{A.6})$$

assuming specific heat (c_p) is constant.

Sensors that used to determine the heat transfer rate are the thermocouples at the heat exchanger inlet and outlet and the volumetric flow meter. An example of the relative uncertainty in the heat transfer rate measurement for mantle heat exchanger is:

$$\frac{\delta \dot{Q}}{\dot{Q}} = \sqrt{\left(\frac{2.83 \times 10^{-4}}{\dot{m}} \right)^2 + \left(\frac{0.11}{T_i} \right)^2 + \left(\frac{0.11}{T_o} \right)^2} \quad (\text{A.7})$$

Table A.1 and Table A.2 show the uncertainties in total heat transfer rate measurements for both mantle and falling film heat exchangers under typical operating conditions.

Table A.1 Uncertainty in heat transfer rate measurements of mantle heat exchanger.

\dot{m} (kg/s)	$\delta \dot{m}$ (kg/s)	T_i (°C)	T_o (°C)	δT (°C)	UNCERTAINTY IN \dot{Q} (%)
0.0331	$\pm 2.83 \times 10^{-4}$	28.4	23.1	± 0.11	1.1
0.0340	$\pm 2.83 \times 10^{-4}$	53.3	38.0	± 0.11	0.9
0.0606	$\pm 2.83 \times 10^{-4}$	40.0	33.3	± 0.11	0.6

A. Uncertainty Analysis

Table A.2 Uncertainty in heat transfer rate measurements of falling film heat exchanger.

\dot{m} (kg/s)	$\delta\dot{m}$ (kg/s)	T_i (°C)	T_o (°C)	δT (°C)	UNCERTAINTY IN \dot{Q} (%)
0.0360	$\pm 2.17 \times 10^{-4}$	40.0	28.6	± 0.11	0.8
0.0501	$\pm 2.17 \times 10^{-4}$	60.2	49.2	± 0.11	0.5

Uncertainty in mean Nusselt number

The equation for the mean Nusselt number on the hot side of the heat exchanger is:

$$Nu_{hot} = \frac{\dot{Q}d_h}{Ak\left(\frac{1}{2}(T_i + T_o) - T_{wall}\right)} \quad (A.8)$$

and on the cold side of the heat exchanger is:

$$Nu_{cold} = \frac{\dot{Q}d_h}{Ak(T_{wall} - T_{tank})} \quad (A.9)$$

The uncertainty in the mean Nusselt number on the hot side of the heat exchanger is:

$$(\delta Nu)^2 = \left(\frac{\partial Nu}{\partial \dot{Q}} \delta \dot{Q}\right)^2 + \left(\frac{\partial Nu}{\partial T_i} \delta T_i\right)^2 + \left(\frac{\partial Nu}{\partial T_o} \delta T_o\right)^2 + \left(\frac{\partial Nu}{\partial T_w} \delta T_w\right)^2 \quad (A.10)$$

assuming area (A) and thermal conductivity (k) are constant.

In a similar way the uncertainty in the mean Nusselt number on the cold side of the heat exchanger is:

$$(\delta Nu)^2 = \left(\frac{\partial Nu}{\partial \dot{Q}} \delta \dot{Q}\right)^2 + \left(\frac{\partial Nu}{\partial T_w} \delta T_w\right)^2 + \left(\frac{\partial Nu}{\partial T_{tank}} \delta T_{tank}\right)^2 \quad (A.11)$$

Table A.3 and Table A.4 show the uncertainties in mean Nusselt number on the hot and cold sides of both mantle and falling film heat exchangers.

A. Uncertainty Analysis

Table A.3 Uncertainty in mean Nusselt number on hot-side and cold-side of mantle heat exchanger.

\dot{m} (kg/s)	UNCERTAINTY IN Nu_{hot} (%)	UNCERTAINTY IN Nu_{cold} (%)
0.0340	1.3	1.1
0.0606	1.1	0.6

Table A.4 Uncertainty in mean Nusselt number on hot-side and cold-side of falling film heat exchanger.

\dot{m} (kg/s)	UNCERTAINTY IN Nu_{hot} (%)	UNCERTAINTY IN Nu_{cold} (%)
0.0340	1.4	1.6
0.0501	0.8	0.9

- Appendix B -

Fluid Properties

The fluid property data used in all the data analysis is presented. The properties of pure water are given in heat transfer textbook (Incropera and DeWitt, 1996). The properties of the propylene glycol/water mixture obtained from Engineering Equation Solver (EES) (Klein, 2006) are given in the following:

- Density (kg/m³)

$$\rho = B + C \times T + D \times T^2 \quad (\text{B1})$$

$$B = 875.54696219 + 2.151387542 \times \text{per}$$

$$C = 1.1191046068 - 0.0007599907262 \times \text{per} - 4.9236799989 \times 10^{-5} \times \text{per}^2$$

$$D = -0.002377960199 - 9.1377252136 \times 10^{-6} \times \text{per} + 1.0872237562 \times 10^{-7} \times \text{per}^2$$

- Specific heat capacity (kJ/kgK)

$$C_p = B + C \times T \quad (\text{B2})$$

$$B = 3.8649883866 - 0.023691954902 \times \text{per} - 0.00011278222908 \times \text{per}^2$$

$$C = 0.001023655712 + 5.6633876714 \times 10^{-5} \times \text{per}$$

- Thermal conductivity (W/mK)

$$k = B + C \times T + D \times T^2 \quad (\text{B3})$$

$$B = -0.78595253278 + 0.015561899561 \times \text{per} - 4.8933521576 \times 10^{-5} \times \text{per}^2$$

$$C = 0.0076866167254 - 0.0001155974176 \times \text{per} + 3.6603360830 \times 10^{-7} \times \text{per}^2$$

B. Fluid Properties

$$D = -9.9976810237 \times 10^{-6} + 1.4560615474 \times 10^{-7} \times per - 4.5879383578 \times 10^{-10} \times per^2$$

- Kinematic viscosity (m^2/s)

$$\nu = \exp(B + C \times per) \quad (B4)$$

$$B = 71.639163222 - 0.66981698459 \times T + 0.0019150513174 \times T^2 - 1.8587687783 \times 10^{-6} \times T^3$$

$$C = 0.27019804611 - 0.0012299975866 \times T + 1.5045427918 \times 10^{-6} \times T^2$$

where: T is the fluid temperature (K),

per is the percentage of propylene glycol in the mixture (%).